

ARL-TR-82-8

Copy No. 51

**A STUDY OF THE
BROADBAND PARAMETRIC ACOUSTIC ARRAY**

John M. Huckabay

**APPLIED RESEARCH LABORATORIES
THE UNIVERSITY OF TEXAS AT AUSTIN
POST OFFICE BOX 8039, AUSTIN, TEXAS 78712**

4 January 1982

Technical Report

**APPROVED FOR PUBLIC RELEASE;
DISTRIBUTION UNLIMITED.**

Prepared for:

**NAVAL SEA SYSTEMS COMMAND
DEPARTMENT OF THE NAVY
WASHINGTON, DC 20362**



82 03 08 035

AD A111746

DTIC FILE COPY

R

UNCLASSIFIED

SECURITY CLASSIFICATION OF THIS PAGE (When Data Entered)

REPORT DOCUMENTATION PAGE		READ INSTRUCTIONS BEFORE COMPLETING FORM
1. REPORT NUMBER	2. GOVT ACCESSION NO.	3. RECIPIENT'S CATALOG NUMBER
4. TITLE (and Subtitle) A STUDY OF THE BROADBAND PARAMETRIC ACOUSTIC ARRAY		5. TYPE OF REPORT & PERIOD COVERED technical report
7. AUTHOR(s) John M. Huckabay		6. PERFORMING ORG. REPORT NUMBER ARL-TR-82-6
9. PERFORMING ORGANIZATION NAME AND ADDRESS Applied Research Laboratories The University of Texas at Austin Austin, Texas 78712		8. CONTRACT OR GRANT NUMBER(s) N00024-79-C-6358
11. CONTROLLING OFFICE NAME AND ADDRESS Naval Sea Systems Command Department of the Navy Washington, DC 20362		10. PROGRAM ELEMENT, PROJECT, TASK AREA & WORK UNIT NUMBERS
14. MONITORING AGENCY NAME & ADDRESS (if different from Controlling Office)		12. REPORT DATE 4 January 1982
		13. NUMBER OF PAGES 240
		15. SECURITY CLASS. (of this report) UNCLASSIFIED
		15a. DECLASSIFICATION/DOWNGRADING SCHEDULE
16. DISTRIBUTION STATEMENT (of this Report) APPROVED FOR PUBLIC RELEASE; DISTRIBUTION UNLIMITED.		
17. DISTRIBUTION STATEMENT (of the abstract entered in Block 20, if different from Report)		
18. SUPPLEMENTARY NOTES		
19. KEY WORDS (Continue on reverse side if necessary and identify by block number)		
20. ABSTRACT (Continue on reverse side if necessary and identify by block number) The characteristics of the broadband parametric acoustic array are studied both theoretically and experimentally as a function of primary frequency directivity. The broadband parametric array describes the sound field produced by the non-linear interaction of the frequency components of a pulsed primary signal. In the present investigation, the secondary sound field of the baseband modulation products is considered. The primary transmissions are produced by physically realizable sources, and the broadband parametric array for nonplane wave fields is developed.		

DD FORM 1 JAN 73 1473

EDITION OF 1 NOV 65 IS OBSOLETE

UNCLASSIFIED

SECURITY CLASSIFICATION OF THIS PAGE (When Data Entered)

UNCLASSIFIED

SECURITY CLASSIFICATION OF THIS PAGE(When Data Entered)

20. (Cont'd)

A general solution for the parametric array for nonplane wave fields is presented in the form of the superposition of primary field components. These components are assumed to be spherically spreading from the origin and characterized throughout the sound field by a single, frequency dependent directivity function, or off-axis transfer function. The general solution is reduced from a four-dimensional integration to a two-dimensional integration by assuming the directivity to be symmetric about the acoustic axis and restricting the region of validity to the farfield of the parametric array. The farfield solution is obtained for a Gaussian pulse primary transmission emitted by a circular piston source. The solution is evaluated in limiting forms as a function of directivity. When the primary beam is extremely narrow, the parametric array is absorption limited and the parametric array for plane wave fields is recovered. The characteristics of the secondary off-axis transfer function are determined by the absorption at the primary frequencies and are monotonically decreasing with angle off-axis and secondary frequency. When the Rutherford beamwidth is small compared to the primary beamwidths, the parametric array is diffraction limited. The characteristics of the secondary off-axis transfer function in the diffraction limit generally follow that of the primary off-axis transfer function with off-axis angle but are relatively insensitive to secondary frequency. As the parametric array shifts from absorption limited to the diffraction limited, the dependence on secondary frequency changes from quadratic to linear. This change is characterized by a shift toward lower frequencies in the secondary spectra and a reduction in the on-axis frequency at the spectral peak by a factor of $\sqrt{2}$ for a Gaussian pulse primary transmission.

An experimental study of the broadband parametric array is presented which provides data with variations in experimental parameters and an emphasis on the behavior as a function of primary directivity. The results for low amplitude primary signals generally confirm the theoretical predictions. An extreme sensitivity to the sidelobe structure in the primary off-axis transfer function is noted in the frequency at the spectral peak of the secondary power spectra. No such sensitivity was noted in the level at the spectral peak or in the secondary power beam pattern. For high amplitude primary signals, the results indicate that envelope distortion due to finite amplitude effects in the primary signal causes spectral distortion in the secondary signals. The spectral distortion is greatest on-axis where the frequency at the spectral peak is reduced. Far off-axis, the characteristics are the same as those for low amplitude primary transmissions.

Accession For	
NTIS Grant	<input checked="" type="checkbox"/>
DTIC F & S	<input type="checkbox"/>
Unpublished	<input type="checkbox"/>
Justification	
By	
Distribution	
Availability Codes	
Dist	

DTIC
COPY
UNPUBLISHED

UNCLASSIFIED

SECURITY CLASSIFICATION OF THIS PAGE(When Data Entered)

TABLE OF CONTENTS

	<u>Page</u>
LIST OF FIGURES	v
LIST OF TABLES	xi
LIST OF SYMBOLS	xiii
CHAPTER I INTRODUCTION	1
CHAPTER II THEORETICAL BACKGROUND	5
A. The Inhomogeneous Wave Equation	5
B. The Narrowband Parametric Array for Plane Wave Fields	14
C. The Narrowband Parametric Array for Nonplane Wave Fields	19
D. The Broadband Parametric Array for Plane Wave Fields	26
E. The Broadband Parametric Array for Nonplane Wave Fields	29
F. The Parametric Acoustic Array with Finite Amplitude	33
Primary Waves	
CHAPTER III THEORETICAL CONSIDERATIONS FOR THE BROADBAND	37
PARAMETRIC ARRAY	
A. Radiation in the Farfield of the Broadband Parametric	37
Array for Plane Wave Fields with Low Amplitude Primary	
Waves	
1. General Solution	37
2. On-Axis Radiation	38
3. Off-Axis Radiation	48
B. Radiation in the Farfield of the Broadband Parametric	51
Array for Nonplane Wave Fields with Low Amplitude	
Primary Waves	

	<u>Page</u>
1. General Solution	51
2. Farfield Solution	56
3. Farfield Solution with a Gaussian Pulse Primary Transmission from a Circular Piston	67
CHAPTER IV EXPERIMENTAL STUDY OF THE BROADBAND PARAMETRIC ARRAY	81
A. Equipment and Procedures	82
B. The Broadband Parametric Array with Low Amplitude Primary Waves	89
1. High Primary Directivity	89
2. Performance as a Function of Primary Directivity	106
3. Cross Function Analysis	122
C. The Broadband Parametric Array with High Amplitude Primary Waves	127
1. The Primary Field	127
2. The Secondary Field	138
CHAPTER V SUMMARY AND CONCLUSIONS	161
APPENDIX A RADIATION OF A PULSED CARRIER IN THE FARFIELD OF A CIRCULAR PISTON	169
APPENDIX B EXPERIMENTAL EQUIPMENT	189
APPENDIX C ANALYSIS OF UNGATED SECONDARY OUTPUTS	215
REFERENCES	223

LIST OF FIGURES

<u>Figure</u>	<u>Title</u>	<u>Page</u>
2.1	Geometry for Analysis of a Parametric Acoustic Array for Plane Wave Fields	16
2.2	Geometry for Analysis of a Parametric Acoustic Array for Nonplane Wave Fields	22
2.3	Geometry for Analysis of a Parametric Acoustic Array for Nonplane Wave Fields	24
3.1	Off-Axis Power Transfer Function for the Radiation in the Farfield of the Broadband Parametric Array for Plane Wave Fields	39
3.2	On-Axis Pulse Shape for the Broadband Parametric Array for Plane Wave Fields with a Gaussian Pulse Primary Transmission	42
3.3	Frequency at Which the On-Axis Secondary Pressure is a Maximum as a Function of the Primary Center Frequency with the Q of a Gaussian Pulse Primary Transmission as a Parameter	44
3.4	Power Density Spectra for the On-Axis Transmission of the Broadband Parametric Array for Plane Wave Fields with the Q of the Gaussian Pulse Primary Transmission as a Parameter	46
3.5	Spherical Geometry for Analysis of a Parametric Acoustic Array for Nonplane Wave Fields with the Acoustic Axis Along the z-Axis	58
3.6	Spherical Geometry for Analysis of a Parametric Acoustic Array for Nonplane Wave Fields with the Field Point on the z-Axis	64
3.7	Off-Axis Power Transfer Function versus Frequency for the Extreme Diffraction Limited Broadband Parametric Array for Nonplane Wave Fields	72

<u>Figure</u>	<u>Title</u>	<u>Page</u>
3.8	Off-Axis Power Transfer Function versus Off-Axis Angle for the Extreme Diffraction Limited Broadband Parametric Array for Nonplane Wave Fields	74
3.9	Off-Axis Power Transfer Function versus Frequency for the Extreme Diffraction Limited Broadband Parametric Array for Nonplane Wave Fields	77
3.10	Off-Axis Power Transfer Function versus Off-Axis Angle for the Extreme Diffraction Limited Broadband Parametric Array for Nonplane Wave Fields	78
4.1	Block Diagram of Experiments	84
4.2	Selectable Radius Circular Piston Projector (ARL 384-1)	86
4.3	On-Axis Acoustic Waveforms for the Broadband Parametric Array	91
4.4	Off-Axis Acoustic Waveforms for the Broadband Parametric Array	92
4.5	Autocorrelation of the Off-Axis Acoustic Signals for the Broadband Parametric Array	93
4.6	Normalized Power Density Spectra On-Axis for the Broadband Parametric Array	95
4.7	Normalized Power Density Spectra for the Broadband Parametric Array at Off-Axis Angles from 0.00° to 1.75°	97
4.8	Normalized Power Density Spectra for the Broadband Parametric Array at Off-Axis Angles from 1.75° to 3.00°	98
4.9	Frequency and Level at the Spectral Peak Off-Axis for the Broadband Parametric Array	99
4.10	Secondary Power Beam Pattern for the Broadband Parametric Array	104
4.11	Comparison of Secondary Power Beam Pattern Representations	105
4.12	Frequency and Level at the Spectral Peak Off-Axis for the Broadband Parametric Array	107
4.13	Secondary Power Beam Pattern for the Broadband Parametric Array	110

<u>Figure</u>	<u>Title</u>	<u>Page</u>
4.14	Frequency and Level at the Spectral Peak Off-Axis for the Broadband Parametric Array	111
4.15	Secondary Power Beam Pattern for the Broadband Parametric Array	113
4.16	Frequency and Level at the Spectral Peak Off-Axis for the Broadband Parametric Array	114
4.17	Secondary Power Beam Pattern for the Broadband Parametric Array	116
4.18	Frequency and Level at the Spectral Peak Off-Axis for the Broadband Parametric Array and Several Source Piston Radii	117
4.19	Frequency at the Spectral Peak for the Broadband Parametric Array Off-Axis for Several Source Piston Radii	119
4.20	Relative Level at the Spectral Peak for the Broadband Array Off-Axis for Several Source Piston Radii	120
4.21	Relationship Between Primary and Secondary Directivity and Source Piston Radius for the Broadband Parametric Array	121
4.22	Crosscorrelation of On-Axis and Off-Axis Signals for the Broadband Parametric Array	124
4.23	Normalized Cross-Power Amplitude Spectra of On-Axis and Off-Axis Signals for the Broadband Parametric Array	125
4.24	Cross-Power Phase Spectra of On-Axis and Off-Axis Signals for the Broadband Parametric Array	126
4.25	On-Axis Primary Waveforms as a Function of Source Level	128
4.26	Primary Peak Sound Pressure Level	130
4.27	Primary Peak Source Level at R_0	132
4.28	Primary Source Directivity as a Function of Source Level	134
4.29	Primary Source Directivity as a Function of Source Level	135
4.30	Primary Source Directivity as a Function of Source Level	136
4.31	Primary Source Directivity as a Function of Source Level	137
4.32	Off-Axis Acoustic Waveforms for the Broadband Parametric Array with High Amplitude Primary Level	140

<u>Figure</u>	<u>Title</u>	<u>Page</u>
4.33	Normalized Power Density Spectra for the Broadband Parametric Array with High Amplitude Primary Level at Off-Axis Angles from 0.00° to 2.25°	142
4.34	Normalized Power Density Spectra for the Broadband Parametric Array with High Amplitude Primary Level at Off-Axis Angles from 2.25° to 4.00°	143
4.34	Frequency and Level at the Spectral Peak Off-Axis for the Broadband Parametric Array with High Amplitude Primary Level	144
4.36	Secondary Source Directivity as a Function of Primary Peak Sound Pressure Level	145
4.37	Frequency and Level at the Spectral Peak Off-Axis for the Broadband Parametric Array with High Amplitude Primary Level	146
4.38	Secondary Source Directivity as a Function of Primary Peak Sound Pressure Level	148
4.39	Frequency and Level at the Spectral Peak Off-Axis for the Broadband Parametric Array with High Amplitude Primary Level	149
4.40	Secondary Source Directivity as a Function of Primary Peak Sound Pressure Level	150
4.41	Frequency and Level at the Spectral Peak Off-Axis for the Broadband Parametric Array with High Amplitude Primary Level	151
4.42	Secondary Source Directivity as a Function of Primary Peak Sound Pressure Level	152
4.43	Secondary Peak Sound Pressure Level at the Spectral Peak	154
4.44	Primary and Secondary Half-Power Beamwidth	155
4.45	Crosscorrelation of On-Axis and Off-Axis Signals for the Broadband Parametric Array with High Amplitude Primary Level	157

<u>Figure</u>	<u>Title</u>	<u>Page</u>
4.46	Normalized Cross Power Amplitude Spectra of On-Axis and Off-Axis Signals for the Broadband Parametric Array with High Amplitude Primary Level	158
4.47	Cross-Power Phase Spectra of On-Axis and Off-Axis Signals for the Broadband Parametric Array with High Amplitude Primary Level	159
A.1	Off-Axis Power Transfer Function for the Radiation in the Farfield of a Circular Piston Set in an Infinite Rigid Baffle	173
A.2	Normalized Power Density Spectra Predicted for a Circular Piston at Off-Axis Angles from 0.00° to 2.25°	182
A.3	Frequency and Level at the Spectral Peak Predicted Off-Axis for a Circular Piston	183
A.4	Normalized Power Density Spectra Predicted for a Circular Piston at Off-Axis Angles from 0.00° to 2.25°	185
A.5	Frequency and Level at the Spectral Peak Predicted Off-Axis for a Circular Piston	187
B.1	Transmitter	192
B.2	Block Diagram of Shaped Pulse Signal Generator	193
B.3	Transmit Voltage Response for the Selectable Radius Circular Piston Projector (ARL 384-1)	196
B.4	600 kHz Primary Frequency Beam Patterns Measured at 11.7 m for the Selectable Radius Circular Piston Projector (ARL 384-1)	198
B.5	600 kHz Primary Frequency Beam Patterns Measured at 11.7 m for the Selectable Radius Circular Piston Projector (ARL 384-1)	199
B.6	600 kHz Primary Frequency Beam Patterns Measured at 11.7 m for the Selectable Radius Circular Piston Projector (ARL 384-1)	200
B.7	600 kHz Primary Frequency Beam Patterns Measured at 11.7 m for the Selectable Radius Circular Piston Projector (ARL 384-1)	201

<u>Figure</u>	<u>Title</u>	<u>Page</u>
B.8	Receive Systems	203
B.9	Characteristics of the High Frequency Receive System	205
B.10	Freefield Voltage Sensitivity, ARL 239-1 Hydrophone (Low Frequency)	207
B.11	Freefield Voltage Sensitivity for the ARL 239-1 Hydrophone (High Frequency)	208
B.12	Freefield Voltage Sensitivity for the ARL 239-1 Low Frequency Receiver with 40 dB Gain	209
B.13	Freefield Voltage Sensitivity for the ARL 239-1 High Frequency Receiver with 40 dB Gain	210
B.14	Farfield Beam Pattern at 150 kHz for the ARL 239-1 Hydrophone Measured at 11.7 m	211
B.15	Freefield Voltage Sensitivity, E27-130P	213
C.1	Off-Axis Acoustic Waveforms for the Broadband Parametric Array	218
C.2	Normalized Power Density Spectra for the Broadband Parametric Array at Off-Axis Angles from 0.00° to 1.75°	219
C.3	Normalized Power Density Spectra for the Broadband Parametric Array at Off-Axis Angles from 1.75° to 3.00°	220

LIST OF TABLES

<u>Table</u>	<u>Title</u>	<u>Page</u>
IV.1	Experimental Parameter Values	83
IV.2	Directional Properties of the Selectable Radius Circular Piston Projector (ARL 384-1) at 600 kHz	87
IV.3	Summary of Measured Primary Source Data	139
A.1	Example Parameter Values for Radiation from a Circular Piston	181
B.1	Electrical Properties at Low Level of the Selectable Radius Circular Piston Projector (ARL 384-1) at 600 kHz	202

LIST OF SYMBOLS

Symbol

a	radius of a circular piston
\vec{A}	reference vector along the acoustic axis
B/A	the parameter of nonlinearity
c'	propagation speed
c_o	small signal sound speed
c_1, c_2	simplifying variables
$D(\cdot)$	directivity function
$D_{1n}(\cdot), D_{2n}(\cdot)$	directivity function of the nth frequency components of the primary and secondary waves, respectively
$D_v(\cdot)$	directivity function for the convolution integral
$D_{vN}(\cdot)$	normalized directivity function for the convolution integral
e	Naperian base
$E_{xx}(f)$	energy spectral density function
$E_{xxN}(f)$	normalized energy spectral density function
f	frequency
f_1, f_2	frequency of the primary and secondary waves, respectively
f_{1c}, f_{2c}	carrier or center frequency of the primary and secondary waves, respectively
f_{1n}, f_{2n}	the nth frequency components of the primary and secondary waves, respectively
f_{2p}	secondary frequency at which the on-axis pressure is a maximum
f_d	$ f_{1n} - f_{1m} $, difference primary frequency
$f(t)$	primary pulse shape function
$F_{11}, F_{12}, F_{21}, F_{22}$	lower and upper half energy or power frequencies for the primary and secondary transmissions, respectively

$F(f)$	$\mathcal{F}\{f(t)\}$, Fourier transform of the primary envelope function
$\mathcal{F}\{.\}$	Fourier transform
$\mathcal{F}^{-1}\{.\}$	inverse Fourier transform
$g(t)$	inverse Fourier transform
$G(f)$	Fourier transform
$h(\cdot)$	impulse response function
$h_{1\theta}(t), h_{2\theta}(t)$	off-axis impulse response function for the first order (primary) and the second order (secondary) fields, respectively
$H(\cdot)$	transfer function
$H_{1\theta}(f), H_{2\theta}(f)$	off-axis transfer function for the first order (primary) and the second order (secondary) fields, respectively
$i(t)$	input time function
I	integral
k	ω/c_0 , wave number
k_1, k_2	wave number for the nth frequency components of the primary and secondary waves, respectively
k_d	$ k_{1n} - k_{1m} $, difference primary wave number
K	undetermined constant
l	upper limit of integration
n	constant which determines the effective duration of a Gaussian pulse
\vec{n}	unit vector in the direction of sound propagation
$O(t)$	output time function
p	pressure
p_0, p_1, p_2	static, first order (primary), and second order (secondary) pressure, respectively
p_0	peak primary pressure amplitude at a reference range
p_{on}	primary pressure amplitude of the nth frequency component at a reference range
P_1, P_2	Fourier transform of the first and second order pressure, respectively

$P_{xx}(f)$	power spectral density function
$P_{1xxN}(f), P_{2xxN}$	normalized power spectral density function for the primary and secondary signals, respectively
$P_{2xyN}(f)$	normalized cross power amplitude spectral density function for the secondary signal
q	source strength density
q_n	nth frequency component of the source strength density
Q	quality factor
Q_1, Q_2	quality factor for the primary and secondary transmissions, respectively
Q_{lp}	quality factor for the primary transmission which yields a peak secondary transmission
r	magnitude of \vec{r}
\vec{r}	vector from the origin to the field point
r_o	magnitude of \vec{r}_o
\vec{r}_o	vector from the origin to the volume element of integration
R	magnitude of \vec{R}
\vec{R}	vector from the volume element of integration to the field point
R_o	nearfield parameter = S_o / λ
S	entropy
S_o	crosssectional area
$S(t)$	simplified time function
SL_1, SL_2	primary and secondary peak source level, respectively
SDR	step-down ratio
SPL_1, SPL_2	primary and secondary peak sound pressure level, respectively
t	time
t_o	reference time
T	duration of a pulse
u	magnitude of the sound velocity

\vec{u}	sound velocity
$\vec{u}_0, \vec{u}_1, \vec{u}_2$	static, first order (primary), and second order (secondary) sound velocity, respectively
$u(t)$	gate time function
v_0	interaction volume
x	rectilinear coordinate
y	rectilinear coordinate
z	rectilinear coordinate
α	absorption coefficient
$\bar{\alpha}$	$(\alpha_{1n} + \alpha_{1m})/2$, average absorption coefficient for the primary wave
α_{1c}	absorption coefficient at the carrier or primary center frequency
α_{1n}, α_{2n}	absorption coefficient for the nth frequency components of the primary and secondary waves, respectively
α_d	absorption coefficient corresponding to the difference frequency
β	$1 + B/2A$
γ	angle between \vec{r}_0 and \vec{r}
$\delta(\cdot)$	Dirac delta function
Δ	strength of a delta function
ϵ	angle between the acoustic axis and the projection of the acoustic axis in the x,z plane
ψ	angle of rotation about the acoustic axis for the projection of \vec{r} , angle of rotation about \vec{r} (Muir), angle between the projection of \vec{r}_0 on the x-y plane and \vec{r}_0 (Blue)
ψ_0	angle of rotation about the acoustic axis for the projection of \vec{r}_0
Ψ	angle between the projection of \vec{r}_0 on the x-y plane and the x axis (Blue)

ϕ	angle between \vec{r}_0 and \vec{r} (Muir), angle between the projection of \vec{r}_0 on the x-y plane and the x axis (Blue)
ϕ_e	angular increment
ϕ	angle between the projection of \vec{r} on the x-y plane and the x axis (Blue)
ω	$2\pi f$, angular frequency
ω_1, ω_2	angular frequency of the primary and secondary waves, respectively
ω_{1n}, ω_{2n}	the nth angular frequency components of the primary and secondary waves, respectively
ω_{1c}	angular frequency of the carrier or primary center frequency
ω_d	$ \omega_{1n} - \omega_{2m} $, difference angular frequency
ρ	density
ρ_0, ρ_1, ρ_2	static, first and second order density, respectively
σ	angle between \vec{r}_0 and the acoustic axis
θ	angle measured with respect to the acoustic axis
θ_0	angle between the acoustic axis and \vec{r}_0
θ_{3dB}	half power angle
θ_{HP}	half power beamwidth
$\theta_{1HP}, \theta_{2HP}$	primary and secondary half power beamwidth, respectively
ξ	total distance, $r_0 + R$; angle between r and the projection of the acoustic axis in the x-z plane
$\vec{\nabla}$	differential operator
∇^2	Laplacian operator
\square^2	d'Alembertian operator
*	complex conjugate as a superscript, convolution between two functions

CHAPTER I

INTRODUCTION

The parametric acoustic array, as originally described by Westervelt,¹ has been the subject of numerous theoretical and experimental studies. In the most general sense, the parametric array is the sound field of the interaction products that result from the mixing of two or more frequency components in a common volume of a medium. The sound field of the baseband interaction products or difference frequencies has been of greatest interest since these components survive after the primary components from which they were generated have been severely attenuated because of the increasing absorption of energy in the medium at higher frequencies. The characteristics of the secondary sound field are unconventional by comparison with linear sources in that highly directive low frequency sound with very low sidelobe radiation may be transmitted with physically small apertures.

The most widely studied parametric array is the absorption limited narrowband parametric array for plane wave fields, which was the subject of Westervelt's¹ study. This parametric array requires a physically unrealizable primary source configuration for implementation and therefore may only be approximated in practice. This array is termed absorption limited since the off-axis properties are determined by the absorption at the primary frequencies in the medium. The narrowband parametric array for nonplane wave fields, which allows for realizable primary source configurations, has been addressed in additional treatments. This type of parametric array is difficult to express in closed form except for a few limiting cases. This array may be dominantly absorption limited in some configurations; but in most cases, the off-axis characteristics are influenced by the off-axis properties of the primary source and the parametric array is termed

diffraction limited. The broadband parametric array is described by the secondary field produced by a pulsed primary transmission where a continuum of primary frequencies interact to produce a continuum of secondary frequencies. The broadband parametric array for plane wave fields, which is the absorption limited broadband parametric array, has been described in a few investigations which will be discussed. The broadband parametric array for nonplane wave fields results from physically realizable primary source configurations and may be dominantly absorption or diffraction limited. The broadband parametric array for nonplane wave fields is the physically realizable broadband parametric array and is the principal subject of this dissertation.

In the second chapter, a theoretical review is presented that describes the derivation of an inhomogeneous wave equation characterizing the secondary sound field for an unbounded medium. The various types of parametric arrays are discussed which include narrowband and broadband parametric arrays for both plane wave and nonplane wave fields. Included in this discussion are references and descriptions of many of the principal treatments which contribute to the understanding of parametric arrays.

Detailed theoretical considerations of broadband parametric arrays are addressed in the third chapter. These considerations include a detailed study of the broadband parametric array for plane wave fields. Off-axis characteristics are related to on-axis characteristics through a linear systems representation of an off-axis impulse response and transfer function. The properties of the secondary field are evaluated in both the time and frequency domains. A source strength density is derived that is generally applicable for the broadband parametric array for plane wave fields. Solutions for the secondary pressure derived from this source strength density are expressed in general and for a Gaussian pulse primary transmission from a circular piston source. The limiting forms of these expressions are also considered.

The results of a comprehensive experimental evaluation of the broadband parametric array for nonplane wave fields are presented in Chapter IV. Both the on-axis and off-axis properties of broadband parametric arrays are examined for low amplitude primary waves transmitted with a Gaussian pulse from circular pistons of different radii. Data are obtained for directivity ratios (ratio of the primary half-power beamwidth to the Rutherford beamwidth from 0.54 to 3.69. This span of parameter values transition from dominantly absorption limited behavior to diffraction limited behavior. These data are compared with theoretical results in the farfield of the parametric array and with absorption and diffraction limited forms of the solution. The performance of the broadband parametric array is also evaluated experimentally for high amplitude primary waves.

The summary and conclusions regarding these investigations of the broadband parametric array are considered in Chapter V. Several appendices are included that contain supportive theoretical and experimental details.

CHAPTER II

THEORETICAL BACKGROUND

The physical basis of the parametric acoustic array (and of nonlinear acoustics in general) is the variability of the speed of an acoustic wave. This variability results from the nonlinearity of the medium as described by an equation of state and from the convection of a sound wave with the speed of the particles within it sets in motion. As sound waves propagate, amplitude dependent effects occur which include harmonic and intermodulation distortion in the frequency domain and waveform distortion in the time domain. The parametric acoustic array is a special case of the intermodulation distortion effect which accompanies the propagation of an acoustic signal in a nonlinear medium.

The theoretical development of the parametric acoustic array was developed from the work of Lighthill^{2,3} who obtained an exact equation describing the radiation of sound produced by turbulence. Westervelt^{4,5} used Lighthill's results in studying the scattering of sound by sound and in the original development of the parametric acoustic array.¹ In this development, Lighthill's equation was reduced to an inhomogeneous wave equation describing the secondary pressure field that is generated by the interaction of acoustic signals.

In the next section a derivation of the inhomogeneous wave equation is given which begins with the equations of fluid mechanics and an isentropic equation of state. Following this derivation, specific types of parametric arrays are reviewed.

A. The Inhomogeneous Wave Equation

The equations which describe the continuity of mass, the conservation of momentum, and the state of a fluid are the fundamental

relations governing acoustics. For a lossless fluid with no real sources present, the continuity and momentum equations in Eulerian coordinates may be written as follows:

mass continuity equation

$$\frac{\partial \rho}{\partial t} + \vec{\nabla} \cdot (\rho \vec{u}) = 0 \quad , \text{ and} \quad (2.1)$$

momentum balance equation

$$\frac{\partial}{\partial t} (\rho \vec{u}) + \vec{\nabla} p + \rho \vec{u} (\vec{\nabla} \cdot \vec{u}) + (\vec{u} \cdot \vec{\nabla}) \rho \vec{u} = 0 \quad , \quad (2.2)$$

where

- ρ is total density,
- t is time,
- $\vec{\nabla}$ is a spatial differential operator,
- \vec{u} is particle velocity, and
- p is total pressure.

For a lossless fluid, the entropy remains constant and the fluid remains at equilibrium during the passage of a sound wave. Under these conditions the state of the fluid may be described by an isentropic equation of state relating pressure and density given by

$$p = p(\rho)_{S=\text{constant}} \quad , \quad (2.3)$$

where S is entropy.

This equation may be expanded in a Taylor series about the ambient or static density of the fluid. When the first three terms of this expansion are retained, the isentropic equation of state may be expressed as

$$p = p_o + c_o^2(\rho - \rho_o) + \frac{1}{2} \frac{c_o^2}{\rho_o} \left(\frac{B}{A} \right) (\rho - \rho_o)^2, \quad (2.4)$$

where

p_o is the ambient or static pressure,

ρ_o is the ambient or static density,

c_o is the small signal sound speed, which is defined by the relation

$$c_o^2 = \left(\frac{\partial p}{\partial \rho} \right)_{\rho=\rho_o, S=\text{constant}}, \quad (2.5)$$

and

$$\frac{B}{A} = \frac{\rho_o}{c_o^2} \left(\frac{\partial^2 p}{\partial \rho^2} \right)_{\rho=\rho_o, S=\text{constant}}. \quad (2.6)$$

The quantity B/A is known as the parameter of nonlinearity for fluids and must be determined experimentally for specific fluids. Experimental measurements⁶ have indicated a value for B/A of 5.2 for degassed fresh water at 30°C.

The acoustic field may be described more concisely through a combination of the mass continuity equation (2.1), the momentum balance equation (2.2), and the isentropic equation of state (2.4). This is done using a perturbation technique in a manner similar to Muir,⁷ Truchard,⁸ and Westervelt.^{1,4,5,9} This technique consists of replacing the dependent variables appearing in Eqs. (2.1), (2.2), and (2.4) by the sum of their equilibrium and higher order variational components, and then forming separate equations which must be satisfied by the variables of each order. If only static, first, and second order relations are of interest, the field variables may be written

$$\vec{u} = \vec{u}_0 + \vec{u}_1 + \vec{u}_2$$

$$p = p_0 + p_1 + p_2 \quad (2.7)$$

$$\rho = \rho_0 + \rho_1 + \rho_2$$

It is assumed that the fluid is at rest, and therefore $\vec{u}_0 = 0$. When Eq. (2.7) is substituted into Eqs. (2.1), (2.2), and (2.4), the first and second order acoustic relations are found. The first order relations are those of linear acoustics and describe what is referred to as the primary field in the context of the parametric acoustic array. These relations are given by the following:

mass continuity equation

$$\frac{\partial \rho_1}{\partial t} + \rho_0 \vec{\nabla} \cdot \vec{u}_1 = 0 \quad , \quad (2.8)$$

momentum balance equation

$$\rho_0 \frac{\partial \vec{u}_1}{\partial t} + \vec{\nabla} p_1 = 0 \quad , \quad (2.9)$$

isentropic equation of state

$$p_1 = c_0^2 \rho_1 \quad , \quad (2.10)$$

wave equation for p_1

$$\nabla^2 p_1 - \frac{1}{c_0^2} \frac{\partial^2 p_1}{\partial t^2} = \square^2 p_1 = 0 \quad , \quad (2.11)$$

where ∇^2 is the Laplacian operator, and

$$\square^2 = \left(\nabla^2 - \frac{1}{c_o^2} \frac{\partial^2}{\partial t^2} \right) \text{ is the d'Alembertian or wave operator.}$$

The second order relations are extensively studied in nonlinear acoustics and describe the secondary field in the context of the parametric acoustic array. These relations are given as follows:

mass continuity equation

$$\frac{\partial \rho_2}{\partial t} + \rho_o \vec{\nabla} \cdot \vec{u}_2 + \vec{\nabla} \cdot (\rho_1 \vec{u}_1) = 0 \quad , \quad (2.12)$$

momentum balance equation

$$\frac{\partial}{\partial t} (\rho_o \vec{u}_2 + \rho_1 \vec{u}_1) + \vec{\nabla} p_2 + \rho_o \vec{u}_1 (\vec{\nabla} \cdot \vec{u}_1) + (\vec{u}_1 \cdot \vec{\nabla}) \rho_o \vec{u}_1 = 0 \quad , \quad (2.13)$$

isentropic equation of state

$$p_2 = c_o^2 \rho_2 + \frac{B}{2A} \frac{(p_1)^2}{c_o^2 \rho_o} \quad (2.14)$$

wave equation for p_2

$$\square^2 p_2 = - \frac{1}{\rho_o c_o^4} \frac{B}{2A} \frac{\partial^2 (p_1)^2}{\partial t^2} - \rho_o \vec{\nabla} \cdot \left[\vec{u}_1 (\vec{\nabla} \cdot \vec{u}_1) + (\vec{u}_1 \cdot \vec{\nabla}) \vec{u}_1 \right] \quad . \quad (2.15)$$

The first order wave equation (2.11) is homogeneous because of the initial assumption of a source free, lossless medium. However, the second order wave equation (2.15) is inhomogeneous. The source term in Eq. (2.15) exists because of the presence of the primary field and represents a virtual source. Further simplification of this source term is necessary to allow a detailed analysis of the secondary

pressure field. With the assumption that \vec{u} is irrotational, Eq. (2.15) may be written

$$\square^2 p_2 = -\frac{1}{\rho_o c_o^4} \frac{B}{2A} \frac{\partial^2 (p_1)^2}{\partial t^2} - \rho_o \left[\left(\vec{\nabla} \cdot \vec{u}_1 \right)^2 + \vec{u}_1 \cdot \nabla^2 \vec{u}_1 + \frac{1}{2} \nabla^2 |\vec{u}_1|^2 \right]. \quad (2.16)$$

When the mass continuity equation (2.8), the momentum balance equation (2.9), the isentropic equation of state (2.10), and the wave equation for particle velocity in the form of Eq. (2.11) are combined, Eq. (2.16) becomes

$$\square^2 p_2 = -\frac{1}{\rho_o c_o^4} \frac{B}{2A} \frac{\partial^2 (p_1)^2}{\partial t^2} - \rho_o \left[\frac{1}{\rho_o c_o^4} \left(\frac{\partial v_1}{\partial t} \right)^2 - \frac{2}{\rho_o c_o^2} \vec{u}_1 \cdot \vec{\nabla} \frac{\partial p_1}{\partial t} + \frac{1}{2} \square^2 |\vec{u}_1|^2 + \frac{1}{2} \frac{\partial^2}{\partial t^2} (\vec{\nabla} p_1 \cdot \vec{\nabla} p_1) \right]. \quad (2.17)$$

Simplification of Eq. (2.17) is accomplished with identities which are obtained by utilizing the momentum balance equation (2.9) and the wave equation for pressure (2.11). These identities are given by

$$\square^2 \left(\frac{\partial p_1}{\partial t} \int p_1 dt \right) = -2\rho_o \left(\vec{u}_1 \cdot \vec{\nabla} \frac{\partial p_1}{\partial t} \right) - \frac{2}{c_o^2} p_1 \frac{\partial^2 p_1}{\partial t^2} \quad (2.18)$$

and

$$\square^2 (p_1^2) = 2\vec{\nabla} p_1 \cdot \vec{\nabla} p_1 - \frac{2}{c_o^2} \left(\frac{\partial p_1}{\partial t} \right)^2. \quad (2.19)$$

When Eqs. (2.18) and (2.19) are substituted into Eq. (2.17), the result is

$$\square^2 p_2 = - \frac{1}{\rho_o c_o^4} \left(1 + \frac{B}{2A}\right) \frac{\partial^2 (p_1)^2}{\partial t^2} \quad (2.20)$$

$$- \square^2 \left[\frac{1}{\rho_o c_o^2} \left(\frac{\partial p_1}{\partial t} \int p_1 dt \right) + \frac{\rho_o}{2} |\vec{u}_1|^2 + \frac{1}{2\rho_o c_o^2} p_1^2 \right]$$

Westervelt^{1,4,9} interpreted the d'Alembertian operation in the source term of Eq. (2.20) as a local contribution to the secondary pressure field. This local pressure does not exist external to the region determined by the primary pressure field and gives no contribution to the radiated secondary pressure field. Muir⁷ analyzed the magnitude of the local secondary pressure. His results indicate that for plane harmonic primary waves there is no local secondary pressure, and for spherical harmonic waves the local secondary pressure vanishes asymptotically with range. After the local secondary pressure terms are dropped, Eq. (2.20) becomes

$$\square^2 p_2 = - \frac{\beta}{\rho_o c_o^4} \frac{\partial^2 (p_1)^2}{\partial t^2}, \quad (2.21)$$

where $\beta=1+(B/2A)$. Westervelt¹ derived this equation initially by assuming the small signal plane wave impedance relation. He re-derived¹⁸ this equation in the manner which has been presented, thereby extending the validity of the original result to arbitrary wave configurations. Equation (2.21) may be rewritten in the form adopted by Westervelt,

$$\square^2 p_2 = -\rho_o \frac{\partial q}{\partial t}, \quad (2.22)$$

where $q = (\beta/\rho_o c_o^4) (\partial(p_1)^2/\partial t)$ is the source strength density. This inhomogeneous wave equation (2.22) has the same form as the small signal

wave equation for a medium in which there are real mass sources of source strength density q . The source strength density in Eq. (2.22) gives rise to the generation of secondary acoustic waves which result from the nonlinear interaction of primary acoustic waves. The properties of the source strength density are those associated with a virtual source that is distributed in space over the region occupied by the primary waves and delayed in time by the propagation speed in the medium. The secondary waves are sometimes referred to as the scattered waves, by analogy with scattering theory where each elemental volume or scatterer in the interaction volume acts as a secondary sound source. The general solution¹⁰ of Eq. (2.22) for a distributed source of source strength density q is given in the time domain by

$$\begin{aligned}
 p_2(\vec{r}, t) &= \rho_o \iiint \frac{\partial}{\partial t_o} q(\vec{r}_o, t_o) \left[\frac{\delta(t - t_o - R/c_o)}{4\pi R} \right] dt_o dv_o \\
 &= \frac{\rho_o}{4\pi} \iiint \frac{1}{R} \left\{ \frac{\partial}{\partial t_o} q(\vec{r}_o, t_o) \right\}_{t_o = t - R/c_o} dv_o, \quad (2.23)
 \end{aligned}$$

where

\vec{r}_o is a vector from the origin to the volume element of integration,

\vec{r} is a vector from the origin to the field point,

$\vec{R} = \vec{r} - \vec{r}_o$,

$R = |\vec{r} - \vec{r}_o|$,

v_o is the interaction volume,

t_o is an initial reference time,

$\delta(\cdot)$ is the Dirac delta function, and

$[\cdot]$ is the time dependent Green's function for a three dimensional unbounded medium.

If the source strength density is a periodic function of time, then the solution of Eq. (2.22) in the time domain may also be written

$$p_2(\vec{r}, t) = \frac{\rho_0}{4\pi} \iiint \sum_n \left[\frac{\partial}{\partial t} q_n(\vec{r}_o, t) \right] \left[\frac{e^{-jk_{2n}R}}{R} \right] dv_o, \quad (2.24)$$

where

$q_n(\vec{r}_o, t)$ is the n th harmonic component of the source strength density,

$k_{2n} = \omega_{2n}/c_o$, and

ω_{2n} is the angular frequency of the n th component of the secondary signal.

The general solution of Eq. (2.22) may also be expressed in the frequency domain using Fourier transform relationships given by

$$g(t) = \mathcal{F}^{-1}\{G(f)\} = \int_{-\infty}^{\infty} G(f) e^{j2\pi ft} df, \quad (2.25)$$

and

$$G(f) = \mathcal{F}\{g(t)\} = \int_{-\infty}^{\infty} g(t) e^{-j2\pi ft} dt, \quad (2.26)$$

where

$\mathcal{F}\{\cdot\}$ is the Fourier transform,

$\mathcal{F}^{-1}\{\cdot\}$ is the inverse Fourier transform,

$f = \frac{\omega}{2\pi}$, and

$j = \sqrt{-1}$.

The general solution of Eq. (2.22) in the frequency domain is written

$$P_2(\vec{r}, f) = \rho_0 \iiint \mathcal{F}\left\{ \frac{\partial}{\partial t} q(\vec{r}_o, t_o) \right\} \left[\frac{e^{-jk_2 R}}{4\pi R} \right] dv_o, \quad (2.27)$$

where $[\cdot]$ is the frequency domain Green's function for a three-dimensional unbounded medium.

The assumptions under which Eqs. (2.23) and (2.27) were derived include the assumption of lossless fluid medium with no real sources. This assumption may now be relaxed without seriously compromising the validity of the solutions for the secondary field components. The existence of a primary field which gives rise to a secondary field through the source density function implies the presence of a real source which generates the primary field. This real source can be included through the specification of both the spatial and the signal characteristics of the primary radiation. Losses may be included in an ad hoc manner by noting the average attenuation over frequency bands or the attenuation of each frequency component in the primary and secondary radiation and applying the principle of superposition. The solutions of Eqs. (2.23) and (2.27) have been studied for a variety of source strength density functions which are derived through variations in the spatial configuration of the interaction volume and in the primary acoustic signal. It is the differences in characteristics of the source strength density function which give rise to different types of parametric arrays. Several kinds of parametric arrays have been considered and include both narrowband and broadband transmissions for plane and nonplane wave fields.

B. The Narrowband Parametric Array for Plane Wave Fields

The narrowband parametric array for plane wave fields is the subject of the original study by Westervelt¹ and of numerous subsequent developments. Westervelt assumed a small amplitude primary signal which is the linear combination of two monochromatic plane waves. The first order pressure is given by

$$p_1(r_o, 0, t) = P_o e^{-\alpha r_o} [\cos(\omega_{11}t - k_{11}r_o) + \cos(\omega_{12}t - k_{12}r_o)]. \quad (2.28)$$

where

P_o is the amplitude of each wave at the origin,
 $\bar{\alpha} = (\alpha_{11} + \alpha_{12})/2$ is the average absorption coefficient for the
 primary waves, and
 $r_o = |\vec{r}_o|$.

The primary waves are collimated along the x axis in a region of
 circular cross section S_o , and are attenuated as a function of range
 by absorption. The geometry for this configuration is shown in
 Fig. 2.1.

The source strength density may be found by substituting
 Eq. (2.28) into Eq. (2.22). Through the dependence on the square of
 the primary pressure, the second harmonic at each primary frequency and
 modulation products given by the sum and difference of each primary
 frequency are generated in the source strength density. The absorption
 coefficient varies generally as the square of the frequency; therefore,
 the difference frequency component will experience less rapid attenua-
 tion as a function of range than the other modulation components. With
 the retention of only the difference frequency component, the source
 strength density may be expressed in complex form as

$$q(r_o, 0, t) = \frac{j\omega_d \beta P_o^2}{2\rho_o c_o^4} e^{-2\bar{\alpha}r_o} e^{j(\omega_d t - k_d r_o)} \quad (2.29)$$

where

$\text{Re}\{q\}$ or $\text{Im}\{q\}$ must be taken to give physical meaning, and

$$\omega_d = |\omega_{12} - \omega_{11}|,$$

$$k_d = |k_{12} - k_{11}|.$$

The source strength density is periodic; therefore, the
 solution in the time domain for the pressure at the difference fre-
 quency is given by Eq. (2.24) and written

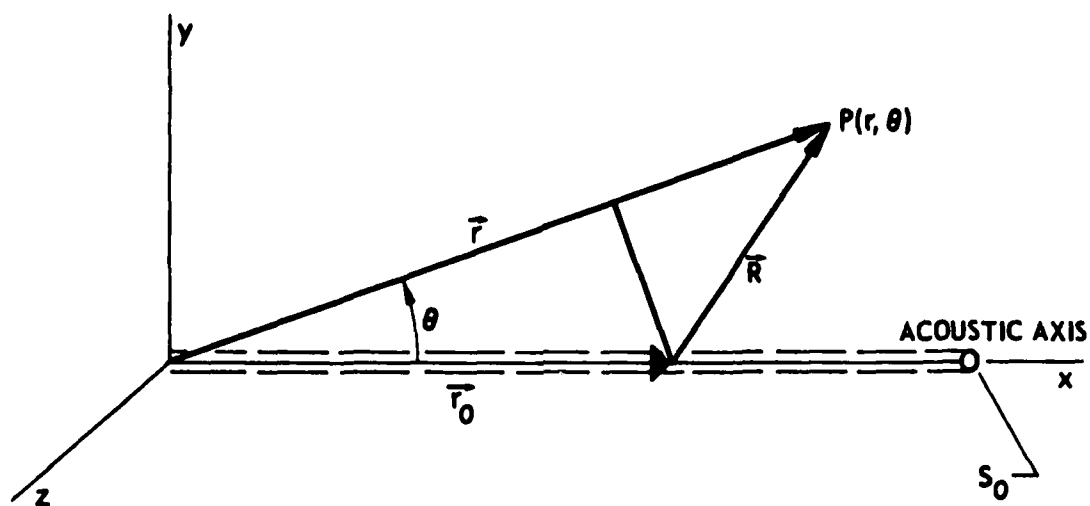


FIGURE 2.1
GEOMETRY FOR ANALYSIS OF A PARAMETRIC
ACOUSTIC ARRAY FOR PLANE WAVE FIELDS

$$p_2(r, \theta, t) = - \frac{\omega_d^2 \beta P_o^2}{4\pi \rho_o c_o^4} \iiint e^{-2\bar{\alpha} r_o} e^{j(\omega_d t - k_d r_o)} \frac{e^{-jk_d R}}{R} dv_o \quad (2.30)$$

It is assumed that the field point P is far from the zone of interaction, or $r \gg r_o$. With this assumption, the Fraunhofer, or farfield approximation may be invoked, which amounts to representing R by the law of cosines and performing a binomial expansion, giving

$$R = r - r_o \cos \theta + \dots, \quad (2.31)$$

where

$$r = |\vec{r}|, \text{ and}$$

θ is the angle between \vec{r} and the acoustic axis.

In Eq. (2.30), the slowly varying part of the Green's function is replaced by the first term of the expansion and, in the rapidly varying part or phase of the Green's function, R is replaced by the first two terms of the expansion. The interaction volume has simple cylindrical geometry which physically may be attained only approximately. The volume integration in Eq. (2.30) reduces to a one-dimensional integral along the x axis given by

$$p_d(r, \theta, t) = - \frac{\omega_d^2 \beta P_o^2 S_o}{4\pi \rho_o c_o^4 r} e^{j(\omega_d t - k_d r)} \int_0^\ell \exp[-j(k_d - 2j\bar{\alpha} - k_d \cos \theta) r_o] dr_o \quad (2.32)$$

This integration must be carried out to a distance ℓ , such that the source strength density is attenuated to a negligible value and the generation of pressure at the difference frequency is effectively completed. The effective length of the parametric array, given by $r=1/(2\alpha)$, is the distance at which the amplitude of the source strength density drops to $1/e$ of its original value. Operationally, the upper

limit of the integral may be extended to infinity, which yields the solution for the pressure at the difference frequency in the farfield of the parametric array as

$$p_d(r, \theta, t) = j \frac{\omega_d^2 \beta_o^2 S_o}{8\pi \rho_o c_o^4 r} e^{j(\omega_d t - k_d r)} e^{-\alpha_d r} \left[k_d \sin^2\left(\frac{\theta}{2}\right) - j\bar{\alpha} \right]^{-1}, \quad (2.33)$$

where attenuation as a function of range due to viscous absorption at the difference frequency has been included ad hoc.

The amplitude directivity factor for the secondary pressure from Eq. (2.33) is given by

$$\frac{p_d(r, \theta, t)}{p_d(r, 0, t)} = \left[1 + \left(\frac{k_d}{\bar{\alpha}} \right)^2 \sin^4\left(\frac{\theta}{2}\right) \right]^{-1/2}, \quad (2.34)$$

which yields a half-power beamwidth of

$$\theta_{HP} = 4 \sin^{-1} \left(\frac{\bar{\alpha}}{k_d} \right)^{1/2} \quad (2.35)$$

The directivity, given by Eq. (2.34), is referred to as the Rutherford directivity because of its similarity in form to Rutherford scattering in atomic physics.

The narrowband parametric array for plane wave fields is an end-fire volumetric array of virtual sources which is exponentially shaded in length by absorption. As a result of this shading, the directional response for the parametric array is absorption limited and is practically devoid of sidelobe radiation. In addition, the dependence of the half-power beamwidth on $\bar{\alpha}$ and k_d allows highly directive radiation at relatively low frequencies from physically small apertures. Experimental investigations to verify Westervelt's theoretical results were performed by Bellen and Beyer,¹¹ Berkay and Smith,¹²

Hobaek,¹³ Zverev and Kalachev,¹⁴ and Muir and Blue.¹⁵ Westervelt's¹ analysis was generally confirmed in these investigations; however, several of the experiments indicated greater directivity at the difference frequency than predicted. To account for this increase in directivity, Westervelt's treatment was extended by Naze and Tjøtta,¹⁶ Berkta, ¹⁷ and Berkta and Smith¹² to allow for an aperture factor. This factor is simply the directivity function at the difference frequency that is associated with the finite cross section of the interaction volume. The aperture factor is included as a multiplier to the Rutherford directivity and can dominate the directivity of the parametric array if the cross section of the interaction volume is large in terms of wavelengths at the difference frequency.

There are several limitations associated with the analytical development of the narrowbeam parametric array for plane wave fields. It is assumed that the primary signal consists of plane waves which are collimated in a narrow beam of uniform cross-sectional area. These spatial characteristics are unrealistic in practice and may only be approximated by an appropriate selection of parameters such that all the interaction takes place in the nearfield, i.e., the Fresnel region, of a primary source. Another limitation is that narrowband development does not account for the initiation and the termination of the primary transmission, which must occur in all physical situations. Finally, the analytical results are valid only far from the interaction region, i.e., in the farfield of the parametric array. Some of the limitations which have been discussed are overcome in the theoretical models which are presented in the next section.

C. The Narrowband Parametric Array for Nonplane Wave Fields

The narrowband parametric array for nonplane wave fields includes arrays with realizable spatial distributions of the primary waves. These parametric arrays differ from those for plane wave fields in that much of the interaction takes place in the farfield or

Fraunhofer region of the primary source and the parametric array is diffraction limited. One of the earliest investigations of nonplane wave fields was by Lauvstad, Naze, and Tjøtta¹⁸ who obtained an approximate solution for the radiation at the difference frequency in the far-field of the parametric array produced by diverging primary sound beams with directivity associated with a circular piston. Lauvstad¹⁹ and Berkta^{17,20,21} also derived farfield solutions for both cylindrical and spherical primary waves. Mellen and Moffett²² noted that with bounded aperture primary sources, the radiation at the difference frequency resulted from plane wave interaction in the nearfield of the source and from nonplane wave interaction in the farfield of the source. Matched plane wave and nonplane wave farfield solutions for the parametric array were studied by Moffett and Mellen²³ for circular apertures and by Moffett, Mellen, and Konrad²⁴ for rectangular apertures. Berkta²⁵ and Leahy²⁵ examined the farfield performance of the parametric array for primary waves emitted from circular and rectangular apertures by computing correction factors to Westervelt's plane wave solution. Investigations restricted to the nearfield of the parametric array were conducted by Rolfeigh,²⁶ Novikov, Rudenko, and Soluyan,²⁷ and Novikov, Rybachek, and Timoshenko.²⁸ In each of these studies, small signal absorption was ignored in order to obtain theoretical results. Other treatments of the narrowband parametric array for nonplane wave fields include an investigation of the parametric array in air by Bennett and Blackstock²⁹ and several studies based on approximate differential equations by Fenlon,³⁰ Fenlon and McKendrie,³¹ and Tjøtta and Tjøtta.³² The experimental data which were presented with many of the theoretical developments establish the range of validity for each theoretical treatment and the effect of various approximations.

Closed form solutions for the pressure at the difference frequency for nonplane wave fields are generally not tractable when a bounded aperture is considered as the primary source. Muir¹⁶ analyzed the narrowband parametric array for spherical wave fields. In his analysis, no approximations were made regarding position vectors and the

scattering integral was evaluated numerically. He assumed a low amplitude primary signal which is a linear combination of two monochromatic spherical waves emitted from a circular piston in an infinite baffle. The primary signal which he assumed has the form

$$p_1(r_o, \theta, t) = P_{o1} \frac{R_o}{r_1} D(k_{11} a \sin \sigma) e^{-\alpha_{11} r_o} \cos(\omega_{11} t - k_{11} r_o) \\ + P_{o2} \frac{R_o}{r_o} D(k_{12} a \sin \sigma) e^{-\alpha_{12} r_o} \cos(\omega_{12} t - k_{12} r_o) \quad , \quad (2.36)$$

where

$P_{o1,o2}$ is the amplitude of each wave at R_o ,

R_o is a nearfield parameter,

a is the radius of the circular piston,

σ is the angle between \vec{r}_o and the acoustic axis, and

$D(\cdot)$ is the directivity function for a circular piston in an infinite rigid baffle.

The primary waves described by Eq. (2.36) propagate as spherical waves and are attenuated as a function of range by viscous absorption. The interaction volume is determined by the common region of the farfield beam patterns at each primary frequency. The geometry for this configuration is shown in Fig. 2.2. Using the form given in Eq. (2.36) for the primary waves, the source strength density may be computed using Eq. (2.22). Retaining only the difference frequency component, the resulting source strength density is a periodic function of time; and the solution in the time domain for the pressure at the difference frequency is given by Eq. (2.24). With the inclusion of attenuation as a function of range due to viscous absorption at the difference frequency, the solution for the secondary pressure is written

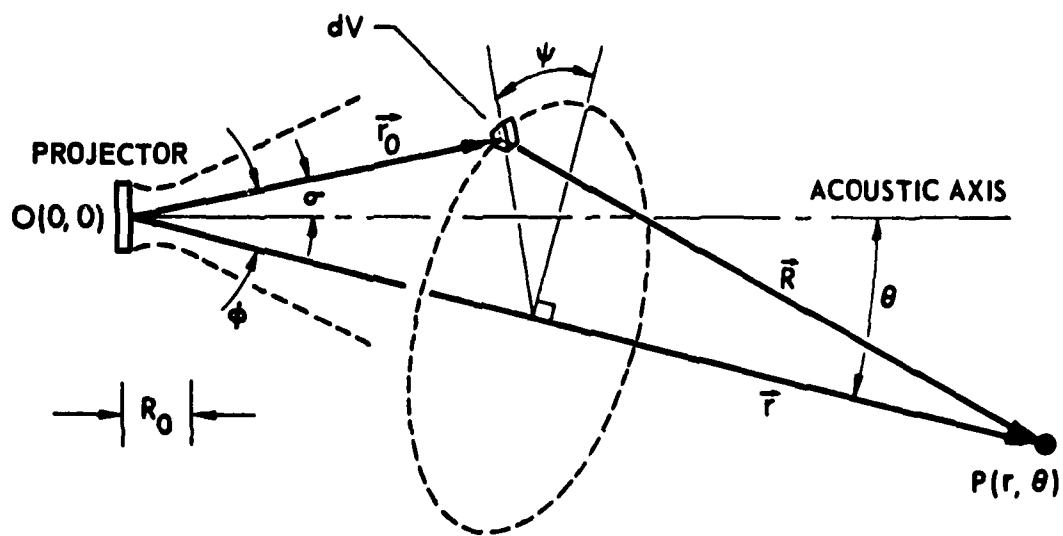


FIGURE 2.2
GEOMETRY FOR ANALYSIS OF A PARAMETRIC
ACOUSTIC ARRAY FOR NONPLANE WAVE FIELDS

(After Muir and Willette)

$$P_d(r, \theta, t) = \frac{2P_{o1}P_{o2}R_o^2\omega_d^2}{\pi\rho_o^4k_{11}k_{12}a^2} \int_{R_o}^r \int_0^{\phi_e+\theta} \int_0^\pi \frac{J_1[k_{11}a \sin\sigma] J_1[k_{12}a \sin\sigma]}{\sin^2\sigma} \\ \times \frac{1}{R} \exp - \{ [jk_d + (\alpha_{11}+\alpha_{12})] r_o + [jk_d+\alpha_d] R \} \sin\phi d\psi d\phi dr, \quad (2.37)$$

where

$$\sin\sigma = \{ [\sin(\theta-\phi) + \sin\phi \cos\theta(1-\cos\psi)]^2 + \sin^2\phi \sin^2\psi \}^{1/2},$$

$$R = (r^2 + r_o^2 - 2rr_o \cos\phi)^{1/2}, \text{ and}$$

ϕ_e is an additional angular increment needed to adequately account for the main lobe of the primary beam patterns.

Muir and Willette⁴² derived the expression given in Eq. (2.37) and evaluated it numerically. Experimental results were presented which support agreement with theory. They also studied the effects of various farfield approximations for the position vector by comparison with the exact position vector. Equation (2.37) completely accounts for the effects of diffraction in the farfield over the main lobe of the primary radiation and is valid in the farfield of the primary waves and throughout the nearfield and the farfield of the parametric array.

A solution similar to that of Muir and Willette was derived by Blue⁴³ utilizing the geometry shown in Fig. 2.3. He assumed an equation in the form of Eq. (2.36) for the primary waves and of Eq. (2.24) for the secondary pressure. Blue also made the usual farfield approximation and wrote the solution as

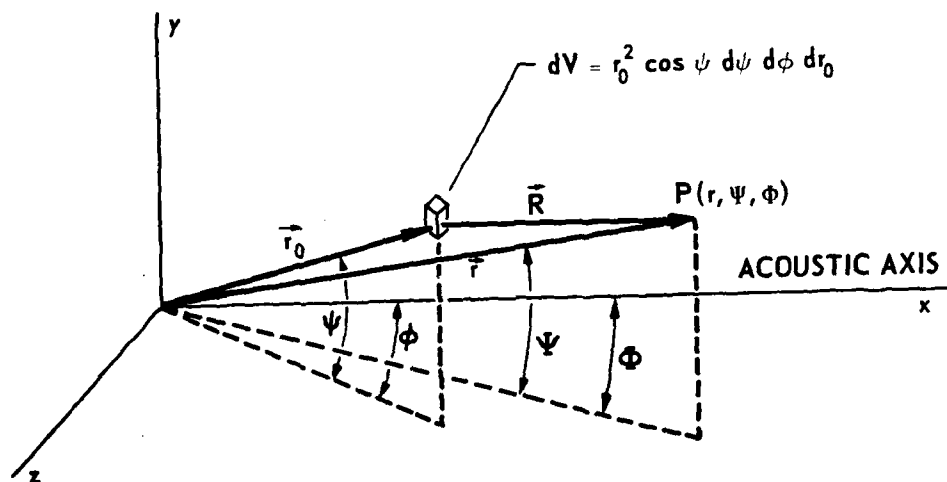


FIGURE 2.3
GEOMETRY FOR ANALYSIS OF A PARAMETRIC
ACOUSTIC ARRAY FOR NONPLANE WAVE FIELDS

(After Blue)

ARL:UT
AS-80-967-P
JMH-GA
3-25-80

$$p_d(r, \theta, t) = \frac{\omega_d^2 \beta P_{11} P_{12} R_o^2}{8\pi \rho_o c_o^4 r} e^{j(\omega_d t - k_d r)} \quad (2.38)$$

$$\times \iint_{-\pi/2}^{\pi/2} \frac{D_{11}(\psi, \phi) D_{12}(\psi, \phi) \cos \psi d\phi d\psi}{\frac{1}{2} (\alpha_{11} + \alpha_{12}) + j k_d \sin^2 \left\{ \frac{1}{2} \cos^{-1} [\cos(\psi - \psi) \cos(\phi - \phi)] \right\}}$$

where $D(\cdot)$ is a primary directivity function. This solution provides good insight into the directivity of the parametric array in general. Equation (2.38) is a double convolution integral of the cosine weighted product of the primary beam functions with the Rutherford directivity. This realization implies that the directivity of the parametric array follows the Rutherford directivity when one or both of the primary beam functions can be treated as spatial impulse functions. Conversely, when the Rutherford directivity acts as a spatial impulse function, the product of the beam functions at the primary frequencies determines the directivity of the parametric array. Experimental results have been presented by Smith,³⁵ Bennett and Slack,³⁶ and Huckabay³⁷ to confirm this behavior.

The aperture factor, or the directivity function at the difference frequency associated with the effective cross section of the interaction volume, can dominate the directivity of the parametric array for plane wave fields. The aperture factor associated with the parametric array for nonplane wave fields was studied by Muir,⁷ Moffett and Mellen,^{23,38} and Hobæk and Vestrheim.³⁹ The results of these studies indicate that the aperture factor may be included as a simple multiplier of the convolution integral in Eq. (2.38). If the convolution integral is dominated by the Rutherford directivity, then the aperture factor can be important; however, if the primary product directivity dominates the convolution integral, then the aperture factor becomes negligible.

D. The Broadband Parametric Array for Plane Wave Fields

The broadband parametric array for plane wave fields was first studied by Berkta¹⁷ who, like Westervelt, assumed a primary signal collimated in a narrowbeam of cross-sectional area S_o , as shown in Fig. 2.1. In contrast to the narrowband parametric array for plane wave fields, Berkta assumed a small amplitude primary signal in which a single frequency carrier wave is modulated by an envelope function. This signal is written

$$p_1(r_o, 0, t) = P_o e^{-\alpha_{1c} r_o} f\left(t - \frac{r_o}{c_o}\right) \cos(\omega_{1c} t - k_{1c} r_o) \quad (2.39)$$

It is assumed that the envelope function $f(t - r_o/c_o)$ varies slowly compared to $\cos(\omega_{1c} t - k_{1c} r_o)$, and that the absorption coefficient at the carrier frequency may be used to represent the absorption of the band-limited signal. Only the lowest frequency components are retained from the source density function, which is found by substituting Eq. (2.39) into Eq. (2.22). The source density function is not a periodic function of time; therefore, the solution in the time domain for the secondary pressure is found from Eq. (2.23). After introducing the farfield approximation given by Eq. (2.31), the solution is written

$$p_2(r, \theta, t) = \frac{\beta P_o^2 S_o}{8\pi \rho_o c_o^4 r} \int_0^{\ell \rightarrow \infty} e^{-2\alpha_{1c} r_o} \frac{\partial^2}{\partial t^2} f^2 \left\{ t - \frac{r}{c_o} - \frac{r_o}{c_o} \left[2 \sin^2\left(\frac{\theta}{2}\right) \right] \right\} dr_o, \quad (2.40)$$

which, on axis ($\theta=0$), reduces to

$$p_2(r, 0, t) = \frac{\beta P_o^2 S_o}{16\pi \rho_o c_o^4 r \alpha_{1c}} \frac{\partial^2}{\partial t^2} f^2 \left(t - \frac{r}{c_o} \right) \quad (2.41)$$

Again, the upper limit of integration may be extended to $r_o = \infty$ since viscous absorption at the carrier frequency will diminish the integrand and effectively truncate the secondary generation. Moffett⁴⁰ derived the result given in Eq. (2.40) and compared it with experimental data^{40,41} for various envelope functions. Additional theoretical and experimental comparisons were reported by Moffett, Westervelt, and Beyer,^{42,43} Merklinger,^{44,45} Mellen and Browning,⁴⁶ and Davy and Hixson.⁴⁷

Berkta¹⁷ analyzed the frequency response of the broadband parametric array for plane wave fields by substituting the source strength density into Eq. (2.27), which gives the solution for the secondary pressure in the frequency domain. After introducing the far-field approximation, Eq. (2.31), the solution is written

$$P_2(r, \theta, f) = \frac{\beta P_o^2 S_o}{16 \pi \rho_o c_o r \alpha_{1c}} e^{-jk_2 r} \frac{\omega_2^2 \mathcal{F}\{f^2(t)\}}{1 + j \frac{k_2}{\alpha_{1c}} \sin^2\left(\frac{\theta}{2}\right)} \quad (2.42)$$

Westervelt⁹ offered a description of the on-axis and off-axis behavior in the time domain of the broadband parametric array for plane wave fields. He returned to the solution for the narrowband parametric array for plane wave fields, Eq. (2.33), and noted the primary pressure dependence given by

$$p_d(r, \theta, t) \propto \frac{j\omega_d^2}{k_d \sin^2\left(\frac{\theta}{2}\right) - j\alpha} e^{-j\omega_d t} \quad ; \quad (2.43)$$

on-axis, this dependence may be written

$$p_d(r, 0, t) = \frac{1}{\alpha} \frac{\partial^2}{\partial t^2} e^{-j\omega_d t} \quad , \quad (2.44)$$

and off-axis, where $k_d \gg \alpha$, the dependence may be written

$$p_d(r, \theta, t) \approx -\frac{c_o}{\sin^2\left(\frac{\theta}{2}\right)} \frac{\partial}{\partial t} e^{-j\omega_d t} \quad (2.45)$$

Westervelt generalized the results of Eq. (2.44) and (2.45) and noted that the on-axis secondary pressure of the broadband parametric array for plane wave fields should be proportional to the second time derivative of the envelope function, and the off-axis secondary pressure should be proportional to the first time derivative of the envelope function.

The broadband nature of the parametric array for plane wave fields was analyzed by Muir,^{7,48} and Muir and Blue⁴⁹ by applying the principle of superposition to the steady state solution obtained by Westervelt.¹ In the frequency domain, the solution for the secondary pressure at a discrete difference frequency may be written

$$P_2(r, \theta, f_d) = \Delta(r, \theta, f_d) \delta(f - f_d) \int_{-\infty}^{\infty} F^*(f) F(f + f_d) df \quad , \quad (2.46)$$

where

* denotes complex conjugate,

$$\Delta(r, \theta, f_d) \delta(f - f_d) = \mathcal{F} \left\{ [p_d(r, \theta, t)] / P_o^2 \right\} ,$$

$f_d = \omega_d / 2\pi$, and

$F(f) = \mathcal{F}\{f(t)\}$, the amplitude spectrum of the primary pressure waveform.

The validity of Eq. (2.46) is subject to the same assumptions under which Westervelt's steady state solution was derived. These assumptions require the frequencies in the primary band to be much greater than the difference frequency; therefore, the envelope function given by

Eq. (2.39) must be slowly varying with respect to the carrier frequency. The autocorrelation theorem may be used to transform the integral in Eq. (2.46) to give

$$P_2(r, \theta, f_d) = \Delta(r, \theta, f_d) \delta(f - f_d) \mathcal{F}\{f^2(t)\} \quad , \quad (2.47)$$

where only the slowly varying component of $f^2(t)$ is retained. The secondary pressure may be expressed as a continuous function of frequency through the superposition of each difference frequency component as given in the frequency domain by

$$\begin{aligned} P_2(r, \theta, f) &= \int P_2(r, \theta, f_d) df_d \\ &= \Delta(r, \theta, f) \mathcal{F}\{f^2(t)\} \quad . \end{aligned} \quad (2.48)$$

The waveform, or the solution for the secondary pressure in the time domain, is obtained from the inverse Fourier transform of Eq. (2.48), which is written

$$p_2(r, \theta, t) = \mathcal{F}^{-1}\{\Delta(r, \theta, f)\} * f^2(t) \quad , \quad (2.49)$$

where $\mathcal{F}^{-1}\{\Delta(r, \theta, f)\}$ is the impulse response of the parametric array for plane wave fields and $*$ between two functions denotes convolution. The solutions obtained by superposition, Eqs. (2.48) and (2.49), are straightforward and in forms which are suitable for computer analysis.

E. The Broadband Parametric Array for Nonplane Wave Fields

The broadband parametric array for nonplane wave fields is an extension of Berkta's¹⁷ broadband parametric array development where most of the interaction occurs in the farfield or Fraunhofer region of the primary source radiation. The primary signal has features associated with both the narrowband array for nonplane wave fields,

Eq. (2.36), and the broadband array for plane wave fields, Eq. (2.39). A small amplitude primary signal which conforms to the geometry in Fig. 2.2 is given by

$$p_1(\vec{r}_o, t) = \frac{R_o}{r_o} P_o e^{-\alpha_1(r_o - R_o)} D(\sigma) f\left(t - \frac{r_o}{c_o}\right) \cos(\omega_1 t - k_1 r_o) . \quad (2.50)$$

This form for the primary signal has been used in previous studies^{59,60,61} and is applicable when it is assumed that the primary signal is sufficiently narrowband that parameters characterising the primary signal are constant over the bandwidth of the transmission. Under this assumption, the directivity function simply determines the amplitude dependence of the primary signal as a function of angle off-axis. The source density function is found by substituting Eq. (2.50) into Eq. (2.22) and retaining only the slowly varying term.

The resulting source density function is not a periodic function of time; therefore, the solution for the secondary pressure in the time domain is given by Eq. (2.23). This solution is written

$$p_2(r, \theta, t) = \frac{\beta P_o^2 R_o^2}{8\pi \rho_o c_o^2} e^{2\alpha_1 R_o} \iiint \frac{1}{R r_o^2} e^{-2\alpha_1 r_o} D^2(\sigma) \times \frac{\partial^2}{\partial t^2} f^2\left(t - \frac{r_o}{c_o} - \frac{R}{c_o}\right) dv_o . \quad (2.51)$$

In the frequency domain, the solution is found from Eq. (2.27) and is given by

$$P_2(r, \theta, f) = \frac{\beta P_o^2 R_o^2 \omega_o^2}{8\pi \rho_o c_o^4} e^{2\alpha_1 R_o} \iiint \frac{1}{Rr_o^2} e^{-2\alpha_1 r_o} D^2(\sigma) \times \mathcal{F} \left\{ f^2 \left(t - \frac{r_o}{c_o} \right) \right\} e^{-jk_2 R} dv_o \quad (2.52)$$

The similarities between the forms of the narrowband and broadband parametric arrays for nonplane wave fields are evident. Much of the detailed theoretical and experimental work has concentrated on narrowband parametric arrays and the broadband parametric array for plane wave fields. There have been few treatments devoted to the broadband parametric array for nonplane wave fields.

Moffett and Mello⁵⁰ presented a model in which the secondary pressure in the frequency domain was found by superposition of solutions for the narrowband parametric array for nonplane wave fields. They assumed only amplitude dependent directivity functions and restricted the details of the analysis to the on-axis behavior of the broadband array for plane wave fields. This treatment is similar to that of Muir who obtained the broadband parametric array for plane wave fields by superposition of Westervelt's result over the primary frequency components.

Rolleigh⁵¹ and Mize et al.⁵² considered the broadband parametric array for nonplane wave fields as a linear system. A primary signal similar to that of Eq. (2.50) and a solution in the form of Eq. (2.51) were assumed. Spherical geometry was assumed, a change of variables was made, and Eq. (2.51) was put in the form of a spatial convolution integral given by

$$p_2(r, \theta, t) = \int_{R_0}^{\infty} h(\xi, \phi, \psi) S\left(t - \frac{\xi}{c_0}\right) d\xi, \quad (2.53)$$

where

$$\xi = r_0 + R,$$

$S(t - \xi/c_0)$ involves the double time derivative of the square of the envelope function, and

$h(\xi, \phi, \psi)$ is the spatial impulse response for the parametric array with real primary beam functions.

The spatial impulse response $h(\xi, \phi, \psi)$ involves a double integration over angles. Rolfeigh reduced this double integration to a single integration with the assumption of a Gaussian beam function for the primary signal. The solution in the frequency domain for the secondary pressure is given by

$$P_2(r, \theta, f) = H(r, \theta, f) \mathcal{F}\left\{S\left(t - \frac{\xi}{c_0}\right)\right\}, \quad (2.54)$$

where

$$H(r, \theta, f) = \mathcal{F}\{h(\xi, \phi, \psi)\}, \text{ and}$$

$$h(\xi, \phi, \psi) = 0 \text{ for } \xi < R_0.$$

Rolleigh showed that $\mathcal{F}\{h(\xi, \phi, \psi)\}$ was amenable to numerical analysis due to the well behaved properties of the integrand, and that on the acoustic axis $\mathcal{F}\{h(\xi, \phi, \psi)\}$ could be evaluated in closed form. The off-axis behavior was examined in the farfield of the parametric array for angles near the acoustic axis. The results of this analysis indicated that spherical spreading and diffraction change the off-axis spectral distortion relative to that for the broadband parametric array for plane wave fields.

F. The Parametric Acoustic Array with Finite Amplitude Primary Waves

The various parametric acoustic arrays which have been discussed were derived for small amplitude primary signals. For large amplitude primary waves, finite amplitude effects must be considered in order to adequately describe the behavior of a parametric array.

Finite amplitude effects are the result of variations in sound speed with the particle velocity in the direction of sound propagation. In a fluid, these variations are described by

$$c' = c_0 + u + \frac{B}{2A} u^2, \quad (2.55)$$

where

c' is the propagation speed of any particular point on the acoustic wave,

$u = \vec{u} \cdot \vec{n}$ is the particle velocity in the direction of sound propagation, and

\vec{n} is a unit vector in the direction of sound propagation.

The varying propagation speed, as discussed by Blackstock,⁵³ is a function of the small signal sound speed in the medium and the particle velocity. The second term in Eq. (2.55) results from convection and the third term results from the nonlinearity of the pressure-density relation. According to Eq. (2.55), the portions of an acoustic wave in a compression phase and in an expansion phase propagate faster and slower, respectively, than the small signal sound speed. This behavior results in cumulative waveform distortion with propagation distance and the eventual formation of a shock wave. Larger amplitude waves form shock waves at shorter distances than lower amplitude waves. For very weak waves, small signal dissipation is dominant over cumulative waveform distortion and the formation of a shock wave is precluded. The cumulative effects of waveform distortion with propagation distance

have been studied by Blackstock^{54,55} in the frequency domain. He obtained a general solution in the form of a Fourier series for the distortion with propagation distance for an originally sinusoidal pressure wave. The fundamental component of this series decreases monotonically with propagation distance. Each harmonic component first increases, and then decreases, with range. This behavior suggests that as an originally sinusoidal wave propagates with finite amplitude, energy is converted from the fundamental to the harmonic components during the formation of a shock wave. An increase in the level of the original wave causes an increase in the harmonic component growth rate. Eventually, the amplitude of the fundamental component saturates at an upper limit which cannot be increased with a further increase in level of the original wave.

The parametric acoustic array with finite amplitude primary levels has been the subject of many theoretical and experimental studies. As large amplitude primary waves propagate coaxially, waveform distortion and the growth of harmonic components will occur. Each frequency component will interact with each other component to produce modulation products, as indicated by Brinkmann.⁵⁶ The higher order interactions are very weak; therefore, in the context of the parametric array, the secondary signal or difference frequency component is the most important. The primary effect which results from finite amplitude primary levels is that the conversion of energy from the fundamental to harmonic components acts as a range dependent attenuation, in addition to viscous absorption. The effects of finite amplitude attenuation on the parametric array have been studied by Bartram and Westervelt,⁵⁷ Bartram,⁵⁸ and Zverev, Kalachev, and Stepanov.⁵⁹ The ratio of initial power at the fundamental to the final power of the secondary signal, or the conversion efficiency of the parametric array, is lower for finite amplitude primary waves than for small signal primary waves. As the primary level of the parametric array is increased, the dependence of the secondary level on the primary level changes from quadratic to linear because of the onset of finite amplitude effects. The

performance of the parametric array for saturated primary signals has been evaluated by Mellen and Browning,⁴⁵ Mellen, Browning, and Konrad,⁶⁰ and Willette and Moffett.⁶¹ The length of the parametric array becomes shorter as the total attenuation is increased with the inclusion of finite amplitude attenuation. With parametric arrays for plane wave fields, the increase in attenuation results in an increase in the half-power beamwidth, given by Eq. (2.35), as shown by Merklinger.⁴³ In considering parametric arrays for nonplane wave fields, the amplitude response of the primary beam functions varies such that the effects of finite amplitude attenuation are greatest on the acoustic axis. This results in a blunting of the secondary radiation pattern relative to the small signal case with an increase in the half-power beamwidth. The effects which finite amplitude primary waves have on parametric arrays for nonplane wave fields are discussed by Muir,⁷ Moffett and Mellen,^{22,23} and Moffett, Mellen, and Konrad.²⁴ The increase in half-power beamwidth for the parametric array is a direct result of the truncation of the virtual end-fire parametric array at shorter ranges due to finite amplitude attenuation. Additional treatments of the parametric array with finite amplitude primary waves are given by Fenlon.^{62,63}

CHAPTER III
THEORETICAL CONSIDERATIONS FOR THE BROADBAND PARAMETRIC ARRAY

A. Radiation in the Farfield of the Broadband Parametric Array for Plane Wave Fields with Low Amplitude Primary Waves

The absorption limited broadband parametric array for plane wave fields was reviewed in Chapter II. Several on-axis and off-axis properties were described. In this section, the on-axis and off-axis analysis is extended with the assumption of a particular primary signal envelope function. The properties of the secondary transmission are evaluated in terms of the primary transmission and expressed in both the time and frequency domains. This study is preparatory to the development of the broadband parametric array for nonplane wave fields which reduces to the broadband parametric array for plane wave fields in the absorption limit.

1. General Solution

The general solutions for the pressure field of the broadband parametric array for plane wave fields are summarized in Eqs. (2.39), (2.40), (2.41), and (2.42). An analysis of the spectral distortion of a broadband signal which is transmitted by the parametric array for plane wave fields as a function of off-axis angle may be considered by treating the on-axis and the off-axis properties of Eq. (2.42) as the respective input and output of a linear system. This relationship is given by

$$P_2(r, \theta, f) = P_2(r, 0, f) H_{2\theta}(f) \quad , \quad (3.1)$$

where $H_{2\theta}$ is the off-axis transfer function for the second order field.

From Eq. (2.42) the off-axis transfer function for the broadband parametric array for plane wave fields is given by

$$H_{2\theta}(f) = \left[1 + j \frac{k_2}{\alpha_{1c}} \sin^2\left(\frac{\theta}{2}\right) \right]^{-1}, \quad (3.2)$$

which is closely related to the amplitude directivity factor for the parametric array for plane wave fields given by Eq. (2.34). The off-axis power transfer function $|H_{2\theta}(f)|^2$ is shown in Fig. 3.1. Continuing the linear system approach, the solution for the secondary pressure field in the time domain is expressed by

$$p_2(r, \theta, t) = p_2(r, 0, t) * h_{2\theta}(t), \quad (3.3)$$

where $h_{2\theta}(t)$ is the off-axis impulse response function, which is written

$$h_{2\theta}(t) = \mathcal{F}^{-1} \{ H_{2\theta}(f) \}. \quad (3.4)$$

The linear system approach separates the radiation characteristics of the parametric array into on-axis and off-axis components. Analyses of off-axis spectral distortion of specified or measured signals are developed from the on-axis signal characteristics to yield off-axis solutions in both the time and frequency domains.

2. On-Axis Radiation

The on-axis pressure in the farfield of the broadband parametric array for plane wave fields is given in the time domain by Eq. (2.41). In the frequency domain, the on-axis solution is given by Eq. (2.42) evaluated at $\theta=0$, and expressed by

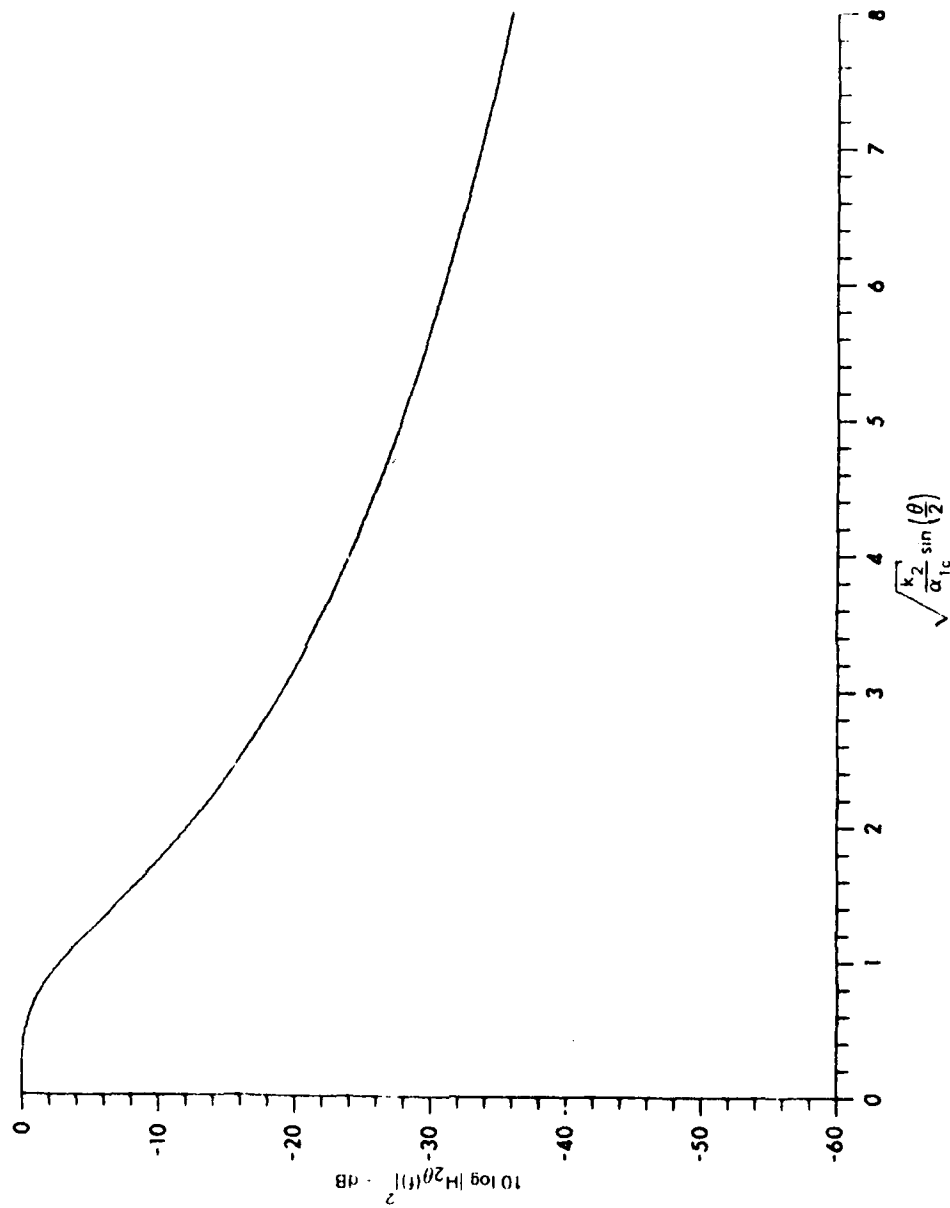


FIGURE 3.1
OFF-AXIS POWER TRANSFER FUNCTION FOR THE RADIATION IN THE FARFIELD
OF THE BROADBAND PARAMETRIC ARRAY FOR PLANE WAVE FIELDS

ARL-UT
AS-80-1512
JMH-GA
7-30-80

$$P_2(r, 0, f) = \frac{\beta P_o^2 S_o}{16 \pi \rho_o c_o^4 \alpha_{1c}} e^{-jk_2 r} \omega_2^2 \mathfrak{F}\{f^2(t)\} \quad (3.5)$$

The analysis of specific signal properties associated with the broadband parametric array for plane wave fields requires the specification of a pulse envelope function for the primary transmission. The assumption of a Gaussian pulse envelope is mathematically tractable and is a reasonable approximation to pulse envelopes which may be attained in practice. The particular characteristics of a Gaussian pulse transmission are detailed in Appendix A.

A Gaussian envelope function is assumed to have the form

$$f(t) = e^{-n^2 t^2} \quad , \quad (A.12)$$

which has a Fourier transform given by

$$\mathfrak{F}\{f(t)\} = F(f) = \frac{\sqrt{\pi}}{n} \exp\left[-\left(\frac{\pi}{n}\right)^2 f^2\right] \quad , \quad (A.13)$$

where n is a constant which determines the effective duration of the pulse and therefore the effective width of the frequency spectrum. The spectral characteristics of the Gaussian pulse transmission may be specified by defining the constant n in the frequency domain given by

$$n = 2.668 \frac{f_{1c}}{Q_1} \quad , \quad (A.18)$$

where Q_1 is the quality factor for the primary transmission determined by the center frequency divided by the half-power bandwidth. If the pulse duration is defined as the inverse of the half-power bandwidth, then the pulse duration is the interval in time between the

0.17 amplitude levels of the pulse envelope. Using Eq. (A.12) in Eq. (2.41), the on-axis solution for the farfield secondary pressure with a Gaussian pulse transmission is given in the time domain by

$$p_2(r,0,t) = \frac{\beta P_o^2 S_o}{16\pi \rho_o c_o^4 r \alpha_{1c}} \left\{ 4n^2 \left[4n^2 \left(t - \frac{r}{c_o} \right)^2 - 1 \right] \right. \\ \left. \times \exp \left[-2n^2 \left(t - \frac{r}{c_o} \right)^2 \right] \right\} . \quad (3.6)$$

This result was derived by Berkay;⁷ the shape of the pressure pulse is shown in Fig. 3.2. The on-axis solution in the frequency domain for the farfield secondary pressure with a Gaussian pulse transmission is found from Eqs. (A.13) and (3.5) and is given by

$$p_2(r,0,f) = \frac{\beta P_o^2 S_o}{16\pi \rho_o c_o^4 r \alpha_{1c}} e^{-jk_2 r} \omega_2^2 \frac{1}{n} \sqrt{\frac{\pi}{2}} \exp \left[-\frac{1}{2} \left(\frac{\pi}{n} \right)^2 f_2^2 \right] . \quad (3.7)$$

For a constant value of n , the frequency at which the on-axis secondary pressure is a maximum is found by maximizing Eq. (3.7) with respect to f_2 . Differentiating Eq. (3.7) and setting the result to zero gives

$$\left[-\frac{1}{2} \left(\frac{\pi}{n} \right)^2 f_2^2 + 1 \right] f_2 \exp \left[-\frac{1}{2} \left(\frac{\pi}{n} \right)^2 f_2^2 \right] = 0 . \quad (3.8)$$

This expression indicates a maximum when

$$f_{2p} = \frac{\sqrt{2}}{\pi} n . \quad (3.9)$$

This result was derived by Findeisen.⁶⁴ Using the definitions of n given in Eqs. (A.16) and (A.18), the peak frequency for the on-axis

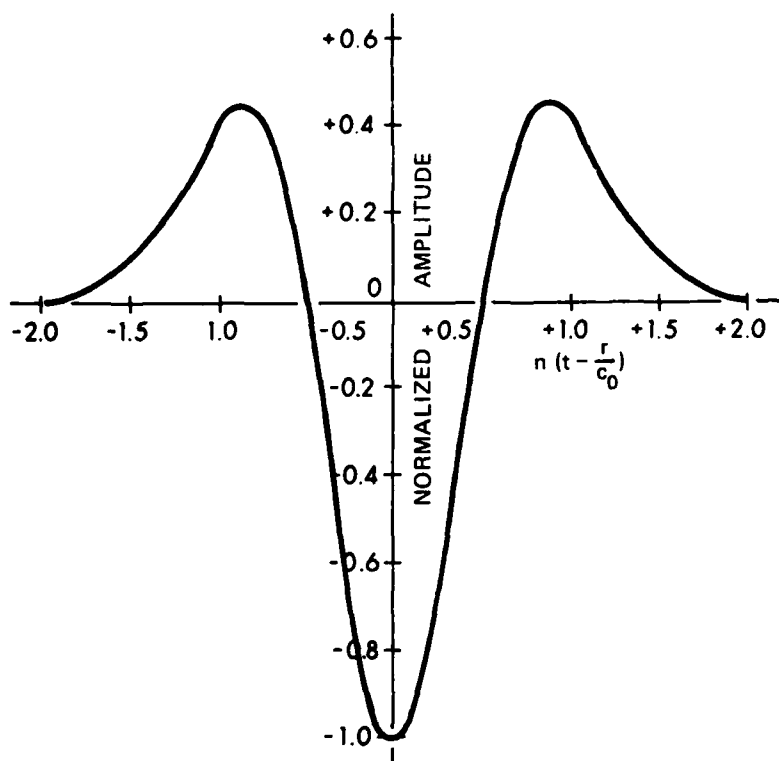


FIGURE 3.2
ON-AXIS PULSE SHAPE FOR THE BROADBAND
PARAMETRIC ARRAY FOR PLANE WAVE FIELDS
WITH A GAUSSIAN PULSE PRIMARY TRANSMISSION

ARL:UT
 AS-80-1513
 JMH - GA
 7 - 30 - 80

secondary transmission can be related to the half-power bandwidth and Q_1 . The frequency at which the on-axis secondary pressure is a maximum may also be expressed by

$$\begin{aligned} f_{2p} &= 1.2 |F_{11} - F_{12}| \\ &= 1.2 \frac{f_{1c}}{Q_1}, \end{aligned} \quad (3.10)$$

where F_{11} and F_{12} are the lower and upper half-power frequencies, respectively, for the primary transmission. The step-down ratio (SDR), the ratio of primary center frequency to secondary frequency at which the on-axis secondary pressure is a maximum, is defined by Eq. (3.10) and is written

$$\text{SDR} = \frac{f_{1c}}{f_{2p}} = \frac{Q_1}{1.2}. \quad (3.11)$$

As Q_1 diminishes, the SDR becomes small and the frequency at which the on-axis secondary pressure is a maximum approaches the primary center frequency. This situation violates the assumption that the Gaussian pulse envelope function varies slowly compared to $\cos(\omega_{1c}t)$ and represents an unrealistic case for the broadband parametric array. If the SDR is restricted to values of 2 or greater, then Q_1 is restricted to values of 2.4 or greater. The frequency at which the on-axis secondary pressure is a maximum as a function of the primary center frequency is shown in Fig. 3.3.

A representation⁶⁵ of the power spectral density function for finite duration signals may be derived from the energy spectral density function by weighting the energy spectral density function with respect to the duration of the signal, or

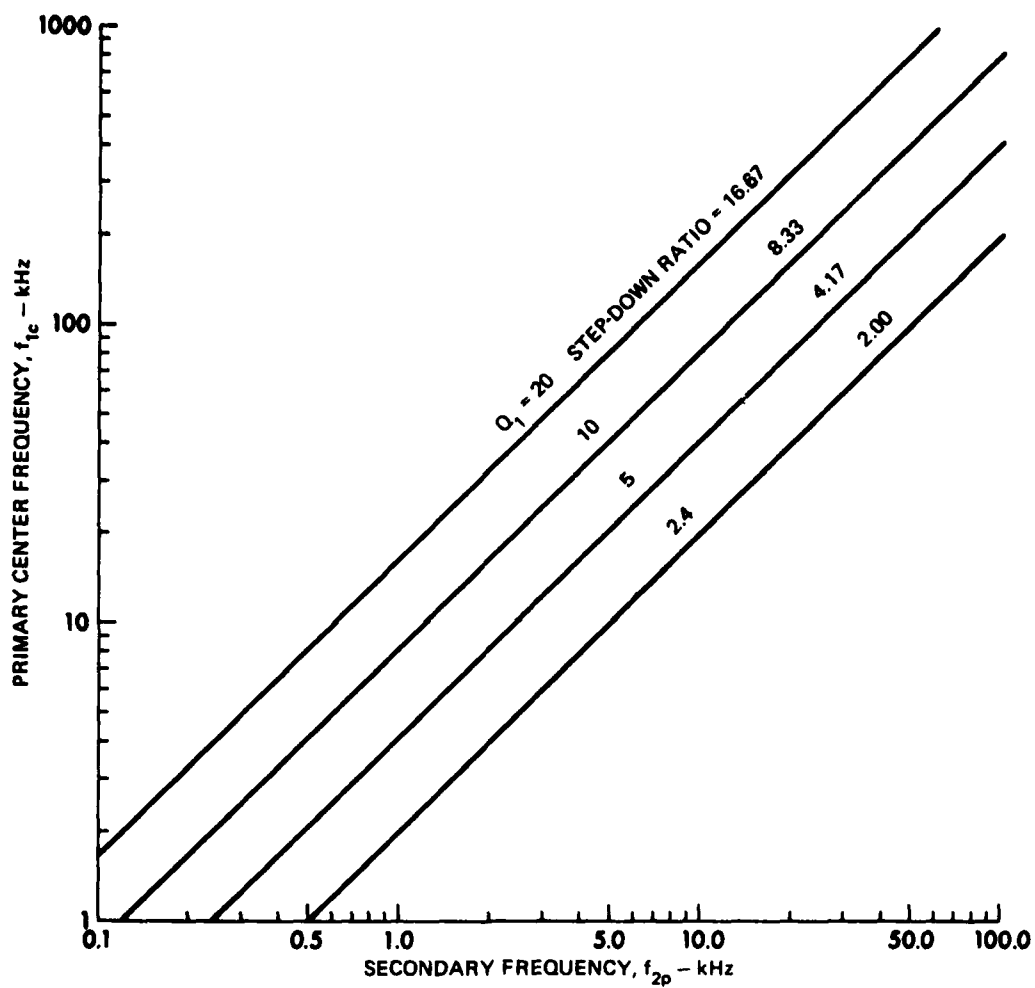


FIGURE 3.3
FREQUENCY AT WHICH THE ON-AXIS SECONDARY PRESSURE IS A MAXIMUM
AS A FUNCTION OF THE PRIMARY CENTER FREQUENCY WITH THE Q OF
A GAUSSIAN PULSE PRIMARY TRANSMISSION AS A PARAMETER

ARL:UT
 AS-80-1514
 JMH - GA
 7 - 30 - 80

$$P_{xx}(f) = \frac{1}{T} E_{xx}(f) \quad , \quad (3.12)$$

where

$P_{xx}(f)$ is the power spectral density function,

$E_{xx}(f)$ is the energy spectral density function, and

T is the duration of the signal.

The normalized power spectral density function for the on-axis transmission of the broadband parametric array for plane wave fields with a Gaussian pulse primary transmission is derived from Eq. (3.7) and given by

$$P_{2xxN}(f) = \frac{P_2(r,0,f) P_2^*(r,0,f)}{P_2(r,0,f_{2p}) P_2^*(r,0,f_{2p})} \quad . \quad (3.13)$$

If the power spectral density function for the on-axis secondary signal is normalized to the on-axis signal produced by a Gaussian pulse primary transmission with a quality factor of Q_{1p} , then Eq. (3.13) becomes

$$P_{2xxN}(f) = \left[\frac{\pi Q_{1p}}{\sqrt{2}(2.668)} \right]^4 \left(\frac{f_2}{f_{1c}} \right)^4 \exp \left\{ - \left[\left(\frac{\pi Q_1}{2.668} \right)^2 \left(\frac{f_2}{f_{1c}} \right)^2 - 2 \right] \right\} \quad . \quad (3.14)$$

The power spectral density function for the on-axis secondary signal is shown in Fig. 3.4 for several values of Q_1 of the Gaussian pulse primary transmission and a Q_{1p} of 2.4. The highest frequency at a spectral peak and relative spectral power level occurs for the lowest value of Q_1 . As the value of Q_1 is increased, both the frequency at the spectral peak and the relative power levels decrease. The asymmetry of the spectra and the reduction in relative power levels result from f_2^4 weighting in the power spectral density function.

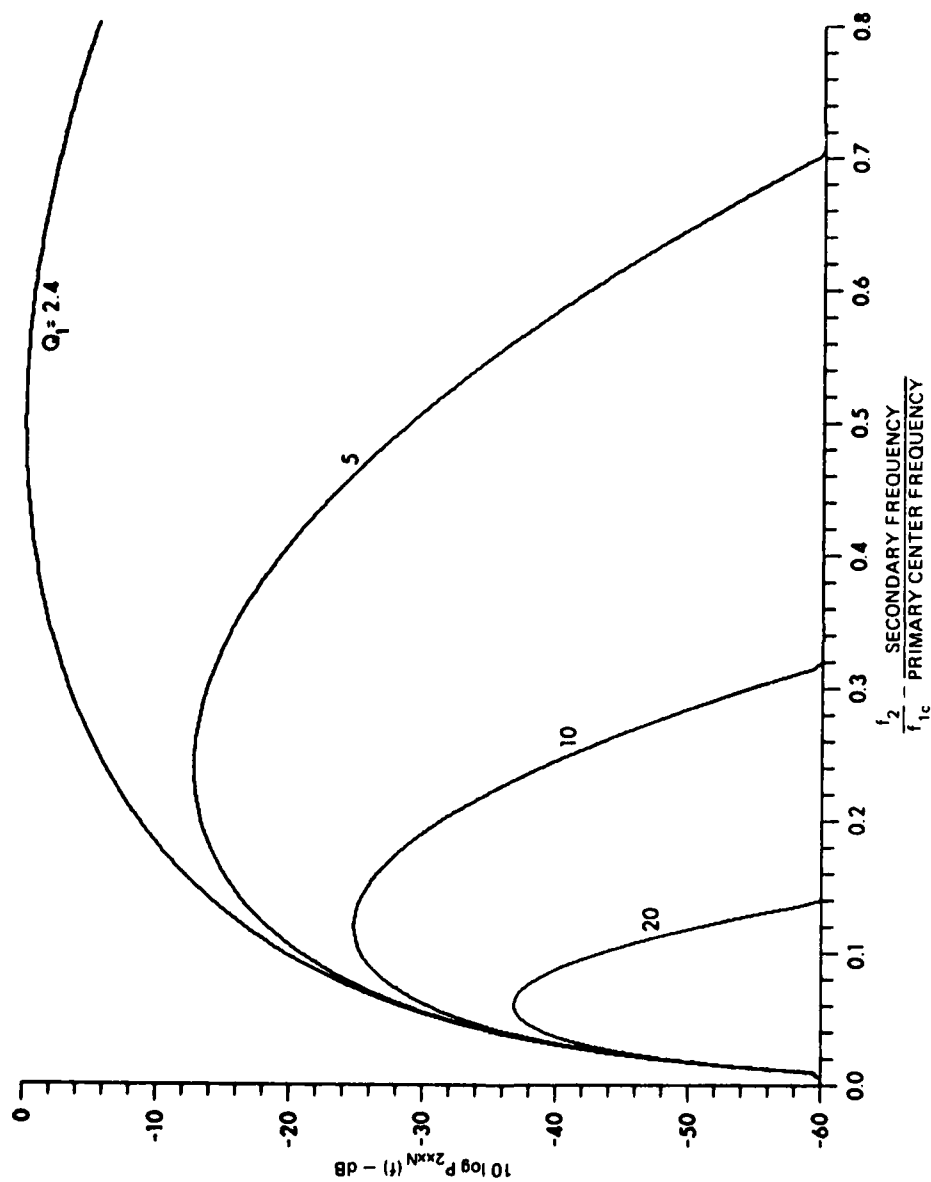


FIGURE 3.4
POWER DENSITY SPECTRA FOR THE ON-AXIS TRANSMISSION OF THE BROADBAND PARAMETRIC
ARRAY FOR PLANE WAVE FIELDS WITH THE Q OF THE GAUSSIAN PULSE PRIMARY TRANSMISSION
AS A PARAMETER

ARL:UT
AS-80-1515
JMH:GA
7-30-80

The half-power bandwidth of the on-axis secondary transmission is determined by identifying the frequencies, F_{21} and F_{22} , at which the normalized power spectral density function, given by Eq. (3.14), equals 0.5. Using Eq. (A.18) in Eq. (3.9), the condition which must be satisfied is written

$$P_{2xxN}(f) = \left(\frac{\pi}{\sqrt{2} n} \right)^4 f_2^4 \exp \left\{ - \left[\left(\frac{\pi}{n} \right)^2 f_2^2 - 2 \right] \right\} = 0.5 \quad . \quad (3.15)$$

This equation is transcendental and must be solved numerically. The solutions of Eq. (3.15) are combined to give a half-power bandwidth of

$$\begin{aligned} |F_{21} - F_{22}| &= |0.873 - 2.039| \frac{n}{\pi} \\ &= 1.166 \frac{n}{\pi} \quad . \end{aligned} \quad (3.16)$$

Using Eq. (A.16) for n in terms of primary bandwidth, Eq. (3.15) becomes

$$\begin{aligned} |F_{21} - F_{22}| &= 0.990 |F_{11} - F_{12}| \\ &\cong |F_{11} - F_{12}| \quad . \end{aligned} \quad (3.17)$$

This result indicates the approximate equivalence of the half-power bandwidths for the Gaussian pulse primary transmission and the signal produced on axis with the broadband parametric array for plane wave fields. This is the same result which Muir⁷ obtained qualitatively for the narrowband parametric array for plane wave fields.

The quality factor Q_2 of the on-axis secondary transmission may be put in the form of Eq. (A.17) which, when combined with Eqs. (3.10) and (3.17), gives

$$Q_2 = \frac{f_{2p}}{|F_{21} - F_{22}|} \cong 1.2 \quad (3.18)$$

On axis, Q_2 is a constant which is approximately equal to 1.2 for a Gaussian pulse primary signal.

3. Off-Axis Radiation

The off-axis pressure in the farfield of the broadband parametric array for plane wave fields is given in the time domain as before by the convolution of the on-axis solution with the off-axis impulse response function. Similarly in the frequency domain, the off-axis solution is given by the product of the on-axis solution with the off-axis transfer function.

With a Gaussian pulse primary transmission, the off-axis solution in the time domain is found by substituting Eqs. (3.4) and (3.6) into Eq. (3.3), which gives

$$p_2(r, \theta, t) = \left[\frac{8P_o^2 S_o}{16\pi\rho_o c_o^4 r \alpha_{1c}} \left\{ 4n^2 \left[4n^2 \left(t - \frac{r}{c_o} \right)^2 - 1 \right] \right. \right. \\ \left. \left. \times \exp \left[-2n^2 \left(t - \frac{r}{c_o} \right)^2 \right] \right\} \right] * \left[\mathcal{F}^{-1} \left[H_{2\theta}(f) \right] \right] \quad (3.19)$$

In the frequency domain the off-axis solution is found by substituting Eqs. (3.2) and (3.7) in Eq. (3.1), which gives

$$P_2(r, \theta, f) = \frac{8P_o^2 S_o}{16\pi \rho_o c_o^4 r \alpha_{1c}} e^{-jk_2 r} \omega_2 \frac{1}{n} \sqrt{\frac{\pi}{2}} \times \left\{ \exp \left[-\frac{1}{2} \left(\frac{\pi}{n} \right)^2 f_2^2 \right] \right\} \left[1 + j \frac{k_2}{\alpha_{1c}} \sin^2 \left(\frac{\theta}{2} \right) \right]^{-1} . \quad (3.20)$$

Evaluation of the spectral distortion as a function of off-axis angle involves the computation of the normalized power spectral density function and its behavior as a function of off-axis angle. The normalized power spectral density function is given by

$$P_{2xxN}(f) = \frac{P_2(r, \theta, f) P_2^*(r, \theta, f)}{P_2(r, 0, f_{2p}) P_2^*(r, 0, f_{2p})} . \quad (3.21)$$

With the use of Eqs. (A.18), (3.9), and (3.20), the normalized power spectral density function becomes

$$P_{2xxN}(f) = \left[\frac{\pi Q_1}{\sqrt{2}(2.668)} \right]^4 \left(\frac{f_2}{f_{1c}} \right)^4 \left\{ \exp \left[- \left[\left(\frac{\pi Q_1}{2.668} \right)^2 \left(\frac{f_2}{f_{1c}} \right)^2 - 2 \right] \right] \right\} \times \left[1 + \left(\frac{k_2}{\alpha_{1c}} \right)^2 \sin^4 \left(\frac{\theta}{2} \right) \right]^{-1} . \quad (3.22)$$

For a given primary transmission, the on-axis secondary signal has a spectral peak which occurs at a secondary frequency given by Eq. (3.10) and a half-power spectral width given by Eqs. (3.16) or (3.17). As the angle off-axis increases, the spectral shape changes with a downward shift in frequency at the spectral peak and a reduction in relative spectral power level.

The frequency at the spectral peak as a function of angle off axis may be found by maximizing the normalized power spectral density function with respect to frequency. Retaining the dependence on f_2 in Eq. (3.22) and differentiating with respect to frequency gives

$$\begin{aligned} \frac{d}{df_2} P_{2xxN}(f) = & 2f_2^3 \left\{ \exp \left[- \left(\frac{\pi Q_1}{2.668} \right)^2 \left(\frac{f_2}{f_{1c}} \right)^2 \right] \right\} \left[1 + \left(\frac{k_2}{\alpha_{1c}} \right)^2 \sin^4 \left(\frac{\theta}{2} \right) \right]^{-2} \\ & \times \left\{ \left[1 + \left(\frac{k_2}{\alpha_{1c}} \right)^2 \sin^4 \left(\frac{\theta}{2} \right) \right] \left[2 - \left(\frac{\pi Q_1}{2.668} \right)^2 \left(\frac{f_2}{f_{1c}} \right)^2 \right] \right. \\ & \left. - \left[\left(\frac{k_2}{\alpha_{1c}} \right)^2 \sin^4 \left(\frac{\theta}{2} \right) \right] \right\} . \quad (3.23) \end{aligned}$$

Setting Eq. (3.23) equal to zero and solving for f_2 , the frequency at the spectral peak is given by

$$\begin{aligned} f_{2p}(\theta) = & \left\{ \frac{1}{2} \left[\left(\frac{2.668 f_{1c}}{\pi Q_1} \right)^2 - \left(\frac{c_o \alpha_{1c}}{2\pi} \right)^2 \sin^{-4} \left(\frac{\theta}{2} \right) \right] \right. \\ & \pm \frac{1}{2} \left[\left(\frac{2.668 f_{1c}}{\pi Q_1} \right)^4 + \left(\frac{c_o \alpha_{1c}}{2\pi} \right)^4 \sin^{-8} \left(\frac{\theta}{2} \right) \right. \\ & \left. \left. + 6 \left(\frac{2.668 f_{1c}}{\pi Q_1} \right)^2 \left(\frac{c_o \alpha_{1c}}{2\pi} \right)^2 \sin^{-4} \left(\frac{\theta}{2} \right) \right]^{1/2} \right\}^{1/2} . \quad (3.24) \end{aligned}$$

This equation is valid for angles off axis only. On the acoustic axis the frequency at the spectral peak is given by Eqs. (3.9) and (3.10).

B. Radiation in the Farfield of the Broadband Parametric Array for Nonplane Wave Fields with Low Amplitude Primary Waves

Some preliminary theoretical considerations for the broadband parametric array for nonplane wave fields were discussed in Chapter II. The analytical description for the primary field, given by Eq. (2.50), included a narrowband directivity function as a simple multiplier. This analytical form only determines the off-axis amplitude dependence of the field and does not account for frequency dependence over the bandwidth of the primary transmission. If a parametric array is formed with a conventional linear source, then the primary field will be frequency dependent off-axis over the bandwidth of the primary transmission. The off-axis properties of the parametric array for nonplane wave fields can be influenced by the frequency dependence of the primary field.

In this chapter, the broadband parametric array for nonplane wave fields will be developed for a primary field with frequency dependent directivity functions. The limiting forms of this development will be considered and the off-axis spectral properties quantified.

1. General Solution

The primary field associated with the radiation from a conventional linear source is discussed in Appendix A for the radiation from a circular piston. This type of field may be expressed in the time domain as

$$p_1(r_o, \theta, t) = p_1(r_o, 0, t) * h_{1\theta}(t) \quad , \quad (A.5)$$

where $p_1(r_o, 0, t)$ is the on-axis solution and $h_{1\theta}(t)$ is the off-axis impulse response. An on-axis primary signal is assumed which is spherically spreading from the origin. This signal is a good representation for the on-axis primary signal in the farfield of a conventional source, i.e., at ranges $r_o > R_o$, but is a poor representation close to the source. The limitations of this signal representation in the nearfield is minimal in terms of the analytical representation of the parametric array for nonplane wave fields provided the dimensions of the conventional source are not too large in terms of wavelength at the secondary frequency and provided low amplitude primary levels are dominant. This assumption will be discussed further elsewhere in this section. The assumed signal is expressed by

$$p_1(r_o, 0, t) = \frac{R_o}{r_o} P_o e^{-\alpha_1(r_o - R_o)} f\left(t - \frac{r_o}{c_o}\right) \cos(\omega_{1c}t - k_{1c}r_o) \quad , \quad (3.25)$$

where P_o is the peak pressure amplitude at R_o . It is also assumed that the envelope function $f(t - r_o/c_o)$ is slowly varying compared to $\cos(\omega_{1c}t - k_{1c}r_o)$ and that the absorption coefficient α_1 at the primary center frequency or carrier frequency may be used to represent the absorption of the bandlimited signal.

The source strength density q , which is a representation of the strength of the virtual sources distributed in the interaction volume, is found from Eq. (2.22) with Eqs. (3.25) and (A.5), and is expressed by

$$q(r_o, \theta, t_o) = \frac{\beta R_o^2 P_o^2}{\rho_o c_o^4 r_o^2} e^{-2\alpha_1(r_o - R_o)} \times \frac{\partial}{\partial t_o} \left\{ f\left(t_o - \frac{r_o}{c_o}\right) \cos(\omega_{1c}t_o - k_{1c}r_o) * h_{1\theta}(t_o) \right\}^2 \quad . \quad (3.26)$$

In the frequency domain, the source strength density becomes

$$\begin{aligned} \mathcal{F}\left\{q(r_o, \theta, t_o)\right\} &= \frac{j\omega_2 \beta R_o^2 P_o^2}{\rho_o^2 c_o^4 r_o^2} e^{-2\alpha_1(r_o - R_o)} \\ &\times \mathcal{F}\left\{f\left(t_o - \frac{r_o}{c_o}\right) \cos(\omega_{1c} t_o - k_{1c} r_o) * h_{1\theta}(t_o)\right\} \\ &* \mathcal{F}\left\{f\left(t_o - \frac{r_o}{c_o}\right) \cos(\omega_{1c} t_o - k_{1c} r_o) * h_{1\theta}(t_o)\right\} \quad (3.27) \end{aligned}$$

The frequency domain representation of the source strength density function involves the self-convolution of the primary pressure in the frequency domain. Using the shift, convolution, and modulation theorems, Eq. (3.27) may be written

$$\begin{aligned} \mathcal{F}\left\{q(r_o, \theta, t_o)\right\} &= \frac{j\omega_2 \beta R_o^2 P_o^2}{\rho_o^2 c_o^4 r_o^2} e^{-2\alpha_1(r_o - R_o)} \\ &\times \left\{ \frac{1}{2} e^{-jk_{1c} r_o} [F(f_1 - f_{1c}) + F(f_1 + f_{1c})] H_{1\theta}(f_1) \right\} \\ &* \left\{ \frac{1}{2} e^{-jk_{1c} r_o} [F(f_1 - f_{1c}) + F(f_1 + f_{1c})] H_{1\theta}(f_1) \right\} \quad (3.28) \end{aligned}$$

In this equation $F(f)$ is the Fourier transform of the primary envelope function given by $\mathcal{F}\{f(t)\}$ and $H_{1\theta}(f)$ is the off-axis transfer function for the primary transmission given by $\mathcal{F}\{h_{1\theta}(t)\}$.

When written as a convolution integral, the source strength density in Eq. (3.28) may be expressed as the sum of four terms which

are the modulation products resulting from the nonlinear process. Each of the four terms is a convolution integral which may be expressed as a correlation integral utilizing the properties of the Fourier transform of real signals. Equation (3.28) then becomes

$$\begin{aligned} \mathfrak{F} \left\{ q(r_o, \theta, t_o) \right\} &= \frac{j\omega_2 \beta R_o^2 P_o^2}{4\rho_o^2 c_o^4 r_o^2} e^{-2\alpha_1(r_o - R_o)} \\ &\times \left\{ \int_{-\infty}^{\infty} F^*(f_1 - f_{1c}) F(f_2 + f_1 - f_{1c}) H_{1\theta}^*(f_1) H_{1\theta}(f_1 + f_2) df_1 \right. \\ &+ \int_{-\infty}^{\infty} F^*(f_1 - f_{1c}) F(f_2 + f_1 + f_{1c}) H_{1\theta}^*(f_1) H_{1\theta}(f_1 + f_2) df_1 \\ &+ \int_{-\infty}^{\infty} F^*(f_1 + f_{1c}) F(f_2 + f_1 - f_{1c}) H_{1\theta}^*(f_1) H_{1\theta}(f_1 + f_2) df_1 \\ &\left. + \int_{-\infty}^{\infty} F^*(f_1 + f_{1c}) F(f_2 + f_1 + f_{1c}) H_{1\theta}^*(f_1) H_{1\theta}(f_1 + f_2) df_1 \right\} . \end{aligned} \quad (3.29)$$

Each of these correlation integrals is a function of frequency shift or frequency difference which is a secondary frequency component. The modulation products which each of the integrals represent may be determined by evaluation of the integrand and recalling that $F(f)$ is symmetric and has a peak at $f=0$ and that $H_{1\theta}(f)=1$ on-axis. The first integral yields a baseband secondary spectrum which results from the interaction of positive primary frequency components. The second and third integrals yield the negative and positive secondary spectra, respectively, centered at the second harmonic of the carrier frequency. The last integral yields another baseband secondary spectrum, which results from

interaction of negative primary frequency components. Retaining the lowest frequency components of the source strength density and restricting the analysis to positive frequencies, the source strength density in the frequency domain reduces to a function of the first correlation integral only and is given by

$$\mathcal{F} \left\{ q(r_o, \theta, t_o) \right\} = \frac{j \omega_2 \beta R_o^2 P_o^2}{2 \rho_o c_o^4 r_o^2} e^{-2\alpha_1(r_o - R_o)} \times \int_{-\infty}^{\infty} F^*(f_1 - f_{1c}) F(f_1 + f_2 - f_{1c}) H_{1\theta}^*(f_1) H_{1\theta}(f_1 + f_2) df_1 \quad (3.30)$$

The general solution for the secondary pressure field produced by the interaction of primary field components is given in the frequency domain by Eq. (2.27). Using the representation of the source strength density in the frequency domain given by Eq. (3.30), the general solution is written

$$P_2(r, \theta, f) = - \frac{\omega_2^2 \beta R_o^2 P_o^2}{8 \pi \rho_o c_o^4} e^{2\alpha_1 R_o} \int_{-\infty}^{\infty} F^*(f_1 - f_{1c}) F(f_1 + f_2 - f_{1c}) \times \int_{V_o} H_{1\theta}^*(f_1) H_{1\theta}(f_1 + f_2) e^{-2\alpha_1 r_o} e^{-jk_2 r_o} \times e^{-jk_2 R} \frac{1}{r_o^2} dV_o df_1 \quad (3.31)$$

This four-dimensional solution is a superposition of first order

interaction components determined by the primary frequency spectra. The amplitude dependence of each interaction component results in part from the volumetric integration over the virtual sources. The representation of the secondary field given by Eq. (3.31) is general for nonplane wave fields and similar in form to Eq. (2.46), which is a representation of the broadband parametric array for plane wave fields used by Muir^{7,48} and Muir and Blue.⁴⁹

Equation (3.31) was derived assuming primary radiation which is spherically spreading from the origin. This assumption is valid if the effects of the aperture factor can be ignored in the nearfield of the primary radiation. The aperture factor which was discussed in Chapter II is the directivity function at the secondary frequency associated with the effective cross section of the interaction volume. The aperture factor which results in the farfield of the primary radiation is a diffraction effect for diverging waves and is included in the formalism of Eq. (3.31). An implicit assumption which is included in the derivation is placed on the off-axis transfer function. This function must be valid throughout the interaction volume. Since the aperture factor is ignored in the nearfield of the primary radiation, the specification of an off-axis transfer function which is valid only in the farfield of the primary radiation is required.

2. Farfield Solution

The volumetric integration in Eq. (3.31) is fundamental to solutions for the parametric array for nonplane wave fields. It has been evaluated for the narrowband parametric array by numerical integration and by making various approximations and simplifying assumptions in the integrand to fit specific physical situations. For the current analysis a solution to Eq. (3.31) is sought in the farfield of the parametric array. A farfield solution is indicative of many trends which occur in the nearfield of the parametric array. These trends remain after the energy associated with the primary frequencies has been

removed by absorption in the medium and the farfield of the parametric array is attained.

Conventional spherical geometry is assumed and indicated in Fig. 3.5 where the acoustic axis is along the z-axis. The subscripted variables indicate position of virtual volumetric sources in the primary field and unprimed variables indicate position relative to the field points. It is assumed that the field point is far from the interaction volume or $r \gg r_0$. Under this assumption the Fraunhofer or far-field approximation is justified where R is given by two terms of the binomial expansion of the law of cosines approximate representation, or

$$R \approx r - r_0 \cos \gamma + \dots \quad (3.32)$$

In this relation γ is the angle between the vector to the source point and the vector to the field point and is defined by

$$\cos \gamma = \cos \theta_0 \cos \theta + \sin \theta_0 \sin \theta \cos(\psi - \psi_0) \quad (3.33)$$

In the numerator of the Green's function, R is replaced by the first two terms in Eq. (3.33) and in the denominator by only the first term. After making the farfield approximations, including the differential volume in spherical coordinates, and collecting terms, Eq. (3.31) becomes

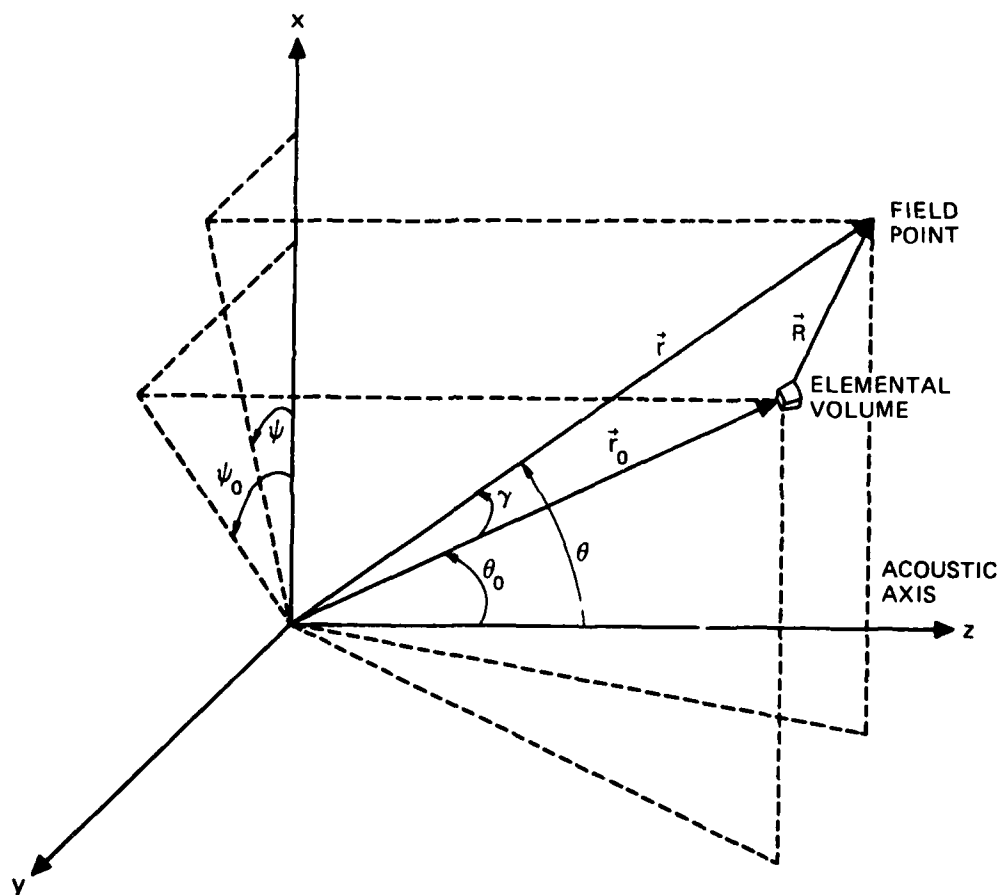


FIGURE 3.5
 SPHERICAL GEOMETRY FOR ANALYSIS OF A PARAMETRIC ACOUSTIC ARRAY
 FOR NON PLANE WAVE FIELDS WITH THE ACOUSTIC AXIS ALONG THE z-AXIS

$$\begin{aligned}
P_2(r_o, \theta, f) = & - \frac{\omega_2^2 R_o^2 P_o^2}{8\pi \rho_o c_o^4 r} e^{2\alpha_1 R_o} e^{-(\alpha_2 + jk_2)r} \\
& \times \int_{-\infty}^{\infty} F^*(f_1 - f_{1c}) F(f_1 + f_2 - f_{1c}) \\
& \times \int_0^{\infty} \int_0^{2\pi} \int_0^{\pi/2} H_{1\theta}^*(f_1) H_{1\theta}(f_1 + f_2) \exp\{-[\alpha_T + jk_2(1 - \cos\gamma)r_o]\} \\
& \times \sin\theta_o d\theta_o d\psi_o dr_o df_1, \quad (3.34)
\end{aligned}$$

where $\alpha_T = 2\alpha_1 - \alpha_2$. As a result of the use of the farfield approximations, the range integral is trivial and may be expressed in closed form. The secondary pressure in the farfield is written

$$\begin{aligned}
P_2(r_o, \theta, f) = & - \frac{\omega_2^2 R_o^2 P_o^2}{8\pi \rho_o c_o^4 r \alpha_T} e^{2\alpha_1 R_o} e^{-(\alpha_2 + jk_2)r} \\
& \times \int_{-\infty}^{\infty} F^*(f_1 - f_{1c}) F(f_1 + f_2 - f_{1c}) \\
& \times \int_0^{2\pi} \int_0^{\pi/2} \frac{H_{1\theta}^*(f_1, \theta_o, \psi_o) H(f_1 + f_2, \theta_o, \psi_o) \sin\theta_o}{1 + j \frac{k_2}{\alpha_T} (1 - \cos\gamma)} d\theta_o d\psi_o df_1. \quad (3.35)
\end{aligned}$$

where the dependence of $H_{1\theta}(f)$ on angles has been included explicitly. The surface integral in Eq. (3.35) is similar to a form derived by Berkta and Leahy²⁵ for the narrowband parametric array. It has been referred to as the convolution integral for the parametric array after Blue³⁴ assumed different geometry, made small angle approximations, and derived the result given by Eq. (2.38), which involves the double convolution of the weighted product of the primary beam functions with the Rutherford directivity.

The solution for the secondary pressure on the acoustic axis is given by $P_2(r,0,f)$ and obtained by setting $\theta=0$ in Eq. (3.35). In this case, $\cos\gamma$ reduces to $\cos\theta_0$. The off-axis transfer function $H_{2\theta}(f)$ may be computed from Eq. (3.1) and the normalized power spectral density function $P_{2xxN}(f)$ is given by Eq. (3.21).

A simplification of the general farfield solution for the broadband parametric array, Eq. (3.35), is obtained when the directivity or off-axis transfer functions have circular symmetry about the acoustic axis or an independence with respect to ψ . Referring to Fig. 3.5 for this case, γ is given by

$$\cos\gamma = \cos\theta_0 \cos\theta + \sin\theta_0 \sin\theta \cos\psi_0, \quad (3.36)$$

where an arbitrary rotation of coordinates about the acoustic axis removes the ψ dependence. Under these conditions the integral over ψ_0 may be performed and Eq. (3.35) becomes

$$P_2(r, \theta, f) = - \frac{\omega_o^2 R_o^2 P_o^2}{4 \rho_o c_o^4 r \alpha_T} e^{2\alpha_1 R_o} e^{-(\alpha_2 + jk_2)r} \int_{-\infty}^{\infty} F^*(f_1 - f_{1c}) F(f_1 + f_2 - f_{1c})$$

$$\times \int_0^{\pi/2} \frac{H_{1\theta}^*(f_1, \theta_o) H_{1\theta}(f_1 + f_2, \theta_o) \sin \theta_o d\theta_o df_1}{\left\{ 1 + j \frac{k_2}{\alpha_T} [1 - \cos(\theta_o - \theta)] \right\}^{1/2} \left\{ 1 + j \frac{k_2}{\alpha_T} [1 - \cos(\theta_o + \theta)] \right\}^{1/2}} \quad (3.37)$$

The space integral in this equation is similar to a result which Berkay and Leahy²⁵ derived for the narrowband parametric array. Equation (3.37) is the general solution in the farfield of the broadband parametric array for nonplane wave fields with directivity or off-axis transfer functions which are symmetric about the acoustic axis. With the far-field assumption and the assumption of circular symmetry, the four-dimensional integral in the general solution given by Eq. (3.31) is reduced to a two-dimensional integral in Eq. (3.37). Further analytical reduction for cases of practical interest is difficult but may be attempted by appropriate selections of $F(f)$ and $H_{1\theta}(f)$. A more straightforward approach is evaluation by double numerical integration. This is accomplished by separating Eq. (3.37) into real and imaginary parts, performing separate double integrations and computing the magnitude of the result.

Physical insight into the characteristics of the broadband parametric array for nonplane wave fields may be gained by examining several limiting forms of Eq. (3.35) which occur as a result of dominant directional characteristics. The characteristics of a parametric source which is formed by radiation from a conventional linear source are always a combination of effects due to the primary directivity or off-axis transfer functions and the Rutherford directivity. Limiting forms of the convolution integral have been evaluated by Berkay and Leahy.²⁵

There are two limiting conditions associated with Eq. (3.35) which are important. The first condition occurs when the parametric array is diffraction limited or strongly dominated by the product of the directivity or off-axis transfer functions at the primary frequencies. The second condition occurs when the parametric array is absorption limited and the Rutherford directivity function is strongly dominant.

If the primary directivity functions are extremely narrow, then θ_o is small and

$$\cos \gamma \approx \cos \theta \quad . \quad (3.38)$$

Under this condition Eq. (3.35) becomes

$$P_2(r, \theta, f) = - \frac{\omega_2^2 \beta R_o^2 P_o^2}{8\pi \rho_o c_o^4 r \alpha_T} e^{2\alpha_1 R_o} e^{-(\alpha_2 + jk_2)r} \int_{-\infty}^{\infty} F^*(f_1 - f_{1c}) F(f_1 + f_2 - f_{1c}) \\ \times \frac{1}{1 + j \frac{k_2}{\alpha_T} (1 - \cos \theta)} \int_0^{2\pi} \int_0^{\pi/2} H_{1\theta}^*(f_1, \theta_o, \psi_o) H_{1\theta}(f_1 + f_2, \theta_o, \psi_o) \sin \theta_o d\theta_o d\psi_o df_1. \quad (3.39)$$

The term which emerges from the convolution integral is simply the Rutherford directivity function which was identified in Eq. (2.34). The primary beams act as spatial impulse functions with strength given by the remaining integrals over the interaction volume in Eq. (3.39). The strength of the impulse function vanishes as the primary beamwidths go to zero. This trend leads to a physically unrealizable situation which is supported by operational considerations of the parametric array. If a parametric array is operated with constant radiated acoustic power, then the on-axis source level at the primary frequencies becomes infinite as the primary beamwidths go to zero. Conversely, if a

parametric array is operated with constant on-axis source levels at the primary frequencies, then the radiated acoustic power vanishes as the primary beamwidths go to zero. This limiting form is simply a spherical wave representation of the broadband parametric array for plane wave fields which was discussed in detail in the previous section. In this limit of Eq. (3.35), the assumption of primary waves which are spherically spreading from the origin results in physical inaccuracies. If radiation is considered from a conventional source and the primary beams are extremely narrow, then the primary source has a long nearfield characterized by plane wave behavior which is generally confined to the volume in front of and determined by the area of the source. In this case, most of the nonlinear interaction takes place in the Fresnel diffraction region of the source, the parametric array is absorption limited, and the theoretical development for the broadband parametric array for plane wave fields is applicable.

The other limiting case of interest is identified when the half-power beamwidth associated with the Rutherford directivity is small compared to the half-power beamwidths of the primary radiations. The evaluation of this special case is aided by the adoption of the geometry shown in Fig. 3.6. This geometry differs from that of Fig. 3.5 in that the field point rather than the acoustic axis lies on the z-axis. If the half-power beamwidth of the Rutherford directivity is small, the convolution integral in Eq. (3.35) may be written

$$I = \int_0^{2\pi} \int_0^{\pi/2} \frac{H_{1\theta}^*(f_1, \sigma) H_{1\theta}(f_1+f_2, \sigma) \sin\theta_o}{1 + j \frac{8}{\theta_{HP}^2} (1 - \cos\theta_o)} d\theta_o d\psi_o \quad . \quad (3.40)$$

With the spherical geometry in Fig. 3.5, the primary directivity functions or off-axis transfer functions are simple functions of angle while the Rutherford directivity is a complicated function of angle.

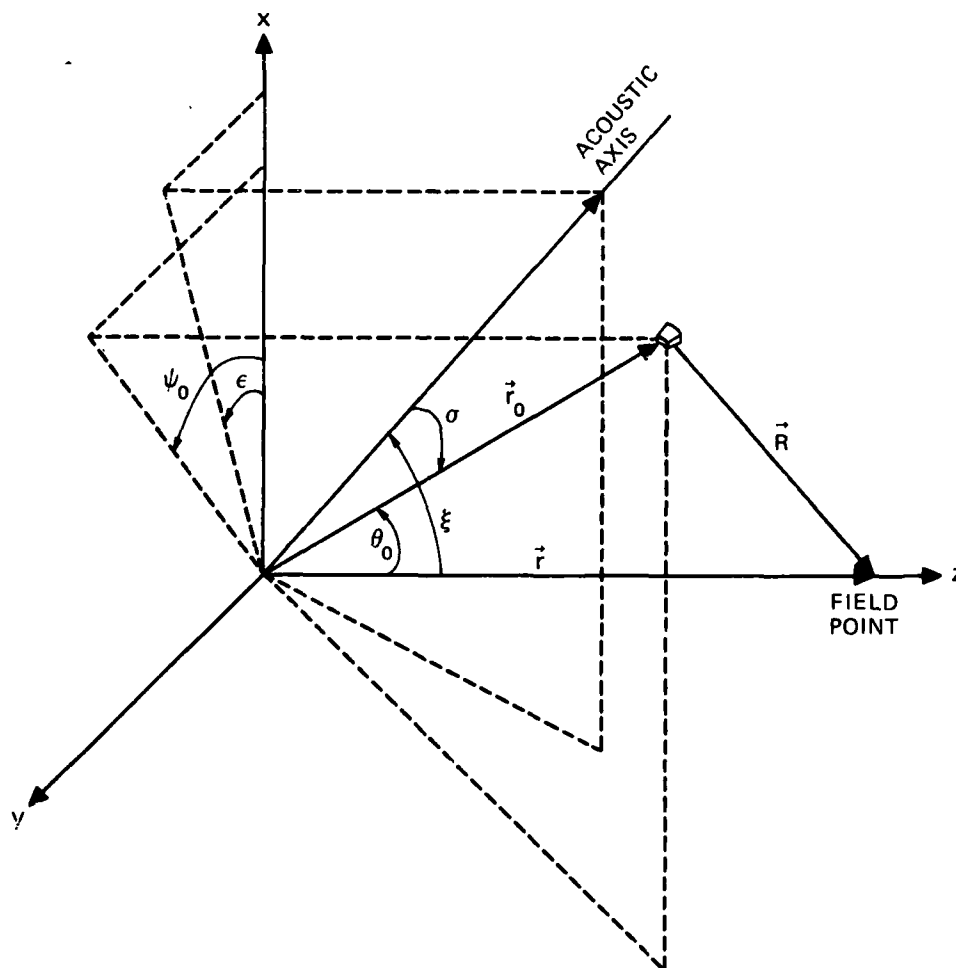


FIGURE 3.6
 SPHERICAL GEOMETRY FOR ANALYSIS OF A PARAMETRIC ACOUSTIC ARRAY
 FOR NON PLANE WAVE FIELDS WITH THE FIELD POINT ON THE z-AXIS

The new geometry in Fig. 3.6 reverses this functional dependence. The directivity for the parametric array is now a function of ξ and ϵ , which are angles that determine the position of the acoustic axis. The directivity function at the primary frequencies is a function of σ , given by

$$\cos\sigma = \cos\theta_o \cos\xi + \sin\theta_o \sin\xi \cos(\psi_o - \epsilon) \quad . \quad (3.41)$$

As θ_{HP} becomes small, the convolution integral of Eq. (3.40) has significant value only when θ_o is small also, when the elemental volume is near the vector to the field point. Under these conditions σ may be approximated by

$$\cos\sigma \approx \cos\xi \quad , \quad (3.42)$$

and the value of $H_{1\theta}(f)$ which contributes to the integral is just the value near the fixed angle ξ . The convolution integral becomes

$$I = H_{1\theta}^*(f_1, \xi) H_{1\theta}(f_1 + f_2, \xi)$$

$$\times \int_0^{2\pi} \int_0^{\pi/2} \frac{\sin\theta_o}{1 + j \frac{k_2}{\alpha_T} (1 - \cos\theta_o)} d\theta_o d\psi_o \quad . \quad (3.43)$$

After performing the integrals in Eq. (3.43), the general result for this limiting case is obtained from Eq. (3.35) and written

$$P_2(r, \theta, f) = - \frac{\omega_o^2 B R_o^2 P_o^2}{4 \rho_o c_o^4 r \alpha_T} e^{2\alpha_1 R_o} e^{-(\alpha_2 + jk_2)r} \int_{-\infty}^{\infty} F^*(f_1 - f_{1c}) F(f_1 + f_2 - f_{1c}) \\ \times H_{1\theta}^*(f_1) H_{1\theta}(f_1 + f_2) \frac{\alpha_T}{k_2} \left\{ \arctan\left(\frac{k_2}{\alpha_T}\right) - j \ln \left[1 + \left(\frac{k_2}{\alpha_T}\right)^2 \right]^{1/2} \right\} df_1 \quad . \quad (3.44)$$

When the half-power beamwidth corresponding with the Rutherford directivity is small in general and also small compared with the half-power beamwidths at the primary frequencies, the Rutherford directivity acts as a spatial impulse function and the parametric array is diffraction limited. Most of the nonlinear interaction takes place in the Fraunhofer region of the primary source and the directivity of the parametric array is determined by the product of the directivity or off-axis transfer functions at the primary frequencies. For this limiting form, the assumption of spherically spreading primary waves from the origin does not compromise validity of the result given by Eq. (3.44).

In deriving Eq. (3.44) it was assumed that the half-power beamwidth was small in general. According to Eq. (2.35), this assumption is valid as the absorption at the primary center frequency α_{1c} goes to zero and as the secondary frequency goes to infinity. Both of these conditions are physically unreasonable. The other assumption, which requires that the half-power beamwidth associated with the Rutherford directivity be small compared to the half-power beamwidths associated with the primary frequencies, is physically reasonable. It is this condition for which the limiting form given by Eq. (3.44) should be considered.

It should be noted that the limiting form for broadband radiation at the primary frequencies is linearly dependent on the secondary frequency in contrast to the quadratic dependence on secondary frequency for the broadband parametric array for plane wave fields. This trend was noted by Berkta and Leahy²⁵ and by Blue,³⁴ and has strong influence on the broadband parametric array. In going from an absorption limited parametric array to a diffraction limited parametric array, a shift in the power spectra toward lower frequencies will occur for a given primary transmission.

3. Farfield Solution with a Gaussian Pulse Primary Transmission from a Circular Piston

The general solutions for the secondary pressure fields which result with the broadband parametric array for nonplane wave fields are difficult to evaluate. Analyses of the limiting forms of these solutions are helpful especially when the primary directivity acts as a spatial impulse function and the broadband parametric array for plane wave fields is recovered. The results for this case are described in Section III.A. When the Rutherford directivity acts as a spatial impulse function, another limiting form is recovered where the product of the off-axis transfer functions is dominant in determining the secondary field. The detailed characteristics of the secondary sound field with the parametric array for nonplane wave fields may be described more concisely by considering a particular primary pulse transmission from a given conventional linear source.

The characteristics of a Gaussian pulse primary transmission from a circular piston is considered in detail in Appendix A. This transmission is mathematically tractable and is characterized by a spectrum with a single frequency peak on-axis. The transmission from a circular piston source is symmetric about the acoustic axis; therefore the solution for secondary pressure in the farfield of the broadband parametric array is obtained from Eq. (3.37). Utilizing the properties of the Gaussian pulse transmission given by Eqs. (A.13) and (A.18) and the circular piston given by Eq. (A.4), the solution is written

$$\begin{aligned}
P_2(r, \theta, f) = & - \frac{\omega_0^2 \beta R_o^2 P_o^2}{\rho_o c_o^4 r \alpha_T} \frac{\pi}{(2.668)^2} \left(\frac{Q_1}{f_{1c}} \right) e^{2\alpha_1 R_o} e^{-(\alpha_2 + j k_2) r} \\
& \times \int_{-\infty}^{\infty} \exp - \left\{ \left[\frac{\pi}{2.668} \frac{Q_1}{f_{1c}} \right]^2 \left[(f_1 - f_{1c})^2 + (f_1 + f_2 - f_{1c})^2 \right] \right\} \\
& \times \int_0^{\pi/2} \frac{J_1[k_1 a \sin \theta_o] J_1[(k_1 + k_2) a \sin \theta_o]}{[k_1 a \sin \theta_o] [(k_1 + k_2) a \sin \theta_o]} \left\{ 1 + j \frac{k_2}{\alpha_T} [1 - \cos(\theta_o - \theta)] \right\}^{-1/2} \\
& \times \left\{ 1 + j \frac{k_2}{\alpha_T} [1 - \cos(\theta_o + \theta)] \right\}^{-1/2} \sin \theta_o d\theta_o df_1 \quad . \quad (3.45)
\end{aligned}$$

In this form the secondary pressure depends on the quality factor Q_1 of the primary transmission and the primary center frequency f_{1c} . For a given f_{1c} , the secondary pressure is directly proportional to Q_1 . This behavior is a fundamental result of signal analyses which indicates that, if the total energy in the primary transmission is constant, then energy will be concentrated for a high Q_1 transmission over a narrow frequency band for both the primary and secondary transmissions. As Q_1 is decreased, the energy is spread over a broader band and the level at a given frequency component is reduced. For a constant Q_1 transmission, the secondary pressure is inversely proportional to the step-down ratio (ratio of primary center frequency to secondary frequency).

Equation (3.45) is well suited for numerical analysis and was evaluated using a double numerical integration routine⁶⁸ which employs an adaptive variable grid iterative technique. The results of the evaluation are given in Chapter 4 where computations with Eq. (3.45) are compared with experimental results.

Examination of the limiting forms of Eq. (3.45) offer physical insight into the characteristics of the secondary field. When the Rutherford directivity is dominant, the absorption limited parametric array for plane wave fields is recovered. When the directivity or off-axis transfer functions at the primary frequencies are dominant, the solution in this limit is given by Eq. (3.44) with appropriate substitutions, and written

$$\begin{aligned}
 P_2(r, \theta, f) = & - \frac{\omega_2^2 R_o^2 P_o^2}{\rho_o c_o^3 r} \left(\frac{\pi}{2.668} \right)^2 \left(\frac{Q_1}{f_{1c}} \right)^2 e^{2\alpha_1 R_o} e^{-(\alpha_2 + jk_2)r} \\
 & \times \left\{ \arctan\left(\frac{k_2}{\alpha_T}\right) - j \ln \left[1 + \left(\frac{k_2}{\alpha_T} \right)^2 \right]^{1/2} \right\} \\
 & \times \int_{-\infty}^{\infty} \exp - \left\{ \left[\frac{\pi}{2.668} \frac{Q_1}{f_{1c}} \right]^2 \left[(f_1 - f_{1c})^2 + (f_1 + f_2 - f_{1c})^2 \right] \right\} \\
 & \times \frac{J_1[k_1 a \sin \theta] J_1[(k_1 + k_2) a \sin \theta]}{[k_1 a \sin \theta] [(k_1 + k_2) a \sin \theta]} df_1 \quad . \quad (3.46)
 \end{aligned}$$

On the acoustic axis where $\theta=0$, Eq. (3.46) reduces to

$$\begin{aligned}
r_2(r, 0, f_2) = & - \frac{\omega_2 \beta R_o^2 P_o^2}{\rho_o c_o^3 r} \left(\frac{\sqrt{\pi}}{\sqrt{2} \cdot 2.668} \right) \left(\frac{Q_1}{f_{1c}} \right) e^{2\alpha_1 R_o} e^{-(\alpha_2 + jk_2)r} \\
& \times \left\{ \arctan \left(\frac{k_2}{\alpha_T} \right) - j \ln \left[1 + \left(\frac{k_2}{\alpha_T} \right)^2 \right]^{1/2} \right\} \\
& \times \exp \left\{ - \frac{\pi^2}{2(2.668)^2} \left(\frac{Q_1}{f_{1c}} \right)^2 f_2^2 \right\} \quad . \quad (3.47)
\end{aligned}$$

This on-axis solution for the extreme case of the diffraction limited broadband parametric array with a Gaussian pulse primary transmission may be compared with Eq. (3.7) which is the on-axis solution for the broadband parametric array for plane wave fields with a Gaussian pulse transmission. The terms in Eq. (3.47) involving k_2/α_T are slowly varying with respect to secondary frequency for values of $k_2/\alpha_T \gg 1$, which are of practical importance. Comparison of Eqs. (3.47) and (3.7) indicates that the spectral shapes for the two limiting cases are similar except for the shift from quadratic to linear dependence on secondary frequency in going from absorption to diffraction limited parametric arrays. Equation (3.47) yields a spectral peak at a frequency given by

$$f_{2p} = \frac{n}{\pi} = \frac{2.668}{\pi} \frac{f_{1c}}{Q_1} \quad . \quad (3.48)$$

This result is the peak frequency for the on-axis secondary transmission produced in the extreme case of a diffraction limited broadband parametric array. The peak frequency given by Eq. (3.48) may be compared with the result given by Eq. (3.9) for the broadband parametric array for plane wave fields. This comparison indicates that the peak

secondary frequency on-axis is higher for the absorption limited broadband parametric array by a factor of $\sqrt{2}$.

The off-axis transfer function $H_{2\theta}(f)$ for the extreme diffraction limited parametric array is obtained by using Eqs. (3.46) and (3.47) in Eq. (3.1). The off-axis transfer function is given by

$$H_{2\theta}(f_2) = \frac{4\sqrt{2}\pi}{2.668} \left(\frac{Q_1}{f_{1c}} \right) \exp \left[\frac{1}{2} \left(\frac{\pi}{2.668} \right)^2 \left(\frac{Q_1}{f_{1c}} \right)^2 \right] \\ \times \int_{-\infty}^{\infty} \exp - \left\{ \left[\left(\frac{\pi}{2.668} \right)^2 \left(\frac{Q_1}{f_{1c}} \right)^2 \right] \left[(f_1 - f_{1c})^2 (f_1 + f_2 - f_{1c})^2 \right] \right\} \\ \times \frac{J_1[k_1 a \sin\theta] J_1[(k_1 + k_2) a \sin\theta]}{[k_1 a \sin\theta] [(k_1 + k_2) a \sin\theta]} df_1 \quad (3.49)$$

The off-axis transfer function describes the spectral distortion which occurs at angles with respect to the acoustic axis. The square of the magnitude of the off-axis transfer function is a representation of the secondary power spectrum if on-axis this spectrum is uniform over all secondary frequencies.

The off-axis transfer function was evaluated for a fixed value of Q_1 and f_{1c} . In Fig. 3.7, the frequency dependence is examined as a function of off-axis angle. The off-axis angle is included in the dimensionless parameter $(a \sin\theta)_0 / c_0$. On the acoustic axis, $H_{2\theta}(f)$ is uniform as a function of frequency. Off-axis $H_{2\theta}(f)$ decreases at all frequencies with only a slightly larger decrease at the higher frequencies. This trend persists until a value of off-axis parameter of 1.05, where $H_{2\theta}(f)$ shows a decrease and then an increase in level as a function of frequency. At the next value of off-axis parameter 1.31,

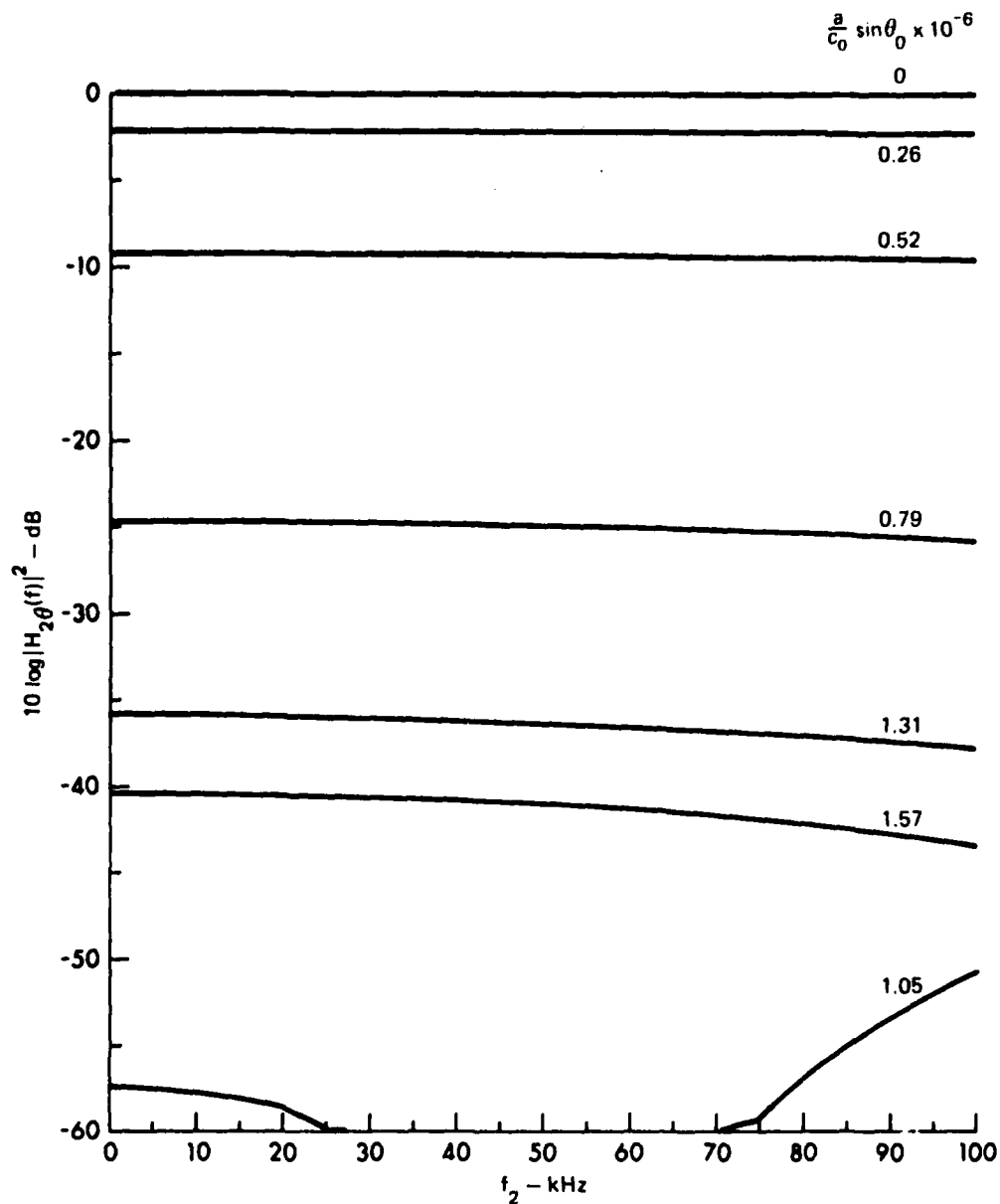


FIGURE 3.7
OFF-AXIS POWER TRANSFER FUNCTION versus FREQUENCY
FOR THE EXTREME DIFFRACTION LIMITED BROADBAND
PARAMETRIC ARRAY FOR NON PLANE WAVE FIELDS

$f(t) - \text{GAUSSIAN}, H_1 \theta(f) - \text{CIRCULAR PISTON}$

$Q_1 = 10.91 \quad f_{1c} = 600 \text{ kHz}$

$H_{2\theta}(f)$ again exhibits the original pattern. This behavior of the off-axis transfer function is better understood in Fig. 3.8, where $H_{2\theta}(f)$ is plotted as a function of the off-axis parameter. There are two curves on the plot. For zero secondary frequency $H_{2\theta}(f)$ has characteristics of a conventional off-axis transfer function exhibited by primary and secondary lobes. For a secondary frequency of 100 kHz, the curves are almost the same with a slight divergence around the amplitude null and a difference of about 3 dB at the common secondary peak. This off-axis transfer function for the broadband parametric array in the extreme diffraction limit is very unconventional. It is acute in angular response but is very insensitive in frequency response. In this limit the broadband parametric array exhibits very stable directional characteristics which are almost frequency independent. One feature which may be noted in the 100 kHz curve is the small peak near a value of 1.31 for the off-axis parameter. This peak occurs in integrating across the nulls of two off-axis transfer functions in the primary band, which differ in frequency by 100 kHz.

A representation of Eq. (3.46) which is applicable over the main beam of the off-axis transfer function may be obtained by approximating the principal maximum of $H_{1\theta}(f)$ for the circular piston with a Gaussian off-axis transfer function. The approximate $H_{1\theta}(f)$ is given by

$$H_{1\theta}(f_1) = \exp -[k_1 a K \sin \theta_0]^2 \quad ,$$

where K is a constant which is chosen to fit the principal maximum at a given amplitude.

If it is required that the Gaussian approximation fit the principal maximum at the one-half amplitude points, then Δ must satisfy

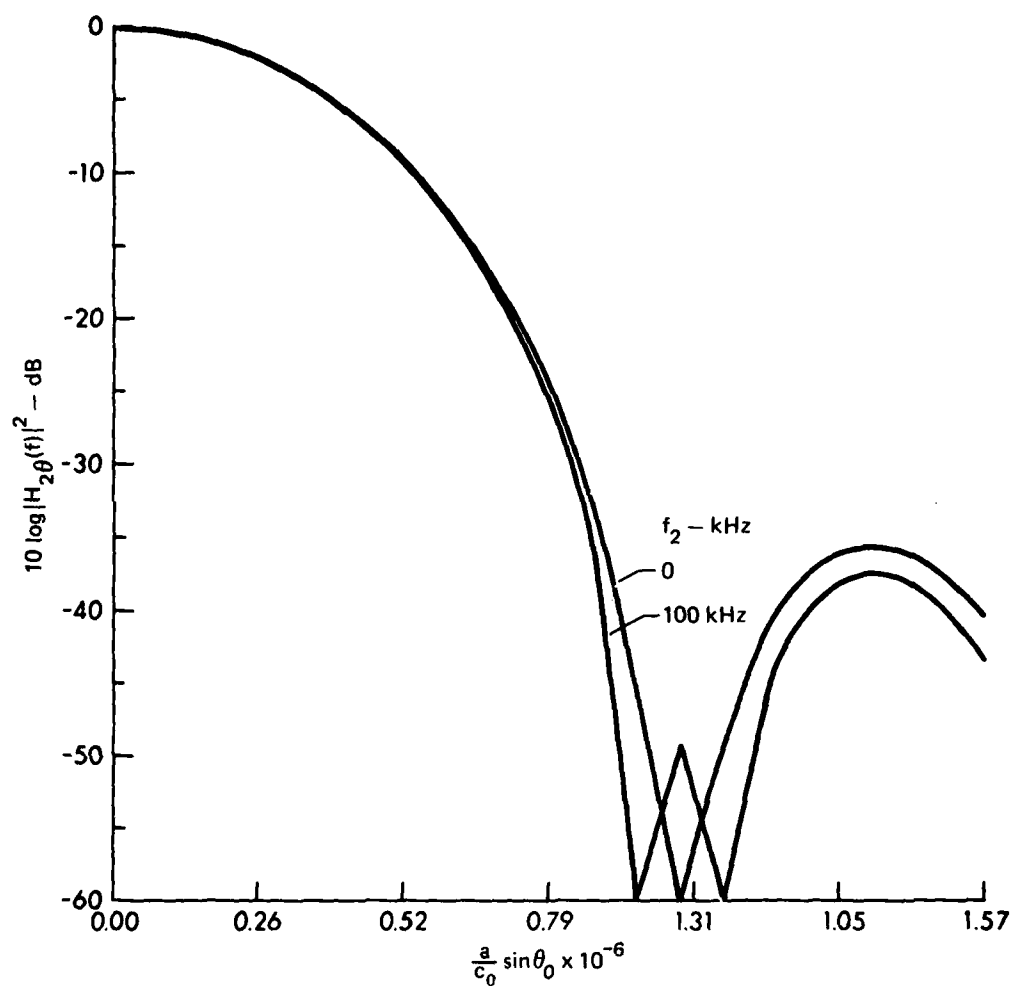


FIGURE 3.8
OFF-AXIS POWER TRANSFER FUNCTION versus OFF-AXIS ANGLE
FOR THE EXTREME DIFFRACTION LIMITED BROADBAND
PARAMETRIC ARRAY FOR NON PLANE WAVE FIELDS

$f(t)$ - GAUSSIAN, $H_1\theta(f)$ - CIRCULAR PISTON
 $Q_1 = 10.91$ $f_{1c} = 600$ kHz

ARL:UT
AS-81-1266
JMH - GA
9 - 15 - 81

$$H_{1\theta}(f_1) = \frac{2J_1[k_1 a \sin\theta_o]}{k_1 a \sin\theta_o} = \exp -[k_1 a K \sin\theta_o]^2 = 0.5 \quad (3.51)$$

Equation (3.51) is satisfied when $K=0.38$. Substituting this function in Eq. (3.44), the secondary field for the extreme diffraction limited parametric array with a Gaussian primary pulse transmission and a Gaussian off-axis transfer function is expressed in closed form by

$$P_1(r, \theta, f) = - \frac{\omega_2 \beta R_o^2 P_o^2}{\rho_o c_o^3 r} \frac{c_2^2}{\sqrt{2\pi}} (c_1^2 + c_2^2)^{-1/2} e^{2\alpha_1 R_o} e^{-(\alpha_2 + jk_2)r}$$

$$\times \left\{ \arctan\left(\frac{k_2}{\alpha_T}\right) - j \ln \left[1 + \left(\frac{k_2}{\alpha_T}\right)^2 \right]^{1/2} \right\}$$

$$\times \exp \left\{ - \left[\frac{1}{2} (c_1^2 + c_2^2) f_2^2 + 2c_1^2 f_2 f_{1c} - \left[\frac{c_2^2}{c_1^2 + c_2^2} - 1 \right] 2c_2^2 f_{1c}^2 \right] \right\} \quad (3.52)$$

where

$$c_1 = \frac{1}{c_o} 2\pi a K \sin\theta_o, \text{ and}$$

$$c_2 = \frac{\pi}{2.668} \frac{Q_1}{f_{1c}}.$$

The on-axis solution $P_2(r, 0, f)$ with the Gaussian approximation is equivalent to Eq. (3.47) which is the on-axis solution previously derived for this limit assuming the off-axis transfer function for the circular piston.

The off-axis transfer function $H_{2\theta}(f)$ with the Gaussian approximation is computed from Eq. (3.1) using Eqs. (3.52) and (3.47), and is given by

$$H_{20}(f) = c_2 (c_1^2 + c_2^2)^{-1/2} \times \exp - \left\{ \frac{1}{2} c_1^2 f_2^2 + 2c_1^2 f_{1c} f_2 - \left[\frac{c_2^2}{c_1^2 + c_2^2} - 1 \right] 2c_2^2 f_{1c}^2 \right\} \quad (3.53)$$

Equation (3.53) was evaluated for the same parameters which were used to evaluate Eq. (3.49). The frequency dependence of $H_{20}(f)$ in the Gaussian approximation is examined in Fig. 3.9 as a function of off-axis angle. A comparison of Figs. 3.7 and 3.9 indicates similar trends for both transfer functions with the exception that there is no case shown in Fig. 3.9, where the transfer function deviates from smooth regular behavior as it did in Fig. 3.7. The performance of $H_{20}(f)$ in the Gaussian approximation is examined as a function angle in Fig. 3.10 for secondary frequencies of 0 and 100 kHz. A comparison of this figure with Fig. 3.8 again indicates similar trends to a value of off-axis parameters of about 0.79. At this value the trends diverge, with $H_{20}(f)$ for the Gaussian approximation continuing to decrease monotonically while $H_{20}(f)$ for the circular piston decreases rapidly and then increases in response to the sidelobes in $H_{10}(f)$. The agreement between the two functions for $H_{20}(f)$ is reasonably good to the -30 dB power level over the principal maximum.

The analyses which have been presented have addressed the broadband parametric array for nonplane wave fields in the extreme diffraction limit. As the characteristics of the parametric transmission shift from the absorption limit to the diffraction limit, the dependence on secondary frequency shifts from quadratic to linear. With this shift in frequency dependence an accompanying shift toward lower frequencies in the power spectra will occur. This shift is characterized by a reduction in the frequency at the spectral peak by a factor of $\sqrt{2}$ on-axis for a Gaussian transmission. In the diffraction limit, the specific primary off-axis transfer function $H_{10}(f)$ is dominant in

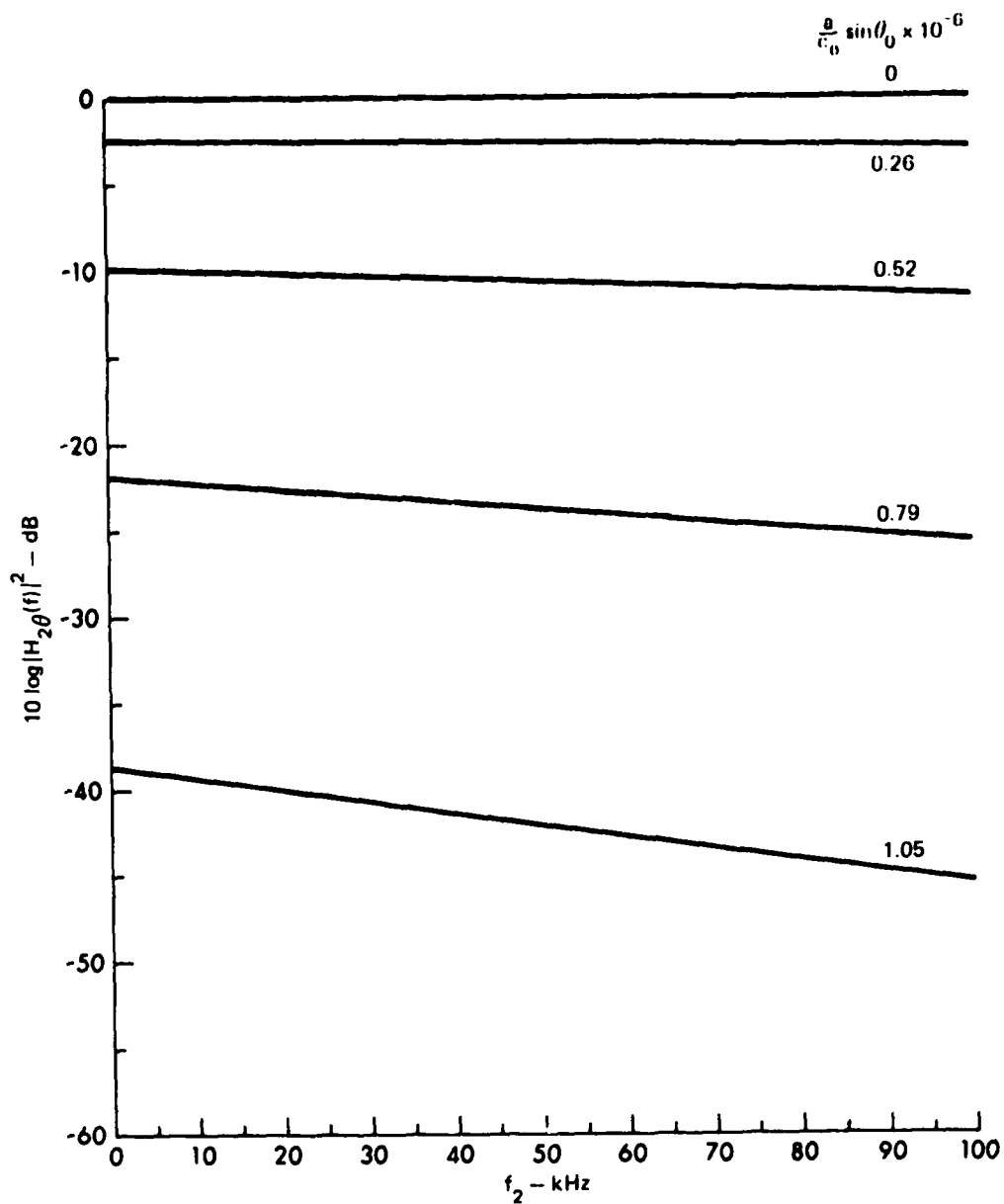


FIGURE 3.9
OFF-AXIS POWER TRANSFER FUNCTION versus FREQUENCY
FOR THE EXTREME DIFFRACTION LIMITED BROADBAND
PARAMETRIC ARRAY FOR NON PLANE WAVE FIELDS

$f(t) - \text{GAUSSIAN}, H_{1\theta}(f) - \text{GAUSSIAN APPROXIMATION}$

$Q_1 = 10.91 \quad f_{1c} = 600 \text{ kHz}$

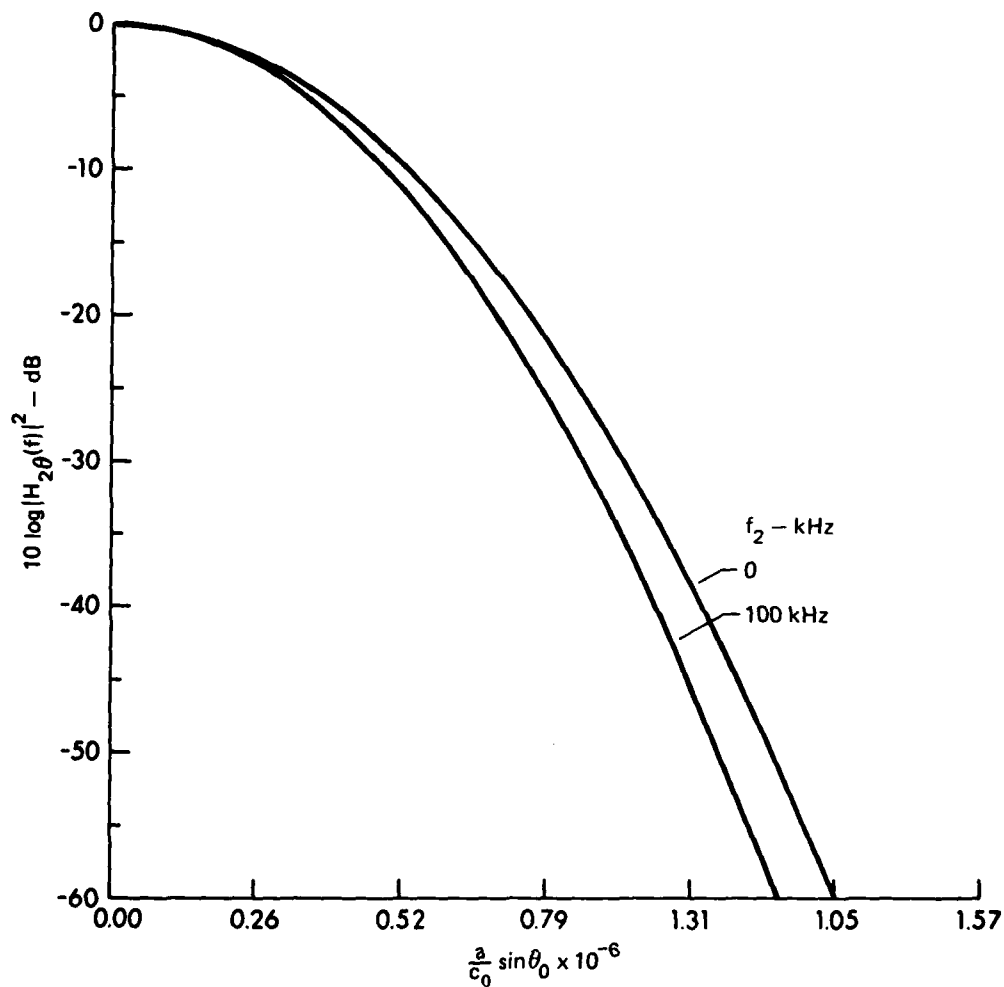


FIGURE 3.10
OFF-AXIS POWER TRANSFER FUNCTION versus OFF-AXIS ANGLE
FOR THE EXTREME DIFFRACTION LIMITED BROADBAND
PARAMETRIC ARRAY FOR NON PLANE WAVE FIELDS

$f(t) - \text{GAUSSIAN}, H_1(\theta, f) - \text{GAUSSIAN APPROXIMATION}$

$Q_1 = 10.91 \quad f_{1c} = 600 \text{ kHz}$

ARL:UT
 AS-81-1268
 JMH - GA
 9 - 15 - 81

determining the characteristics of the off-axis transfer function $H_{2\theta}(f)$ of the secondary transmission. The characteristics of $H_{2\theta}(f)$ generally follow those of $H_{1\theta}(f)$ as a function of angle but are extremely insensitive to secondary frequency.

CHAPTER IV

EXPERIMENTAL STUDY OF THE BROADBAND PARAMETRIC ARRAY

The objective of the experimental study is to measure the characteristics of the broadband parametric array as a function of various parameters. Particular emphasis is directed toward the behavior of the broadband parametric array as a function of primary directivity or off-axis transfer functions.

The experimental approach includes the use of a variable aperture circular piston source. This source provides variable primary directivity and allows parameter values such as primary center frequency and transducer transfer function to be held constant. Highly directive primary radiation with most of the nonlinear interaction occurring in the Fresnel diffraction region of the primary field represents a physical approximation of the absorption limited broadband parametric array for plane wave fields. As the primary directivity decreases, the transition to the diffraction limited broadband parametric array for non-plane wave fields occurs and the nonlinear interaction, which takes place in the Fraunhofer diffraction region, increases. The transition from plane wave to nonplane wave fields occurs most rapidly in going from values of 0.5 to 1.5 in the directivity ratio (ratio of primary half-power beamwidth to Rutherford beamwidth).

Experimental parameter values were selected that allow the formation of broadband parametric arrays which transition from a dominance in the absorption limit to a dominance in the diffraction limit. The aperture factor, which was briefly discussed in Chapters II and III, has greater influence on the off-axis properties of a broadband parametric transmission as the directivity of the primary source increases. Experimental parameter values were selected to minimize the effects of the aperture factor and restrict the effects to the -15 dB level or less in the secondary beam pattern. Other constraints that affect the

selection of experimental parameters include the restriction of step-down ratio to a value of 10 or less and the determination of primary center frequency so that the nearfield extent of the parametric array is mainly confined to measurement ranges that are accessible at the fresh water test site.

The experimental parameter values that were selected are given in Table IV.1. The center frequency for the primary transmission was chosen to be 600 kHz. With this frequency, the parametric array length is from 35.7-47.6 m based on absorption in fresh water from Schulkin and Marsh⁷⁵ and the change in water temperature during the test period. A circular piston with a selectable radius is specified for the source transducer. Four source configurations and directivities are indicated in Table IV.1. The values of primary pulse length, primary pulse quality factor, primary center frequency, and step-down ratio are inter-related and were selected after evaluation of the transmit performance of the selectable radius circular piston projector. The Rutherford beamwidth at 66 kHz and the primary product beamwidths are given for comparison.

A. Equipment and Procedures

The experimental study was conducted in fresh water at Lake Travis Test Station (LTTS), an instrumented, multiple barge facility moored in about 30 m of water. The physical configuration for the experiments consisted of a mechanically instrumented column on which the selectable radius circular piston projector was mounted at a depth of 4.48 m, and two portable columns on which the hydrophones were mounted at a depth of 4.48 m also. The acoustic paths were primarily underneath the floats on which the barges rest.

A block diagram of the experiments is shown in Fig. 4.1. The transmit section consists of an oscillator whose output is multiplied by a Gaussian envelope in the shaped pulse generator. The Gaussian

TABLE IV.1
EXPERIMENTAL PARAMETER VALUES

Primary Center Frequency, f_{1c}	600 kHz
Water Temperature, test period	12-17°C
Absorption Coefficient, 600 kHz, Fresh Water, α_{1c}	0.0105-0.0140 Np/m
Speed of Sound, Fresh Water, 20°C, c_o	1480 m/sec
Parametric Array Length, $1/2\alpha_{1c}$	35.7-47.6 m
Source Transducer	selectable radius, circular piston

<u>Radius (cm)</u>	<u>Half-Power Beamwidth at 600 kHz (deg)</u>
8.89	0.75
5.08	1.33
2.54	2.80
1.27	5.90

Primary Pulse Shape	Gaussian
Primary Pulse Lengths (0.17 amplitude level), T	14.2-16.6 μ sec
Primary Pulse Quality Factors, Q_1	8.5-10.0
Secondary Center Frequencies, f_{2c}	66-68 kHz
Step-Down Ratios, SDR	-9
Rutherford Beamwidth at 66 kHz, $\alpha_{1c}=0.0105$	1.40°
Primary Product Beamwidths	

<u>Radius (cm)</u>	<u>Half-Power Beamwidth (deg)</u>
8.89	0.53
5.08	0.94
2.54	1.98
1.27	4.17

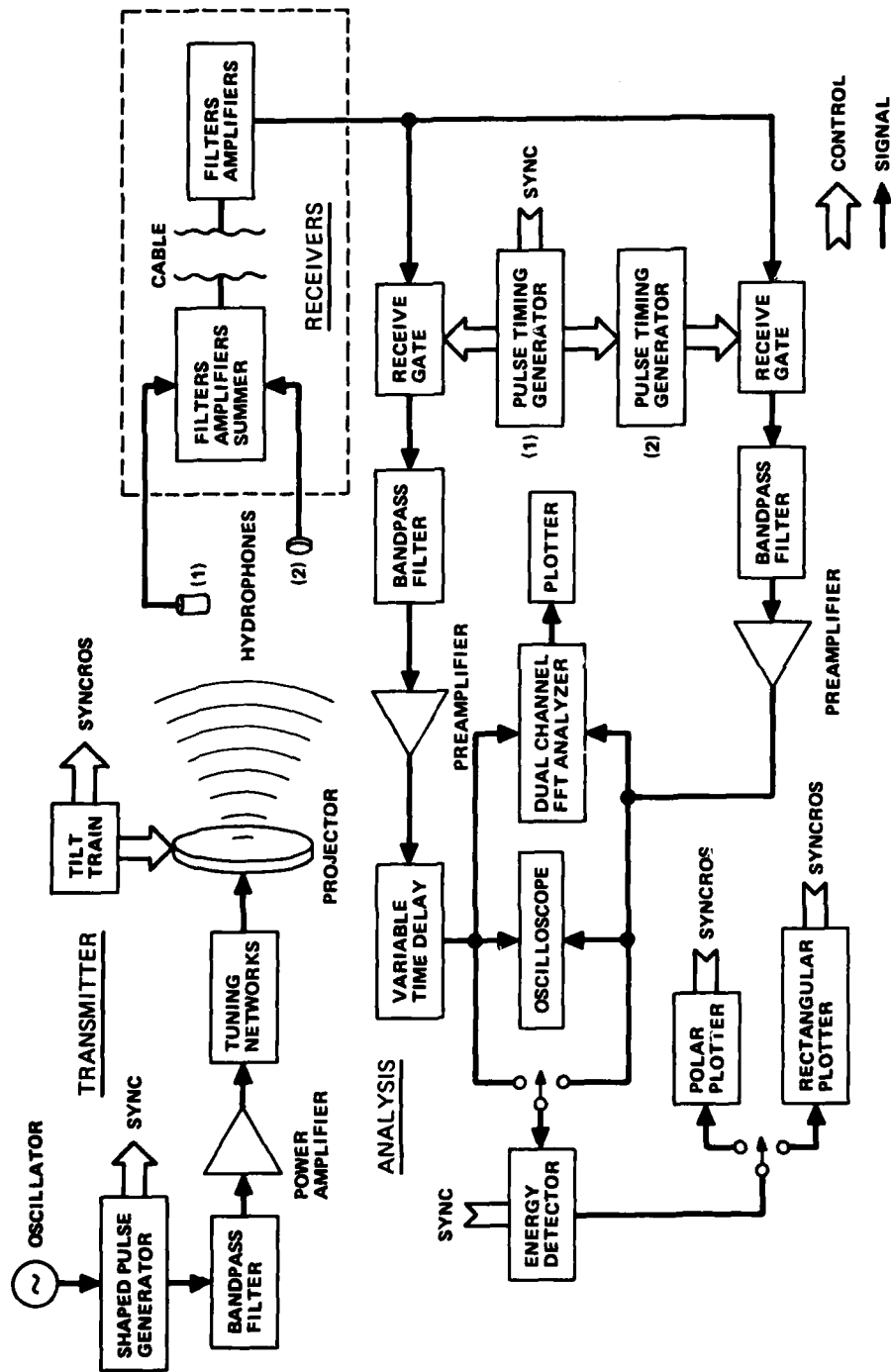


FIGURE 4.1
BLOCK DIAGRAM OF EXPERIMENTS

ARL:UT
AS-81-568
JMH - GA
6 - 16 - 81

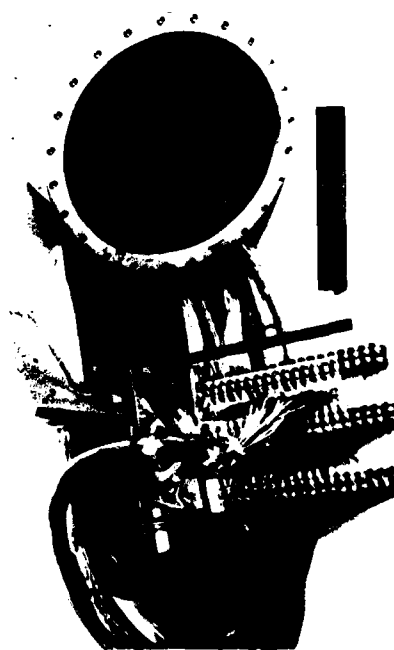
is stored in PROM, which may be clocked at a selectable rate to control the pulse length. The digital representation of the Gaussian envelope is converted to an analog representation and passed through a low pass filter before multiplication by the carrier signal. The Gaussian pulse is passed through a bandpass filter centered at the carrier to remove unwanted frequency components generated in the shaped pulse generator and input to a 2000 V·A power amplifier. The amplified signal is coupled to the projector through impedance matching and tuning networks that maximize the power transfer for each configuration of the projecting array. The shaped pulse generator provides the master sync signal on which all timing is based. Additional details regarding the transmit section and the shaped pulse generator are given in Appendix B. The fixed column that supports the projector is instrumented to provide calibrated electromechanical train, tilt, and depth positioning.

The transmitting array is the selectable radius circular piston projector (ARL 384-1) shown in Fig. 4.2. The transducer consists of 12 concentric circular ceramic rings and a center piston, which are driven in the thickness mode and may be selectively summed to form pistons of different radii. The directional properties of the projector at 600 kHz, which were measured and predicted for a piston set in an infinite rigid baffle, are summarized in Table IV.2. Details of the transducer design, construction, and performance are discussed in Appendix B. Only 4 of the 13 pistons were selected for detailed study of broadband parametric arrays.

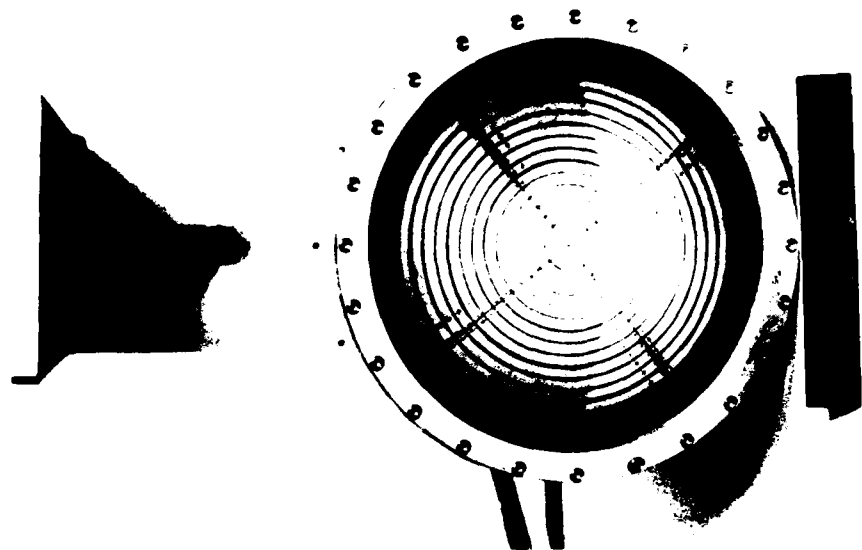
The receive section consists of two probe hydrophones which sampled the sound field. Their orientation was such that they were slightly displaced in range and azimuth. The outputs of these hydrophones were input to separate channels of passive filters and signal amplifiers and summed for transmission over the same cable. The hydrophone outputs were calibrated at the cable output, which was coupled to another group of filters and signal amplifiers. The conditioned signals were input to two analysis channels where the signals that were received



3768-1



3778-9



3778-12

FIGURE 4.2
SELECTABLE RADIUS CIRCULAR PISTON PROJECTOR (ARL 384-1)

TABLE IV.2

DIRECTIONAL PROPERTIES OF THE SELECTABLE
RADIUS CIRCULAR PISTON PROJECTOR (ARL 384-1) AT 600 kHz

<u>Radius (cm)</u>	<u>Measured Half- Power Beamwidth (deg)</u>	<u>Theoretical Half- Power Beamwidth (deg)</u>
*1.27	5.90	5.81
1.91	3.90	3.81
*2.54	2.80	2.91
3.18	2.14	2.32
3.81	1.18	1.94
4.45	1.44	1.66
*5.08	1.33	1.45
5.72	1.24	1.29
6.35	1.12	1.16
6.99	1.02	1.06
7.62	0.93	0.97
8.26	0.86	0.89
*8.89	0.75	0.83

* Indicates pistons that were selected for experimental study with the broadband parametric array.

at each hydrophone were separated by a receive gate. The gated signals on each channel were then passed through a bandpass filter and coupled to the analysis equipment. The analysis equipment included an oscilloscope to view the signal waveforms, an energy detector with both polar and rectilinear plotters to record directivity patterns, and a dual-channel FFT processor. The bulk of the analysis capability was provided by the Nicolet 660A dual-channel FFT processor, which was used for both time domain and frequency domain signal processing. Detail descriptions of the receive systems are given in Appendix B.

The probe hydrophones that were used to measure the sound field characteristics included the ARL-239-1, which was used for all single channel measurements at both the primary and secondary frequencies, and the USRD-E27-130P, which was used in the cross-signal analyses. Each of these hydrophones was operated well below resonance in order to achieve reasonably uniform frequency responses in the secondary band, which are needed for direct comparisons of measured and theoretical results. In addition, these hydrophones are small so that the angle subtended by the hydrophone cross section is small and therefore the ability to determine subtle changes in signal characteristics as a function of angle is not compromised.

A number of steps were required to reduce the experimental data which is presented in this chapter. The measurement error in determining absolute level was estimated to be about 2 dB. This measurement error results from a number of system and environmental considerations and is indicative of the long term total system stability. The short term measurement error in determining relative levels is generally much less than the long term or absolute measurement error and is estimated to be about 0.5 dB. There is also error in determining the peak frequency of a broad smooth spectral peak. This error will be discussed where applicable in the presentation of experimental results.

B. The Broadband Parametric Array With Low Amplitude Primary Waves

The performance of the broadband parametric array with low amplitude primary waves refers to the operating conditions where the behavior of the primary signal is predominately linear. This operating domain is identified by the harmonic characteristics of the primary signal as a function of measurement range. There is a somewhat gradual transition from linear to finite amplitude behavior, and identification of these regions is discussed in Section C.

Experimental data that are presented in this section are compared with theoretical results, which are valid in the farfield of the broadband parametric array. The experimental data were obtained at a measurement range of 23.6 m. This distance is from 50% to 66% of the farfield range, but is also in a region where most of the significant nonlinear interaction has already occurred. Estimates of propagation curves³⁷ for the cases that are discussed indicate that data taken at the measurement range differ in amplitude about 1-1.5 dB from farfield behavior of the parametric array; therefore theoretical results for performance in the farfield of the parametric array should be comparable to experimental results. Inputs to the theoretical models include both assumed and measured parameters. The theoretical results are therefore subject to errors that are implicit in measurement errors associated with the input parameters.

1. High Primary Directivity

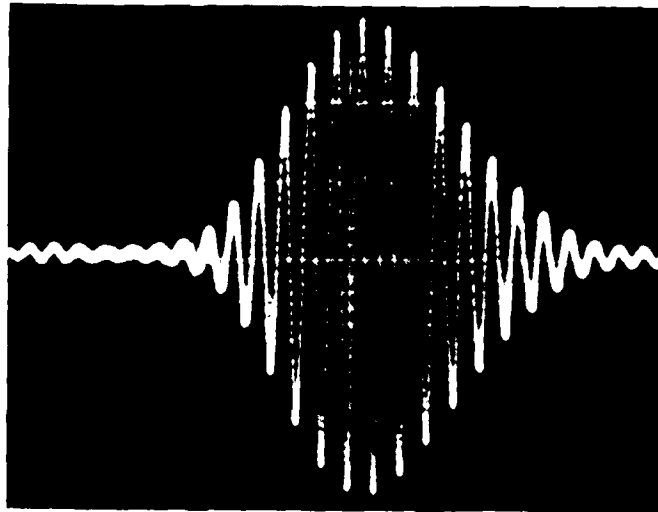
The initial experimental effort involved a primary source configuration that used the full active face, $a = 8.89$ cm, of the selectable radius circular piston projector. In this configuration, the primary half-power beamwidth is 0.75° from Table IV.2, and the Rayleigh distance R_0 is 10.07 m or about 43% of the measurement range. This case represents a physical approximation of the broadband parametric array

for plane wave fields with a directivity ratio of about 0.54. The water temperature during the collection of experimental data was about 17°C.

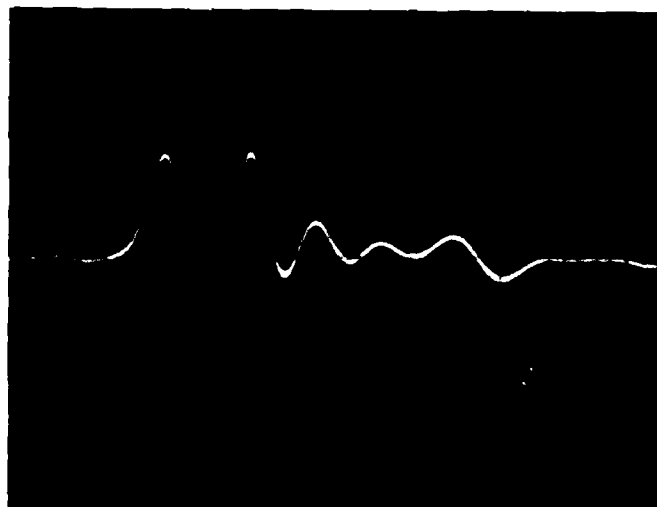
The on-axis acoustic waveforms are shown in Fig. 4.3. The narrowband primary signal, Fig. 4.3(a), is predominantly Gaussian shaped; however, the rise time of the waveform is slightly less than the decay time. This result is due to response characteristics of the tuning networks and the projecting array. The pulse length at the 17% peak amplitude level is about 17-19 μsec and the measured peak sound pressure level is 195.2 dB re 1 μPa . This level is near the transition from linear to finite amplitude behavior at the primary frequency, but is still predominantly linear. The secondary signal output, Fig. 4.3(b), has a finite duration over about 60 μsec but only the first 20-22 μsec is indicative of the secondary signal of Fig. 3.2. The remaining portions of the output result from the impulse response of the hydrophone, a situation which was also noted by Ceen and Pace.⁶⁷

The off-axis behavior of the secondary signal is presented in Fig. 4.4. The waveforms are gated so that only the secondary signal is retained and shown in 0.25° increments to an off-axis angle of 2.75°. As the sequence progresses, the second major positive peak in the signal is progressively diminished and the zeroes and points of inflection are spread in time. This sequence indicates the trend described by Westervelt,⁹ where the secondary signal on-axis is proportional to the second derivative of the square of envelope function and, off-axis, the proportionality is with respect to the first derivative. It should be noted that the display gain was adjusted to aid in viewing each waveform, which accounts for the increase in noise level with increasing angle. An analysis of ungated secondary outputs is given in Appendix C.

The autocorrelation of the secondary signals at each off-axis angle is shown in Fig. 4.5. On-axis, the autocorrelation has three positive and two negative peaks. As the angle off-axis increases, the first and last positive peaks diminish and the absolute time lag between



(a) 600 kHz PRIMARY SIGNAL
5 μ sec/div

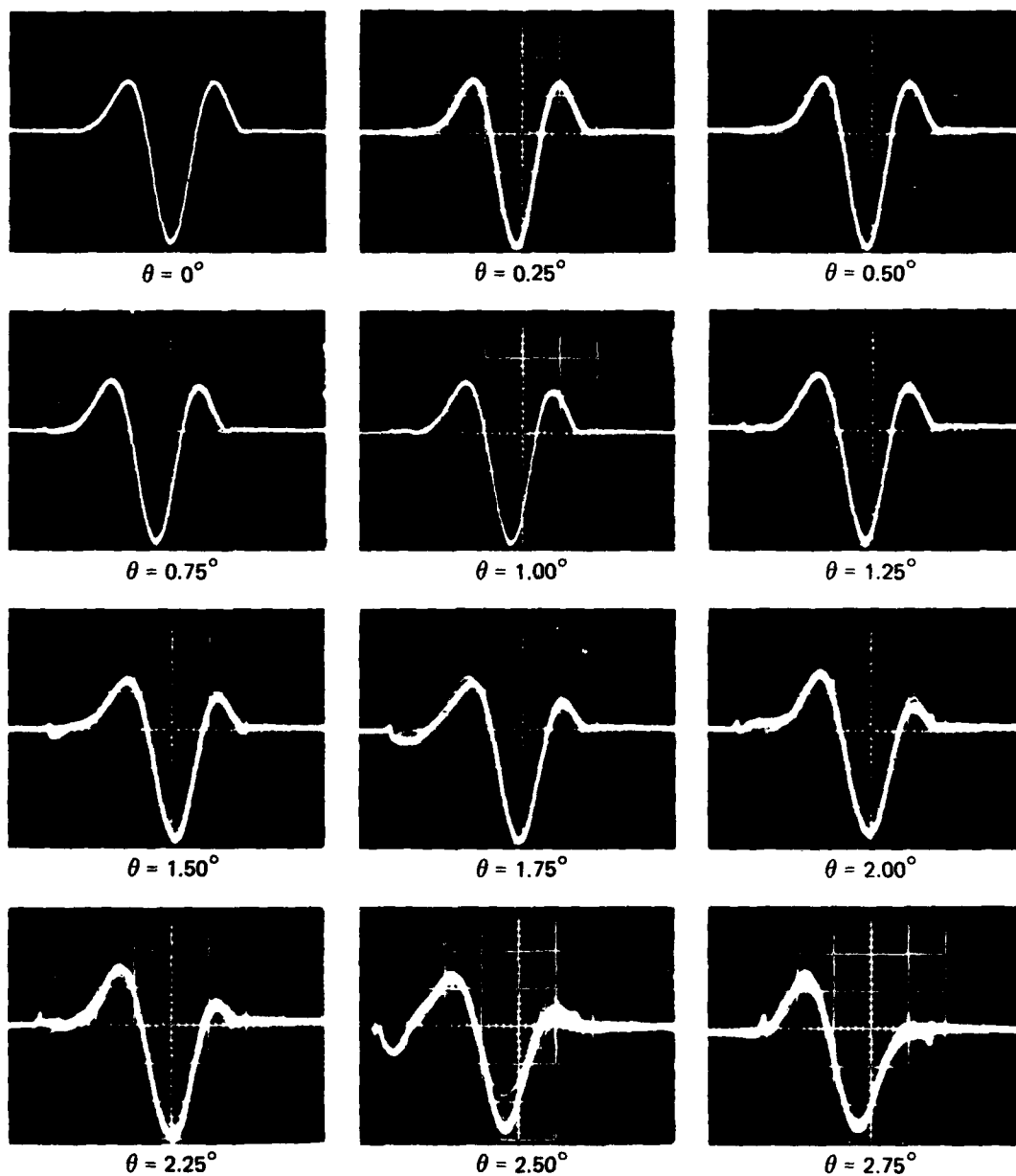


(b) SECONDARY SIGNAL
10 μ sec/div

FIGURE 4.3
ON-AXIS ACOUSTIC WAVEFORMS FOR
THE BROADBAND PARAMETRIC ARRAY

$f(t)$ - GAUSSIAN, $f_{1c} = 600$ kHz, $a = 8.89$ cm
SPL₁ = 195.2 dB re 1 μ Pa, $R_0 = 10.07$ m, $r = 23.6$ m

ARL:UT
AS-81-674
JMH - GA
6 - 16 - 81

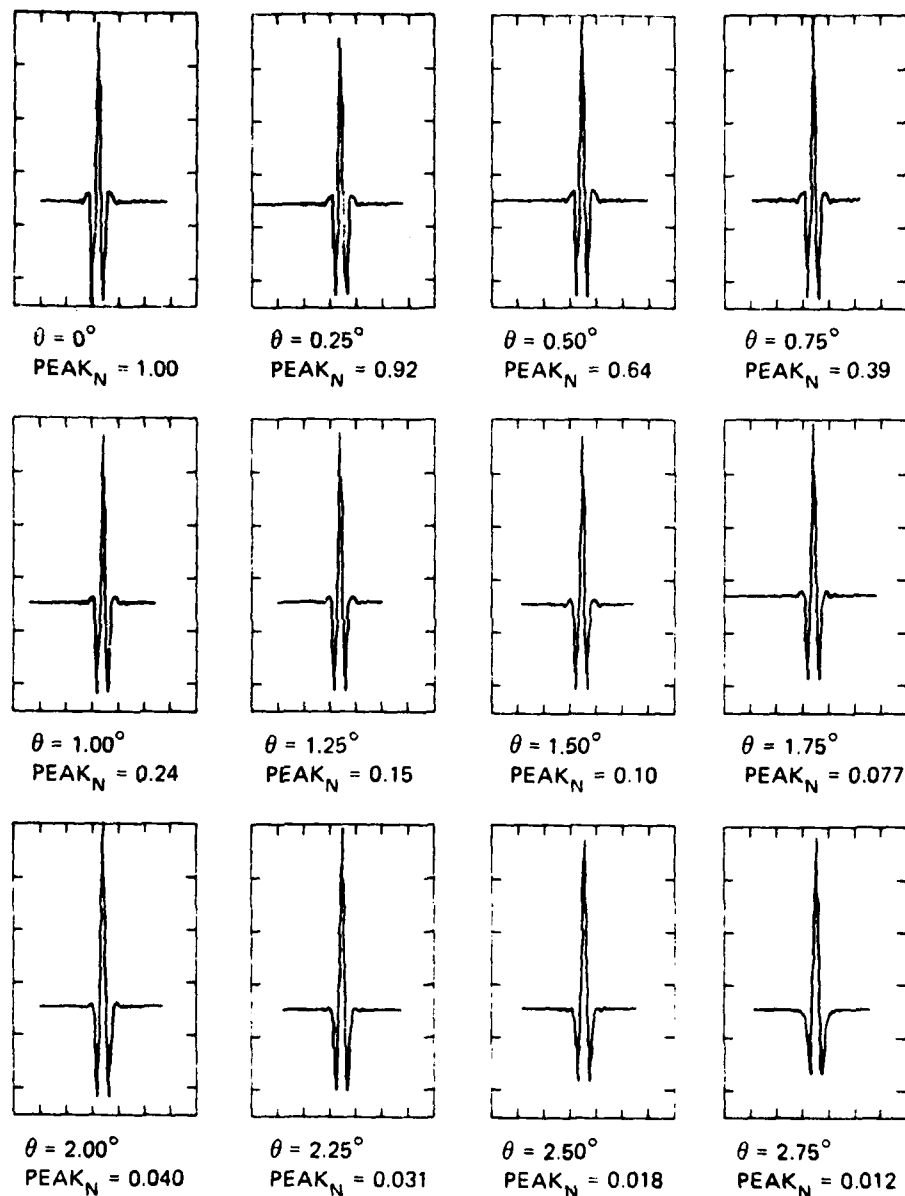


TIME - 5 μ sec/div

FIGURE 4.4
OFF-AXIS ACOUSTIC WAVEFORMS FOR THE BROADBAND PARAMETRIC ARRAY

GATED, $f(t)$ - GAUSSIAN, $f_{1c} = 600$ kHz
 $SPL_1 = 195.2$ dB re 1μ Pa, $a = 8.89$ cm
 $R_0 = 1' 37$ m, $r = 23.6$ m

ARL:UT
 AS-81-575
 JMH - GA
 6 - 16 - 81



TIME = 30 $\mu\text{sec. div}$

FIGURE 4.5
AUTOCORRELATION OF THE OFF-AXIS ACOUSTIC SIGNALS
FOR THE BROADBAND PARAMETRIC ARRAY

$f(t) \rightarrow$ GAUSSIAN, $f_{1c} = 600 \text{ kHz}$
 $\text{SPL}_1 = 195.2 \text{ dB re } 1 \mu\text{Pa}$
 $a = 8.89 \text{ cm}$, $R_0 = 10.07 \text{ m}$, $r = 23.6 \text{ m}$

the two negative peaks increases. The relative amplitude of the autocorrelation at each angle measured at $\tau=0$ is noted in the figure. These relative amplitudes trace the energy beam pattern for the radiation.

A more detailed analysis of the properties of the broadband parametric array may be considered in the frequency domain. The normalized power density spectra for the measured on-axis transmission are shown in Fig. 4.6. This spectrum has 250 Hz resolution and was computed from the incoherent average of 100 individual spectra over successive transmission sequences with a repetition rate of about 4 msec. The spectrum was calibrated at 65 kHz by substituting a pure tone at the calibrated receive system output and adjusting the amplitude to produce an equivalent signal input. The result was adjusted to compensate for the resolution bandwidth of the FFT processor, and the relative duration of the measured signal and the calibration signal. Using this procedure, the peak sound pressure level, SPL_2 , of the 66 kHz spectral component was determined to be 158.0 dB re 1 μ Pa at 23.6 m.

Theoretical results were computed for comparison with measured results by numerical integration of Eq. (3.45). This equation is the solution for the frequency components of the secondary pressure in the farfield of the broadband parametric array assuming a Gaussian pulse primary transmission from a circular piston. Since the primary transmission is not exactly Gaussian, the specific characteristics of the transmission were established from both the experimental data and iterations of Eq. (3.45). The parameters of the primary transmission are given by a Q_1 of 10 and a pulse duration of 16.7 μ sec at the 17% peak amplitude level.

With these parameter values, an on-axis peak secondary sound pressure level at 66 kHz of 162.5 dB re 1 μ Pa at 23.6 m is predicted from Eq. (3.45), which is about 4.5 dB greater than the measured value. About 2 dB of this difference results from the incompleteness of the

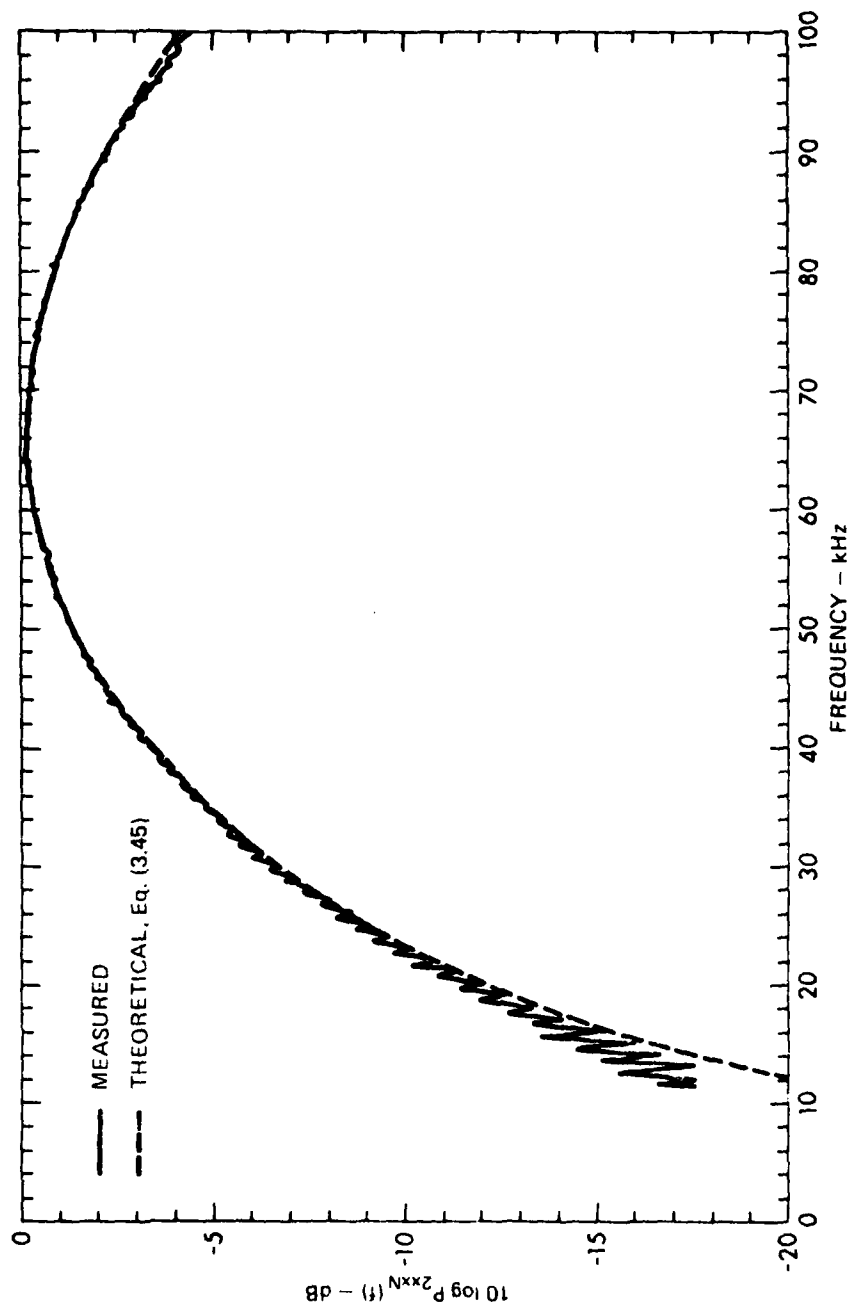


FIGURE 4.6
 NORMALIZED POWER DENSITY SPECTRA ON-AXIS
 FOR THE BROADBAND PARAMETRIC ARRAY
 $f(t)$ - GAUSSIAN, $f_c = 600$ kHz, $SPL_1 = 195.2$ dB re $1 \mu\text{Pa}$
 $Q_1 = 10.0$, $a = 8.89$ cm, $R_0 = 10.07$ m, $r = 23.6$ m

parametric array with the measurement range at the end of the nearfield. The remaining 2.5 dB is due to the cumulative effects of errors in measured values and assumed values. The normalized power spectral density function was computed from Eqs. (3.21) and (3.45) and is shown in Fig. 4.6 with the experimental results. Comparison of the two curves indicates excellent agreement between experimental and theoretical results above the -15 dB power level. Below this level at low frequencies, the curves slightly diverge with more power being present in the experimental data. This behavior results from several considerations including the fact that the pulse shown in Fig. 4.3 is not exactly Gaussian as assumed in the theoretical development. Also, the effect of the frequency response of the receiving hydrophone was greatly reduced (but not totally eliminated) by gating the receive signal as discussed in Appendix C. Finally, as the S/N declines at lower frequencies, the influence of the background noise level is increased.

The normalized power density spectra for the secondary transmissions at off-axis angles from 0.0° to 3.0° are presented at angular increments of 0.25° in Figs. 4.7 and 4.8. As the angle off-axis is increased, the level and the frequency at the spectral peak are reduced, which is the trend predicted for the broadband parametric array for plane wave fields and which is under investigation for the broadband parametric array for nonplane wave fields. Quantitative comparisons of the normalized power spectra for the measured and predicted data are awkward in this presentation format. A format better suited for such comparisons is presented in Fig. 4.9, where the frequency and level at the spectral peak are plotted as a function of normalized off-axis angle. The normalization is with respect to the measured half-power angle $\theta_{3\text{ dB}}$. This data presentation removes the effects of absolute angle and preserves the differences between data that are dominantly absorption or diffraction limited. Each of the power spectra is characterized by a broad peak. In determining the frequency and level at the spectral peak from the experimental measurements, the peaks were assumed to be symmetric above the -1.5 dB normalized level. This

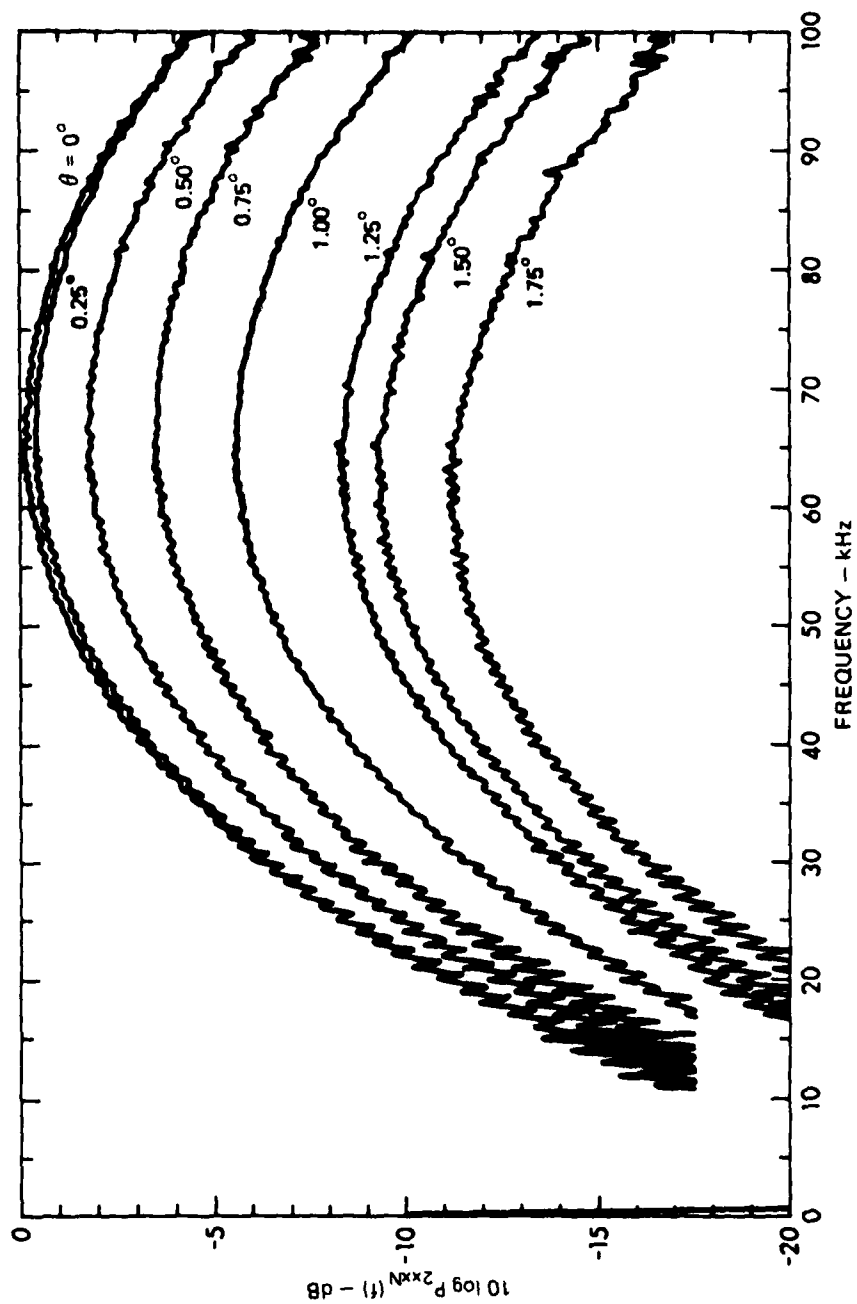


FIGURE 4.7
 NORMALIZED POWER DENSITY SPECTRA FOR THE BROADBAND PARAMETRIC ARRAY
 AT OFF-AXIS ANGLES FROM 0.00° TO 1.75°
 $f(t)$ - GAUSSIAN, $f_{1c} = 600$ kHz, $SPL_1 = 195.2$ dB re $1 \mu Pa$
 $a = 8.89$ cm, $R_0 = 10.07$ m, $r = 23.6$ m

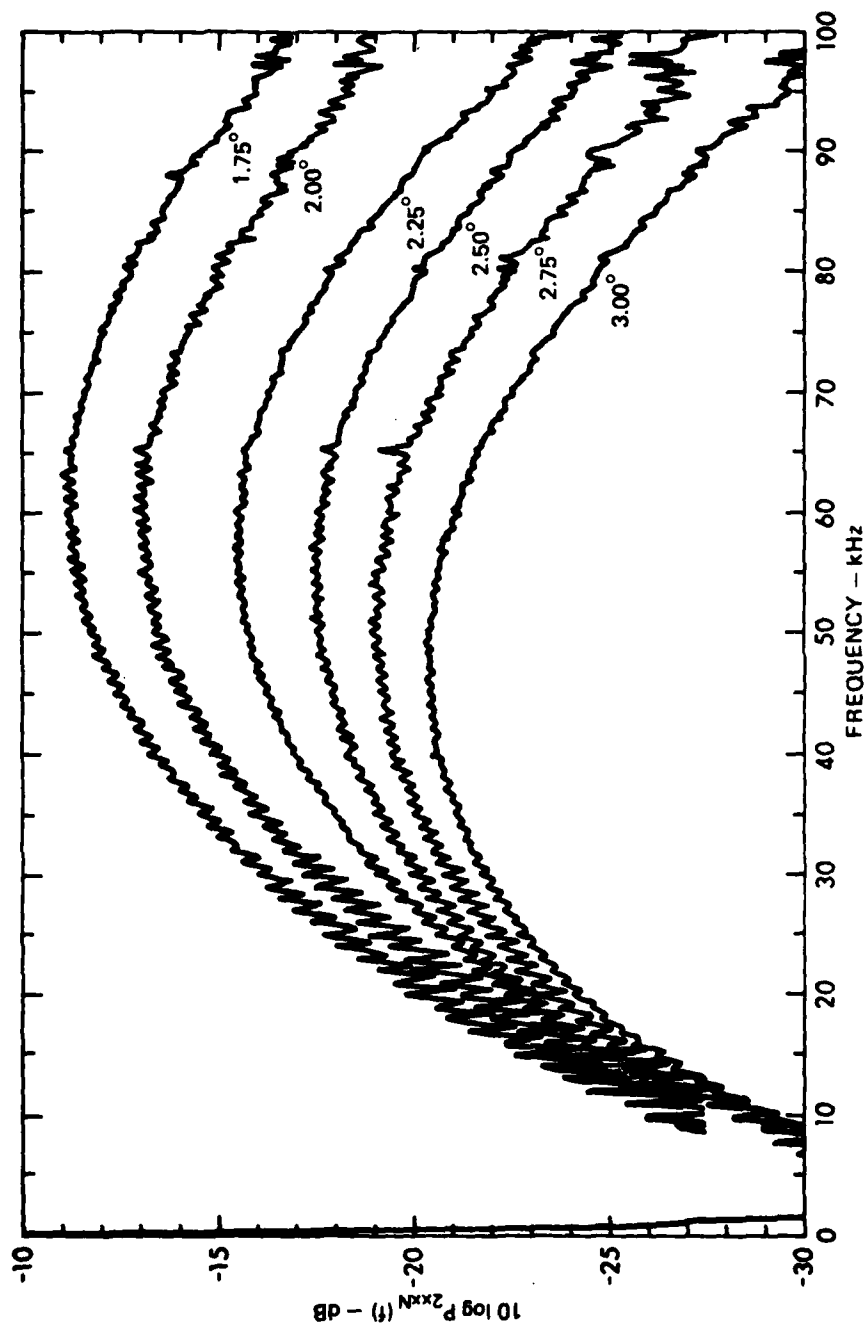


FIGURE 4.8
NORMALIZED POWER DENSITY SPECTRA FOR THE BROADBAND PARAMETRIC ARRAY
AT OFF-AXIS ANGLES FROM 1.75° TO 3.00°

$f(t)$ — GAUSSIAN, $f_{1c} = 600$ kHz, $SPL_1 = 195.2$ dB re $1 \mu Pa$
 $a = 8.89$ cm, $R_0 = 10.07$ m, $r = 23.6$ m

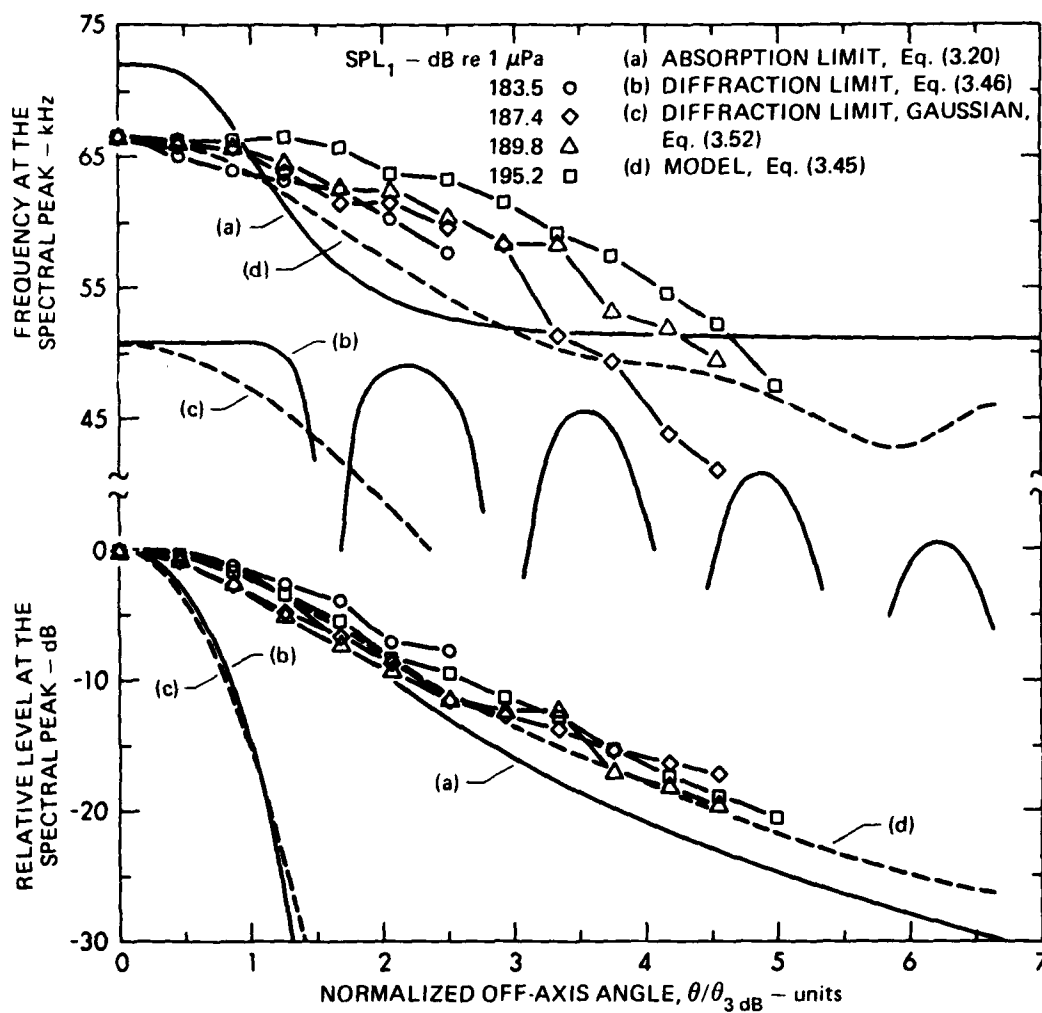


FIGURE 4.9
FREQUENCY AND LEVEL AT THE SPECTRAL PEAK OFF-AXIS
FOR THE BROADBAND PARAMETRIC ARRAY

$f(t)$ - GAUSSIAN, $f_{1c} = 600$ kHz, $a = 8.89$ cm, $R_0 = 10.07$ m, $r = 23.6$ m
 $\theta_{3dB} = 0.70^\circ$ (MEASURED)

assumption leads to an uncertainty of about 2% in determining the frequency at the spectral peak and has a negligible effect on the determination of level. For the data shown in Fig. 4.9, the power spectrum on-axis has a peak at about 66 kHz and a half-power width of about 60 kHz. The theoretical results shown in Fig. 4.9 are computed from the farfield solution given by numerical integration of Eq. (3.45) and several limiting forms. The limiting forms include the absorption limit, Eq. (3.20), and the diffraction limit for a circular piston, Eq. (3.46), and the Gaussian approximation to a circular piston, Eq. (3.52).

Experimental data are shown in Fig. 4.9 for four different primary peak sound pressure levels, SPL_1 , at 23.6 m. These data are predominantly low level in the primary transmission. As the angle off-axis is increased, the trend toward decreasing frequency at the spectral peak is observed. The trend is characterized by a relatively constant frequency for the spectral peak at small angles and transitions to a steady downward shift in frequency for the spectral peak at angles greater than about $\theta_{3\text{ dB}}$. The overall shift was measured to be from about 66 kHz on-axis to about 41 kHz at an angle of $4.6(\theta_{3\text{ dB}})$ or 2.8° . The limitation on the acquisition of data at larger angles was due to deteriorating S/N. It should be noted that S/N's at off-axis angles greater than $3(\theta_{3\text{ dB}})$ were extremely poor for the data taken with an SPL_1 of 187.4 dB. As a result, the low frequency content of the normalized power density spectrum may have been contaminated by ambient noise in the medium, which would contribute to lower indications of frequency at the spectral peak for these data. The relative level at the spectral peak is indicative of the energy beam pattern. These data are monotonically decreasing to a level of -20 dB and yield a half-power beamwidth of about 1.4° for the secondary transmission.

The data are dominantly linear with the exception of the curve taken at the highest on-axis peak sound pressure level, SPL_1 . For these data, the trend toward downward shift in frequency at the spectral peak

is slower and indicates the onset of finite amplitude effects in the primary transmission. This behavior is also noted in the relative level at the spectral peak; however, the trend is not as pronounced. These results indicate that the frequency content of the secondary signal is a more sensitive indicator of the onset of finite amplitude effects in the primary transmission than the relative level. The performance of the broadband parametric array during transition from dominantly linear behavior in the primary transmission to strong finite amplitude behavior is discussed further in Section IV.B.

Theoretical results are presented in Fig. 4.9 for comparison with experimental data. In the absorption limit (from Eq. (3.20)), the peak frequency on-axis is about 6 kHz higher than observed. The trend toward a downward shift in frequency at the spectral peak is slow for small angles, increases to a rapid shift in the region from $0.5(\theta_{3\text{ dB}})$ to $1.5(\theta_{3\text{ dB}})$, and becomes relatively constant at large angles. The level at the spectral peak in the absorption limit is monotonically decreasing and is slightly lower in level than the experimental data.

In the diffraction limit (from Eq. (3.46)), the peak on-axis frequency is about 15 kHz lower than observed. The frequency at the spectral peak is constant to about $\theta_{3\text{ dB}}$, where a rapid decrease occurs. At larger angles, lobes in the frequency at the spectral peak are noted, which result from lobes in the off-axis transfer function shown in Fig. 3.8. No theoretical data are shown between lobes in the diffraction limit. In these regions the frequency at the spectral peak is not well behaved; however, these regions are in the nulls of the off-axis transfer function and little energy is contained in the frequency components. The level at the spectral peak decreases very rapidly and indicates a half-power beamwidth of about 0.3° . In the diffraction limit with a Gaussian approximation (from Eq. (3.52)) for the off-axis transfer function, the frequency at the spectral peak has the same on-axis value as observed with the diffraction limit for the circular piston transfer function. At angles off-axis, the frequency behavior

differs from that of Eq. (3.46). The frequency at the spectral peak decreases monotonically with a 3.5 kHz difference at $\theta_{3\text{ dB}}$. In contrast, the relative level at the spectral peak for both diffraction limited representations are in agreement to the -30 dB level. At some level below -30 dB the curves diverge as the sidelobe structure in the off-axis transfer function for the circular piston becomes dominant.

The limiting forms of the broadband parametric array for nonplane wave fields do not fit the experimental data; but these limiting forms do bracket the trends that are noted in the data. The relative values of the on-axis frequency at the spectral peak may be evaluated in determining the exponent of the overall dependence of the secondary frequency. Recall that the dependence is quadratic in the absorption limit and linear with secondary frequency in the diffraction limit. The overall dependence of the experimental results on secondary frequency is given by $\omega_2^{1.68}$.

The solution in the farfield of the broadband parametric array with a Gaussian pulse primary transmission from a circular piston is given by Eq. (3.45), which was evaluated numerically for comparison with the experimental data. These theoretical results indicate the predicted frequency at the spectral peak on-axis and are in excellent agreement with the experimental data for angles off-axis to $\theta_{3\text{ dB}}$. At larger angles, the theoretical results are in general agreement but predict slightly lower frequencies at the spectral peak. Off-axis, the characteristics of the broadband parametric array for nonplane wave fields are strongly influenced by the sidelobe structure in the off-axis transfer function. The difference between the theoretical predictions and the measured results is due to the difference in the assumed off-axis transfer or directivity function for a piston in an infinite rigid baffle and the real off-axis transfer function measured for the source and shown in Appendix A. The measured off-axis transfer or directivity functions are complex in sidelobe structure. The sidelobes are generally 4-5 dB higher than predicted for a piston in an infinite rigid

baffle and the presence of spacing lobes, which result from the particular design of the source transducer, are noted. The higher sidelobes for the source tend to retard the downward shift in frequency at the spectral peak in the measured data. This trend will be discussed further in relation to the secondary transmissions produced by primary radiation from other source configurations. For the parameters of the broadband parametric array considered in the experiment, the convolution integral is dominated by Rutherford scattering. This dominance tends to reduce and average the effects of the sidelobes in the primary off-axis transfer function. At large angles the influence of the primary transfer function shifts from the main lobe to the sidelobes, and is noted in the theoretical results from Eq. (3.45).

The relative level at the spectral peak is in excellent agreement with the theoretical results predicted by Eq. (3.45). At the half-power angle, the theoretical results in the absorption limit and from Eq. (3.45) are in close agreement with the experimental data. This agreement was noted in earlier studies as verification of the Westervelt model for the parametric array for plane wave fields. This agreement is good at $\theta_{3\text{ dB}}$; however, at larger angles the normalized level in the absorption limit has a more rapid rate of reduction. This result supports the conclusion that the parametric array formed with the given set of experimental parameters is only approximated by the analytical description of the broadband parametric array for plane wave fields.

A power beam pattern for the secondary transmission is shown in Fig. 4.10. This pattern has a half-power width of about 1.2° and the characteristic appearance of the parametric directivity with no discernible sidelobes over about 25 dB of S/N. This measurement was performed with an energy detector. A comparison of power beam pattern representations is shown in Fig. 4.11. In this figure, normalized levels are plotted as a function of angle for the output of an energy detector, the amplitude of the autocorrelation for time shift equal to zero, and the relative level at the spectral peaks. The close agreement of the data

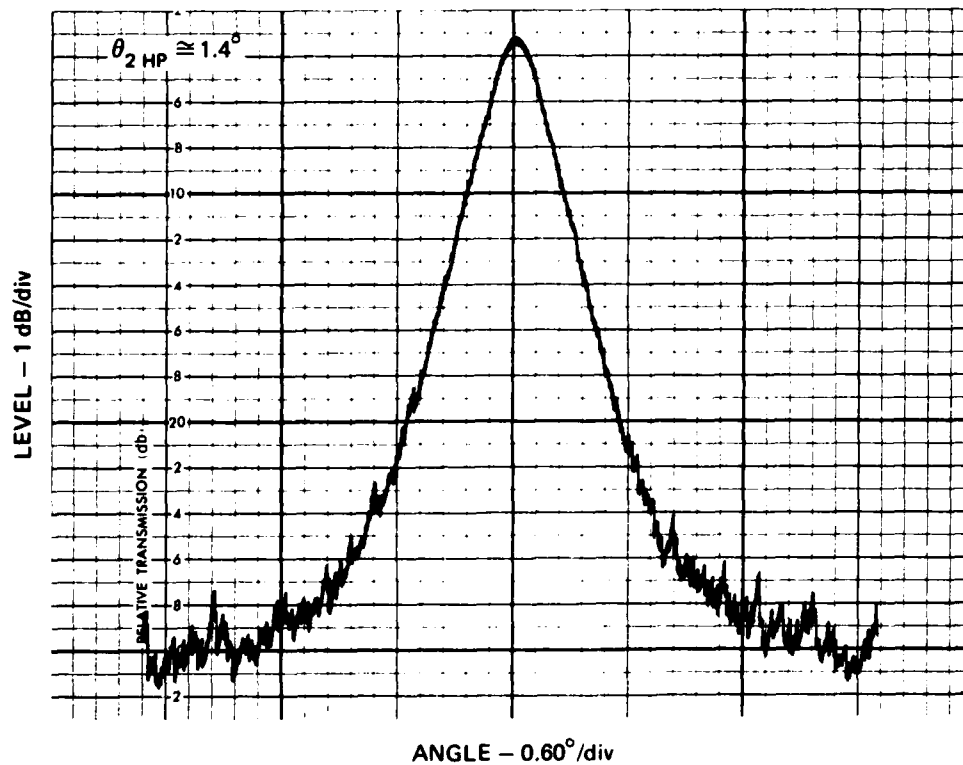


FIGURE 4.10
SECONDARY POWER BEAM PATTERN FOR
THE BROADBAND PARAMETRIC ARRAY
 $f(t)$ - GAUSSIAN, $f_{1c} = 600 \text{ kHz}$, $\text{SPL}_1 = 195.2 \text{ dB re } 1 \mu\text{Pa}$
 $f_{2c} \cong 66 \text{ kHz}$, $a = 8.89 \text{ cm}$, $R_0 = 10.07 \text{ m}$, $r = 23.6 \text{ m}$

ARL:UT
 AS-81-591
 JMH - GA
 6-16-81

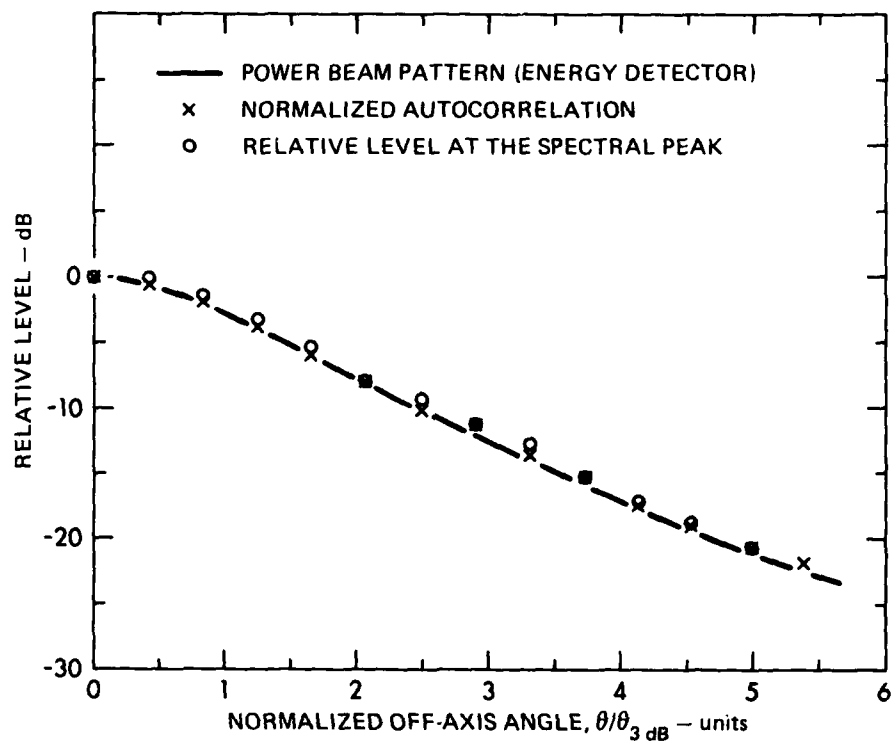


FIGURE 4.11
COMPARISON OF SECONDARY POWER BEAM PATTERN REPRESENTATIONS

$f(t)$ - GAUSSIAN, $f_{1c} = 600$ kHz, $SPL_1 = 195.2$ dB re $1 \mu Pa$, $f_{2c} \cong 66$ kHz
 $a = 8.89$ cm, $R_0 = 10.07$ m, $r = 23.7$ m, $\theta_{3dB} = 0.70$

ARL:UT
 AS-81-592
 JMH - GA
 6-16-81

indicates that each of these methods is indicative of the total energy in the secondary signal for the parametric transmissions and may be used to trace the power beam pattern.

2. Performance as a Function of Primary Directivity

As the primary directivity is decreased, a transition in the characteristics of the broadband parametric array occurs from that of plane wave fields in the absorption limit (physical approximation) to that of nonplane wave fields in the diffraction limit. In conjunction with this trend, the dominance of the off-axis transfer function shifts from that associated with Rutherford scattering to the square of the off-axis primary transfer function. The off-axis characteristics of the secondary field as a function of primary directivity were experimentally evaluated for directivity ratios of 0.89, 1.74, and 3.69. These experimental results are representative of intermediate directivity for the broadband parametric array and may be compared with the results from the preceding section where a physical approximation for the broadband parametric array in the absorption limit was formed with a directivity ratio of 0.54.

The broadband parametric array with a directivity ratio of 0.89 was formed with the selectable radius circular piston set to a radius of 5.08 cm and evaluated in water at a temperature of about 15°C. The parameters of the primary transmission are given by a Q_1 of 9.8, a pulse duration of 16.3 μ sec, and an on-axis primary peak sound pressure level, SPL_1 , of 189.0 dB re 1 μ Pa at the measurement range. The frequency and level at the spectral peak were extracted from measured power density spectra and are shown in Fig. 4.12 with theoretical results presented for comparison. An on-axis secondary peak sound pressure level, SPL_2 , of 147.9 dB re 1 μ Pa at 23.6 m was measured at 66 kHz. This measurement is about 4 dB lower than the value of 152.0 dB re 1 μ Pa predicted from Eq. (3.45). The difference is attributed to the incompleteness of the parametric array and the cumulative effects of errors

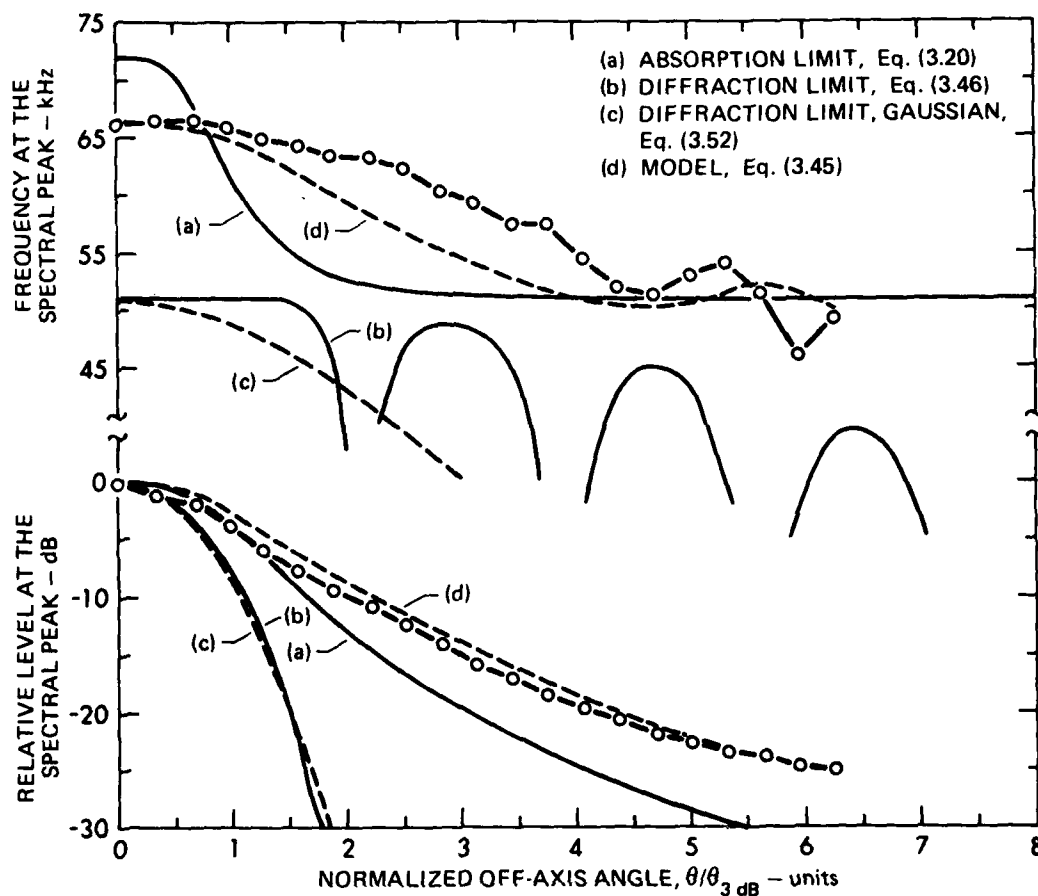


FIGURE 4.12
FREQUENCY AND LEVEL AT THE SPECTRAL PEAK OFF-AXIS
FOR THE BROADBAND PARAMETRIC ARRAY

$f(t)$ - GAUSSIAN, $f_{1c} = 600$ kHz, $SPL_1 = 189.0$ dB re $1 \mu Pa$

$a = 5.08$ cm, $R_0 = 3.29$ m, $r = 23.7$ m

$\theta_{3 dB} = 0.80^\circ$ (MEASURED)

ARL:UT
 AS-81-593
 JMH - GA
 6-16-81

in measured and assumed values. The trends in these data are similar to those for a directivity ratio of 0.54; however, the rate of downward shift in frequency at the spectral peak with angle off-axis is reduced. The frequency shift with angle is not monotonically decreasing as indicated by a minor frequency peak at about $5.3(\theta_{3\text{ dB}})$. The relative level at the spectral peak is monotonically decreasing with no apparent minor peaks or sidelobes.

The theoretical results for the limiting forms of the broadband parametric array are shown for the absorption limit, the diffraction limit, and the Gaussian approximation in the diffraction limit. These limiting forms bracket the trends in the experimental data. The relative values of the on-axis peak spectral frequencies indicate that the overall dependence of the experimental data on secondary frequency is $\omega_2^{1.60}$, indicating a slight shift toward the diffraction limit relative to the data presented for a directivity ratio of 0.54. The theoretical results from the model, Eq. (3.45), are presented in the figure. Good agreement between the experimental data and the theoretical results is noted in the frequency at the spectral peak for off-axis angles to $\theta_{3\text{ dB}}$. For larger angles, the theoretical results indicate frequencies at the spectral peak that are slightly lower than observed. This is the same trend noted in previous analyses, which is attributed to the higher sidelobe levels in the real primary off-axis transfer functions than assumed in the theoretical model. Both Eq. (3.45) and the experimental results indicate minor frequency peaks that result from the cumulative effects of secondary lobes in the primary off-axis transfer function. The minor frequency peaks do not occur at the same angle, which is another indication that the real and the assumed primary transfer functions differ.

Close agreement over all angles is noted in the level at the spectral peak, with the results from Eq. (3.45) only slightly higher than the measured data. There is no apparent influence of the secondary lobes of the primary transfer function on the level at the spectral peak

over a 25 dB range. The energy beam pattern for this parametric array is shown in Fig. 4.13. The measured half-power beamwidth is about 1.6° , and there are no sidelobes apparent in the pattern.

The broadband parametric array with a directivity ratio of 1.74 was formed with a radius of 2.54 cm and evaluated in water at about 12°C . The parameters of the primary transmission are given by a Q_1 of 8.9, a pulse duration of 14.9 μsec , and an on-axis primary peak sound pressure level of 187.8 dB re 1 μPa at the measurement range. The frequency and level at the spectral peak extracted from both measured and theoretical results are shown in Fig. 4.14. The on-axis secondary peak sound pressure level, SPL_2 , is 153.6 dB re 1 μPa at 23.6 m measured at 67 kHz. The predicted value for the secondary sound pressure level computed from Eq. (3.45) is 156.5 dB re 1 μPa at 23.6 m. The predicted value is higher than the measured value by about 3 dB, which again is attributed to the incompleteness of the parametric array and errors in measured and assumed values. A further decrease in the rate of downward shift in frequency as a function of off-axis angle is indicated relative to the results for smaller directivity ratios, and a minor frequency peak is noted at about $4.4(\theta_{3\text{ dB}})$. The relative level at the spectral peak is monotonically decreasing and there is some indication of a secondary peak at about $4.3(\theta_{3\text{ dB}})$. It is not surprising that sidelobes should appear in the secondary beam patterns as the diffraction limit is approached. Sidelobes have been observed in the beam patterns of the narrowband parametric array for high directivity ratios.³⁷

The theoretical results for the limiting forms for the broadband parametric array are shown in Fig. 4.14. The transition toward the diffraction limit is noted in the overall dependence on secondary frequency given by $\omega_2^{1.37}$ and the increased influence of the primary off-axis transfer functions. In comparing the experimental data with the results from Eq. (3.45), the behavior noted is similar to the cases for lower directivity ratios. Good agreement is observed in the frequency at the spectral peak for off-axis angles to $\theta_{3\text{ dB}}$. At

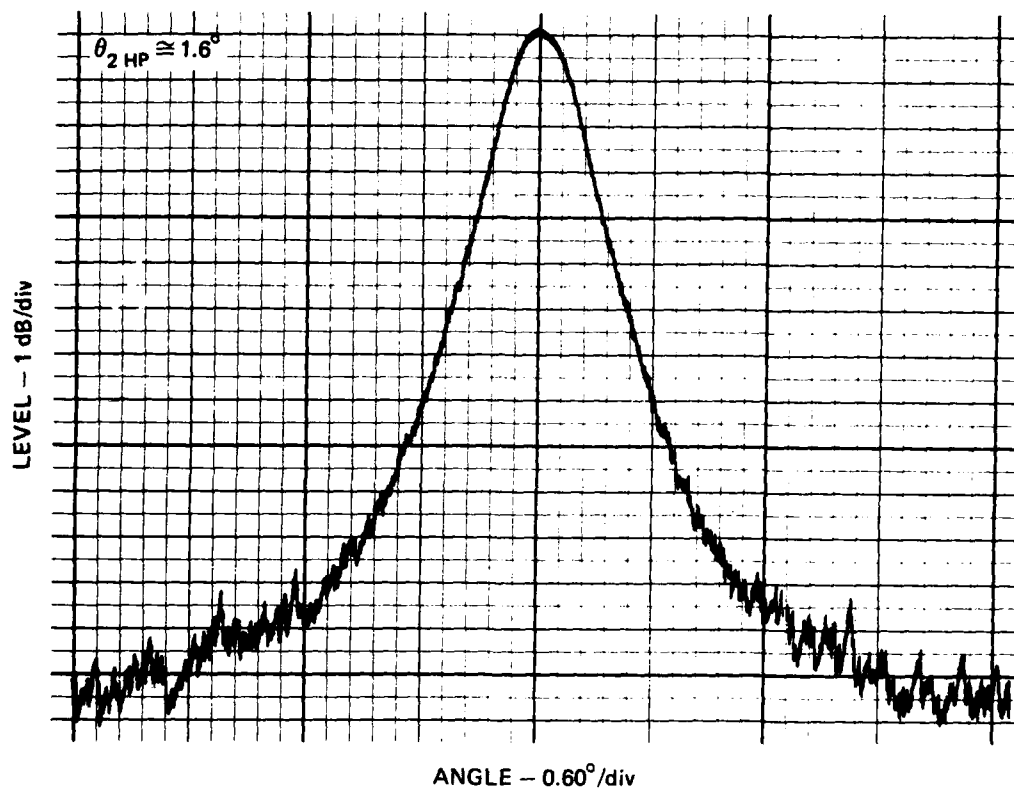


FIGURE 4.13
SECONDARY POWER BEAM PATTERN FOR
THE BROADBAND PARAMETRIC ARRAY
 $f(t)$ - GAUSSIAN, $f_{1c} = 600 \text{ kHz}$, $\text{SPL}_1 = 189.0 \text{ dB re } 1 \mu\text{Pa}$
 $f_{2c} \approx 66 \text{ kHz}$, $a = 5.08 \text{ cm}$, $R_0 = 3.29 \text{ m}$, $r = 23.6 \text{ m}$

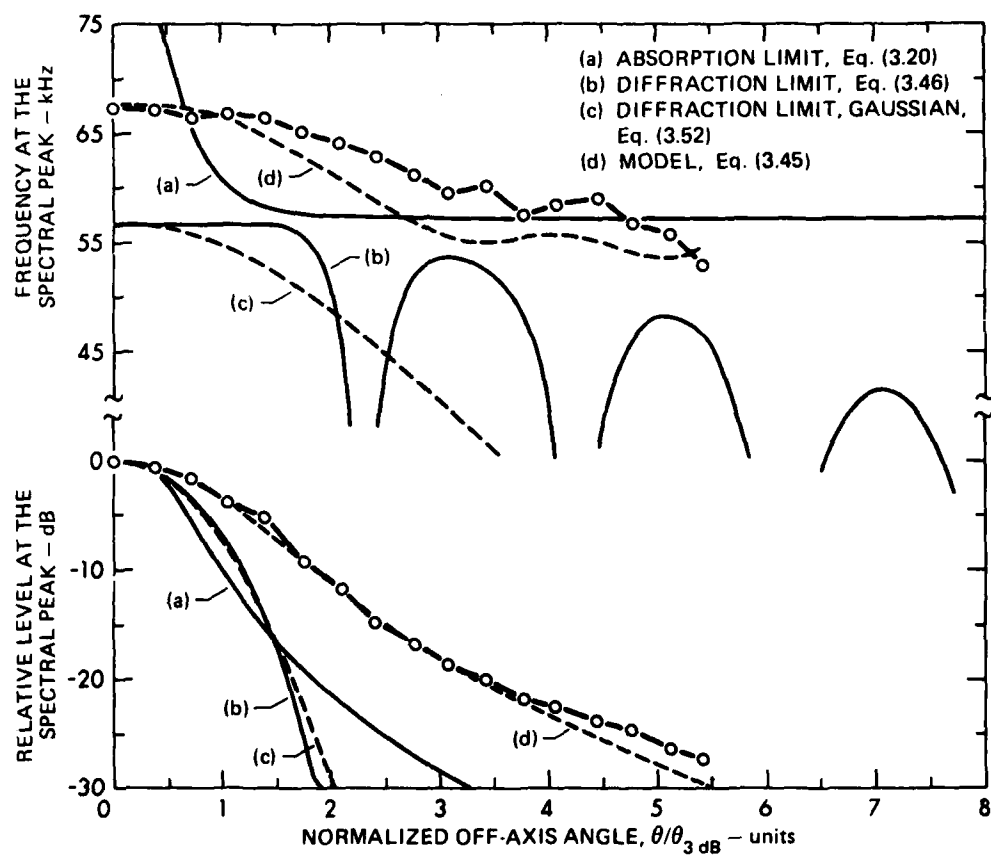


FIGURE 4.14
FREQUENCY AND LEVEL AT THE SPECTRAL PEAK OFF-AXIS
FOR THE BROADBAND PARAMETRIC ARRAY

$f(t)$ - GAUSSIAN, $f_{1c} = 600$ kHz, $SPL_1 = 187.8$ dB re $1 \mu\text{Pa}$
 $a = 2.54$ cm, $R_0 = 0.82$ m, $r = 23.6$ m
 $\theta_{3dB} = 1.47^\circ$ (MEASURED)

larger angles the theoretical results are slightly low because the sidelobe levels in the real off-axis transfer functions are higher than assumed in the model. In these data, however, the minor frequency peaks occurring in both the experimental and theoretical data are approximately aligned over off-axis angles from about $3.5(\theta_{3\text{ dB}})$ to $5(\theta_{3\text{ dB}})$. This behavior is observed even though the sidelobe levels are different. Fewer sidelobes in the primary off-axis transfer function are combined to give the general result. As the directivity of a linear source is decreased, the lower order sidelobes become broader and agreement between theoretical and actual orientation of the lobes generally improves.

The agreement between the theoretical and experimental results is excellent except where the sidelobe is noted in the experimental data. No discernible lobe is predicted in this region from Eq. (3.45). The energy beam pattern is shown in Fig. 4.15 where a half-power beam-width of about 2.9° is indicated.

The final broadband parametric array was formed with a directivity ratio of 3.69 and a piston radius of 1.27 cm and was evaluated in water at about 12°C . The parameters of the primary transmission are given by a Q_1 of 8.5, a pulse duration of 14.2 μsec , and an on-axis primary peak sound pressure level of 182.0 dB re 1 μPa at the measurement range. The measured and theoretical results for the frequency and level at the spectral peak are shown in Fig. 4.16. The on-axis secondary peak sound pressure level, SPL_2 , for this case is 149.6 dB re 1 μPa at 23.6 m measured at 68 kHz. The secondary sound pressure level computed from Eq. (3.45) is predicted to be 151.0 dB re 1 μPa at the measurement range. The predicted value differs from the measured value by about 1.4 dB due to errors in measured and assumed values and to the incompleteness of the parametric array. The rate of downward shift in frequency has further decreased with a broad minor peak in frequency at about $4.3(\theta_{3\text{ dB}})$. The relative level at the

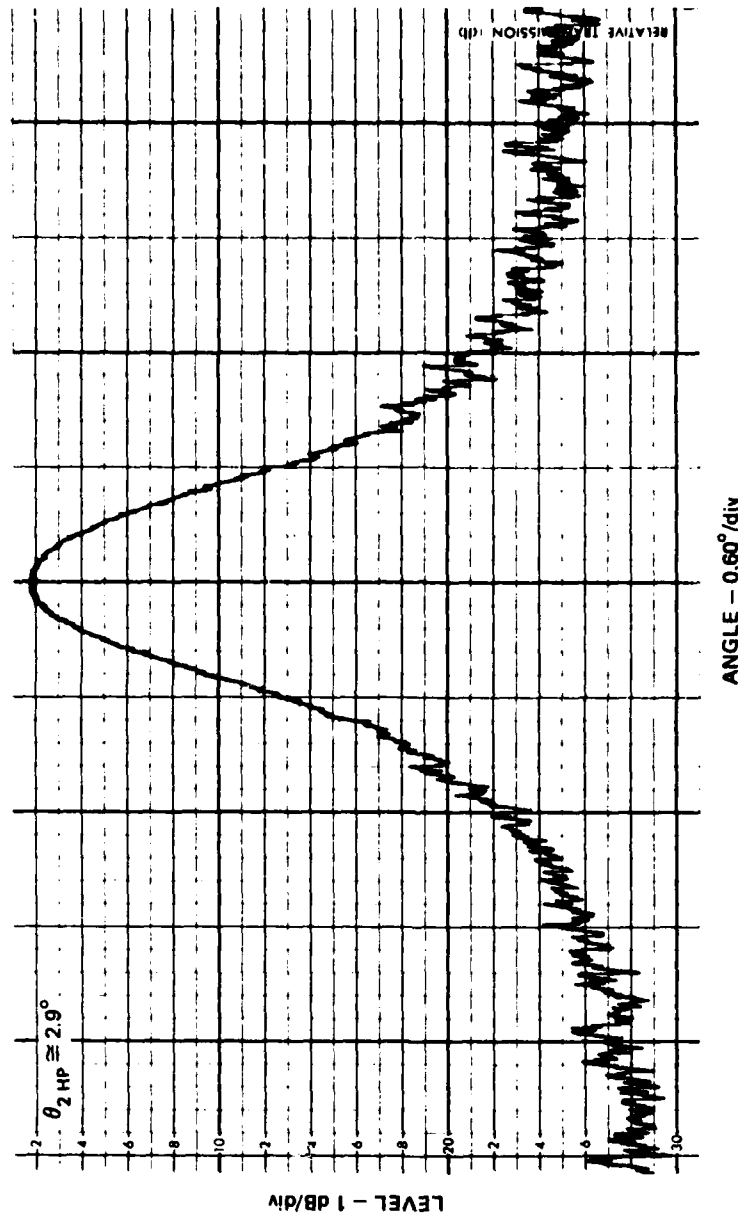


FIGURE 4.15
SECONDARY POWER BEAM PATTERN FOR
THE BROADBAND PARAMETRIC ARRAY
f(t) - GAUSSIAN, $f_{1c} \approx 600$ kHz, $SPL_1 = 187.8$ dB re 1 μ Pa
 $f_{2c} \approx 67$ kHz, $a = 2.54$ cm, $R_0 = 0.82$ m, $r = 23.6$ m

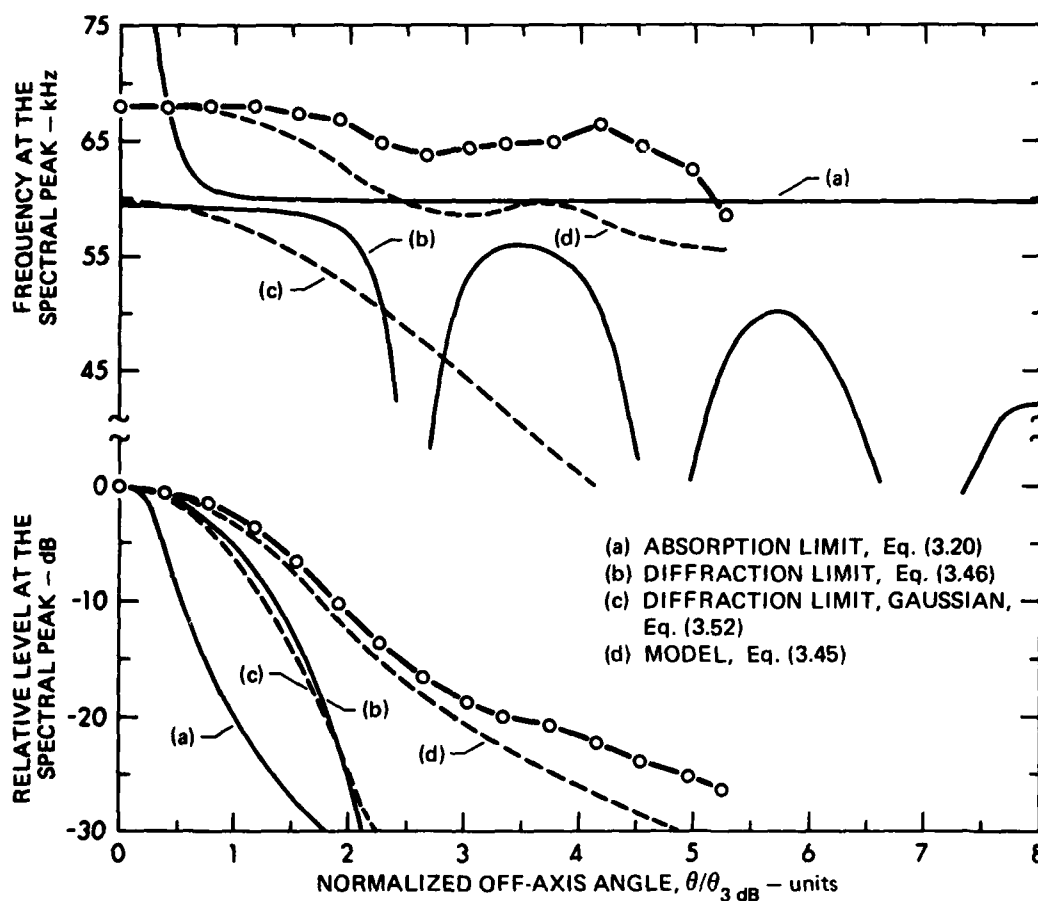


FIGURE 4.16
FREQUENCY AND LEVEL AT THE SPECTRAL PEAK OFF-AXIS
FOR THE BROADBAND PARAMETRIC ARRAY

$f(t)$ - GAUSSIAN, $f_{1c} = 600$ kHz, $SPL_1 = 183.0$ dB re $1 \mu\text{Pa}$

$a = 1.27$ cm, $R_0 = 0.21$ m, $r = 23.6$ m

$\theta_{3dB} = 2.65^\circ$ (MEASURED)

ARL:UT
 AS-81-697
 JMH - GA
 6-16-81

spectral peak is monotonically decreasing with a broad, yet well defined sidelobe indicated near $4.0(\theta_{3\text{ dB}})$.

Analyses of the limiting forms for the broadband parametric array indicate a further transition toward the diffraction limit. The overall dependence on secondary frequency is determined from the frequency at the spectral peak and is given by $\omega_2^{1.3}$. The lobes in frequency at the spectral peak correspond very well with the lobes in the diffraction limit. The level at the spectral peak is also better estimated in the diffraction limit than in the absorption limit.

The experimental data are, as previously noted, higher in frequency at the spectral peak than the theoretical results from Eq. (3.45) for off-axis angles greater than $\theta_{3\text{ dB}}$. However, the broad peak observed in the data is predicted very well by the theoretical results. As the diffraction limit is approached, the Rutherford directivity acts as a sampling function in the convolution integral and the product of the primary off-axis transfer functions is indicated.

The theoretical and experimental results are in close agreement for the relative level at the spectral peak to about -20 dB or an off-axis angle of about $3.0(\theta_{3\text{ dB}})$. At lower levels and larger angles, both the experimental data and the theoretical results from Eq. (3.45) indicate a broad sidelobe; however, the level is several decibels higher for the measured data. The half-power beamwidth for this broadband parametric array is about 5.3° as measured from the energy beam pattern shown in Fig. 4.17.

A composite of the frequency and level at the spectral peak for various directivity ratios or source piston radii is given in Fig. 4.18. Data are included for each directivity ratio. The presentation of the data as a function of angle normalized to the half-power angle for each directivity ratio has removed the effects of absolute angle and allows the characteristics of the off-axis transfer function

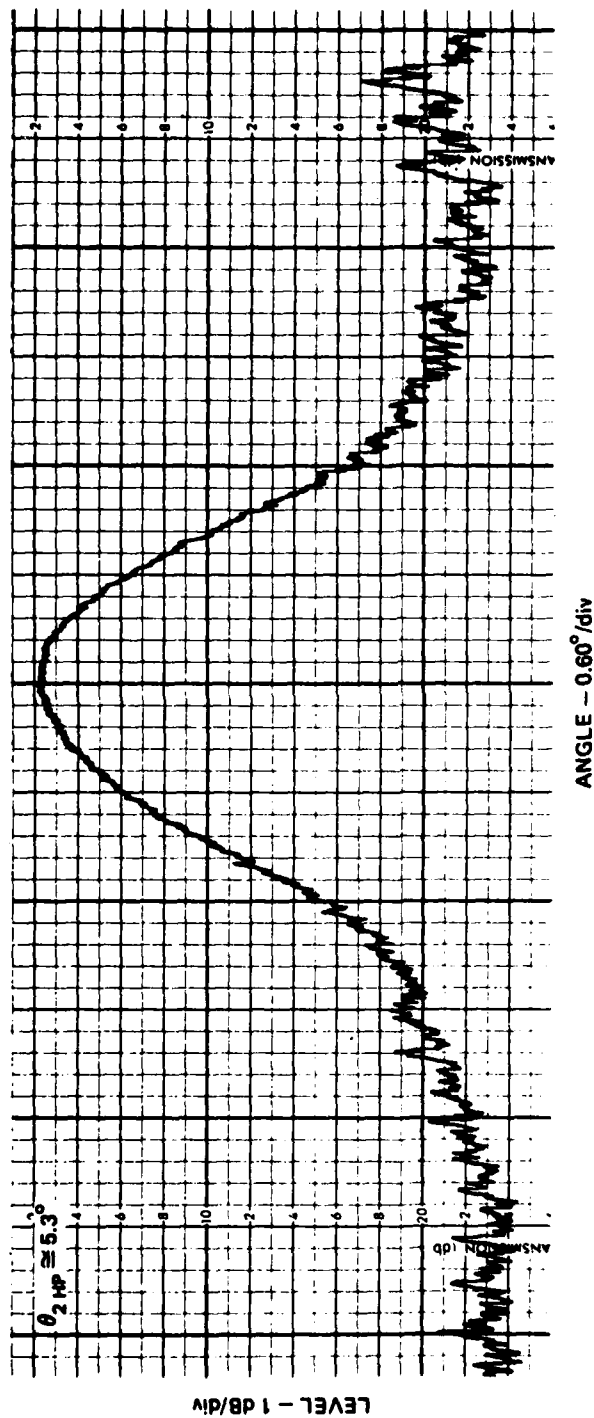


FIGURE 4.17
SECONDARY POWER BEAM PATTERN FOR
THE BROADBAND PARAMETRIC ARRAY
 $f(t)$ - GAUSSIAN, $f_{1c} = 600$ kHz, $SPL_1 = 183.0$ dB re $1 \mu Pa$
 $f_{2c} \approx 68$ kHz, $a = 1.27$ cm, $R_0 = 0.21$ m, $r = 23.6$ m

LEVEL - 1 dB/div

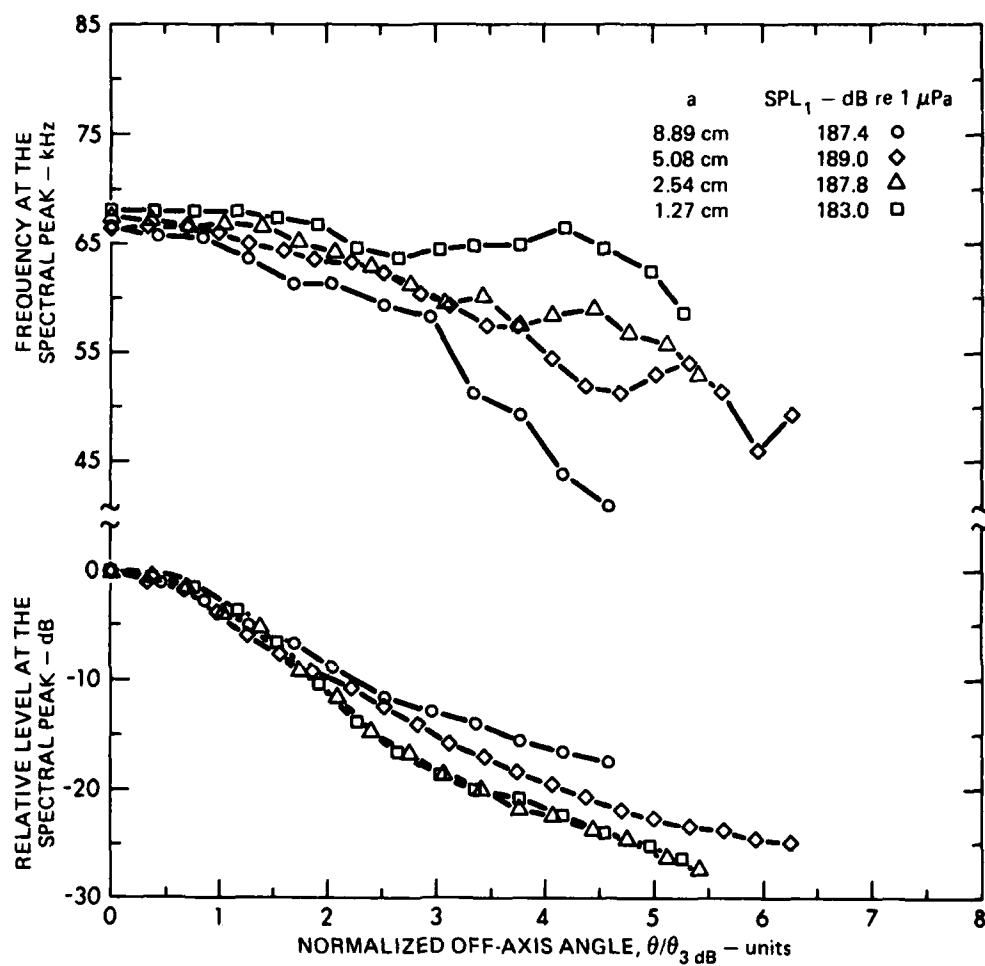


FIGURE 4.18
FREQUENCY AND LEVEL AT THE SPECTRAL PEAK OFF-AXIS
FOR THE BROADBAND PARAMETRIC ARRAY
AND SEVERAL SOURCE PISTON RADII
 $f(t)$ - GAUSSIAN, $f_{1c} = 600 \text{ kHz}$, $r = 23.6 \text{ m}$

to be studied as the transition from the absorption limit to the diffraction limit progresses. The trend of decreasing frequency at the spectral peak with increasing angle off-axis is noted in each case; however, the rate of frequency shift is greater for smaller directivity ratios at off-axis normalized angles greater than about $2.5(\theta_{3\text{ dB}})$. At larger normalized angles, the trends diverge as the off-axis transfer function for each directivity ratio becomes dominant. As the transition from the absorption limit (small directivity ratios) to the diffraction limit (larger directivity ratios) occurs, the trend is toward frequency independence as a function of off-axis angle. The level at the spectral peak is reasonably well behaved at all angles and has the same trend for all directivity ratios to a normalized angle of about $1.6(\theta_{3\text{ dB}})$. The relative behavior of the frequency at the spectral peak and the level at the spectral peak indicates the higher sensitivity of frequency in characterizing the secondary sound field.

A more striking comparison of data for various directivity ratios derived in part from different source piston radii is given in Fig. 4.19, where the frequency at the spectral peak is given as a function of absolute off-axis angle, and in Fig. 4.20, where the level at the spectral peak is given as a function of absolute off-axis angle. Prominent minor peaks in frequency at the spectral peak occur at off-axis angles of about 4° , 6° , and 11° for broadband parametric arrays formed by source piston radii of 5.08 cm, 2.54 cm, and 1.27 cm, respectively. These features are correlated with indications of low sidelobes in the relative level at the spectral peak for the parametric arrays formed with the two smallest source piston radii and highest directivity ratios.

A final comparison of experimental data and theoretical predictions as a function of primary directivity is shown in Fig. 4.21, where the secondary half-power beamwidth is given as a function of primary half-power beamwidth, directivity ratio, and source piston radius. The Rutherford beamwidth is indicated from 1.4° to 1.6° due to the

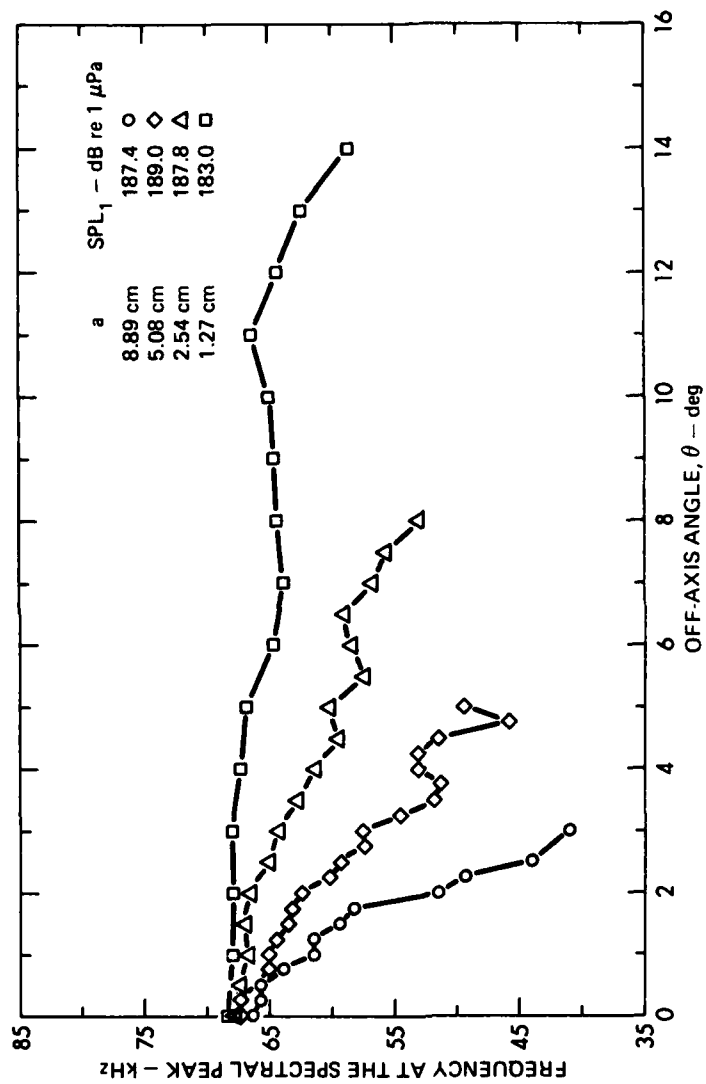


FIGURE 4.19
 FREQUENCY AT THE SPECTRAL PEAK FOR THE BROADBAND PARAMETRIC
 ARRAY OFF-AXIS FOR SEVERAL SOURCE RADIII

f(t) - GAUSSIAN, $f_c = 600$ kHz, $r = 23.6$ m

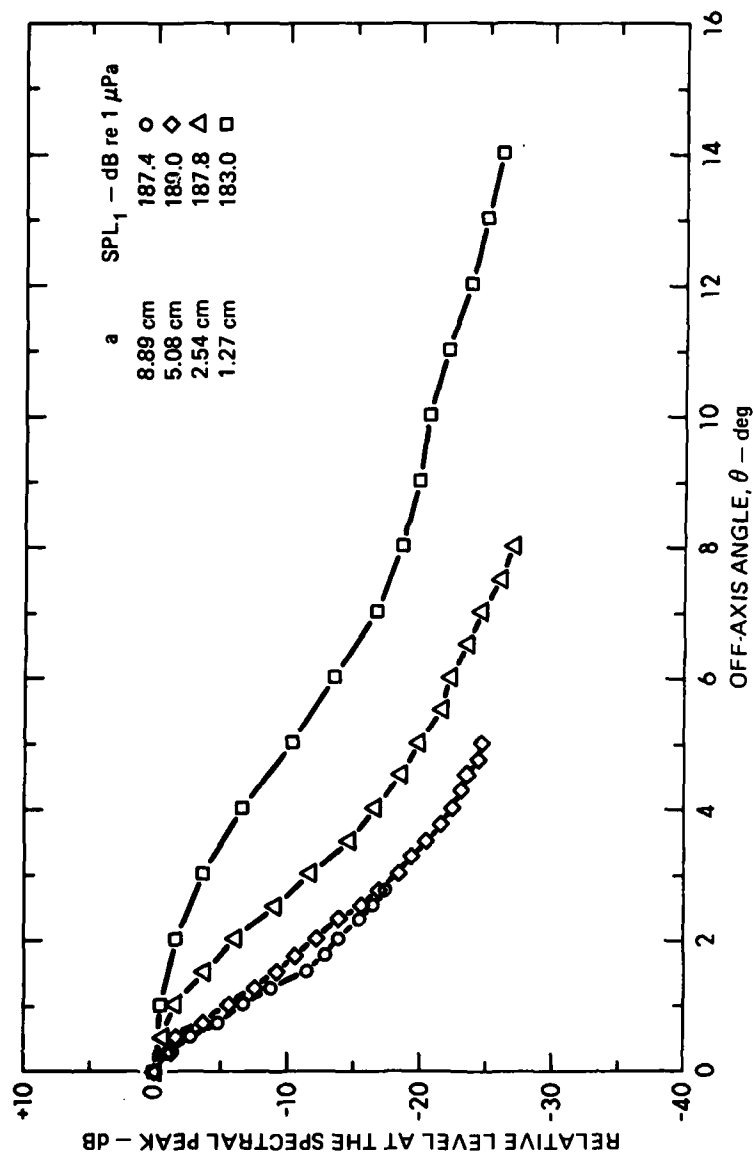


FIGURE 4.20
RELATIVE LEVEL AT THE SPECTRAL PEAK FOR THE BROADBAND
ARRAY OFF-AXIS FOR SEVERAL SOURCE PISTON RADII

$f(t)$ - GAUSSIAN, $f_{1c} = 600$ kHz, $f_{2c} \cong 66$ kHz, $r = 23.6$ m

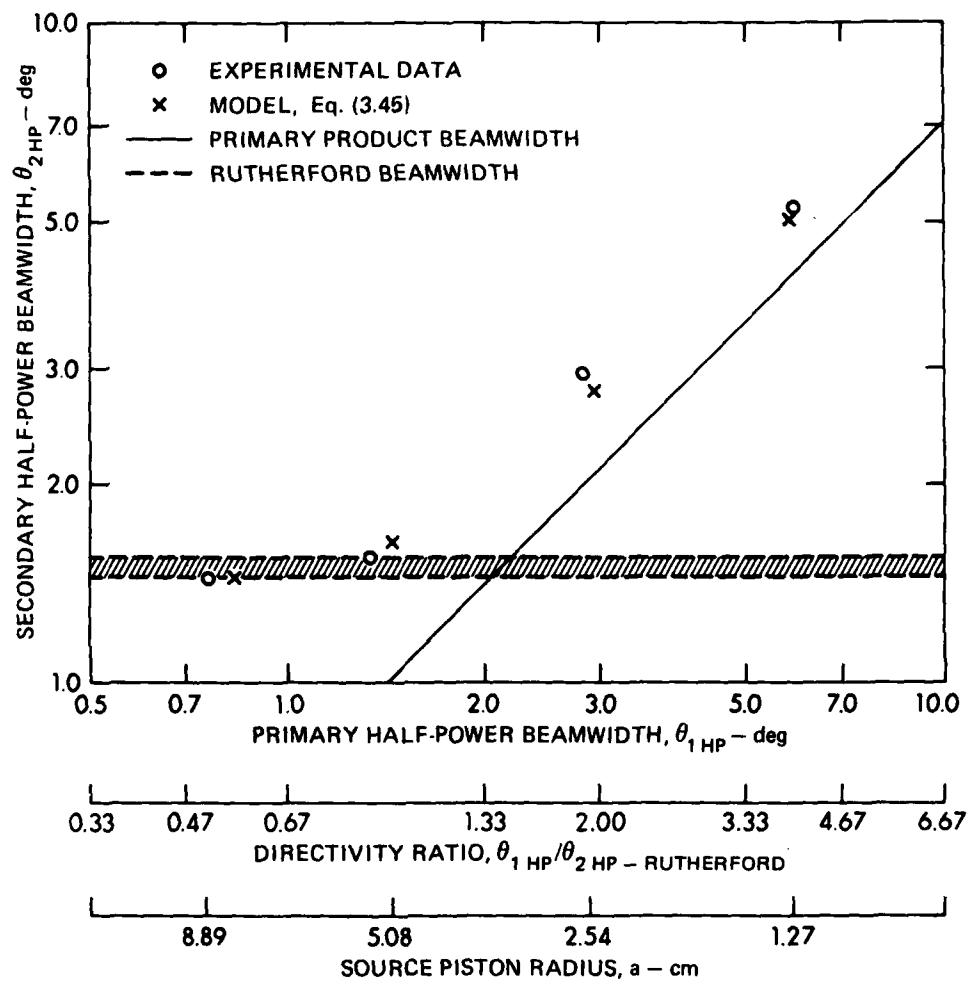


FIGURE 4.21
RELATIONSHIP BETWEEN PRIMARY AND SECONDARY DIRECTIVITY AND
SOURCE PISTON RADIUS FOR THE BROADBAND PARAMETRIC ARRAY

$f(t) - \text{GAUSSIAN}, f_{1c} = 600 \text{ kHz}, f_{2c} \cong 66 \text{ kHz}, r = 23.6 \text{ m}$

variations in absorption imposed by temperature changes in the medium during the acquisition of experimental data. The directivity ratio was computed based on the average Rutherford beamwidth and the primary product beamwidth was computed based on the experimentally determined beamwidths. The agreement between measured and predicted results is good. For very narrow primary beams the directivity ratio is small and spatial performance is asymptotic to the Rutherford directivity, which is predicted in the absorption limit. This case is approximated physically with a large aperture size where most of the nonlinear interaction occurs in the Fresnel diffraction region of the primary source. As the primary directivity and the directivity ratio decrease, the nonlinear interaction that takes place in the Fraunhofer diffraction region increases and a transition occurs in the spatial characteristics to an asymptote determined by the primary product directivity, which is predicted in the diffraction limit. This behavior is the same as noted for narrowband parametric arrays with intermediate directivity.³⁷

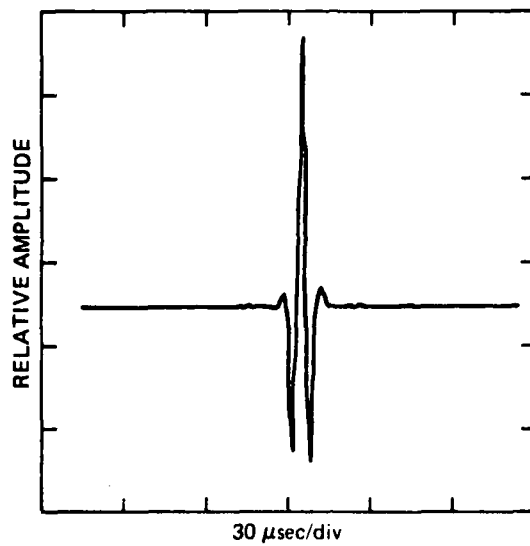
3. Cross Function Analysis

An alternate method for evaluating the off-axis properties of the broadband parametric transmission is the use of cross functions. This method utilizes coherent signal analysis in determining relative signal properties. Experimental results were obtained by evaluating cross function properties of the on-axis signal with various off-axis signals. The ARL 239-1 was used to receive the on-axis signals and the USRD-E27-130P was used to receive the off-axis signals. The hydrophones were oriented at various angles with respect to the source and separated in range from about 0.3 m to 0.6 m. This separation in range allowed the signals to be transmitted over the same cable with a 150-350 μ sec difference in arrival time. The signals were separated by gates and coupled to the dual-channel analyzer where the time delay between signals was artificially corrected. Cross functions were evaluated by setting the time delay so that the crosscorrelation was a maximum of time shift, $\tau=0$.

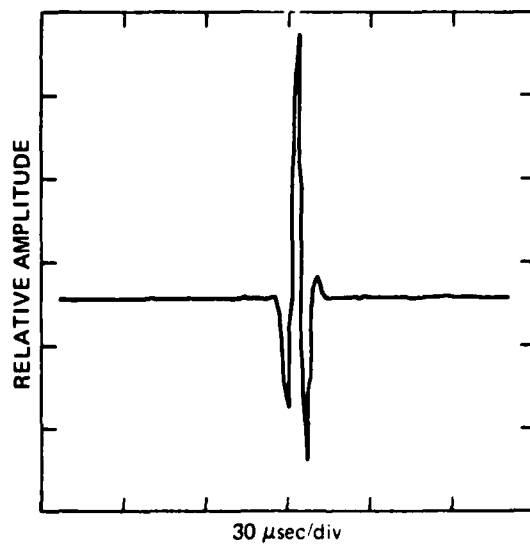
The selectable radius circular piston projector was driven over the full aperture with a radius of 8.89 cm, and at a primary peak sound pressure level of 195.2 dB re 1 μ Pa at 23.6 m. The crosscorrelation of the on-axis and off-axis signals at 1.8° (30₃ dB) and 3° (50₃ dB) are shown in Fig. 4.22. These results may be compared with the autocorrelation on-axis in Fig. 4.5. The duration of the crosscorrelation signals is about 36 μ sec. As the angle is increased the crosscorrelation signals become asymmetric, and the first positive and negative peaks diminish in amplitude relative to the other peaks in the signal.

The changes that occur in the crosscorrelation signals are more readily evaluated in the frequency domain with the crosspower density spectrum. Normalized crosspower amplitude spectra for the on-axis and off-axis signals are shown in Fig. 4.23. These curves result from the product of two secondary signal spectra that have different peak frequencies. Since these are low Q_2 transmissions and the peak frequencies are relatively close, the resultant crosspower amplitude spectrum has a single peak, which is somewhat broader than that associated with the secondary power density spectra in Figs. 4.7 and 4.8. The crosspower amplitude spectrum for 0° and 1.8° has a peak at about 60.9 kHz, which is about 8% lower in frequency than the on-axis value. The crosspower amplitude spectrum for 0° and 3° has a peak at about 54.6 kHz, which is lower in frequency than the on-axis value by about 17%.

The crosspower phase spectrum is the coherent part of the crosspower spectrum and provides an extremely sensitive comparison of signals. The crosspower phase spectra for the on-axis and off-axis signals at 1.8° and 3.0° are shown in Fig. 4.24. The phase spectra are very similar, both relatively constant, and nearly zero over the band. This is not surprising since the phase spectra were derived from the crosscorrelation function, which was a maximum at $\tau=0$. This condition implies phase coherence. The rapid variations in phase at both high and low frequencies are due to poor S/N. It is difficult to draw any



(a) ON-AXIS CROSS 1.8° OFF-AXIS



(b) ON-AXIS CROSS 3.0° OFF-AXIS

FIGURE 4.22
CORRELATION OF ON-AXIS AND OFF-AXIS SIGNALS
FOR THE BROADBAND PARAMETRIC ARRAY

$f(t)$ - GAUSSIAN, $f_{1c} = 600$ kHz, $SPL_1 = 195.2$ dB re $1 \mu Pa$
 $a = 8.89$ cm, $R_0 = 10.07$ m, $r = 23.6$ m

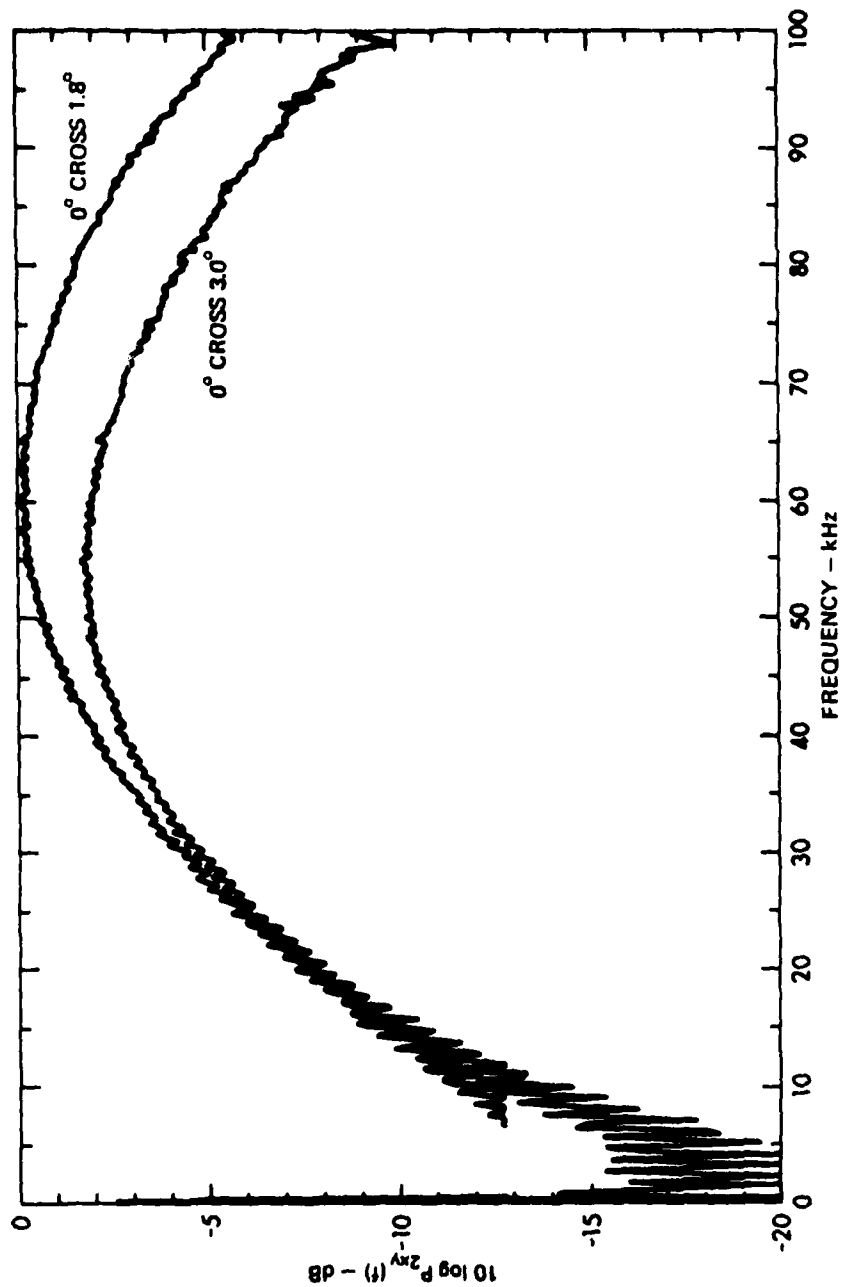
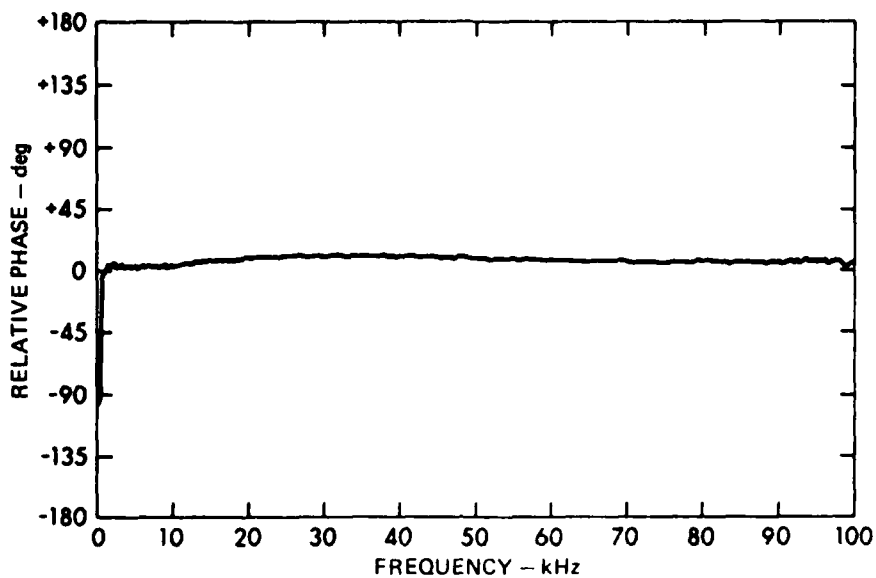
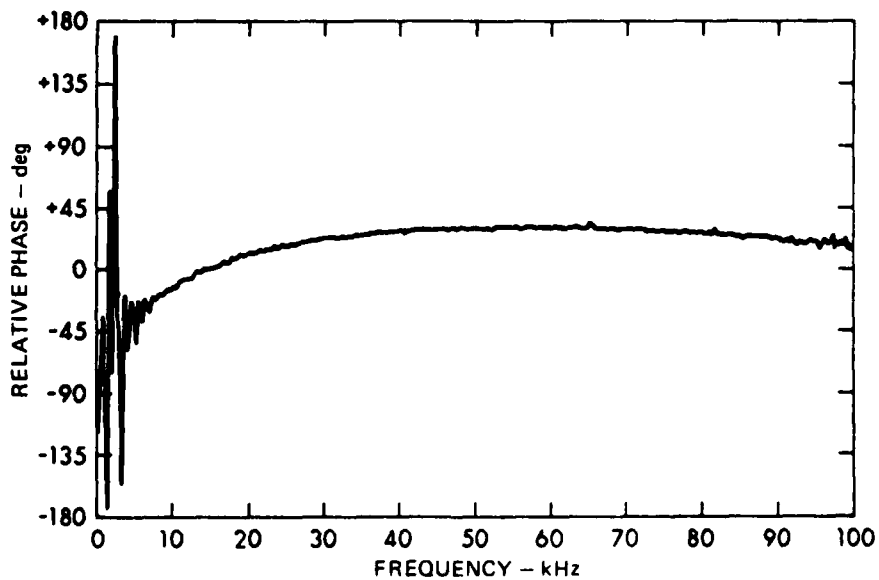


FIGURE 4.23
 NORMALIZED CROSS-POWER AMPLITUDE SPECTRA OF ON-AXIS AND
 OFF-AXIS SIGNALS FOR THE BROADBAND PARAMETRIC ARRAY
 $f(t)$ - GAUSSIAN, $f_c = 600$ kHz, $SPL_1 = 195.2$ dB re $1 \mu Pa$
 $a = 8.89$ cm, $R_0 = 10.07$ m, $r = 23.6$ m



(a) ON-AXIS CROSS 1.8° OFF-AXIS



(b) ON-AXIS CROSS 3.0° OFF-AXIS

FIGURE 4.24
CROSS-POWER PHASE SPECTRA OF ON-AXIS AND OFF-AXIS SIGNALS
FOR THE BROADBAND PARAMETRIC ARRAY

$f(t)$ - GAUSSIAN, $f_{1c} = 600$ kHz, $SPL_1 = 195.2$ dB re $1 \mu\text{Pa}$
 $a = 8.89$ cm, $R_0 = 10.07$ m, $r = 23.5$ m

ARL:L
 AS-81-605
 JMH - GA
 6 - 16 - 81

further conclusions from these data due to limitations in the resolution of the analysis equipment. The maximum resolution in time delay of the dual channel processor is 3.91 μsec , which was extended by external analog delay lines to 0.5 μsec . This time delay resolution indicates a maximum phase determination accuracy of 18.0° at 100 kHz.

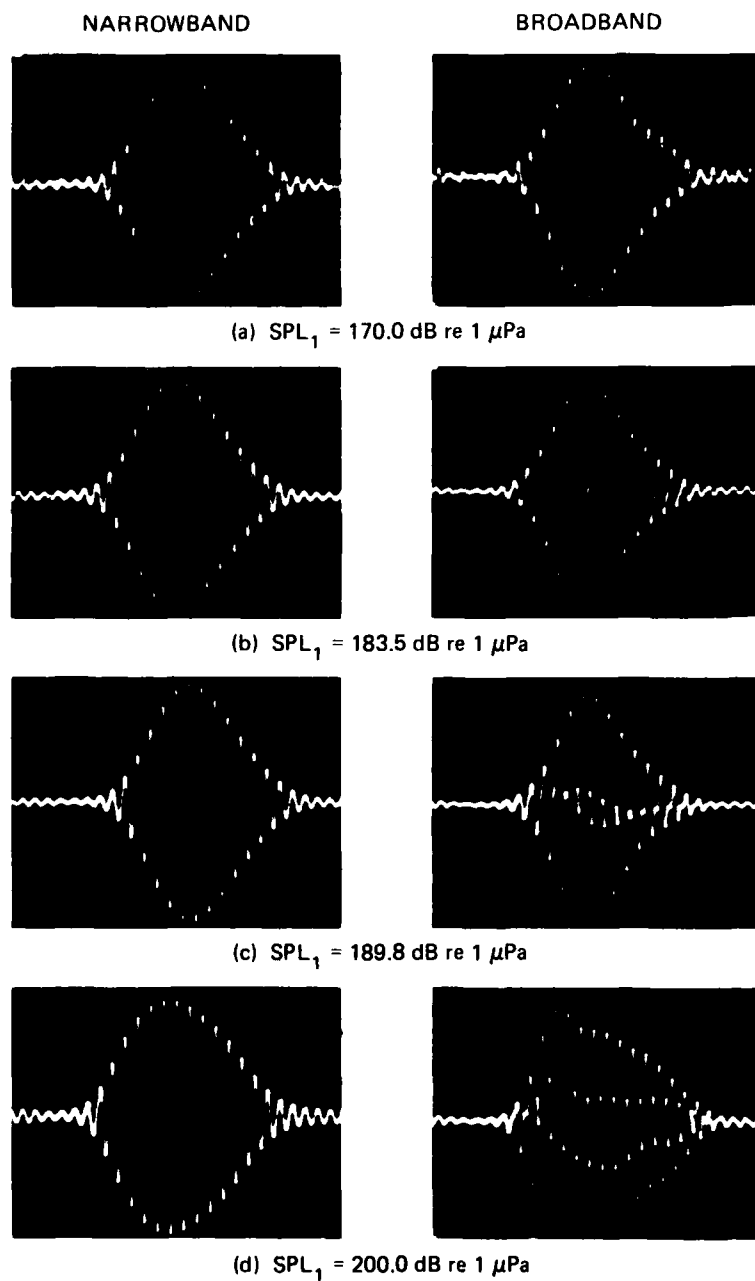
C. The Broadband Parametric Array with High Amplitude Primary Waves

As the amplitude of the primary waves is increased, conditions are reached where the behavior of the primary signal is dominantly non-linear. Under these conditions, the primary radiation exhibits finite amplitude effects and the broadband parametric transmission is subject to finite amplitude attenuation. The primary waveform distorts progressively with propagation range, with the higher amplitude portions distorting more rapidly than lower amplitude portions, resulting in wave steepening. As the waveform distorts, energy at the fundamental is converted to energy at harmonic frequencies which suffer higher attenuation with range as the waves propagate. The interaction of the harmonic components generates energy in the secondary band; however, the conversion efficiency is poor so that the secondary energy that results from interaction of harmonic frequencies is negligible.

The experimental data presented here are high amplitude extensions of conditions that were evaluated to determine low amplitude performance of the broadband parametric array.

1. The Primary Field

The Gaussian pulse primary transmission was evaluated at 23.6 m in the time domain as a function of amplitude. The on-axis acoustic waveforms are shown in Fig. 4.25. The narrowband presentation was achieved with a bandpass filter set at 600 kHz with a 4-pole Butterworth response. The broadband presentation was achieved with a



SCALE - 5 $\mu\text{sec/div}$

FIGURE 4.25
ON-AXIS PRIMARY WAVEFORMS AS A FUNCTION OF SOURCE LEVEL

$f(t)$ - GAUSSIAN, $f_{1c} = 600 \text{ kHz}$, $a = 8.89 \text{ cm}$, $R_0 = 10.07 \text{ m}$, $r = 23.6 \text{ m}$

ARL:UT
AS-81-608
JMH - GA
6-16-81

high pass filter set at 1 kHz with an 8-pole Butterworth response. At low level, both the narrowband and the broadband waveforms are very similar. As the level is increased, waveform distortion is observed. In the broadband presentation, the secondary signal that is generated, the harmonic signals that are converted from the fundamental, and the remaining primary signal are all contained in a complex waveform. It should be noted that the various frequency components are weighted according to the response curves for the ARL 239-1 high frequency and low frequency receive systems (Appendix B). In the narrowband presentation, energy is converted from the fundamental to harmonic frequencies more rapidly at the higher amplitude peaks, causing a rounding off of the pulse envelope. This rounding off or change in pulse envelope shape effectively increases the apparent duration if the pulse transmission is defined by the 0.17 amplitude level of the envelope.

The on-axis sound field was evaluated in a narrowband frequency as a function of input electrical power to determine the various operating regions of the primary transmission. This evaluation was performed as a function of primary directivity by using the four piston radii that were originally identified. The on-axis peak sound pressure level at 23.6 m as a function of level for these configurations is shown in Fig. 4.26. Linear performance lines, which are drawn through each data set, indicate relative differences in level corresponding to differences in directivity for each piston configuration. As the input electrical power is increased, the amount of energy that is converted from the fundamental to harmonic frequencies over the measurement range increases due to progressive finite amplitude effects. This conversion of energy at the expense of the fundamental component indicates the onset of waveform saturation and is noted in Fig. 4.26 by the departure of the data from linear behavior. These same trends were studied by Shooter, Muir, and Blackstock⁷⁷ for the radiation from a single circular piston source.

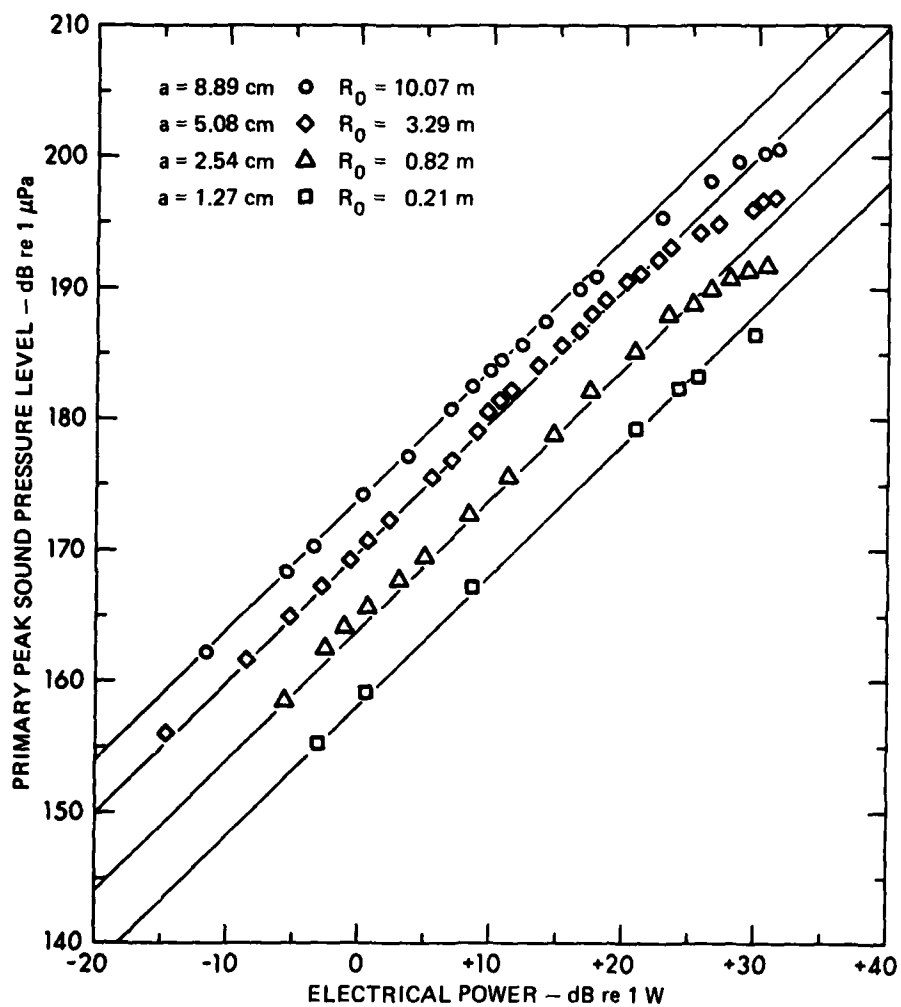


FIGURE 4.26
PRIMARY PEAK SOUND PRESSURE LEVEL
 $f(t)$ - GAUSSIAN, $f_{1c} = 600$ kHz, $r = 23.6$ m

ARL:UT
AS-81-606
JMH - GA
6 - 16 - 81

The departure from linear behavior of the fundamental component becomes progressively greater as the amplitude is increased; however, a rapid departure is noted in the data at input electrical power levels greater than about 23 dB re 1 W. The rapid departure from linearity that is noted in the data was identified arbitrarily as an indicator of those operating regions for the primary source which are dominantly linear and dominantly nonlinear. The low amplitude analysis discussed in previous sections involved primary source amplitudes, which were dominantly linear according to this criterion. The exact status of the primary source for any data presented may be determined from Fig. 4.26.

The data indicate that, for higher directivity source configurations, the departure from linear behavior occurs at higher peak sound pressure levels, at slightly lower input power levels, and increases more rapidly with increasing input power levels. These data were taken in the farfield of each source configuration. If the saturation takes place predominantly in the farfield or spherical spreading region of the sources, then the peak sound pressure level at which departure from linear behavior begins would be higher for the smaller pistons or lower directivity sources. This trend is based on the assumption that plane waves saturate at lower amplitude levels than spherical waves,⁷⁸ and is not noted in the data. The data support the conclusion that finite amplitude effects are occurring predominantly in the nearfield region of the sources, i.e., over distances less than R_0 . This conclusion may be evaluated by presenting the peak sound pressure level measurements as peak source levels at R_0 for each piston, and is given in Fig. 4.27. If the simple model is assumed where the radiation in the nearfield is plane wave and spherical wave in the farfield, then the data in Fig. 4.27 represent the level at the end of the plane wave region, ignoring finite amplitude effects that may have occurred in the farfield. With this presentation, the departure from linear behavior occurs at higher peak source levels for lower directivity sources. Since the lower directivity sources have shorter values for R_0 and

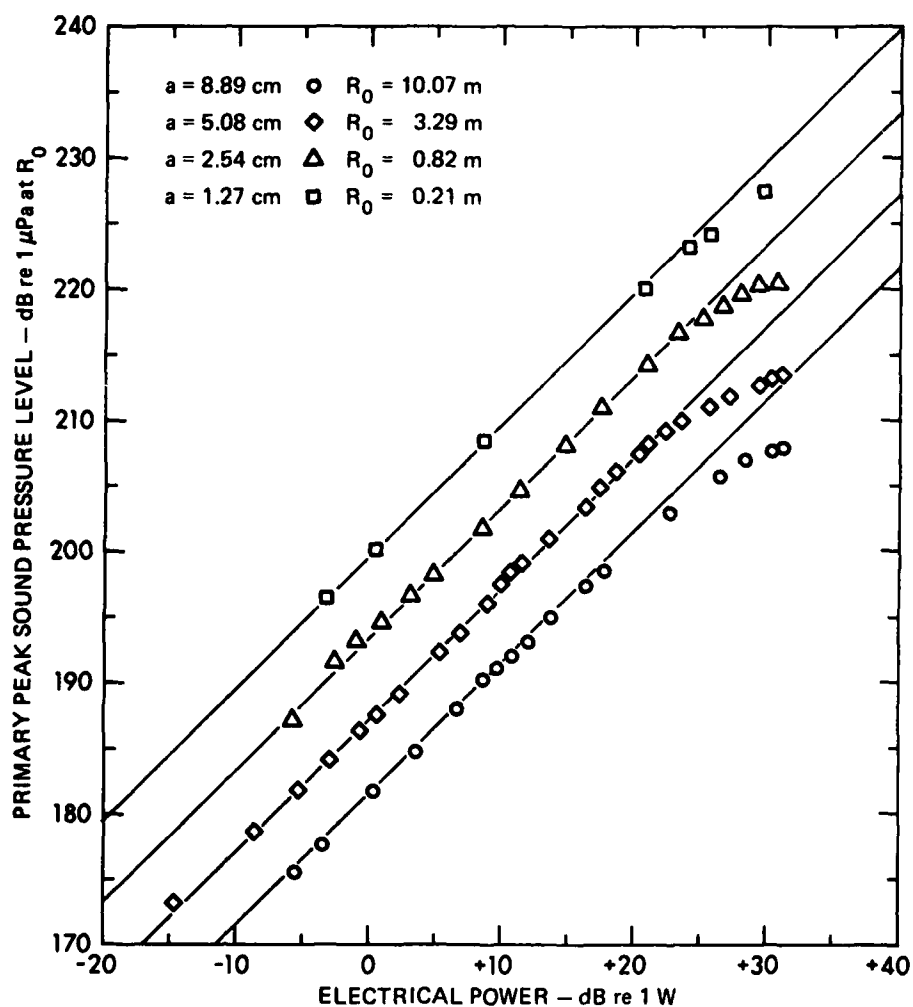


FIGURE 4.27
PRIMARY PEAK SOURCE LEVEL AT R_0
 $f(t)$ - GAUSSIAN, $f_{1c} = 600$ kHz, $r = 23.6$ m

ARL:UT
AS-81-607
JMH - GA
6 - 16 - 81

finite amplitude distortion is progressive, this trend supports the conclusion that the finite amplitude effects occur predominantly in the nearfield or plane wave region of the source. The effects in the farfield or spherical region are noted in the rate at which the departure from linear behavior occurs as a function of input electrical power. In the farfield region for the lower directivity sources, spherical spreading slows the progressive finite amplitude effects and decreases the rate of departure from linear behavior relative to the higher directivity sources.

Another indication of finite amplitude effects is noted in the narrowband energy beam pattern at the fundamental frequency. On the maximum response axis, the highest amplitudes are reached and the finite amplitude effects are greatest. The conversion of energy from the fundamental to harmonic components causes a blunting of the main lobe and apparent increases in half-power beamwidth and in sidelobe levels. These phenomena are observed in the primary beam patterns as a function of increasing peak sound pressure level. The source directivity of the primary transmission as a function of source level from the selectable radius piston projector with radius $a = 8.89$ cm is shown in Fig. 4.28. The energy beam pattern in Fig. 4.28(a) was taken in a linear operating region according to Fig. 4.26 and has a measured half-power beamwidth of about 0.85° with maximum first sidelobe levels of -13 dB. The energy beam patterns in Figs. 4.28(b) and 4.28(c) were taken in a dominantly nonlinear operating region and indicate a broadening of the half-power beamwidth by about 30% and increase in sidelobe levels of about 2.5 dB. Source directivity data for the other configurations of the selectable radius circular piston projector are shown in Figs. 4.29, 4.30, and 4.31. These data indicate performance similar to that presented in Fig. 4.28. For a source piston radius of 5.08 cm, the half-power beamwidth broadened by about 20% and the sidelobe levels increased by about 3 dB. An approximate 11% broadening of the half-power beamwidth was noted for a source piston radius of 2.54 cm and the sidelobe levels increased by about 1 dB. For the lowest directivity data with a piston

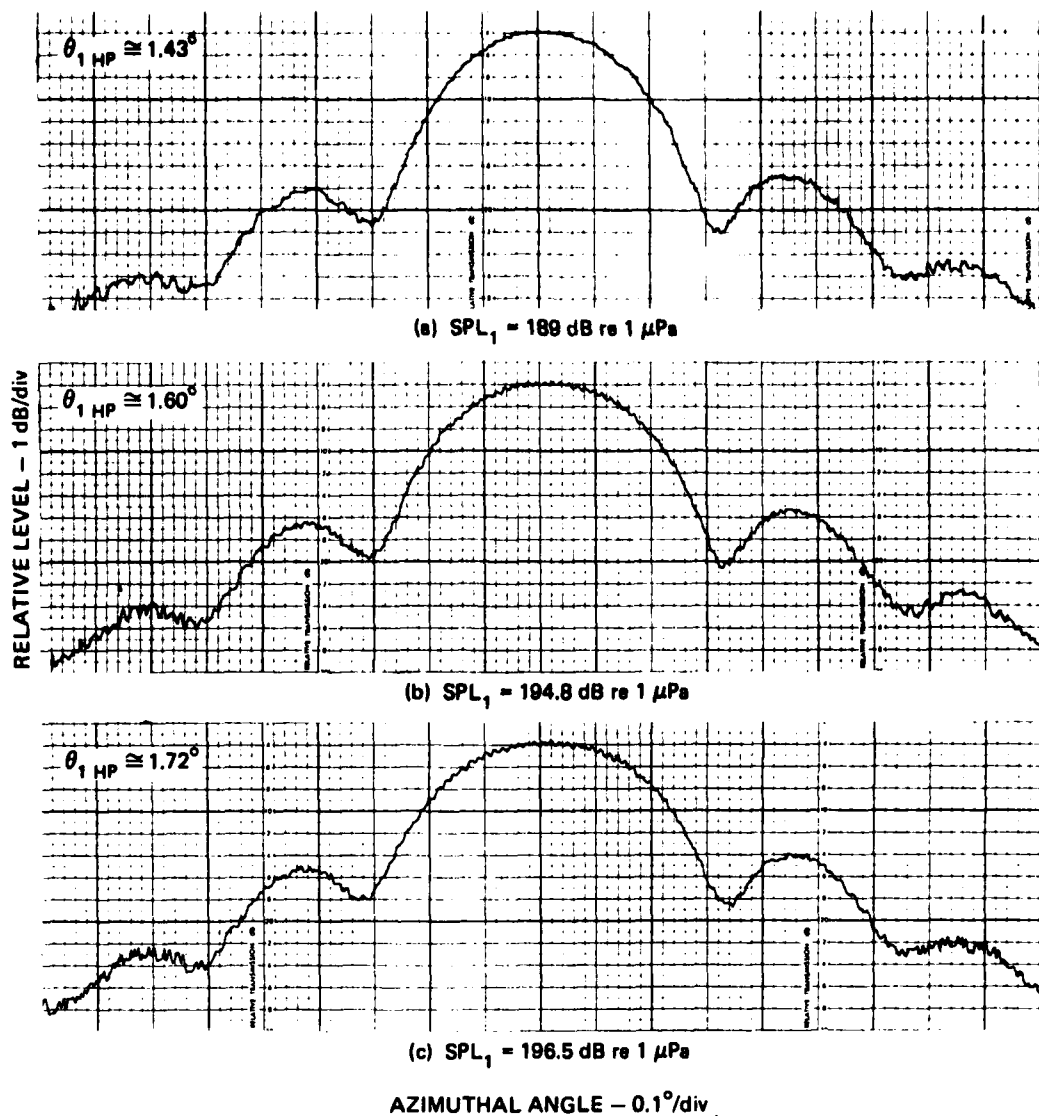


FIGURE 4.29
PRIMARY SOURCE DIRECTIVITY AS
A FUNCTION OF SOURCE LEVEL

$f(t)$ - GAUSSIAN, $f_{1c} = 600 \text{ kHz}$, $a = 5.08 \text{ cm}$
 $R_0 = 3.29 \text{ m}$, $r = 23.6 \text{ m}$

ARL:UT
 AS-81-610
 JMH-GA
 6-16-81

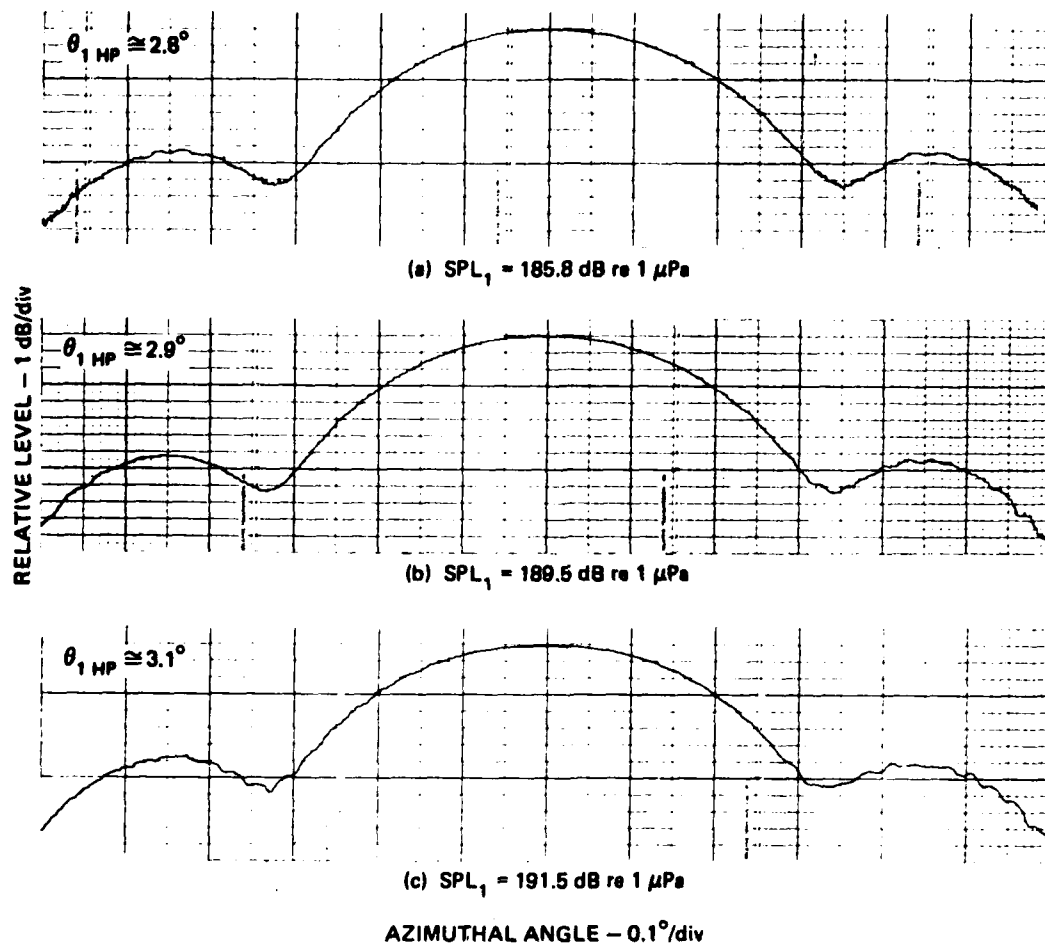


FIGURE 4.30
PRIMARY SOURCE DIRECTIVITY AS
A FUNCTION OF SOURCE LEVEL
 $f(t) - \text{GAUSSIAN}, f_{1c} = 600 \text{ kHz}, a = 2.54 \text{ cm}$
 $R_0 = 0.32 \text{ m}, r = 23.6 \text{ m}$

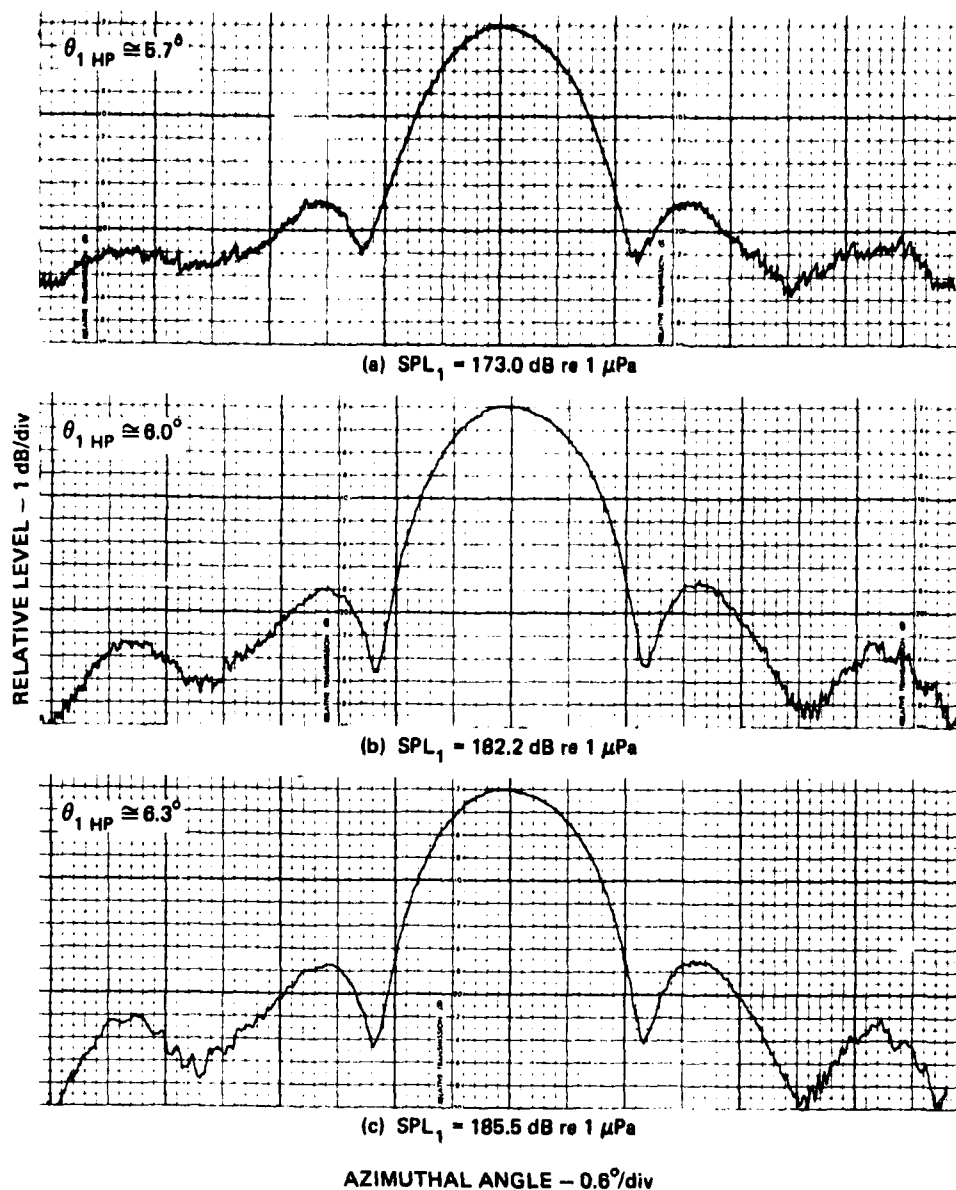


FIGURE 4.31
PRIMARY SOURCE DIRECTIVITY AS
A FUNCTION OF SOURCE LEVEL
 $f(t)$ - GAUSSIAN, $f_{1c} = 600 \text{ kHz}$, $a = 1.27 \text{ cm}$
 $R_0 = 0.21 \text{ m}$, $r = 23.6 \text{ m}$

radius of 1.27 cm, the broadening of the half-power beamwidth was about 10% and the sidelobe levels were increased by about 0.5 dB. A summary of primary source data is presented in Table IV.3.

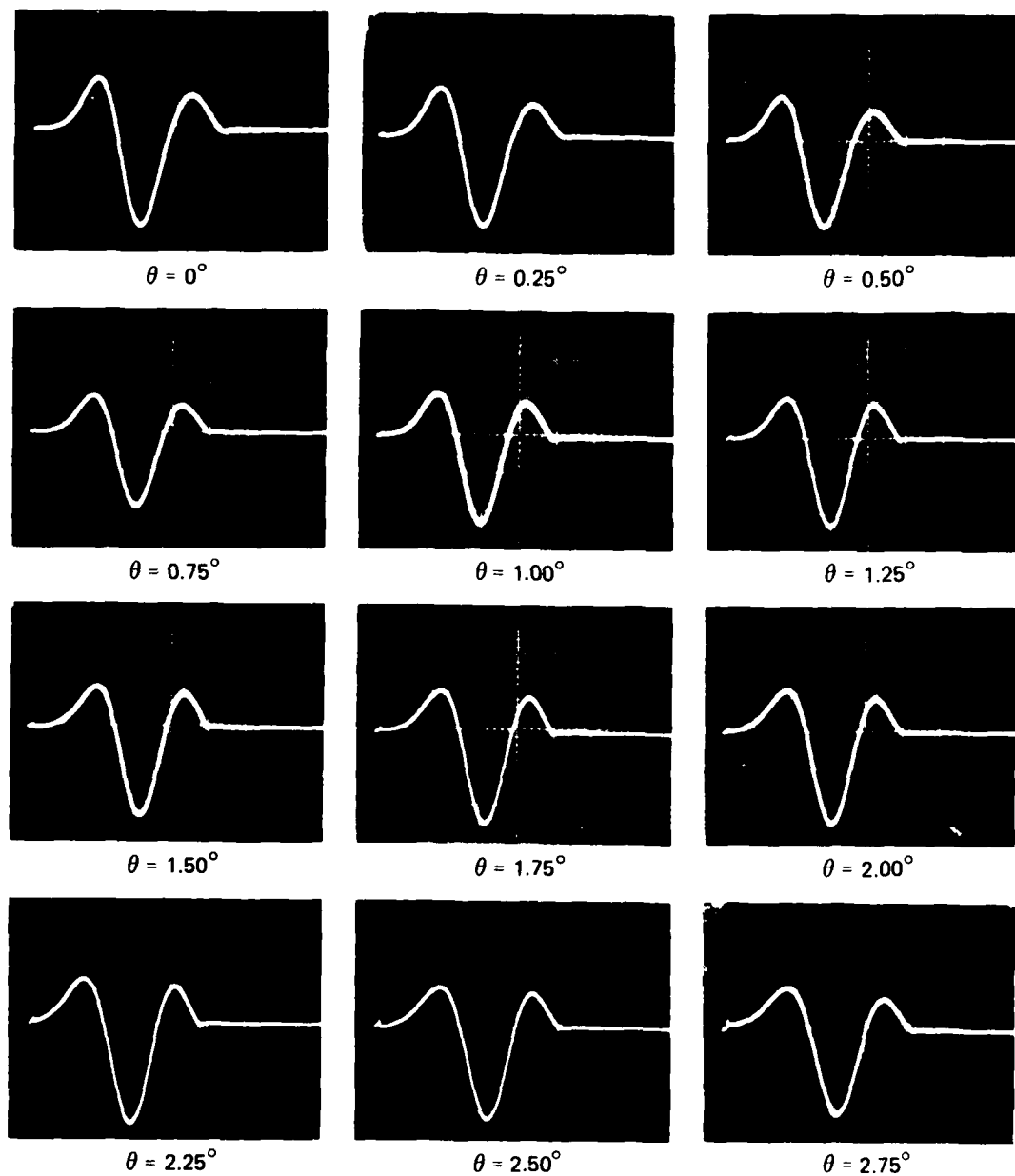
2. The Secondary Field

The secondary field characteristics with high amplitude primary waves were evaluated for several primary source configurations and directivity ratios. For finite amplitude limited parametric transmissions, the concept of directivity ratio is somewhat vague since the Rutherford beamwidth is derived from low amplitude considerations. The classification of the radiation from a parametric source as plane wave or nonplane wave based on the directivity ratio does not depend on the influence of finite amplitude effects. The use of the directivity ratio derived from low amplitude source characteristics may be used to describe finite amplitude limited parametric transmissions.

The broadband parametric array with high amplitude primary waves and high primary directivity was established with a piston radius of 8.89 cm and a directivity ratio of 0.54. The secondary waveforms both on-axis and off-axis are shown in Fig. 4.32 for primary radiations with a peak sound pressure level, SPL_1 , of 200.4 dB re 1 μ Pa at 23.6 m. This value of primary sound pressure level is clearly dominated by finite amplitude effects as about 5 dB of energy at the fundamental has been converted to harmonic frequencies according to the data in Fig. 4.26. A comparison of the on-axis secondary waveform for the high and low (Fig. 4.4) primary amplitude transmissions indicates several differences. A slight increase in signal duration is noted; however, the greatest difference is in the reduction of amplitude of the second positive peak in the waveform. Both of these features result from the distortion of the primary envelope due to finite amplitude effects. As a function of off-axis angle, the relative amplitude of the second positive peak changes little over angles from 0.0° to 3.25° . This behavior

TABLE IV.3
SUMMARY OF MEASURED PRIMARY SOURCE DATA

a (cm)	SPL ₁ (dB re 1 μ Pa)	θ_{HP} (deg)	1st Sidelobe		2nd ∞ (deg)	2nd Sidelobe		3rd ∞ (deg)	3rd Sidelobe		4th ∞ (deg)	4th Sidelobe	
			Position (deg)	Level (dB re max)		Position (deg)	Level (dB re max)		Position (deg)	Level (dB re max)		Position (deg)	Level (dB re max)
8.89	187.4	0.85	1.35	-13.0	1.90	2.25	-18.5	2.80					
8.89	198.5	1.02	1.35	-11.5	1.85	2.25	-18.3	2.90	3.35	-20.5			
8.89	200.0	1.10	1.35	-10.5	1.90	2.25	-17.0	2.90	3.35	-19.0	4.00	4.35	-26.5
5.08	189.0	1.43	2.30	-13	3.20	3.70	-21.0						
5.08	194.8	1.60	2.20	-11.5	3.30	3.70	-18.5						
5.08	196.5	1.72	2.25	-10.5	3.20	3.70	-17.5	4.70					
2.54	185.8	2.80	4.55	-14.5	6.30								
2.54	189.5	2.80	4.50	-14.5	6.20								
2.54	191.5	3.10	4.50	-13.5	6.25								
1.27	173.0	5.70	9.90	-15.5	15.3	19.8	-21.0						
1.27	182.2	6.00	9.90	-15.0	15.6	19.8	-21.0	22.8					
1.27	185.4	6.30	9.90	-15.0	15.6	19.5	-21.1	22.8					



SCALE - 5 μ sec/div

FIGURE 4.32
OFF-AXIS ACOUSTIC WAVEFORMS FOR THE BROADBAND PARAMETRIC
ARRAY WITH HIGH AMPLITUDE PRIMARY LEVEL

GATED, $f(t)$ - GAUSSIAN, $f_{1c} = 600$ kHz, $SPL_1 = 200.4$ dB re 1 μ Pa
 $a = 8.89$ cm, $R_0 = 10.07$ m, $r = 23.6$ m

ARL:UT
AS-81-613
JMH - GA
6 - 16 - 81

contrasts with the decrease and final disappearance of the second positive peak in the data for low amplitude primary levels.

The on-axis and off-axis performance noted in Fig. 4.32 was evaluated in the frequency domain and given in terms of the normalized power density spectrum at each angle as shown in Figs. 4.33 and 4.34. These spectra have the same characteristic Gaussian shapes as noted in the low amplitude analyses. The frequency and level at the spectral peak were extracted from these spectra and are shown in Fig. 4.35 with similar data for other primary peak sound pressure levels, including one that is considered low amplitude as well as the theoretical results from Eq. (3.45). A comparison of these data indicates that finite amplitude effects cause the on-axis frequency at the spectral peak to decrease from the low level value. For the data shown, the decrease is from about 66 kHz to about 62 kHz, or about 6%. As the off-axis angle is increased, the frequency at the spectral peak under finite amplitude limitations first increases, and then decreases and joins the low level trend. The relative level at the spectral peak or the power beam pattern indicates a decrease in directivity as the primary amplitude is increased. Measurements of the energy beam pattern as a function of primary peak sound pressure level are shown in Fig. 4.36. An increase in secondary half-power beamwidth of about 80% is noted with increasing primary level. The decrease in frequency at the spectral peak on-axis results from envelope distortion due to finite amplitude effects in the higher amplitude portions of the Gaussian pulse transmission. The decrease in secondary directivity is due to the finite amplitude effects, which are greatest on the acoustic axis. Both of these trends are rooted in the behavior of the primary field and will continue as the amplitude of the primary waves are increased toward saturation.

The trends established in the analysis of high amplitude primary waves with high primary directivity are also noted in the data as a function of primary directivity. The frequency and level at the spectral peak are shown in Fig. 4.37 for the broadband parametric array

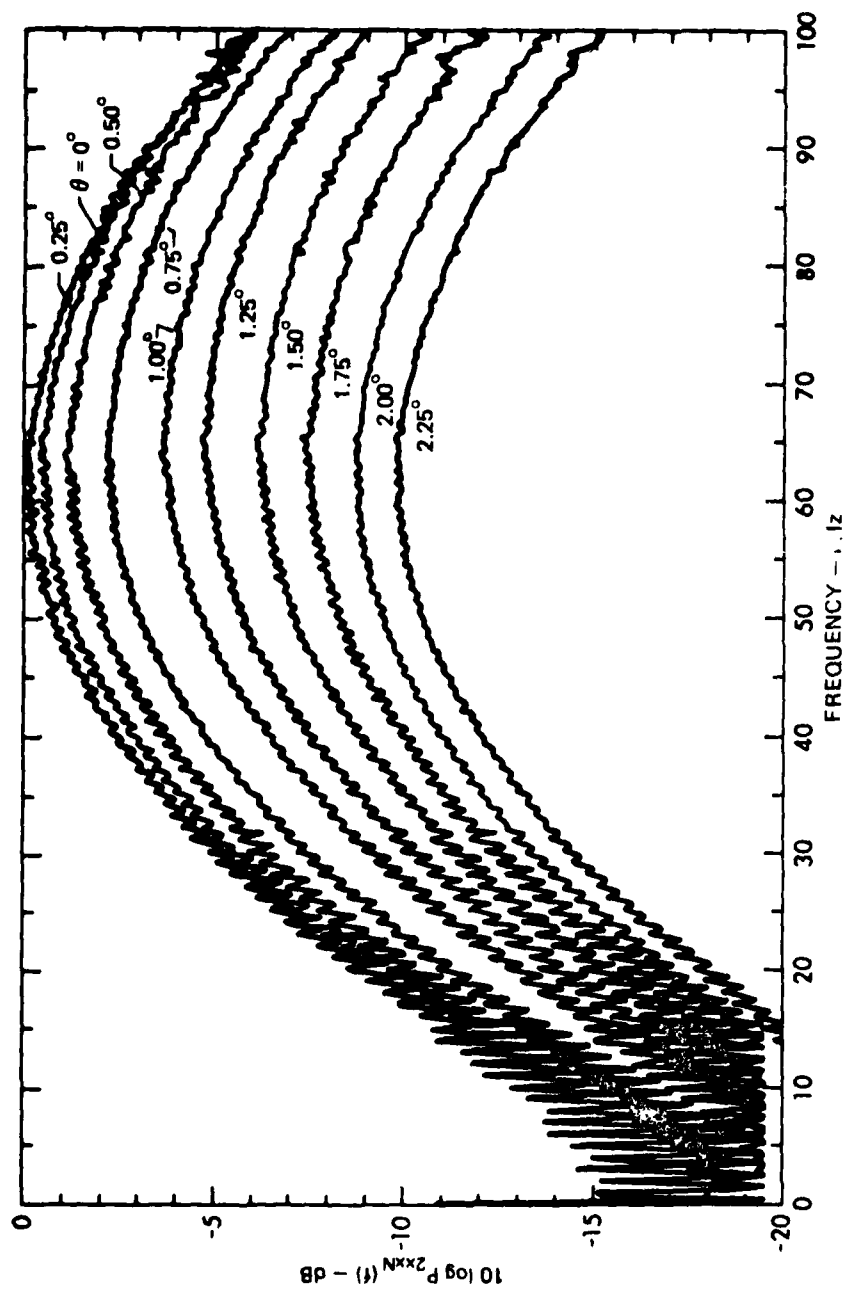


FIGURE 4.33
 NORMALIZED POWER DENSITY SPECTRA FOR THE BROADBAND PARAMETRIC ARRAY
 WITH HIGH AMPLITUDE PRIMARY LEVEL AT OFF-AXIS ANGLES FROM 0.00° TO 2.25°
 $f(t)$ - GAUSSIAN, $f_{1c} = 600$ kHz, $SPL_{1c} = 200.4$ dB re $1 \mu Pa$, $a = 8.89$ cm, $R_0 = 10.07$ m, $r = 23.6$ m

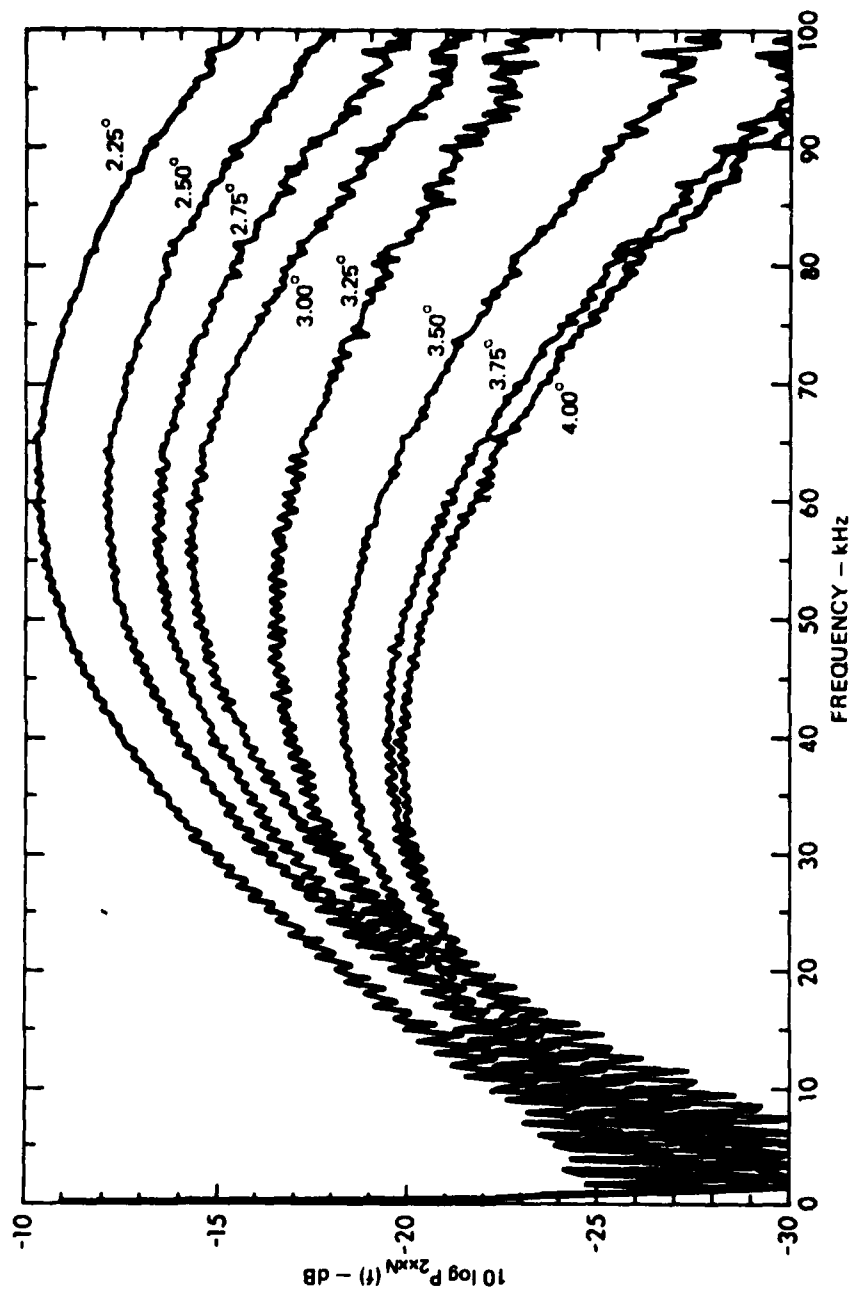


FIGURE 4.34
NORMALIZED POWER DENSITY SPECTRA FOR THE BROADBAND PARAMETRIC ARRAY
WITH HIGH AMPLITUDE PRIMARY LEVEL AT OFF-AXIS ANGLES FROM 2.25° TO 4.00°
 $f(t)$ - GAUSSIAN, $f_c = 600 \text{ kHz}$, $\text{SPL}_1 = 200.4 \text{ dB re } 1 \mu\text{Pa}$, $a = 8.89 \text{ cm}$, $R_0 = 10.07 \text{ m}$, $r = 23.6 \text{ m}$

ARL:UT
 AS-81-615
 JMH - GA
 6-16-81

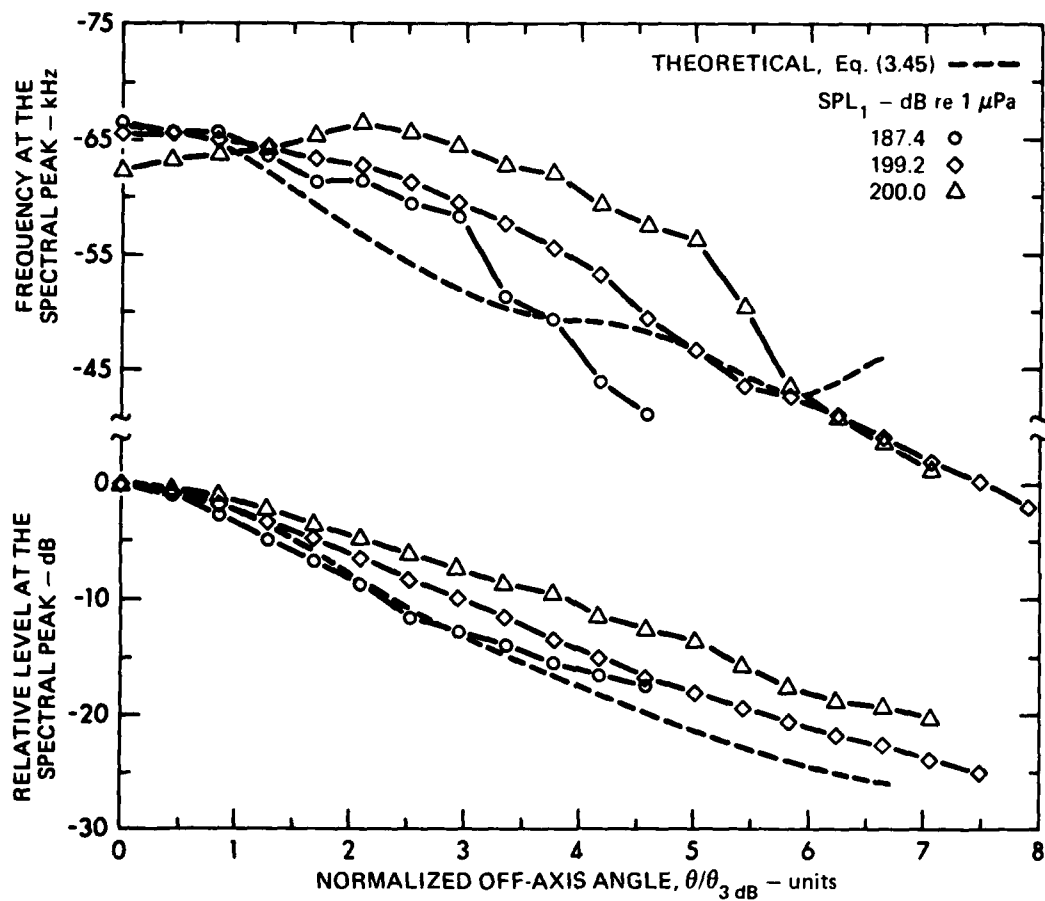


FIGURE 4.35
FREQUENCY AND LEVEL AT THE SPECTRAL PEAK OFF-AXIS FOR THE
BROADBAND PARAMETRIC ARRAY WITH HIGH AMPLITUDE PRIMARY LEVEL

$f(t)$ - GAUSSIAN, $f_{1c} = 600$ kHz, $a = 8.89$ cm, $R_0 = 10.07$ m, $r = 23.6$ m
 $\theta_{3\text{dB}} = 0.70^\circ$ (MEASURED LOW AMPLITUDE)

ARL:UT
 AS-81-616
 JMH - GA
 6-16-81

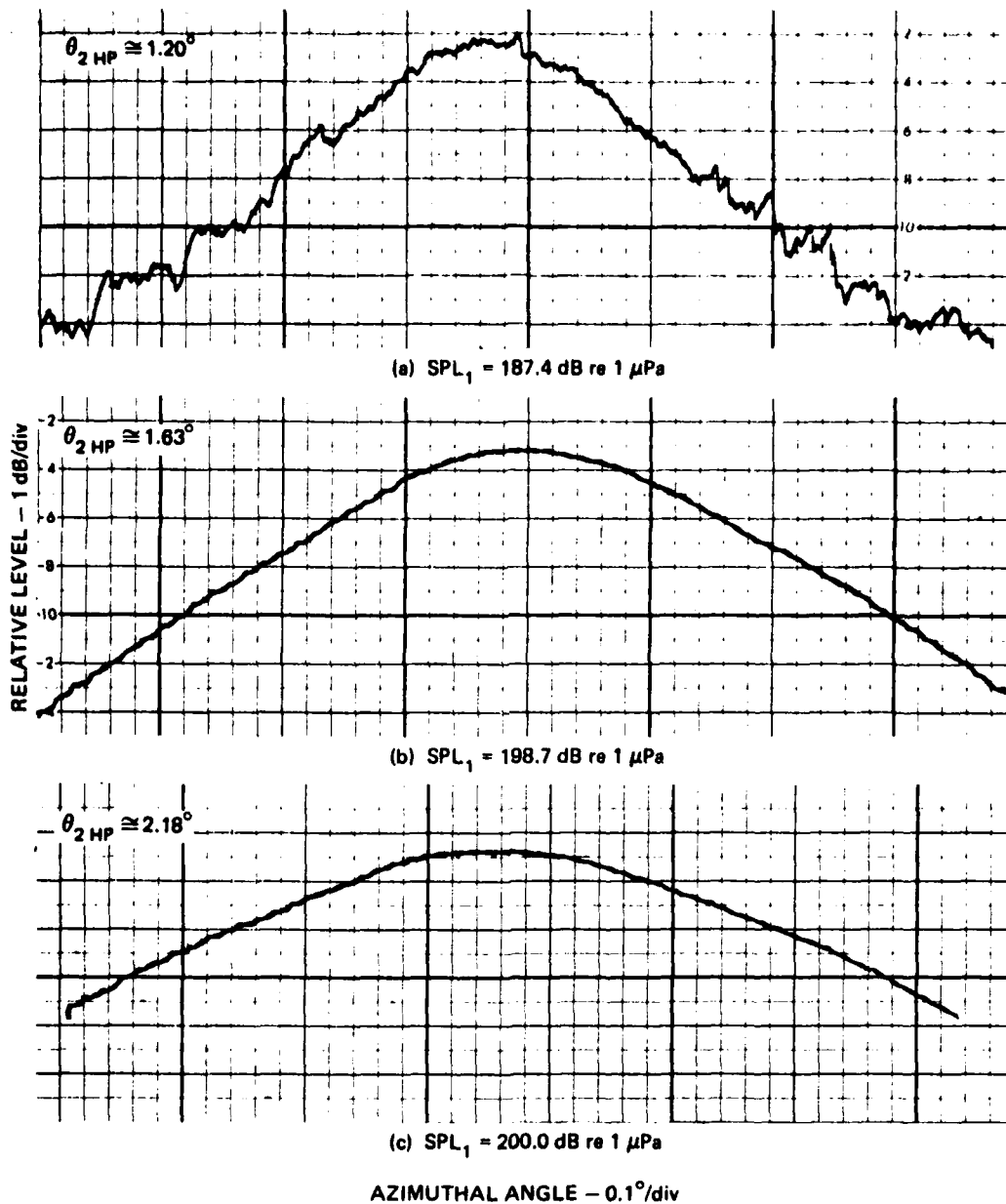


FIGURE 4.36
SECONDARY SOURCE DIRECTIVITY AS A FUNCTION
OF PRIMARY PEAK SOUND PRESSURE LEVEL

$f(t)$ - GAUSSIAN, $f_{1c} = 600 \text{ kHz}$, $a = 8.89 \text{ cm}$
 $R_0 = 10.07 \text{ m}$, $r = 23.6 \text{ m}$

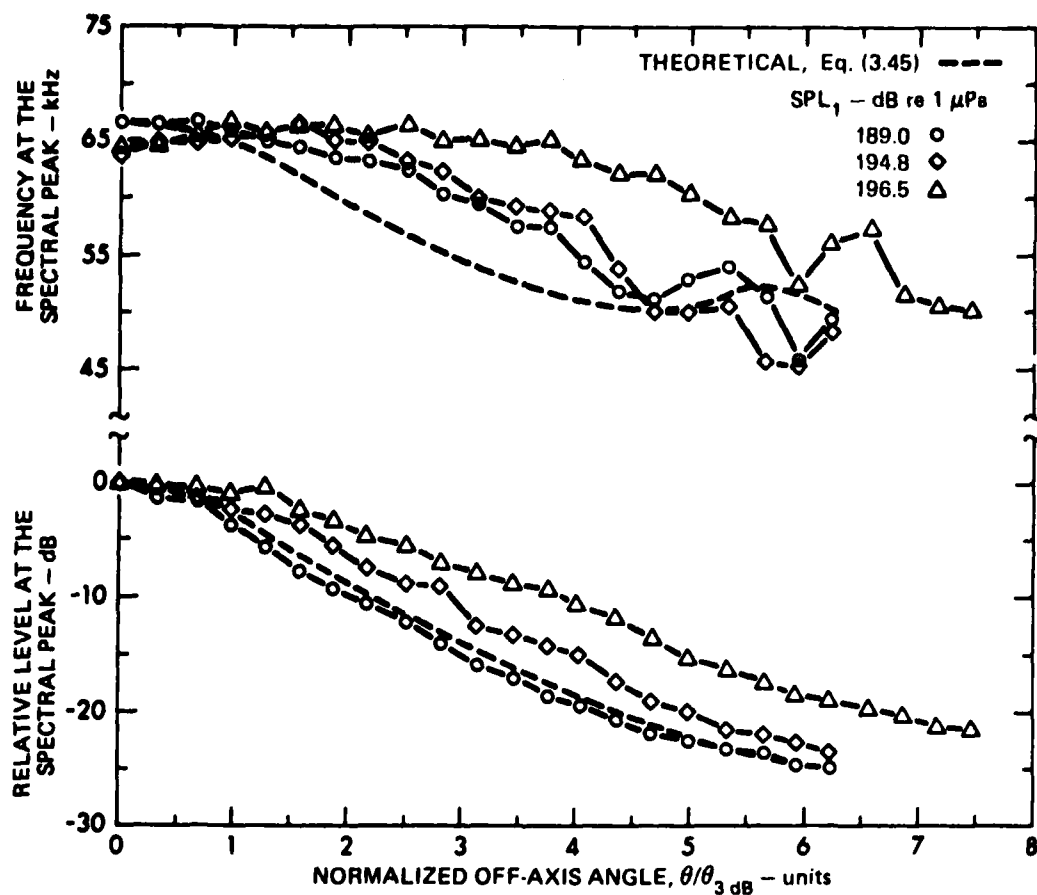


FIGURE 4.37
FREQUENCY AND LEVEL AT THE SPECTRAL PEAK OFF-AXIS FOR THE
BROADBAND PARAMETRIC ARRAY WITH HIGH AMPLITUDE PRIMARY LEVEL

$f(t)$ - GAUSSIAN, $f_{1c} = 600$ kHz, $a = 5.08$ cm, $R_0 = 3.29$ m, $r = 23.6$ m

$\theta_{3\text{ dB}} = 0.80^\circ$ (MEASURED LOW AMPLITUDE)

with a piston radius of 5.08 cm and a directivity ratio of 0.89. The frequency at the spectral peak on-axis is again observed to decrease from 66 kHz for low amplitude primary waves to 64 kHz for high amplitude primary waves. The relative level at the spectral peak indicates a decrease in directivity. This trend is supported in the measurements of energy beam patterns as a function of primary peak sound pressure level, which are shown in Fig. 4.38. A broadening of the secondary half-power beamwidth of about 66% is noted. The broadband parametric array with a directivity ratio of 1.74 was formed with a piston radius of 2.54 cm. The frequency and level at the spectral peak for both low and high amplitude primary transmissions are shown in Fig. 4.39. These data indicate a decrease in the frequency at the spectral peak on-axis from about 68 kHz to 66 kHz or about 3%, and a decrease in directivity at the secondary of about 38%, as noted in the energy beam patterns shown as a function of primary peak sound pressure level in Fig. 4.40. The broadband parametric array with the lowest directivity and a directivity ratio of 3.69 was formed with a piston radius of 1.27 cm. The frequency and level at the spectral peak are presented in Fig. 4.41 where the frequency at the spectral peak on-axis does not decrease under the influence of the high amplitude level that was reached. Only a slight broadening of 6% in half-power beamwidth is noted in the energy beam patterns shown in Fig. 4.42; however, an increase in the level far off-axis is noted in Figs. 4.41 and 4.42.

The data that have been presented cover only a limited range of finite amplitude effects and directivity ratios; however, certain trends are established with this limited set of data. As the amplitude of the primary waves were increased, the frequency at the spectral peak on-axis generally decreased and at off-axis angles, the downward shift in frequency at the spectral peak was reversed or inhibited. These trends result from waveform induced envelope distortion of the primary transmission. The secondary directivity generally decreased with the onset of finite amplitude behavior as determined by an increase in the half-power beamwidth and level far off-axis. The magnitude of these

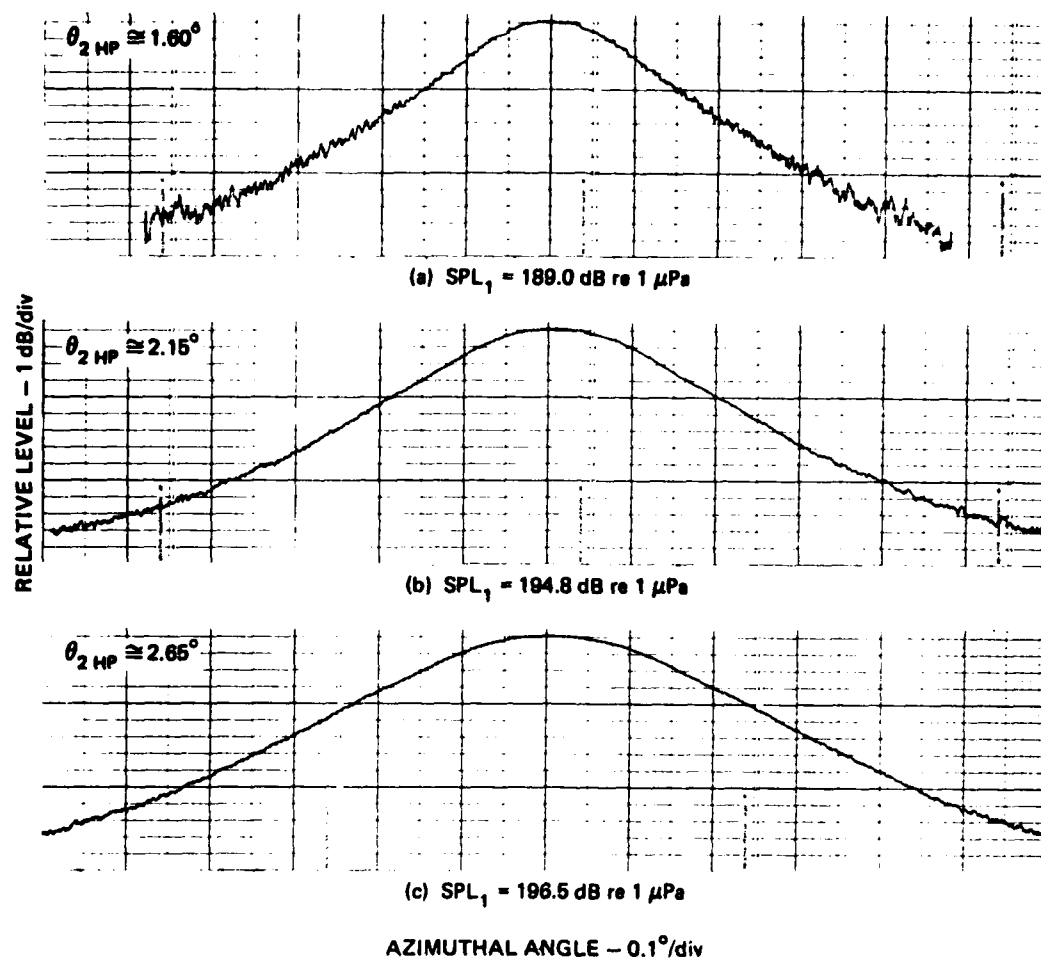


FIGURE 4.38
SECONDARY SOURCE DIRECTIVITY AS A FUNCTION
OF PRIMARY PEAK SOUND PRESSURE LEVEL

$f(t)$ - GAUSSIAN, $f_{1c} = 600 \text{ kHz}$, $a = 5.08 \text{ cm}$
 $R_0 = 3.29 \text{ m}$, $r = 23.6 \text{ m}$

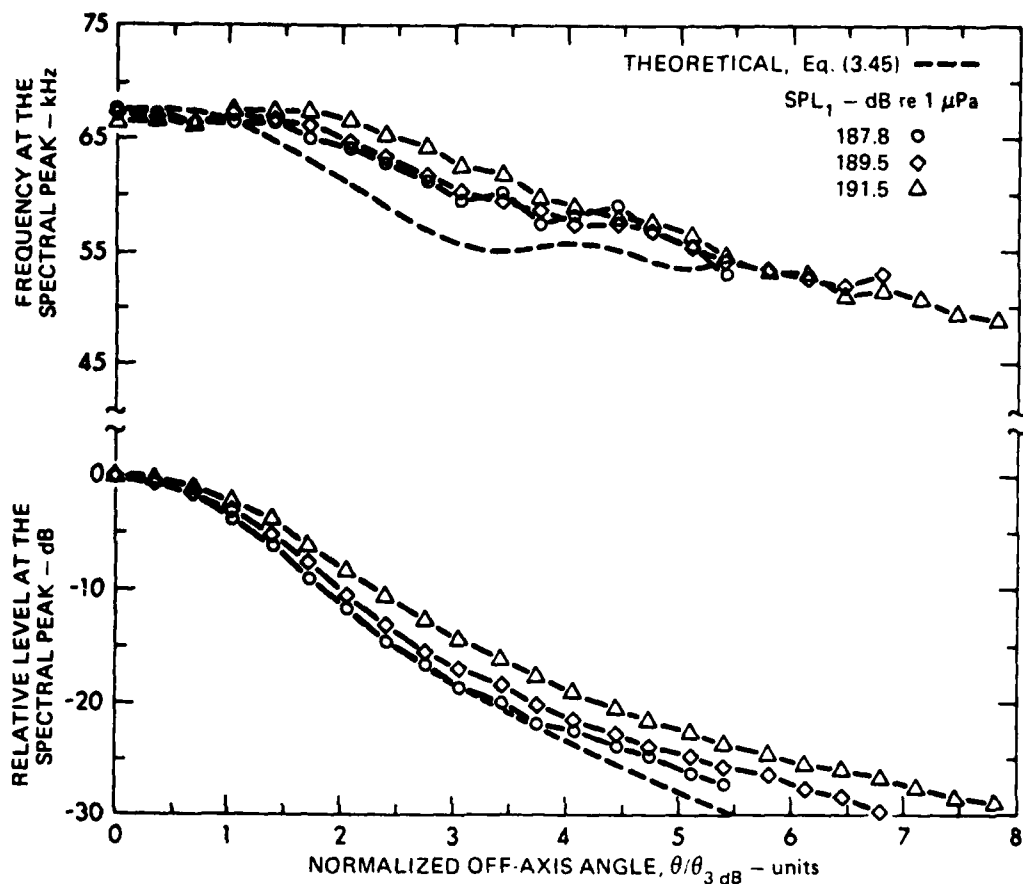


FIGURE 4.39
FREQUENCY AND LEVEL AT THE SPECTRAL PEAK OFF-AXIS FOR THE
BROADBAND PARAMETRIC ARRAY WITH HIGH AMPLITUDE PRIMARY LEVEL

$f(t)$ - GAUSSIAN, $f_{1c} = 600$ kHz, $a = 2.54$ cm, $R_0 = 0.82$ m, $r = 23.6$ m

$\theta_{3\text{ dB}} = 1.47^\circ$ (MEASURED LOW AMPLITUDE)

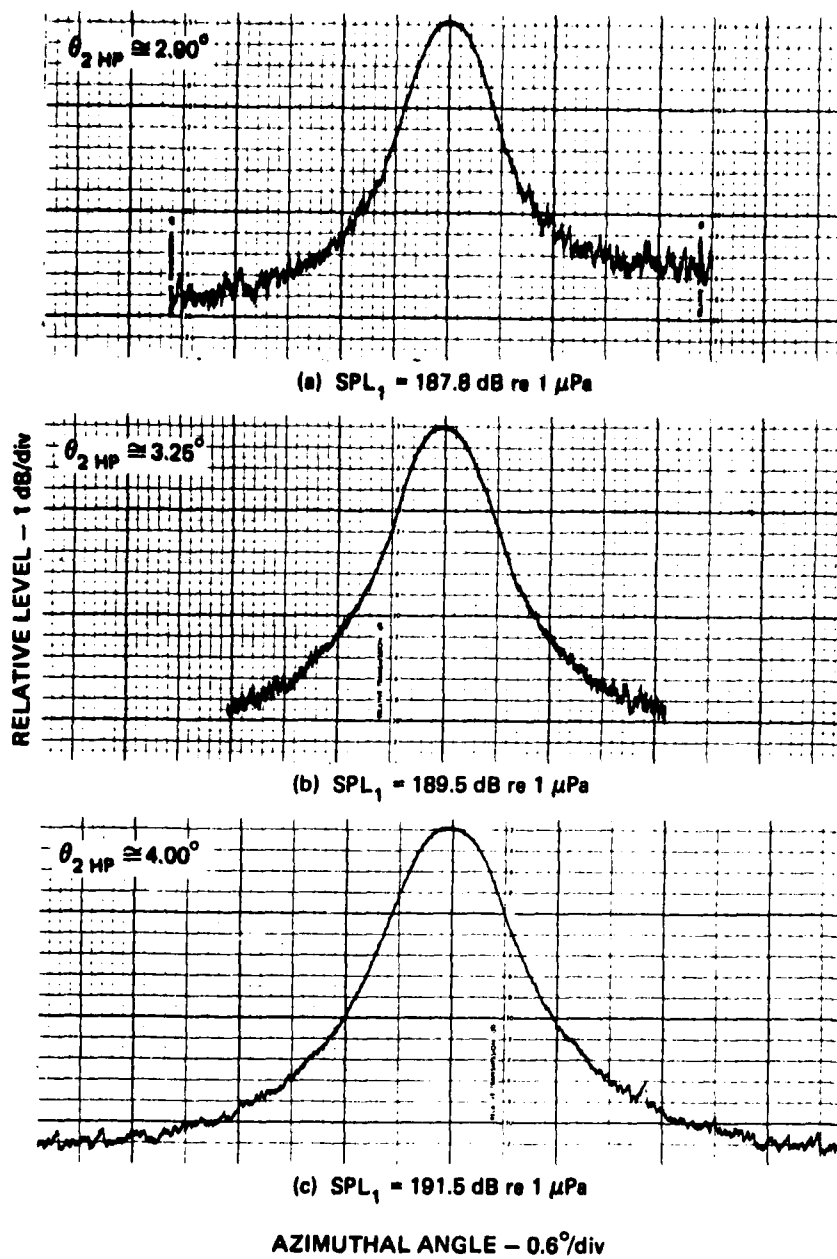


FIGURE 4.40
SECONDARY SOURCE DIRECTIVITY AS A FUNCTION
OF PRIMARY PEAK SOUND PRESSURE LEVEL

$f(t)$ - GAUSSIAN, $f_{1c} = 600 \text{ kHz}$, $a = 2.54 \text{ cm}$
 $R_0 = 0.82 \text{ m}$, $r = 23.6 \text{ m}$

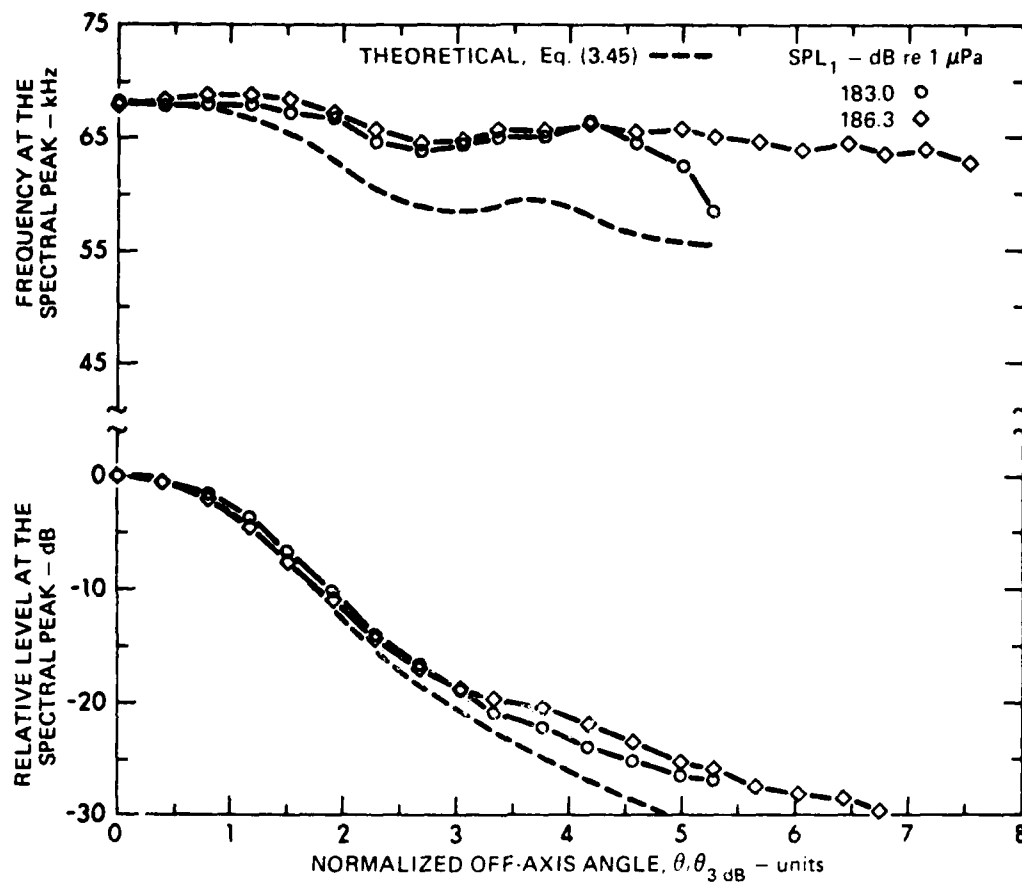


FIGURE 4.41
FREQUENCY AND LEVEL AT THE SPECTRAL PEAK OFF-AXIS FOR THE
BROADBAND PARAMETRIC ARRAY WITH HIGH AMPLITUDE PRIMARY LEVEL

$f(t)$ - GAUSSIAN, $f_{1c} = 600 \text{ kHz}$, $a = 1.27 \text{ cm}$, $R_0 = 0.21 \text{ m}$, $r = 23.6 \text{ m}$

$\theta_{3\text{dB}} = 2.65^\circ$ (MEASURED LOW AMPLITUDE)

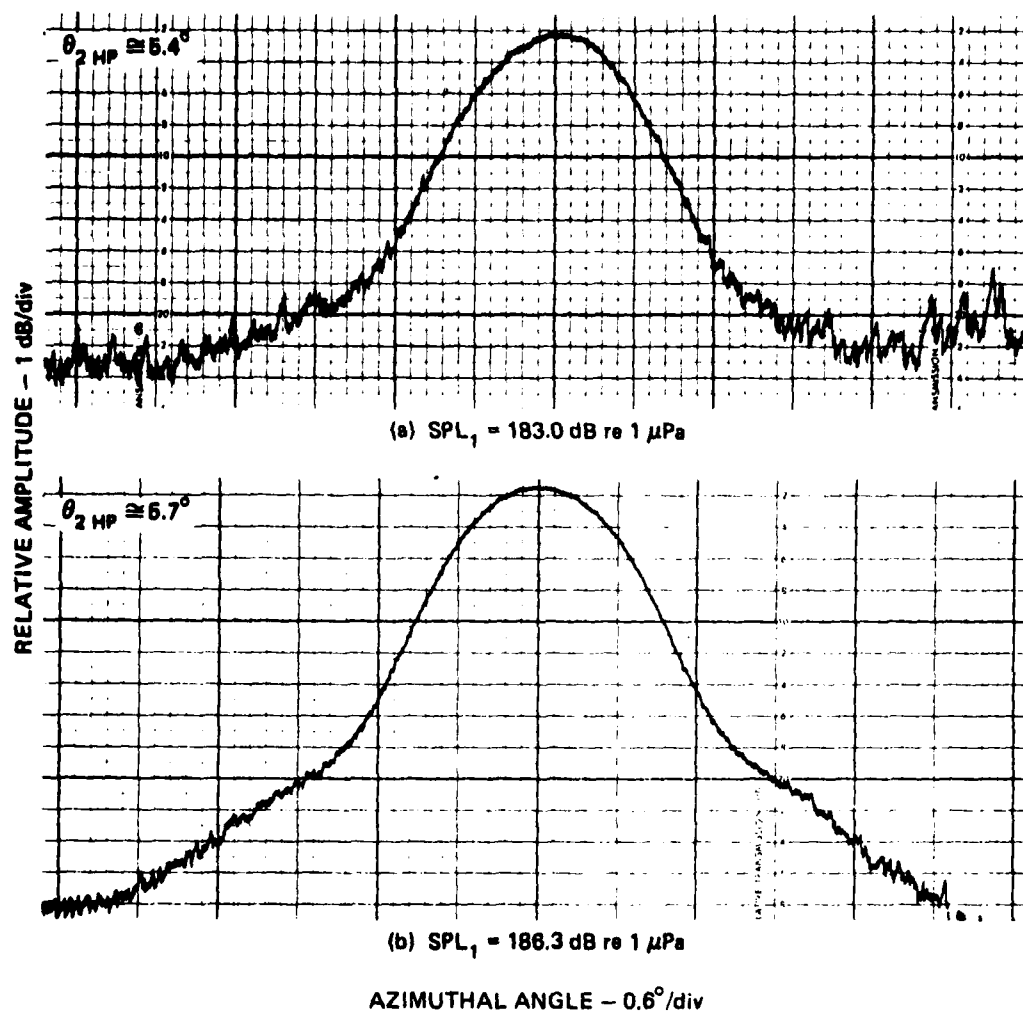


FIGURE 4.42
SECONDARY SOURCE DIRECTIVITY AS A FUNCTION
OF PRIMARY PEAK SOUND PRESSURE LEVEL

$f(t)$ - GAUSSIAN, $f_{1c} = 600 \text{ kHz}$, $a = 1.27 \text{ cm}$
 $R_0 = 0.21 \text{ m}$, $r = 23.6 \text{ m}$

trends tends to diminish as the primary directivity decreases and the directivity ratio increases. This is supported by the slower rate of departure from linear behavior for the primaries with decreasing primary directivity.

The on-axis performance of the secondary sound field with high amplitude primary waves is considered in Fig. 4.43 where the secondary peak sound pressure level is plotted as a function of input electrical power. The trends in this figure are similar to those in Fig. 4.26, which describes the on-axis performance of the primary field. The secondary signal level is proportional to the square of the low amplitude primary signal level, which accounts for the steeper slopes in Fig. 4.43. Departure from linear behavior is a maximum for the broadband parametric array with the highest directivity and varies from about 10 dB to about 3 dB for the data shown.

The off-axis performance of the secondary sound field with high amplitude primary waves is considered in Fig. 4.44. This figure indicates the broadening of the half-power beamwidths of both the primary and secondary radiation patterns for the four broadband parametric arrays that were formed. For each array formed, the secondary beam experiences greater broadening than the primary beam. This is another result of the proportionality of secondary level to the square of the primary level. The observed half-power beamwidths at low level are about 9% broader than their predicted farfield values according to the theory of Berklay and Leahy.²⁵

A cross function analysis was performed with the secondary signals resulting from the transmission of high amplitude primary waves. This analysis has the same format as that conducted for low amplitude primary wave transmissions in Section IV.B.3. This analysis allows the determination of relative signal properties using coherent signal analysis.

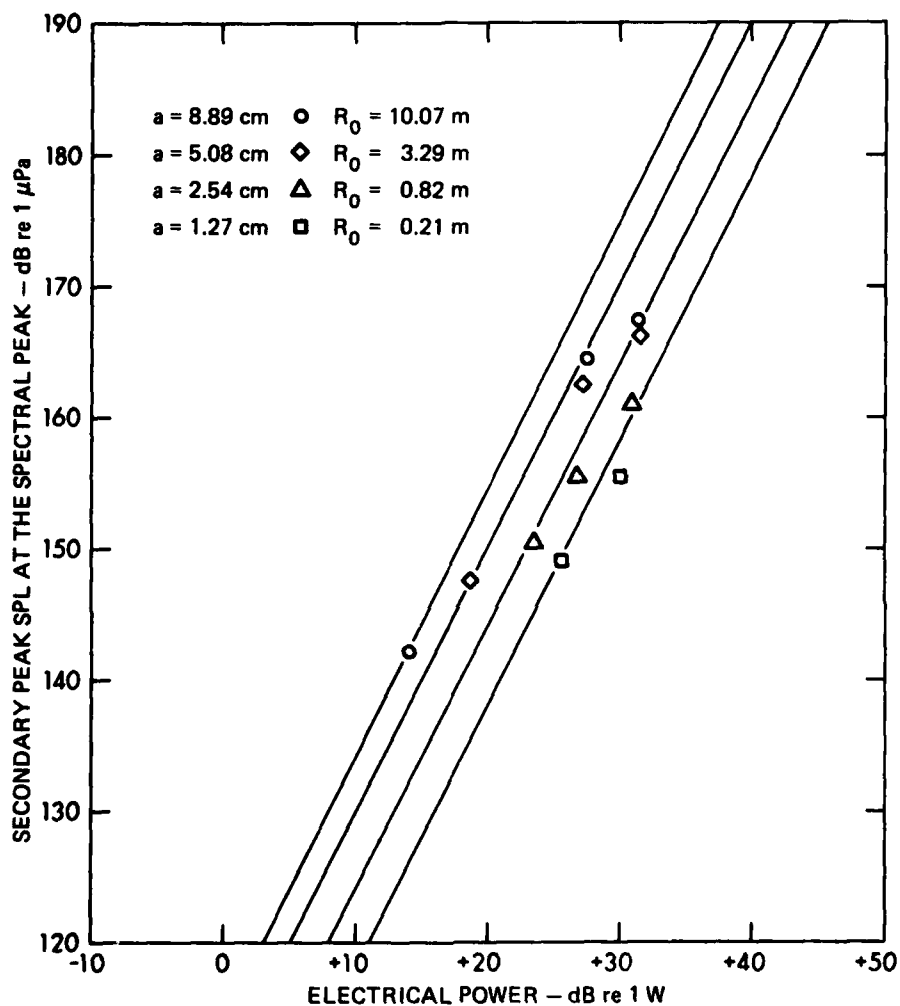


FIGURE 4.43
SECONDARY PEAK SOUND PRESSURE LEVEL AT THE SPECTRAL PEAK
 $f(t) - \text{GAUSSIAN}, f_{1c} = 600 \text{ kHz}, f_{2c} \cong 66 \text{ kHz}, r = 23.0 \text{ m}$

ARL:UT
 AS-81-624
 JMH - GA
 6-16-81

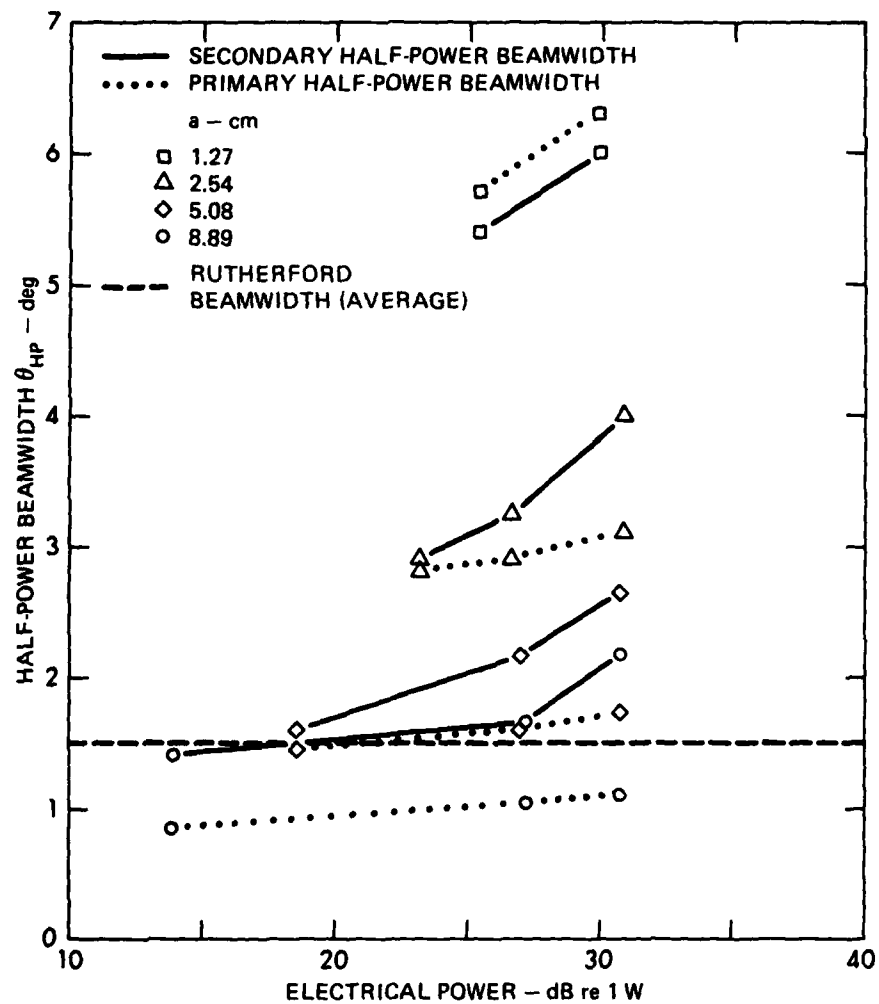
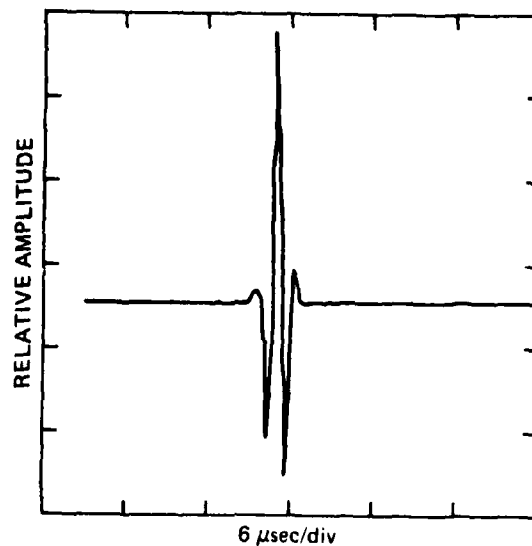


FIGURE 4.44
PRIMARY AND SECONDARY HALF-POWER BEAMWIDTH
 $f(t)$ - GAUSSIAN, $f_{1c} = 600$ kHz, $f_{2c} \cong 66$ kHz, $r = 23.6$ m

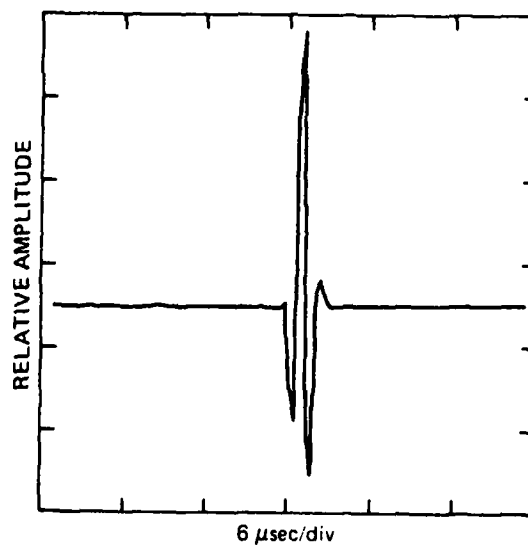
ARL:UT
 AS-81-625
 JMH - GA
 6-16-81

The selectable radius circular piston projector was driven using the full aperture with a radius of 8.89 cm. The primary peak sound pressure level, SPL_1 , was 200.4 dB re 1 μ Pa at 23.6 m. The cross-correlation of the on-axis and off-axis signals at 1.8° ($30_{3\text{ dB}}$) and 3° ($50_{3\text{ dB}}$) are shown in Fig. 4.45. As the angle off-axis is increased, the crosscorrelation transitions from a symmetric signal on-axis to a nonsymmetric signal off-axis. The first positive and negative peaks are diminished in amplitude relative to the other peaks while the overall waveform retains the duration of about 36 μ sec. This behavior is similar to that observed in the data with low amplitude primary waves.

The signal properties were evaluated in the frequency domain with the crosspower density spectrum. The crosspower amplitude spectra are shown in Fig. 4.46 for 0.0° and 1.8° , and for 0.0° and 3.0° . These amplitude spectra have broad peaks that result from the product of two secondary spectra. The spectral peak for 0.0° and 1.8° is at about 60.4 kHz, which is about 3% lower than the on-axis value; and the spectral peak for 0.0° and 3.0° is at about 57.1 kHz, which is about 8% lower than the on-axis value. The phase spectra, which indicate the relative phase between two signals as a function of frequency, are shown in Fig. 4.47. These spectra are reasonably constant with a value of phase difference near zero across the band. This performance is not surprising since the data were derived from crosscorrelation functions that were adjusted to be maximum at $\tau=0$ thereby implying phase coherence. It was noted in the analyses of low level performance that these observations are limited in their contribution to conclusions which may be reached concerning the data. The limitation results from equipment accuracy, which restricted the time delay resolution between signals and established the accuracy of relative phase measurements at about 18° at 100 kHz.



(a) ON-AXIS CROSS 1.8° OFF-AXIS



(b) ON-AXIS CROSS 3.0° OFF-AXIS

FIGURE 4.45
CROSSCORRELATION OF ON-AXIS AND OFF-AXIS SIGNALS
FOR THE BROADBAND PARAMETRIC ARRAY
WITH HIGH AMPLITUDE PRIMARY LEVEL

$f(t)$ — GAUSSIAN, $f_{1c} = 600$ kHz, $SPL_1 = 200.4$ dB re $1 \mu Pa$
 $a = 8.89$ cm, $R_0 = 10.07$ m, $r = 23.6$ m

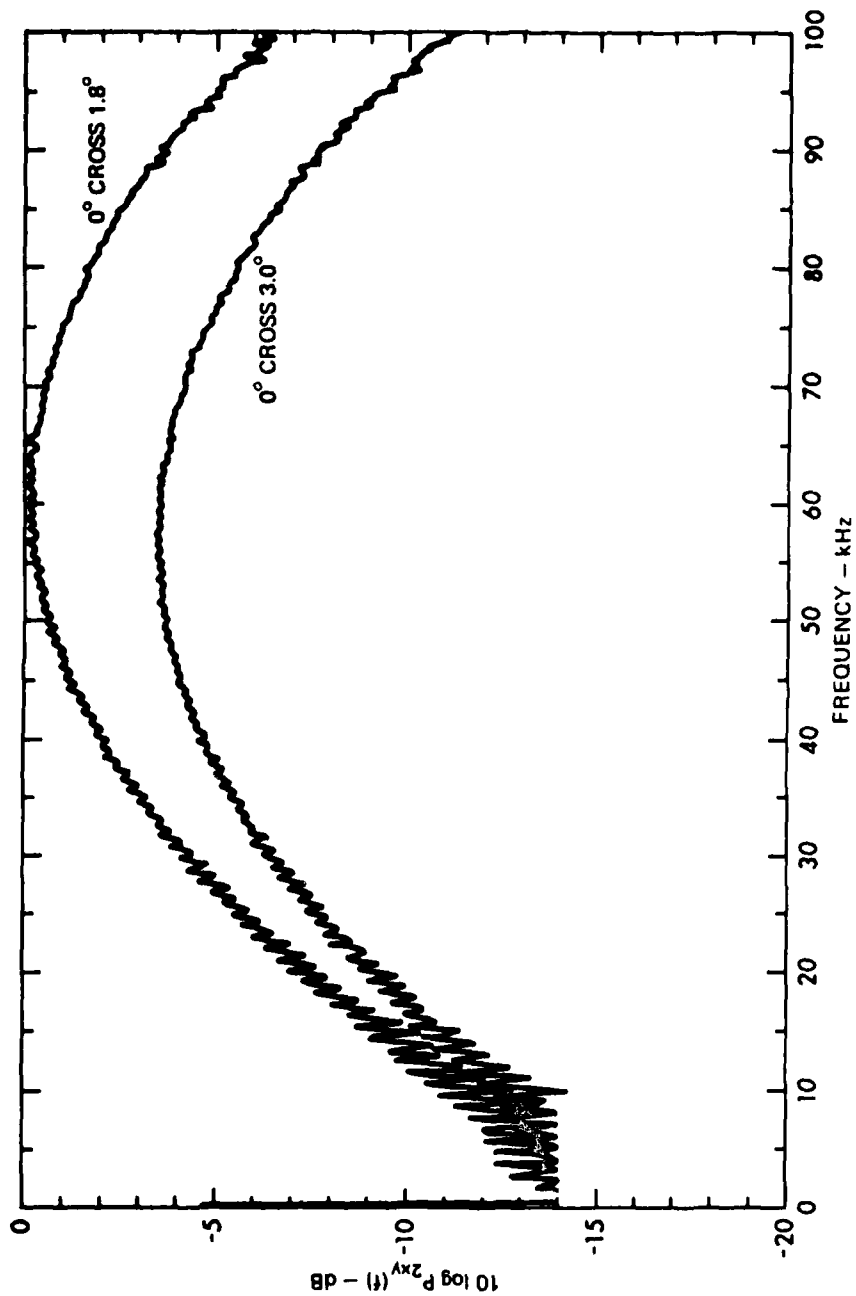
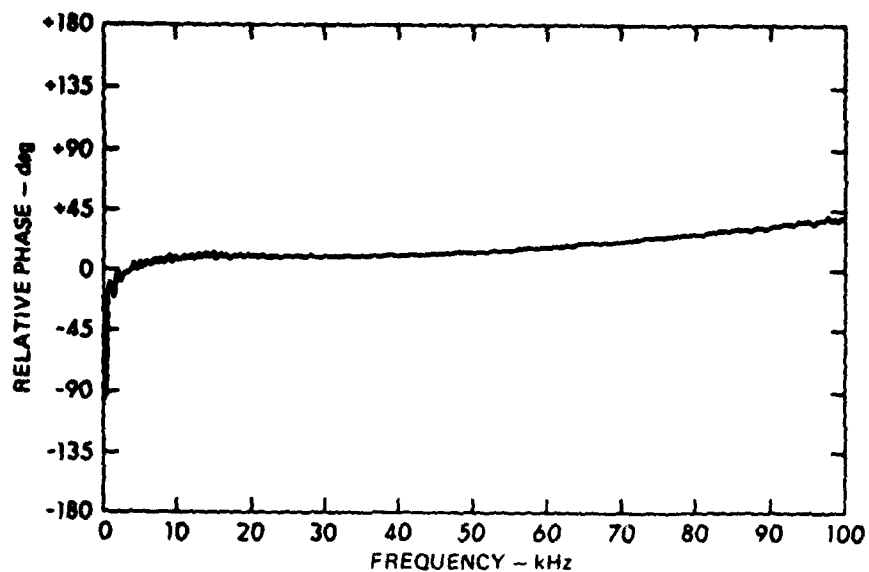
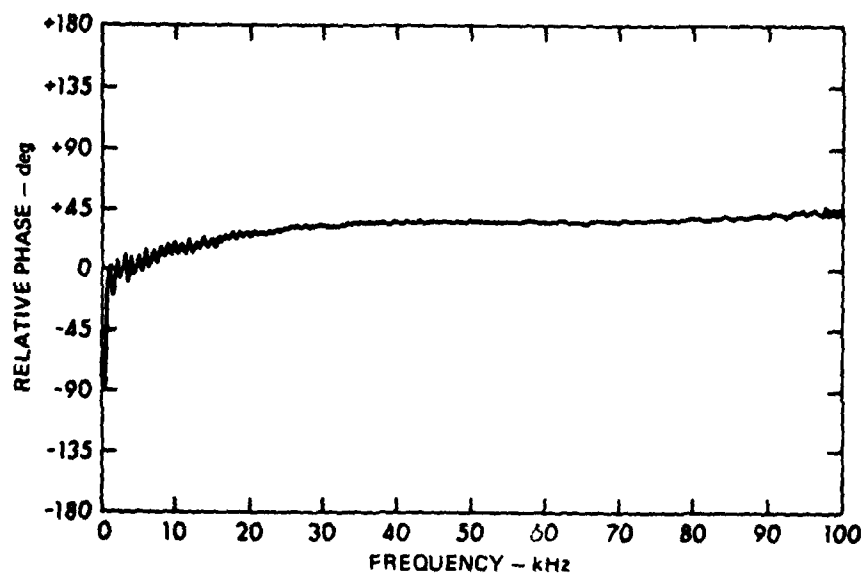


FIGURE 4.46
 NORMALIZED CROSS POWER AMPLITUDE SPECTRA OF ON-AXIS AND OFF-AXIS SIGNALS
 FOR THE BROADBAND PARAMETRIC ARRAY WITH HIGH AMPLITUDE PRIMARY LEVEL
 $f(t)$ - GAUSSIAN, $f_{1c} = 600 \text{ kHz}$, $\text{SPL}_1 \approx 200.4 \text{ dB re } 1 \mu\text{Pa}$, $a = 8.89 \text{ cm}$, $R_0 = 10.07 \text{ m}$, $r = 23.7 \text{ m}$



(a) ON-AXIS CROSS 1.8° OFF-AXIS



(b) ON-AXIS CROSS 3.0° OFF-AXIS

FIGURE 4.47
CROSS-POWER PHASE SPECTRA OF ON-AXIS AND OFF-AXIS
SIGNALS FOR THE BROADBAND PARAMETRIC ARRAY
WITH HIGH AMPLITUDE PRIMARY LEVEL

$f(t)$ - GAUSSIAN, $f_{1c} = 600$ kHz, $SPL_1 = 200.4$ dB re $1 \mu Pa$
 $a = 8.89$ cm, $R_0 = 10.07$ m, $r = 23.5$ m

CHAPTER V

SUMMARY AND CONCLUSIONS

The parametric acoustic array is the sound field of the interaction products that result from the mixing of two or more frequency components in a common volume of an acoustic medium. In the context of this investigation, the sound field of the baseband interaction products is characterized. An inhomogeneous wave equation, which is derived by perturbation of the exact equations of acoustics, leads to analytical descriptions of several types of parametric arrays. The analytical description of parametric arrays may be grouped into four basic classifications which depend on both spatial and temporal boundary conditions. These groups include both the narrowband and broadband parametric arrays for both plane wave and nonplane wave fields. Numerous studies have been conducted on the narrowband parametric array for both plane wave and nonplane wave fields; however only a few studies, which were mostly theoretical, have considered the broadband parametric array. The characteristics of the broadband parametric array for nonplane wave fields have not generally been determined and are the subject of the present theoretical and experimental investigation.

The broadband parametric array for plane wave fields only approximates the physically realizable primary source configurations. The analytical treatment for the broadband parametric array for plane wave fields was extended to allow detailed analyses of the sound field in both the time and frequency domains. The analytical descriptions were cast in terms of a linear system where the general solution off-axis in the frequency domain is given by the product of the on-axis solution with an off-axis transfer function.

The assumption of a Gaussian pulse primary transmission allows detailed evaluation of the on-axis and off-axis signal characteristics of a broadband parametric transmission. A closed form solution for the frequency at the spectral peak on-axis was derived. This peak frequency of the secondary transmission was shown to be directly proportional to the primary center frequency and inversely proportional to Q_1 . The secondary transmission was shown to have a constant Q_2 of 1.2 regardless of the primary pulse length or the primary or secondary center frequency. It was determined that the absolute bandwidth of the secondary transmission is approximately the same as that of the primary transmission. General expressions for the spectral properties off-axis were derived that indicate a shift toward lower frequencies with increasing off-axis angle.

The broadband parametric array for nonplane wave fields describes the physically realizable parametric array that results from a primary transmission from a real source. The source strength density was developed for a pulsed primary transmission that is spherically spreading from the origin and which has an off-axis transfer function that is valid throughout the sound field. These restrictions are generally met in the farfield of a planar source. A general solution for the secondary pressure was given in a form that involves the superposition of primary frequency field components. This solution involves a four dimensional integration over space and frequency. Using spherical geometry, the general solution was reduced from a four-dimensional integration to a two-dimensional integration by assuming symmetry about the acoustic axis and restricting the region of validity to the farfield of the parametric array.

The farfield solution was expressed for a Gaussian pulse primary transmission from a circular piston source and limiting forms of this solution were evaluated as a function of directivity. When the primary beams are extremely narrow and act as spatial impulse functions, the parametric array is absorption limited and the broadband parametric

array for plane wave fields is recovered. When the Rutherford beamwidth is extremely narrow compared to the primary beamwidth and acts as a spatial impulse function, the parametric array is diffraction limited and the directivity is determined by primary directivity products or off-axis transfer functions. The off-axis spectral properties for the diffraction limited case were evaluated by numerical integration of the theoretical off-axis transfer function for a primary signal transmitted from a circular piston in an infinite rigid baffle and in closed form by approximating the main lobe of the off-axis transfer function by a Gaussian function. As the characteristics of the parametric transmission shift from the absorption limit to the diffraction limit, the dependence of secondary frequency changes from quadratic to linear. With this change in secondary frequency dependence, a corresponding change in the shift toward lower frequencies in the power spectra occurs. This shift is characterized by a reduction in the on-axis frequency at the spectral peak by a factor of $\sqrt{2}$ for a Gaussian pulse primary transmission. In the absorption limit, the characteristics of the secondary off-axis transfer function are determined by the absorption at the primary frequencies and are monotonically decreasing with angle off-axis and secondary frequency. In the diffraction limit, the specific primary off-axis transfer function is dominant in determining the characteristics of the secondary off-axis transfer function. The characteristics of the secondary off-axis transfer function generally follow that of the primary off-axis transfer function with off-axis angle but are extremely insensitive to secondary frequency.

A detailed experimental study of the broadband parametric array provided measured data with variations in experimental parameters and emphasized the behavior as a function of primary directivity. A selectable radius circular piston projector was used as the primary source at 600 kHz to transmit Gaussian pulses from 14 to 17 μ sec in duration. Secondary transmissions with a Q_2 near 1 and an on-axis peak frequency of about 66 to 68 kHz were measured. Data were taken for directivity ratios (ratio of low level primary half-power beamwidth

to the Rutherford beamwidth) of 0.54, 0.89, 1.74, and 3.69. The transition from plane wave field (absorption limit) to nonplane wave field (diffraction limit) performance mostly occurs for directivity ratios from about 0.5 to 1.5.

The broadband parametric array formed with a directivity ratio of 0.54 is a physical approximation to the performance for plane wave fields. This parametric array was evaluated with low amplitude primary waves in both the time and frequency domains. The secondary waveforms showed the characteristic pulse shape of the second time derivative of the square of the Gaussian primary envelope on-axis which shifts to the first time derivative off-axis. This is the trend that was predicted by Westervelt.⁹ In the frequency domain, power density spectra of measured signals were evaluated. As the angle off-axis was increased both the frequency and level at the spectral peak decreased. The frequency at the spectral peak was relatively constant at small angles with a steady downward shift in the peak frequency at angles greater than the half-power angle. The relative level at the spectral peak was smooth and monotonically decreasing. Measured data were compared with theoretical results for the farfield absorption and diffraction limits and for the farfield solution from Eq. (3.45), which was evaluated by double numerical integration. In the absorption limit, the predicted peak frequency on-axis is higher than observed. The trend toward a downward shift in frequency at the spectral peak is slow for small angles, increases to a rapid shift, and becomes relatively constant at large angles. The predicted level at the spectral peak in the absorption limit is slightly lower than the experimental data. In the diffraction limit, the predicted frequency at the spectral peak is lower than that observed on-axis and relatively constant out to the half-power angle. At larger angles, secondary maxima in the frequency at the spectral peak are noted which result from spatial lobes in the off-axis transfer function. Comparable behavior at small angles is noted with a Gaussian approximation of the main lobe of the off-axis transfer function. The level at the spectral peak decreases very rapidly

off-axis for both diffraction limit representations. The theoretical results obtained with the farfield solution from Eq. (3.45) indicate generally good agreement with the experimental data. Excellent agreement was noted in the frequency at the spectral peak at small angles. At larger angles the theoretical results are in general agreement but predict slightly lower frequencies at the spectral peak. This difference is attributed to the higher measured sidelobe levels in the primary off-axis transfer function than those assumed in the theoretical representation of a piston in an infinite rigid baffle. The higher sidelobe levels tend to retard the downward shift in frequency at the spectral peak in the measured data. The relative level at the spectral peak is in excellent agreement with the theoretical results predicted by Eq. (3.45). At the half-power angle, the agreement with the absorption limit is also good. This agreement was noted in earlier studies as verification of the Westervelt model for the parametric array for plane wave fields. The agreement with the absorption limit degrades at large angles and supports the conclusion that this parametric array is only a physical approximation for plane wave fields.

The general characteristics that have been described in the comparison of experimental and theoretical results are also noted in the data for the other source configurations which transition toward the diffraction limit. These other source configurations are characterized by a shift in overall weighting of the secondary frequency from $\omega_2^{1.68}$ to $\omega_2^{1.3}$. Recall that the dependence is quadratic in the absorption limit and linear in the diffraction limit. In each data set, the influence of the primary off-axis transfer function increased as the diffraction limit was approached and a trend toward frequency independence as a function of angle off-axis was observed. The experimental data for a directivity ratio of 3.69 represent the most diffraction dominated case that was evaluated. These experimental data indicated a secondary maximum in the frequency at the spectral peak, which is in good agreement with the predictions of Eq. (3.45) and also agrees in angular placement with the diffraction limit of Eq. (3.45). No perceptible sidelobes were

predicted from Eq. (3.45) in the level at the spectral peak; however, there was such a sidelobe in the measured data. This again results from the higher sidelobe levels in the measured primary off-axis transfer or directivity functions. The comparisons between the experimental data and the theoretical results indicate that the frequency at the spectral peak is a more sensitive indicator of the characteristics of the broadband parametric transmission than the level of the spectral peak which as a function of off-axis angle indicates the power beam pattern.

The broadband parametric array was evaluated with high primary levels as a function of primary directivity. An evaluation of the primary field indicated the influence of finite amplitude effects as a function of increased levels with a departure from linear performance of the narrowband primary transmission. An analysis of the on-axis field indicated that most of the finite amplitude distortion occurred in the nearfield of the primary source. Finite amplitude effects compete with spherical spreading and small signal absorption; therefore, as the primary directivity decreased, so did the influence of finite amplitude effects on the primary waves. In the primary field, finite amplitude effects cause envelope distortion of a narrowband primary signal, a broadening of the main primary beam, and an apparent increase in sidelobe levels.

The secondary field was evaluated in the time and frequency domains, where many of the same trends were indicated as observed with low amplitude primary waves. The frequency at the spectral peak, which was extracted from measured power spectra, was lower on-axis than the value with low amplitude primary waves due to the envelope distortion on-axis. As the off-axis angle increased, the frequency at the spectral peak first increased, then decreased and followed the low amplitude trend. A broadening of the secondary beams was also noted.

A comparison of the experimental data for each source configuration with the theoretical results of Eq. (3.45) indicates several deficiencies in the analytical modeling. For low amplitude primary waves, the on-axis experimental and theoretical results agree very well; however, the off-axis theoretical results agree very well for the level at the spectral peak but generally predict lower values of frequency at the spectral peak than observed. This difference results from the assumption of theoretical off-axis transfer functions for a piston in an infinite rigid baffle rather than an exact representation of the measured off-axis transfer function at the primary frequencies. There were also slight differences in the measured and predicted values of SPL_2 that could not be attributed to experimental error. These level differences result primarily from the incompleteness of the parametric array at the measurement range. To account for these differences the farfield approximation must not be assumed and the range integration performed.

The correct modeling of the broadband parametric array with high amplitude primary waves is a more complex problem than the low amplitude primary wave theoretical treatment. The characteristics of the broadband parametric array under these conditions are determined by the characteristics of the primary transmission in both the nearfield and the farfield of the primary source. Finite amplitude effects are cumulative with waveform propagation; therefore the characteristics of the primary field must be described as a function of range throughout the nearfield and the farfield of the source. This characterization must be included in the theoretical modeling and the range integration performed.

APPENDIX A
RADIATION OF A PULSED CARRIER IN THE
FARFIELD OF A CIRCULAR PISTON

The radiation in the farfield of a circular piston set in an infinite rigid baffle has been the subject of many theoretical and experimental studies. The symmetry which is exhibited in the radiation field allows straightforward analyses of off-axis characteristics. In this appendix, the radiation in the farfield of a circular piston will be evaluated to determine the spectral distortion of a broadband signal as a function of off-axis angle. This study will allow a comparison of the off-axis spectral distortion for transmissions from a conventional acoustic source and a parametric array.

A. General Solution

The time independent solution for the pressure field produced by radiation in the farfield of a circular piston set in an infinite rigid baffle is given by Morse and Ingard.¹⁹ Ignoring losses due to dissipation, the solution may be written in the frequency domain in the form

$$P_1(r, \theta, f) = \frac{R_o}{r} P_o e^{-jk_1 r} D(\theta, f) \quad . \quad (A.1)$$

In this equation, P_o is the peak pressure amplitude measured at R_o , and $D(\theta, f)$ is the directivity function given by

$$D(\theta, f) = \frac{2J_1(k_1 a \sin \theta)}{k_1 a \sin \theta} \quad , \quad (A.2)$$

where $J_1(\cdot)$ is the Bessel function of the first kind and first order.

An analysis of the spectral distortion of a broadband signal which is transmitted from a circular piston as a function of off-axis angle is facilitated by treating the on-axis and off-axis properties of

Eq. (A.1) as the input and output, respectively, of a linear system with the form

$$P_I(r, \theta, f) = P_I(r, 0, f) H_{1\theta}(f) \quad , \quad (A.3)$$

where $H_{1\theta}(f)$ is the off-axis transfer function for the first order field. By comparison with Eq. (A.1), it is clear that the off-axis transfer function in the farfield of a circular piston set in an infinite rigid baffle is simply the directivity function given by

$$H_{1\theta}(f) = D(\theta, f) = \frac{2J_1(k_1 a \sin\theta)}{k_1 a \sin\theta} \quad . \quad (A.4)$$

The off-axis power transfer function, $|H_{1\theta}(f)|^2$, is shown in Fig. A.1. Continuing this development, the solution for the pressure field in the time domain is given by

$$p_1(r, \theta, t) = p_1(r, 0, t) * h_{1\theta}(t) \quad , \quad (A.5)$$

where $h_{1\theta}(t)$ is the off-axis impulse response function given by

$$h_{1\theta}(t) = \mathcal{F}^{-1} [H_{1\theta}(f)] = \frac{1}{\pi \left(\frac{a}{c_0} \sin\theta \right)^2} \text{circ} \left[\frac{1}{\frac{a}{c_0} \sin\theta} \right] \quad , \quad (A.6)$$

where

$$\text{circ } |X| = \begin{cases} 1 & |X| \leq 1 \\ 0 & |X| > 1 \end{cases} \quad . \quad (A.7)$$

Analysis of Eqs. (A.6) and (A.7) indicates that the off-axis impulse response function is a pulse with amplitude and duration which are

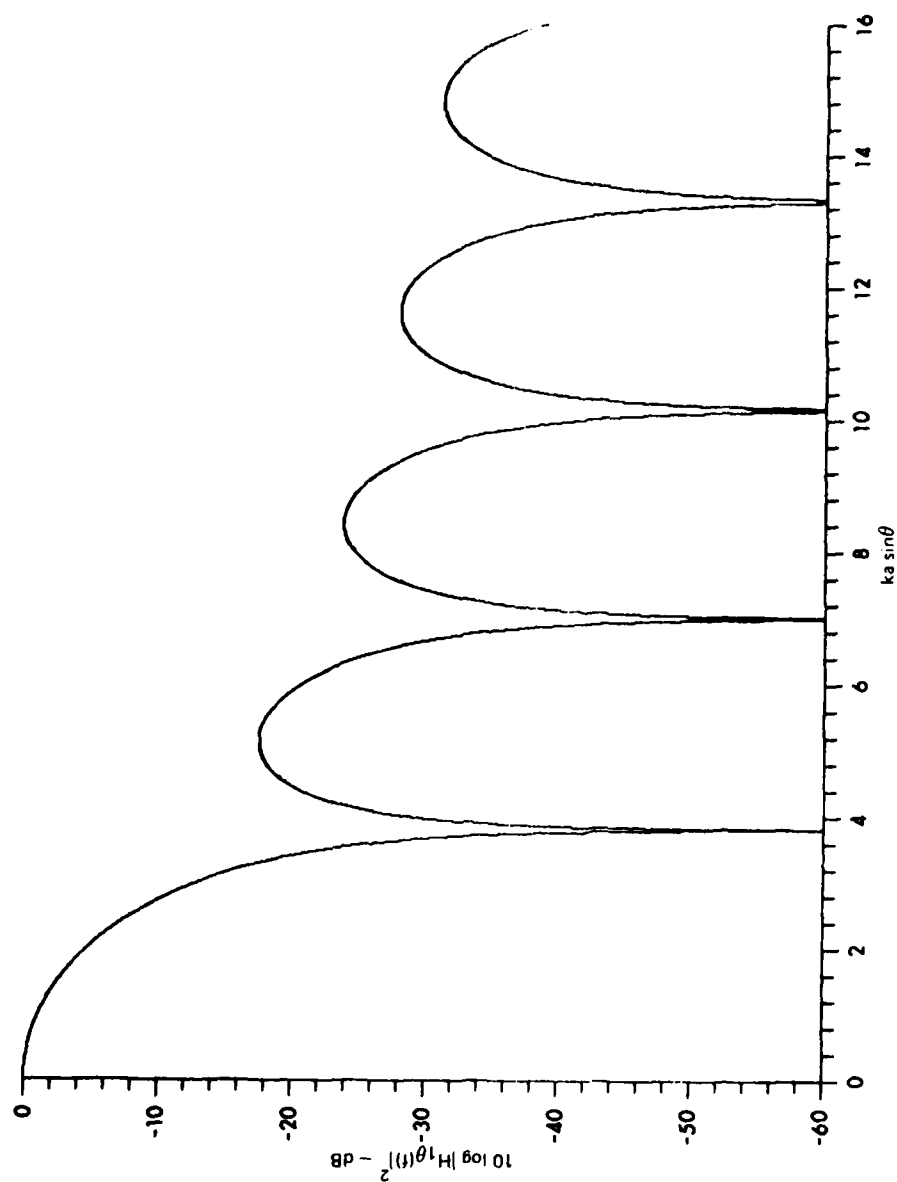


FIGURE A.1
OFF-AXIS POWER TRANSFER FUNCTION FOR THE RADIATION IN THE FARFIELD
OF A CIRCULAR PISTON SET IN AN INFINITE RIGID BAFFLE

functions of θ . On axis, the impulse response function becomes

$$h_{10}(t) = \delta(t) \quad , \quad (A.8a)$$

and at right angles to the acoustic axis,

$$h_{1\pi}(t) = \frac{c_o^2}{a^2 \pi} \text{circ} \left[\frac{tc_o}{a} \right] \quad . \quad (A.8b)$$

The duration of the pulse at $\theta=\pi$ is $t=2a/c_o$ or the propagation time in the medium across the diameter of the piston.

The separation of the on-axis and off-axis radiation characteristics allows the analysis of signal distortion as a function of off-axis angle in both the time and frequency domains. This analysis is based on specified or measured signal characteristics on the acoustic axis.

B. On-Axis Radiation of a Pulsed Carrier in the Farfield of a Circular Piston

The on-axis pressure for a pulsed carrier signal emitted from a circular piston set in an infinite baffle may be written

$$p_1(r,0,t) = \frac{R_o}{r} P_o e^{-\alpha_{1c}(r-R_o)} f\left(t - \frac{r}{c_o}\right) \sin(\omega_{1c}t - k_{1c}r) \quad , \quad (A-9)$$

where α_{1c} is the absorption coefficient at the carrier frequency and ω_{1c} is the angular carrier frequency. It is assumed that the pulse envelope function $f(t)$ is slowly varying with respect to $\sin(\omega_{1c}t)$. Signal level dissipation as a function of range is considered with the inclusion of absorption at the carrier frequency. It is assumed that this signal is bandlimited such that the absorption coefficient at each

frequency throughout the band may be approximated by the absorption coefficient at the carrier frequency. In the frequency domain, the on-axis pressure signal for a pulsed carrier is given by the Fourier transform of Eq. (A.9), which is written

$$P_1(r, 0, f) = \frac{R_0}{r} P_0 e^{-\alpha_{1c}(r-R_0)} \times \left[\mathcal{F}\left\{f\left(t - \frac{r}{c_0}\right)\right\} * \mathcal{F}\left\{\sin(\omega_{1c}t - k_{1c}r)\right\} \right] \quad (A.10)$$

This equation reduces to

$$P_1(r, 0, t) = \frac{R_0}{2jr} P_0 e^{-\alpha_{1c}(r-R_0)} e^{-jk_1r} \times \left[\mathcal{F}\left\{f(t)\right\}_{f=f_1+f_{1c}} - \mathcal{F}\left\{f(t)\right\}_{f=f_1-f_{1c}} \right] \quad (A.11)$$

Equation (A.11) indicates that the on-axis frequency spectrum is determined by the two sided Fourier transform of the pulse envelope function centered at the carrier frequency. Further study of the spectral distortion as a function of off-axis angle of a pulsed carrier signal emitted from a circular piston set in an infinite rigid baffle requires the specification of a pulse envelope function. The assumption of a Gaussian pulse envelope is mathematically tractable and a reasonable approximation to pulse envelopes which may be attained in practice.

A Gaussian envelope function is assumed to have the form

$$f(t) = e^{-n^2 t^2} \quad , \quad (A.12)$$

which has a Fourier transform given by

$$\mathcal{F}\{f(t)\} = F(f) = \frac{\sqrt{\pi}}{n} \exp\left[-\left(\frac{\pi}{n}\right)^2 f^2\right] , \quad (\text{A.13})$$

where n is a constant that determines the effective duration of the pulse and therefore the effective width of the frequency spectrum. The spectral characteristics of the Gaussian pulse transmission may be specified by defining the constant n in the frequency domain. A representation⁷⁴ of the power spectral density function for finite duration signals may be derived from the energy spectral density function by weighting the energy spectral density function with respect to the duration of the signal, or

$$P_{xx}(f) = \frac{1}{T} E_{xx}(f) , \quad (\text{A.14})$$

where $P_{xx}(f)$ is the power spectral density function, $E_{xx}(f)$ is the energy spectral density function, and T is the duration of the signal. It is required that the normalized power spectral density function of the on-axis pulsed carrier transmission be equal to 0.5 at the half-power frequencies, or

$$P_{1xxN}(f) = \left[\frac{P_1(r, \theta, f) P_1^*(r, \theta, f)}{P_1(r, 0, f_{1c}) P_1^*(r, 0, f_{1c})} \right]_{f=F_{11} \text{ or } F_{12}} = 0.5 , \quad (\text{A.15})$$

where $P_{1xxN}(f)$ is the normalized power spectral density function and F_{11} and F_{12} are the lower and upper half-power frequencies, respectively. Substituting Eqs. (A.11) and (A.13) into Eq. (A.15) and solving for n gives

$$n = 2.668 |F_{11} - F_{12}| , \quad (\text{A.16})$$

where $|F_{11}-F_{12}|$ is the half-power bandwidth of the pulsed carrier transmission. If the quality factor is defined by

$$Q_1 = \frac{f_{1c}}{|F_{11}-F_{12}|} \quad , \quad (A.17)$$

then n may also be expressed by

$$n = 2.668 \frac{f_{1c}}{Q_1} \quad . \quad (A.18)$$

If the pulse duration is defined by the inverse of the half-power bandwidth, then

$$T = \frac{1}{|F_{11}-F_{12}|} \quad (A.19)$$

and the pulse duration is determined between the 0.17 amplitude levels of the pulse envelope as computed from Eq. (A.12) for $t=T/2$.

Assuming the Gaussian pulse envelope function described by Eq. (A.12), the on-axis pressure for a pulsed carrier signal emitted from a circular piston set in an infinite rigid baffle is found from Eqs. (A.9) and (A.12) to be given by

$$p_1(r,0,t) = \frac{R_0}{r} P_0 e^{-\alpha_{1c}(r-R_0)} e^{-n^2 t^2} \sin(\omega_{1c} t - k_{1c} r) \quad (A.20)$$

in the time domain. In the frequency domain, the on-axis solution is found from Eqs. (A.11) and (A.13) and is given by

$$P_1(r, 0, f) = \frac{R_o}{2jr} P_o e^{-\alpha_{1c}(r-R_o)} e^{-jk_{1c}r} \\ \times \frac{\sqrt{\pi}}{n} \left\{ \exp \left[- \left(\frac{\pi}{n} \right)^2 (f_1 + f_{1c})^2 \right] - \exp \left[- \left(\frac{\pi}{n} \right)^2 (f_1 - f_{1c})^2 \right] \right\} \quad (A.21)$$

C. Off-Axis Radiation of a Pulsed Carrier in the Farfield of a Circular Piston

The solution for the off-axis pressure in the farfield of a circular piston set in an infinite rigid baffle is given in the time domain by the convolution of the on-axis solution with the off-axis impulse response function and in the frequency domain by the product of the on-axis solution with the off-axis transfer function.

For the Gaussian pulse transmission, the off-axis solution in the time domain is found by substituting Eqs. (A.6) and (A.20) into Eq. (A.5), and can be written as

$$p_1(r, \theta, t) = \left[\frac{R_o}{r} P_o e^{-\alpha_{1c}(r-R_o)} e^{-n^2 t^2} \sin(\omega_{1c} t - k_{1c} r) \right] \\ * \left[\frac{1}{\pi \left(\frac{a}{c_o} \sin \theta \right)^2} \text{circ} \left(\frac{t}{\frac{a}{c_o} \sin \theta} \right) \right] \quad (A.22)$$

In the frequency domain, the off-axis solution is found by substituting Eqs. (A.4) and (A.21) into Eq. (A.3) and can be written as

$$\begin{aligned}
P_1(r, \theta, f) = & \frac{R_0}{2jr} P_0 e^{-\alpha_{1c}(r-R_0)} e^{-jk_{1c}r} \\
& \times \frac{\sqrt{\pi}}{n} \left\{ \exp \left[- \left(\frac{\pi}{n} \right)^2 (f_1 + f_{1c})^2 \right] - \exp \left[- \left(\frac{\pi}{n} \right)^2 (f_1 - f_{1c})^2 \right] \right\} \\
& \times \left[\frac{2J_1(k_1 a \sin \theta)}{k_1 a \sin \theta} \right] \quad . \quad (A-23)
\end{aligned}$$

Recall that n is expressed by Eq. (A.16) or Eq. (A.18).

The spectral distortion of a Gaussian pulse transmission as a function of off-axis angle may be studied by computing the normalized power spectral density function given by

$$P_{1xxN}(f) = \frac{P_1(r, \theta, f) P_1^*(r, \theta, f)}{P_1(r, 0, f_{1c}) P_1^*(r, 0, f_{1c})} \quad . \quad (A.24)$$

Using Eq. (A.23) and n defined by Eq. (A.18), the normalized power spectral density function becomes

$$\begin{aligned}
P_{1xxN}(f) = & \left[\frac{2J_1(k_1 a \sin \theta)}{k_1 a \sin \theta} \right]^2 \\
& \times \left\{ \exp \left[- \left(\frac{\pi Q_1}{2.668 f_{1c}} \right)^2 (f_1 + f_{1c})^2 \right] - \exp \left[- \left(\frac{\pi Q_1}{2.668 f_{1c}} \right)^2 (f_1 - f_{1c})^2 \right] \right\}^2 \\
& \times \left\{ \exp \left[-4 \left(\frac{\pi Q_1}{2.668} \right)^2 \right] - 1 \right\}^{-2} \quad . \quad (A.25)
\end{aligned}$$

Further analysis of the off-axis spectral distortion is considered for the set of parameter values given in Table A.1. These parameter values are comparable with those which were attained in the experimental study of the broadband parametric array discussed in Section IV. The results that are presented in this appendix may be compared with both experimental and theoretical results given in Section IV to determine the differences between linear and parametric implementations of broadband sources with similar characteristics. Figure A.2 shows the normalized power spectral density function plotted as a function of frequency for various off-axis angles and a Gaussian pulse with a Q_1 of 10.91. This value of Q_1 is often attained for transducers used in underwater applications. On axis, the spectrum is symmetric about the carrier or center frequency with a half-power bandwidth of 6.05 kHz. As the off-axis angle is increased, the relative spectral power level decreases and the spectral peak shifts downward in frequency for off-axis angles up to 1.50° . It should be noted that data at 1.50° are not shown in the figure. This results because the level at the spectral peak at this angle is less than -20 dB. Between 1.50° and 2.00° the relative spectral power level increases and the spectral peak shifts upward in frequency to a value higher than the carrier frequency. As the off-axis angle increases from 2.00° to 2.75° , the spectral peak again shifts downward in frequency with a decrease in the relative power level. These characteristics result from the interaction of the relatively narrowband signal with the lobe structure of the off-axis power transfer function shown in Fig. A.1.

The frequency at the spectral peak is determined from the normalized power spectral density function, Eq. (A.25), and shown as a function of normalized off-axis angle in Fig. A.3. The angular axis is in units of the half-power angle. The data in Fig. A.3 correspond with that in Fig. A.2 and initially indicate a downward shift in the frequency at the spectral peak for increasing off-axis angle. Included in this figure is the relative power level at each spectral peak, which is also computed from Eq. (A.25) and indicates the energy or power beam

TABLE A.1
EXAMPLE PARAMETER VALUES FOR RADIATION FROM A
CIRCULAR PISTON

Carrier or center frequency, f_{1c}	66.0 kHz
Speed of sound, c_o	1480 m/sec
Piston radius, a	53 cm
Half-power beamwidth at 66 kHz, θ_{HP}	1.24°
Primary transmission quality factor, Q_1	10.91 or 1.2
Half-power angle at 66 kHz, θ_{3dB}	0.62°

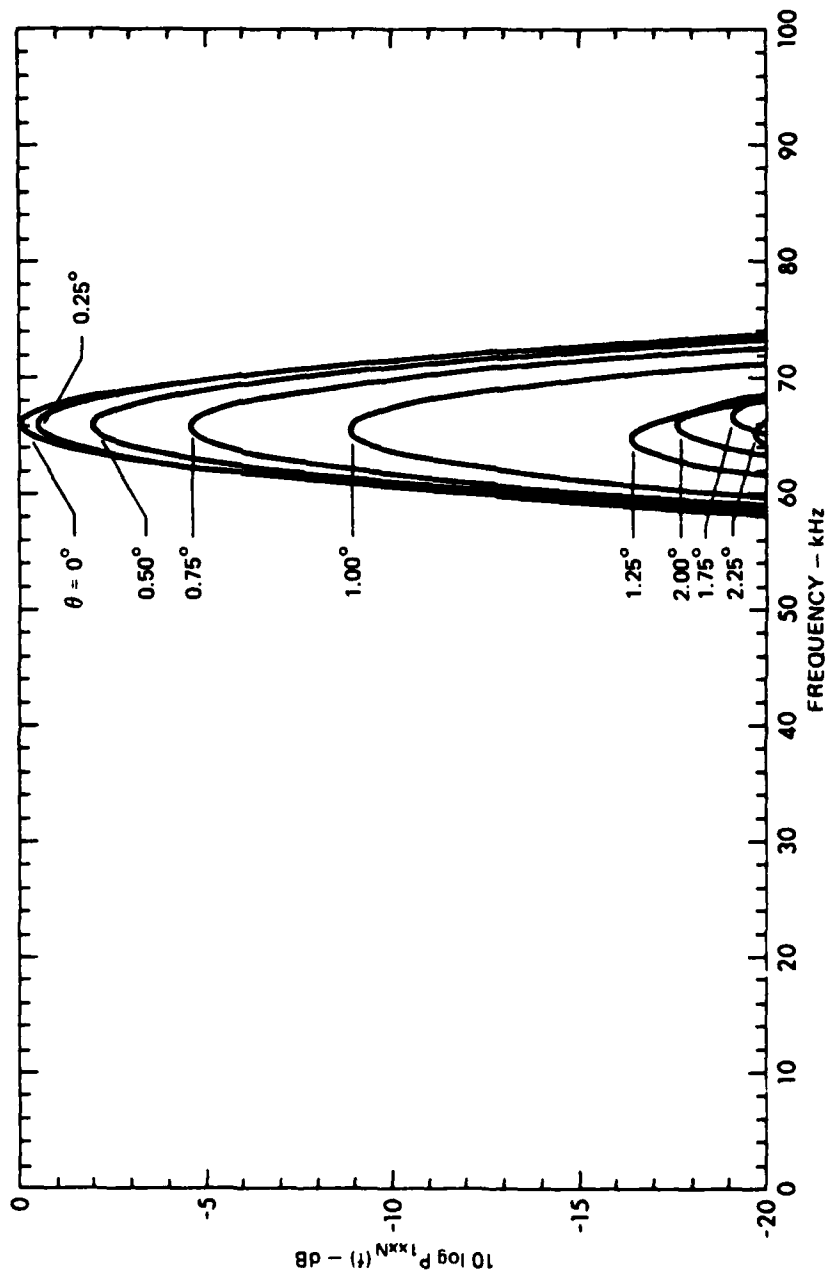


FIGURE A.2
NORMALIZED POWER DENSITY SPECTRA PREDICTED FOR A
CIRCULAR PISTON AT OFF-AXIS ANGLES FROM 0.00° TO 2.25°
 $f(t)$ - GAUSSIAN, $f_{1c} = 66 \text{ kHz}$, $Q_1 = 10.91$, $a = 53 \text{ cm}$, FARFIELD

ARL:UT
 AS-81-586
 JMH - GA
 6 - 16 - 81

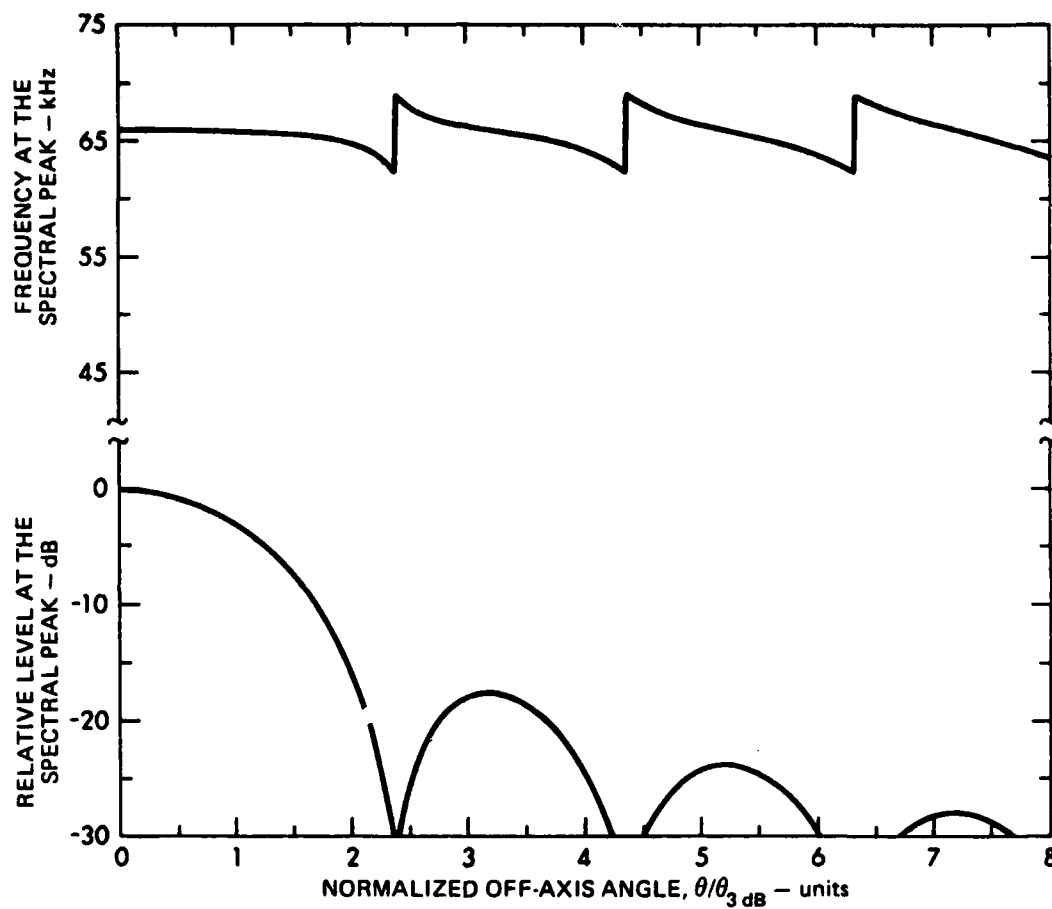


FIGURE A.3
FREQUENCY AND LEVEL AT THE SPECTRAL PEAK
PREDICTED OFF-AXIS FOR A CIRCULAR PISTON

$f(t)$ - GAUSSIAN, $f_{1c} = 66 \text{ kHz}$, $Q_1 = 10.91$
 $a = 53 \text{ cm}$, FARFIELD, $\theta_{3\text{ dB}} = 0.62^\circ$

pattern for the transmission. When the relative power level at the spectral peak has decreased 3 dB, the frequency at the spectral peak has shifted downward about 2.0% to a value of approximately 64.7 kHz. This occurs at an off-axis angle of about 0.62° ($\theta_{3\text{ dB}}$), which is the half-power angle at the carrier. The frequency at the spectral peak shifts downward to about 62.0 kHz, or about 6.0% at an angle of 1.49° ($2.4 \theta_{3\text{ dB}}$), where the frequency shifts discontinuously upward to about 69.0 kHz, or about 6.0% with respect to the carrier frequency. The discontinuous shift upward in frequency at the spectral peak results from passing through a null in the off-axis power transfer function. The Gaussian pulse transmission with a Q_1 of 10.91 is sufficiently narrow-band so that nulls in the power transfer function dominate the behavior of the off-axis power density spectra. The frequency of the spectral peak again decreases from 1.49° and attains the value of the carrier frequency at an angle corresponding to a peak of a lobe in the off-axis transfer function. The frequency of the spectral peak continues to decrease until the next null in the off-axis transfer function becomes dominant. The trend that has been described then repeats for additional nulls.

The normalized power spectral density function as a function of frequency and off-axis angle for a Gaussian pulse transmission with a Q_1 of 1.2 is shown in Fig. A.4. This value of Q_1 is difficult to attain in practice but serves to demonstrate the characteristics of a broadband linear transmission that are comparable with those of the broadband parametric transmission with a constant Q_2 of 1.2. On axis, the power density spectrum is symmetric about the carrier frequency with a half-power bandwidth of 55.0 kHz. As in the example for a Q_1 of 10.91, the relative power levels decrease and the spectral peak shifts downward in frequency as the off-axis angle increases. This trend continues and does not reverse as noted for the higher Q_1 case. The influence of lobes in the off-axis transfer function is clearly evident at off-axis angles of 1.50° ($2.4 \theta_{3\text{ dB}}$) and greater; however, the Q_1 of the Gaussian pulse transmission is sufficiently low that the relative

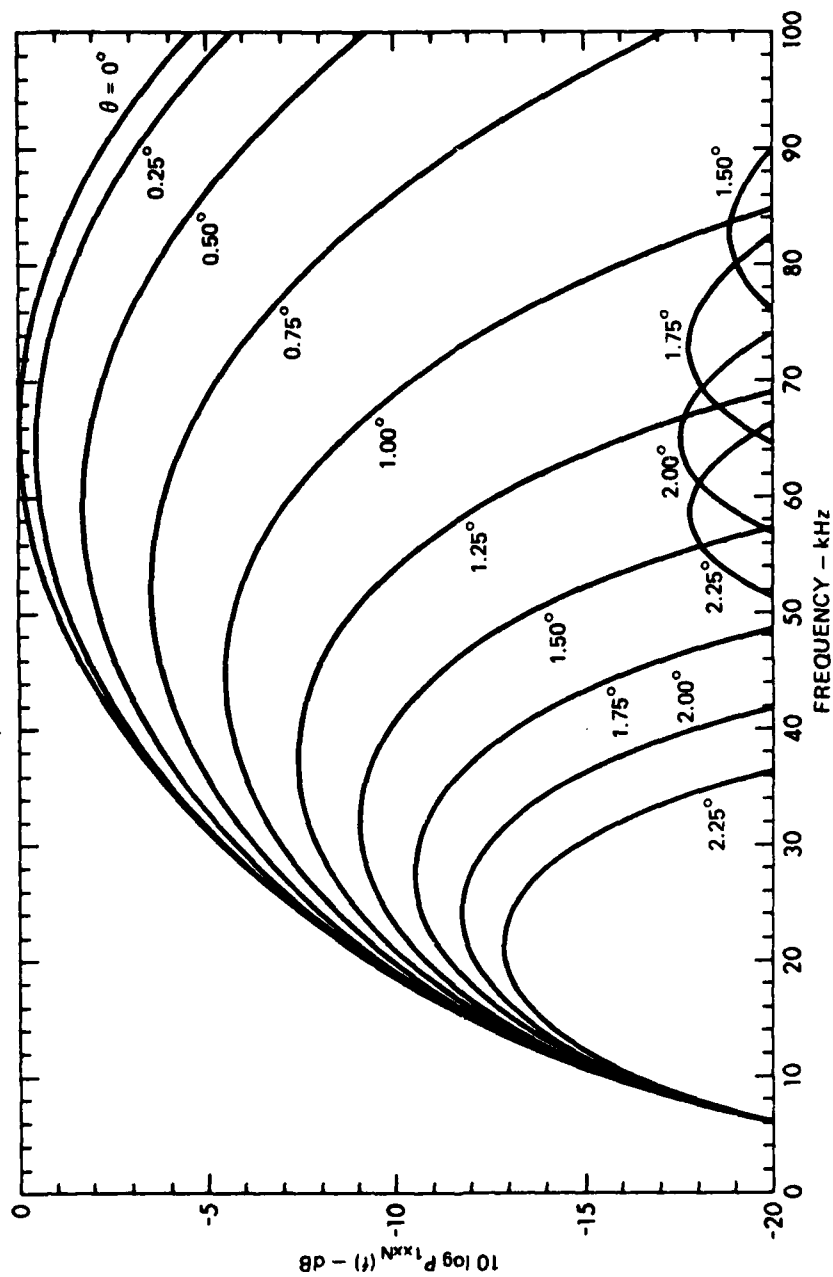


FIGURE A.4
 NORMALIZED POWER DENSITY SPECTRA PREDICTED FOR A
 CIRCULAR PISTON AT OFF-AXIS ANGLES FROM 0.00° TO 2.25°
 $f(t)$ - GAUSSIAN, $f_{1c} = 66 \text{ kHz}$, $Q_1 = 1.2$, $a = 53 \text{ cm}$, FARFIELD

ARL:UT
 AS-81-588
 JMH - GA
 6 - 16 - 81

spectral power is greater at lower frequencies. By comparison with the high Q_1 transmission, the spectral peak shifts downward more rapidly for the low Q_1 transmission, but the decrease in relative power levels is less rapid as a function of off-axis angle. These trends are more explicit in Fig. A.5 where the frequency at the spectral peak from Eq. (A.27) and the relative power levels at each frequency from Eq. (A.25) are plotted as a function of off-axis angle. For the lower Q_1 case, the frequency at the spectral peak and the relative spectral power level both decrease with increasing off-axis angle to about 3° ($4.8 \theta_{3\text{ dB}}$) where the frequency at the spectral peak shifts discontinuously. This is the same trend as noted for the higher Q_1 transmission in Fig. A.3; however, the frequency shifts are greater and the level at the spectral peak is monotonically decreasing with increasing off-axis angle. This trend indicates the dominance of the properties of the relatively low Q_1 transmission over those of the off-axis power transfer function. When the relative power level at each spectral peak off-axis has decreased 3 dB, the frequency at the spectral peak has shifted downward about 18.2% from the on-axis value (66 kHz) to a value of about 54.0 kHz. This occurs at an off-axis angle of about 0.68° , which is about 10% greater than the half-power angle of the carrier. At a relative power level of -10 dB, the frequency at the spectral peak has shifted downward about 56.0% to a value of 29.0 kHz. This occurs at an angle of 1.7° , which is greater than the half-power angle at the carrier by a factor of about 2.7.

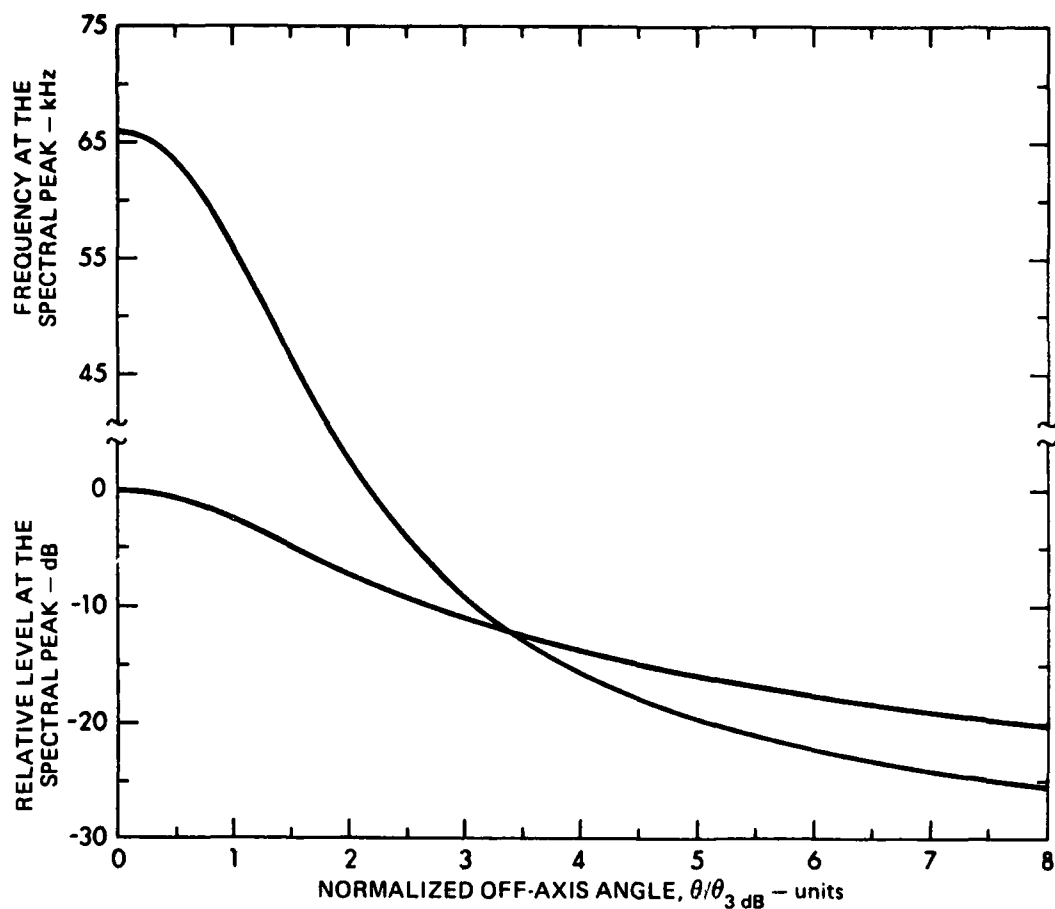


FIGURE A.5
FREQUENCY AND LEVEL AT THE SPECTRAL PEAK
PREDICTED OFF-AXIS FOR A CIRCULAR PISTON

$f(t)$ - GAUSSIAN, $f_{1c} = 66$ kHz, $Q_1 = 1.2$
 $a = 53$ cm, FARFIELD, $\theta_{3\text{ dB}} = 0.62^\circ$

ARL:UT
 AS-81-589
 JMM - GA
 6 - 16 - 81

APPENDIX B
EXPERIMENTAL EQUIPMENT

Details regarding the design, construction, and performance of special purpose experimental equipment are discussed in this appendix. Included in this discussion are individual electronic devices, electro-mechanical transducers, and subsystem performance.

A. Transmit Section

A block diagram of the transmit section is shown in Fig. B.1. The signal source at 600 kHz is an HP3330B frequency synthesizer which is input to the shaped pulse generator. A detailed description of the basic components of the transmit section follows.

1. Shaped Pulse Generator. The shaped pulse generator allows the production of pulsed carrier transmissions with selectable envelope shapes and durations.

A block diagram of the shaped pulse generator is shown in Fig. B.2. The central element is a programmable read only memory (PROM) which is used to store symmetric but otherwise arbitrary bandlimited envelope shapes. One half of the envelope is stored in the PROM. The complete envelope is formed by sequentially addressing all locations in the PROM first in the forward direction and then in reverse. The locations are addressed by a set of up/down counters that are incremented by a clock, which is part of a timing and synchronization circuit. The frequency of the shape clock determines the duration of the envelope, which varies from 5 μ sec to 10 msec. Another portion of the timing and synchronization circuit controls the pulse repetition rate, which may be adjusted from 10 pulses/sec to 5000 pulses/sec, or may be externally adjusted. The pulse repetition rate trigger may be synchronized with either the initiation of an envelope sequence or with the carrier frequency.

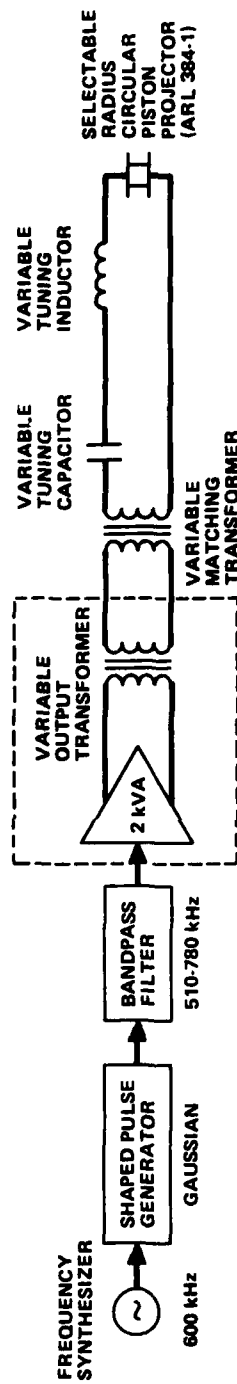


FIGURE B.1
TRANSMITTER

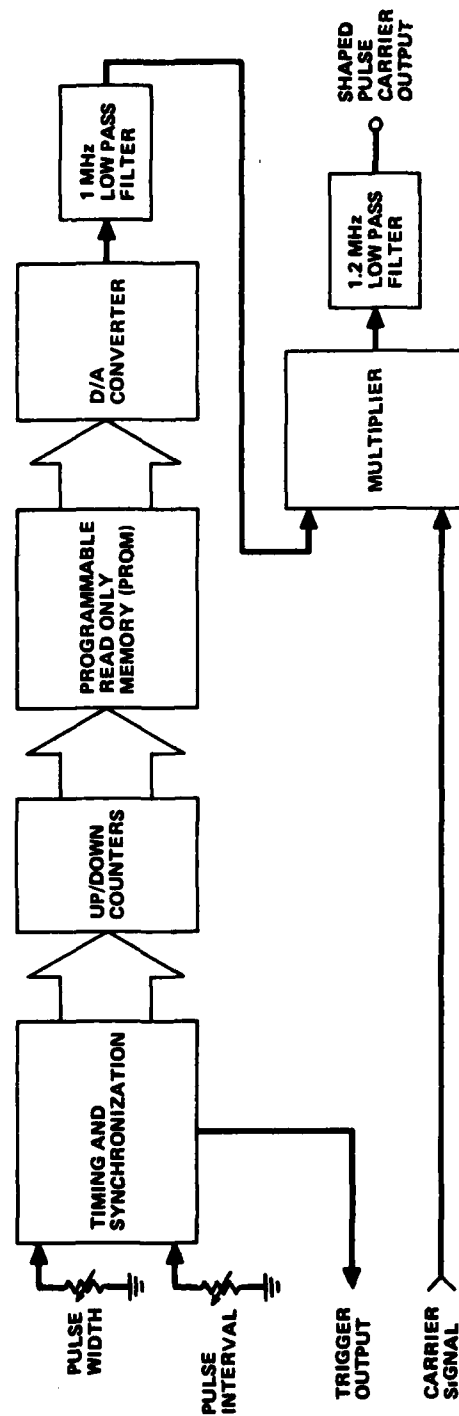


FIGURE B.2
BLOCK DIAGRAM OF SHAPED PULSE SIGNAL GENERATOR

The output of the PROM is input to a D/A converter, which provides a baseband analog envelope. This signal is coupled to a 1.0 MHz low pass filter to reduce the switching noise that is common in high speed digital circuitry. The filtered baseband envelope signal is multiplied by a carrier wave to produce a shaped carrier pulse. This pulse is input to a 1.2 MHz low pass filter for further noise reduction.

2. Power Amplifier. The output of the shaped pulse generator is passed through a bandpass filter for further noise reduction and coupled to an LPPV5-4X, 2000 V·A power amplifier. This power amplifier is a solid state design with eight 250 V·A channels. A variable impedance output transformer is achieved through various series and parallel combinations of individual output transformers from each channel. The resultant impedance range is from 1.5 to 192 Ω in eight steps. The output of the power amplifier is coupled to the projector through an additional impedance matching transformer and tuning elements to provide maximum power transfer for each configuration of the projector array.

3. Source Transducer. The source transducer (ARL 384-1) was designed to allow the formation of parametric arrays for both plane wave (approximately) and nonplane wave fields.

a. Transducer Design. The active transducer elements are 12 concentric circular rings and a center piston which are driven in the thickness mode and may be selectively driven electrically to form pistons of different radii. The ceramic rings have a thickness of 0.32 cm and are equally spaced with a radial width of 0.56 cm. The rings and the center piston were constructed from four polarized squares of Channelite 5400 ceramic, 8.89 cm on a side. The individual squares were separated by 0.08 cm, arranged into a larger composite square, and mounted on a flat surface. Using circular cutting tools with different radii, the concentric rings and the center piston were cut by grinding away a 0.08 cm thickness using carborundum grit mixed with water. This technique allowed the ceramic to be cut without depolarization. The

ceramic pieces were placed face down on a flat surface, separated by 0.08 cm of corprene, and reconstructed electrically into concentric rings and a center piston. This array was then bonded to a 0.64 cm thickness of corprene. The face of the array was electrically tied in common while each ring and the center piston were wired separately on the back side of the array. The array was mounted in an aluminum housing with an opening of 21.59 cm. Electrically separate portions of the array were transferred through feedthrus to an air space in the housing behind the array where they were coupled to 15.24 m of Alpha 1120, 28 ga, stranded, twisted pair, shielded cable. The 13 separate cables were run through 15 m of 1.91 cm i.d. Nalgon tubing. The array space in the housing was covered with an acoustically transparent window 0.32 cm thick, made from Products Research and Chemical Corporation No. 1527 polyurethane and filled with castor oil. Several views of the selectable radius circular piston projector are shown in Fig. 4.2. Each of the cables which represent the sections of the array are terminated on barrier strips. A selected radius piston is driven by summing appropriate array sections in parallel.

b. Transducer Performance. The performance of the selectable radius circular piston projector was evaluated at Lake Travis Test Station (LTTTS) using calibration equipment common to acoustical measurement facilities. The accuracy on amplitude measurements is assumed to be at least ± 1 dB.

The transmit voltage response for the transducer was measured at low level using a NRL/USRD E-8 standard transducer as a hydrophone at a distance of 11.7 m. The transmit voltage response is shown in Fig. B.3 for the center piston alone, and for the large piston formed by summing all array sections in parallel. For the center piston alone, the maximum response is about 188 dB re 1 μ Pa/Vrms at 1 m, which occurs near the thickness mode resonance frequency at 600 kHz. Far below resonance the response generally increases at 6 dB per octave with increasing frequency; however, the variability in the curve indicates

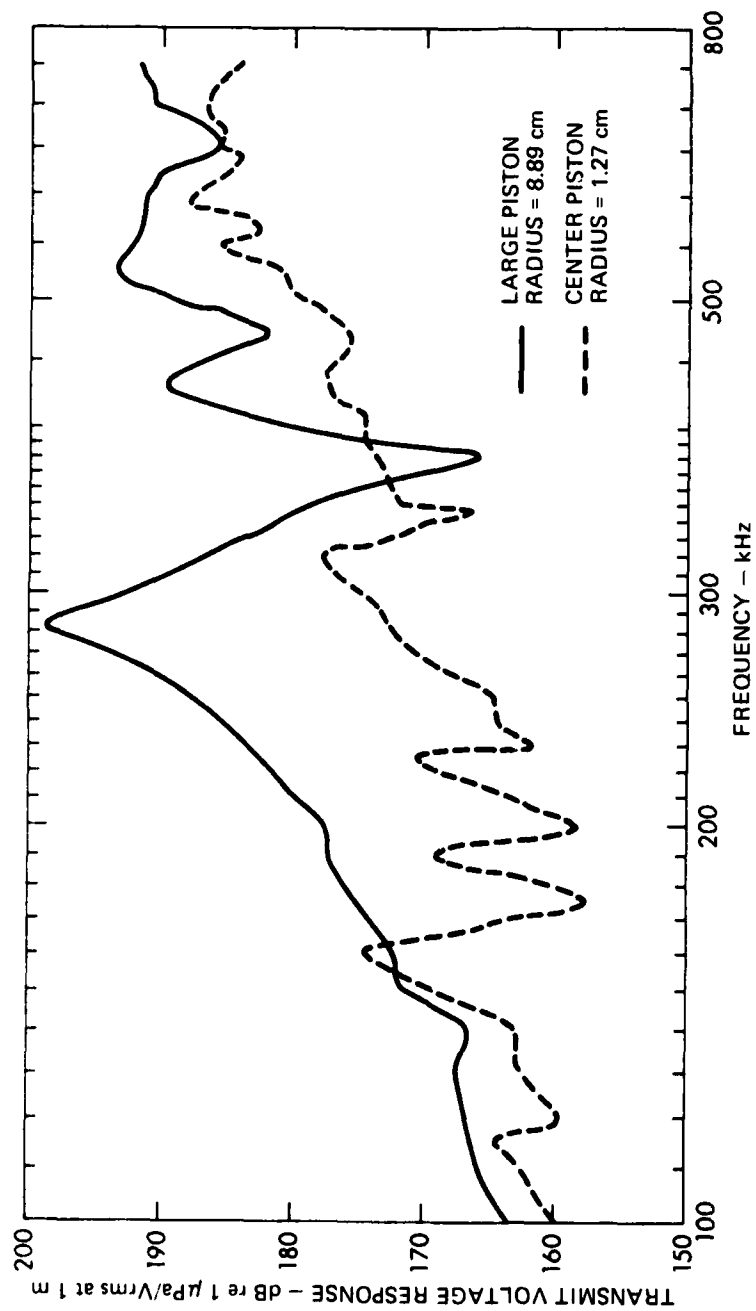


FIGURE B.3
TRANSMIT VOLTAGE RESPONSE FOR THE SELECTABLE
RADIUS CIRCULAR PISTON PROJECTOR (ARL 384-1)

ARL:UT
AS-80-1725
JMH - GA
10 - 24 - 80

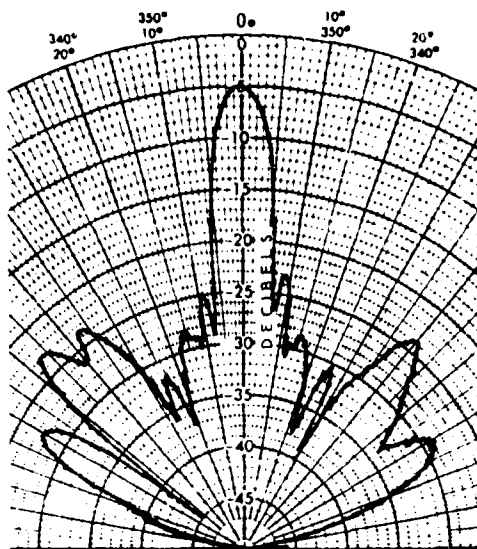
coupling of other modes in the ceramic. This performance is common in high frequency underwater transducers. The response for the large piston has similar behavior except for a peak at about 280 kHz and a minimum at about 380 kHz. These features are caused by a radial mode that results from the equal spacing of the concentric rings and which couples to the thickness mode of the ceramic.

The directional properties of the selectable radius circular piston transducer were evaluated with a 0.5 msec pulsed carrier at 600 kHz. Measurements were made at a range of 11.7 m, which is $1.16 R_0$ for the piston with the largest radius. Beam patterns as a function of radius are shown in Figs. B.4-B.7. The sidelobe structure in the beam patterns is uniform and symmetric. There are grating lobes in each of the patterns due to the 2.5λ center-to-center spacing between the concentric rings, but these spacing lobes are not a problem in terms of parametric operation. The beam patterns were also recorded as a linear function of angle. The half-power beamwidths are given in Table IV.2 with the corresponding theoretical values assuming a circular piston set in an infinite rigid baffle.

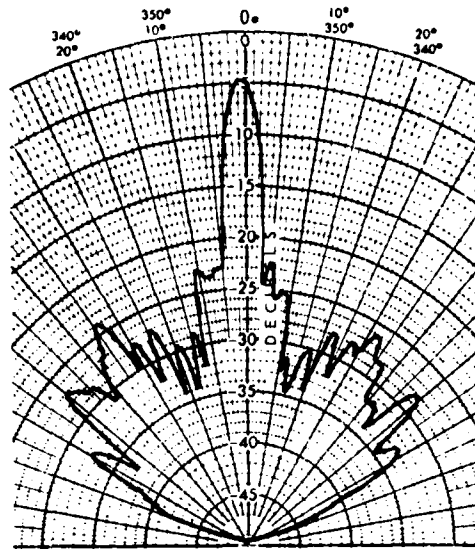
The impedance of the transducer and cable was measured at low level underwater loaded conditions. These measurements are provided in Table B.1.

B. Receive Section

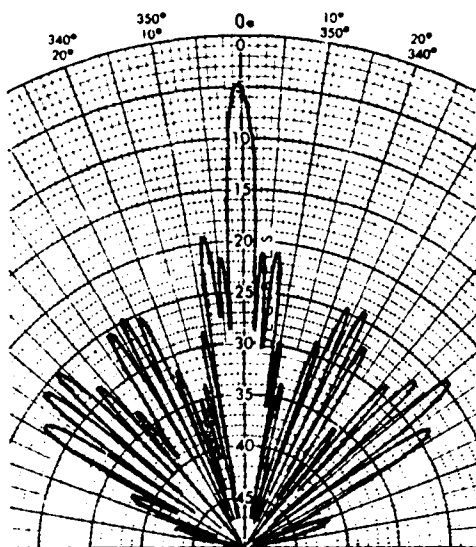
A block diagram of the signal conditioning portions of the receive section is shown in Fig. B.8. The ARL 239-1 hydrophone is used for all of the single channel measurements. Its output is coupled to a preamplifier directly when measuring primary signal characteristics and indirectly through a low pass filter to remove remaining signals at the primary frequency when measuring secondary signal characteristics. The USRL-E-27-130P is used only for cross signal analysis in the secondary band and is coupled to a preamplifier through a voltage follower and a



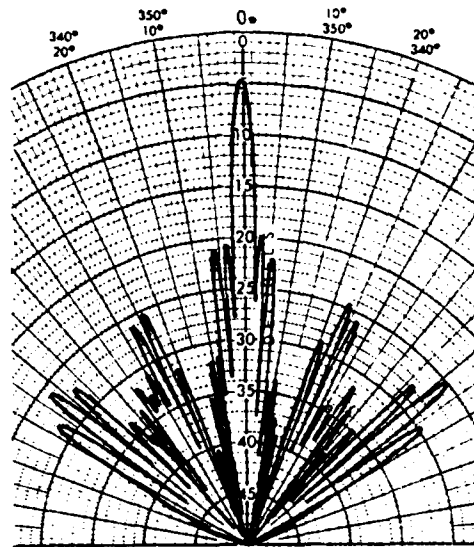
RADIUS = 1.27 cm



RADIUS = 1.91 cm

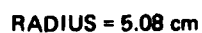
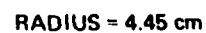
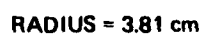


RADIUS = 2.54 cm

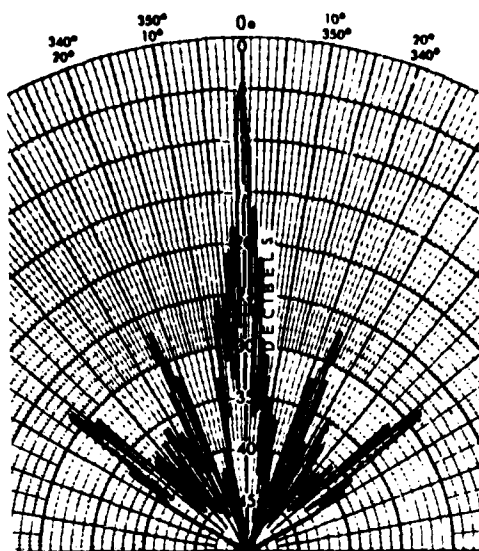


RADIUS = 3.18 cm

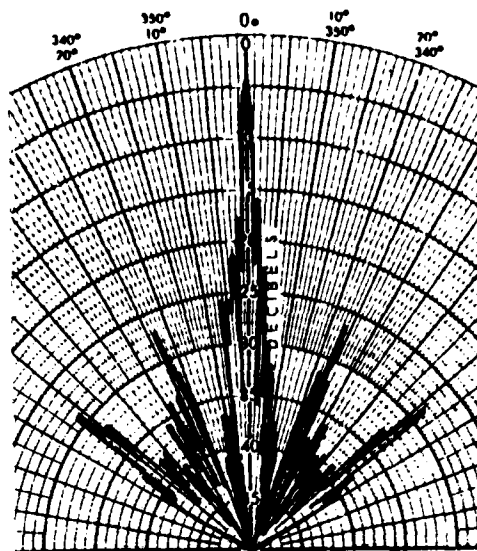
FIGURE B.4
600 kHz PRIMARY FREQUENCY BEAM PATTERNS MEASURED AT 11.7 m FOR
THE SELECTABLE RADIUS CIRCULAR PISTON PROJECTOR (ARL 384-1)
RADII = 1.27 - 3.18 cm



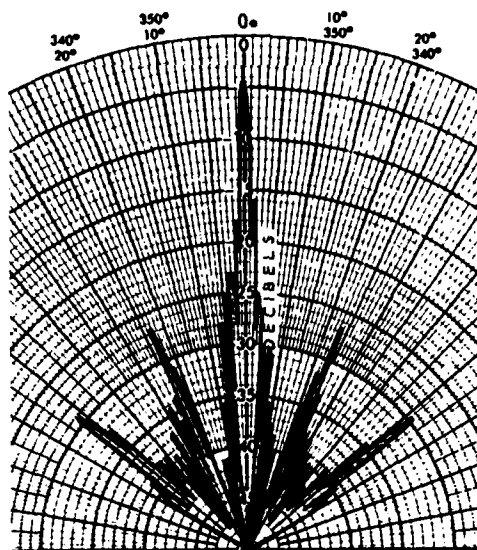
RADII = 3.81 - 5.08 cm



RADIUS = 5.72 cm

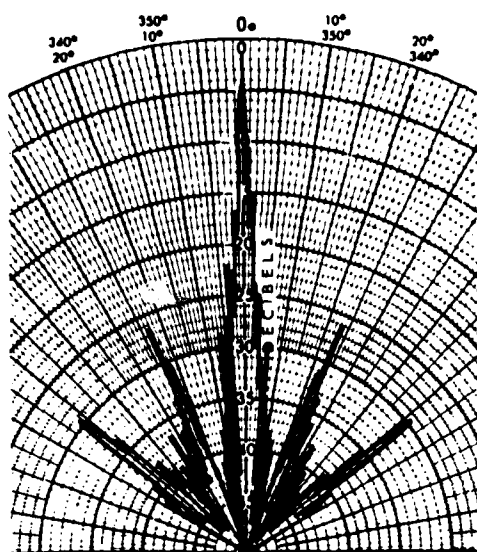


RADIUS = 6.35 cm

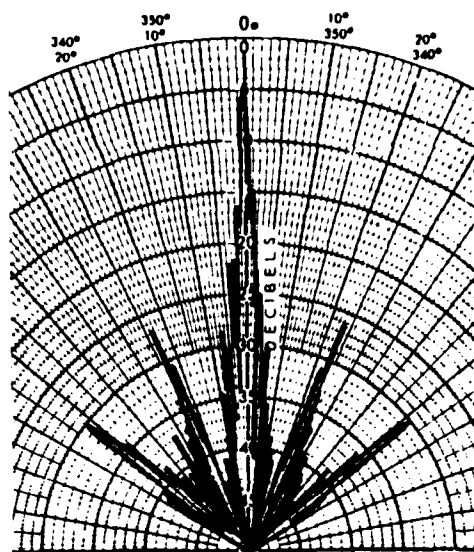


RADIUS = 6.99 cm

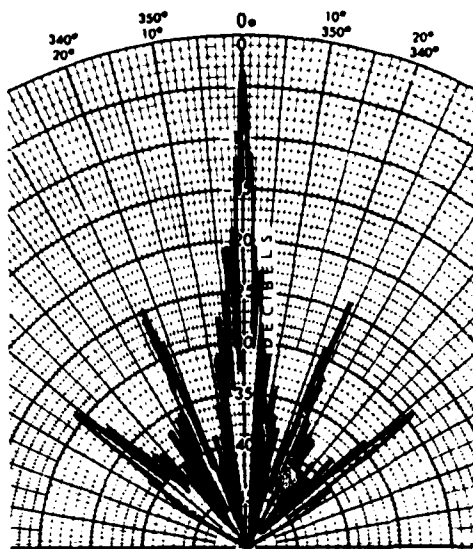
FIGURE B.6
600 kHz PRIMARY FREQUENCY BEAM PATTERNS MEASURED AT 11.7 m FOR
THE SELECTABLE RADIUS CIRCULAR PISTON PROJECTOR (ARL 384-1)
RADI = 5.72 - 6.99 cm



RADIUS = 7.62 cm



RADIUS = 8.26 cm

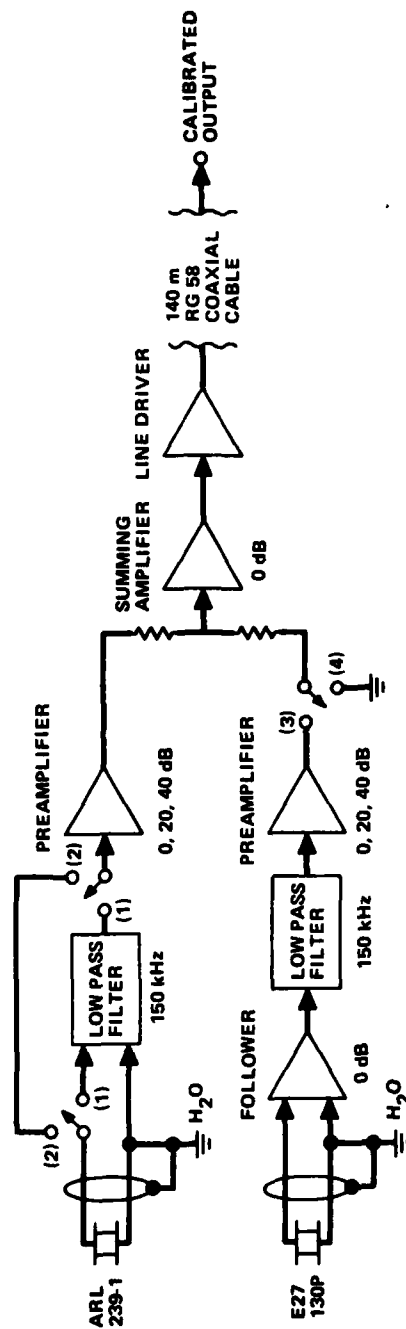


RADIUS = 8.89 cm

FIGURE B.7
600 kHz PRIMARY FREQUENCY BEAM PATTERNS MEASURED AT 11.7 m FOR
THE SELECTABLE RADIUS CIRCULAR PISTON PROJECTOR (ARL 384-1)
RADII = 7.62 - 8.89 cm

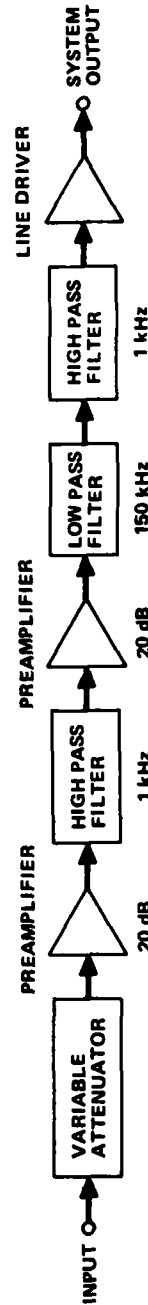
TABLE B.1
ELECTRICAL PROPERTIES AT LOW LEVEL OF THE SELECTABLE
RADIUS CIRCULAR PISTON PROJECTOR (ARL 384-1) AT 600 kHz

<u>Radius (cm)</u>	<u>Magnitude of Impedance (Ω)</u>	<u>Phase Angle (deg)</u>
1.27	35.8	-22.5
1.91	21.0	-18.0
2.54	16.7	- 2.0
3.18	13.8	9.0
3.81	12.9	22.5
4.45	12.5	35.6
5.08	11.7	48.0
5.72	11.5	53.4
6.35	11.4	56.4
6.99	11.4	59.7
7.62	11.4	62.4
8.26	11.4	64.5
8.89	11.4	68.1



POSITIONS
 (1) AND (4) ARL 239-1 LOW FREQUENCY RECEIVER (LFR)
 (2) AND (4) ARL 239-1 HIGH FREQUENCY RECEIVER (HFR)
 (1) AND (3) ARL 239-1 AND E27-130P SUMMED (LFR)

(a)



(b)

FIGURE B.8
 RECEIVE SYSTEMS

low pass filter. The outputs of the two hydrophone channels, which are separated in time by the physical orientation of the hydrophones, are summed and driven through a 140 m length of RG58 coaxial cable. The hydrophones are calibrated as receive systems at the cable output. The calibrated output is coupled to a final set of preamplifiers and filters that are detailed in Fig. B.8(b) and complete the signal conditioning.

The linearity of the high frequency receive system was evaluated by introducing a calibrated tone at 600 kHz at the input to the preamplifier in Fig. B.8(a). The results were recorded at the system output in Fig. B.8(b). These data are shown in Fig. B.9, which indicates good linearity; show a system output of about +5 dB re 1 V_p.

1. Hydrophones. Two probe hydrophones were used to measure the sound field produced by the broadband parametric array. The frequency range of interest is from about 10 to 150 kHz in the secondary band and around 600 kHz in the primary band. Hydrophones which were selected are small in aperture so that the angle subtended by the hydrophone connection is small and the ability to determine subtle changes in signal characteristics as a function of angle is retained. These hydrophones are also operated well below resonance in the secondary band to provide a frequency response that is reasonably uniform.

a. ARL 239-1 Hydrophone. The ARL 239-1 hydrophone is the principal receiving array used to obtain experimental data; it was used for all single channel measurements in both the primary and secondary frequency bands.

The ARL 239-1 hydrophone consists of five radially polarized Channelite 5500 ceramic cylinders. Each ceramic cylinder is 1.14 cm o.d., 0.09 cm in height, with a wall thickness of 0.13 cm. The ceramic cylinders are stacked with 0.01 cm spacers of onion skin paper and are electrically coupled in parallel. The ceramic stack is acoustically loaded on each end with corprene and mounted on a 0.44 cm diam stainless

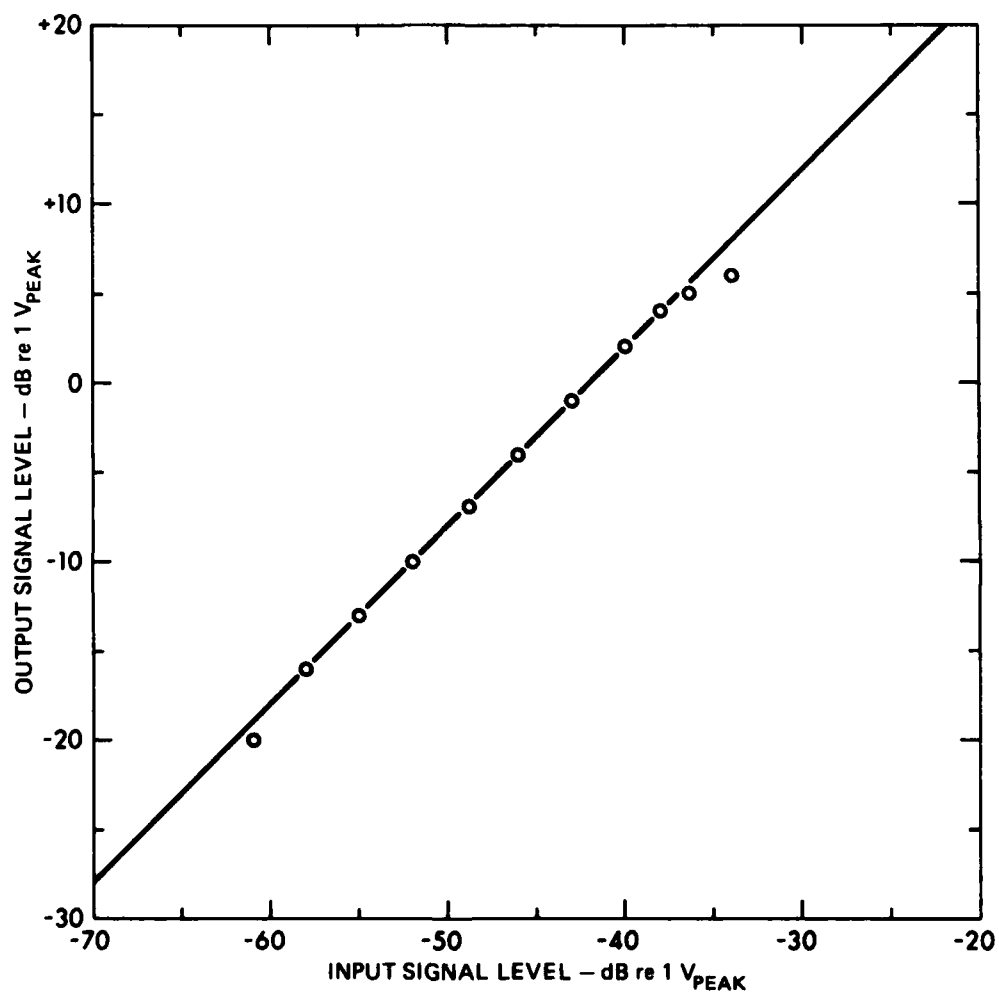


FIGURE B.9
CHARACTERISTICS OF THE HIGH FREQUENCY RECEIVE SYSTEM
 $f = 600 \text{ kHz}$, SYSTEM GAIN = 40 dB

ARL:UT
AS-81-673
JMH-GA
6-16-81

steel shaft. The assembly is covered with Emerson and Cummings CPC-16 polyurethane. The electrical connections are run through the stainless steel shaft and coupled to 12.19 m of Belden 4548 twisted pair, shielded cable.

The freefield voltage sensitivity at the hydrophone output for both the low and the high frequency bands is shown in Figs. B.10 and B.11, respectively. The resonance frequency for the radial mode of the ceramic is about 1 MHz. The sensitivity in the low frequency band varies about 5 dB from 10 to 70 kHz and has a broad peak centered at about 100 kHz. This peak results from a coupled secondary mode in the ceramic. The sensitivity in the high frequency band varies about 10 dB from 350 to 600 kHz but is reasonably flat from 600 to 1000 kHz. Low frequency and high frequency calibrated receive systems were constructed according to Fig. B.8(a). The freefield voltage sensitivity for the low frequency and high frequency receive systems is given in Figs. B.12 and B.13, respectively. Subtle differences in frequency response are noted between the data for the low frequency hydrophone and receive system. These differences result from the interaction of the low pass filter and the hydrophone. The hydrophone output is buffered by an amplifier with a high input impedance in the high frequency receiver; therefore there is little change in the frequency response of the high frequency hydrophone and the receiver system.

A farfield directivity pattern at 150 kHz is shown in Fig. B.14. This pattern was measured at a range of 11.7 m in the plane normal to the axis of the cylinder. This pattern shows only a 1 dB variation over 360°, which is excellent for a probe hydrophone.

b. USRD-E27-130P. The USRD-E27-130P was used only for cross signal experimental analysis. This hydrophone is a U. S. Navy standard and is composed of seven PZT discs, 3.17 mm in diameter and 1.52 mm in thickness, which are spaced inside an 11.1 mm diam circle. The discs are cemented directly to a butyl acoustic window and air backed.

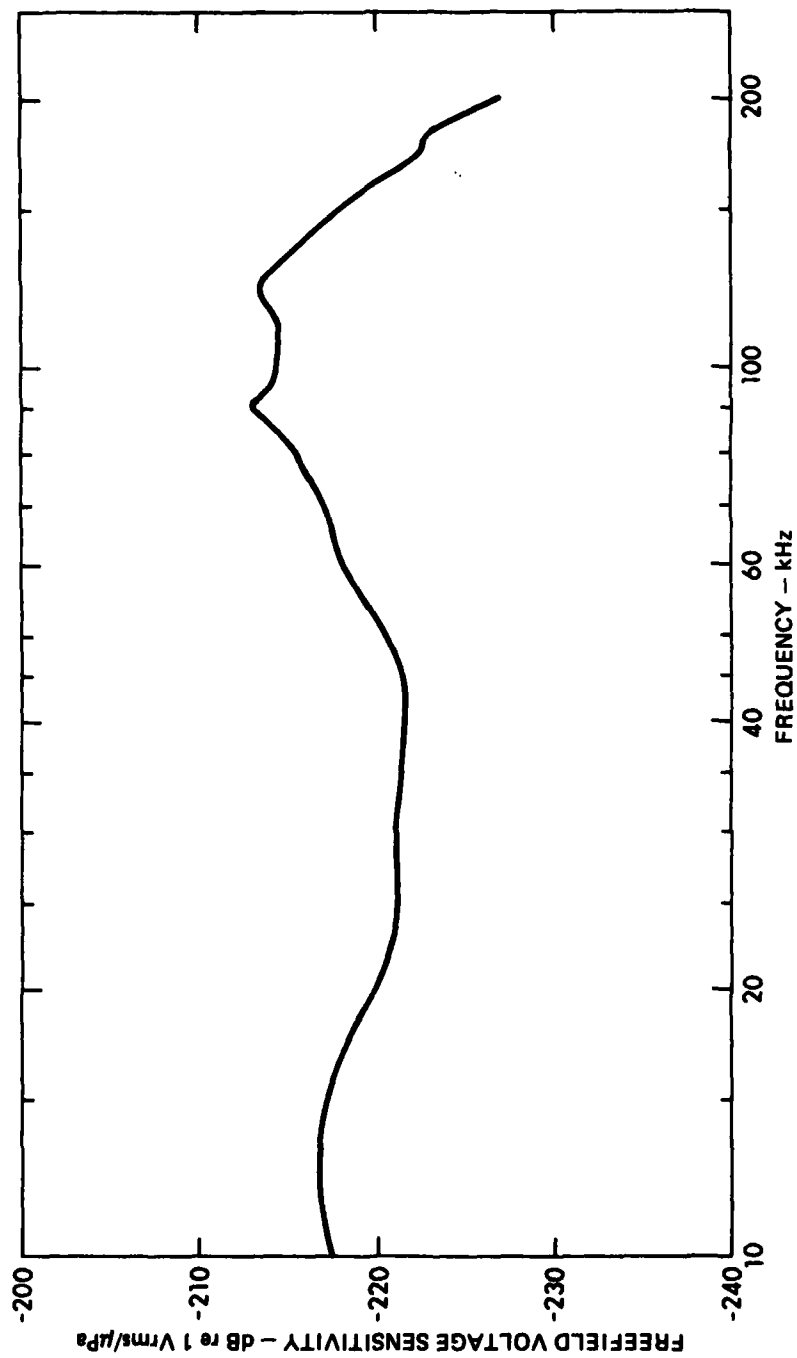


FIGURE B.10
FREEFIELD VOLTAGE SENSITIVITY, ARL 239-1 HYDROPHONE
(LOW FREQUENCY)

ARL:UT
AS-80-1726
JMH - GA
10-27-80

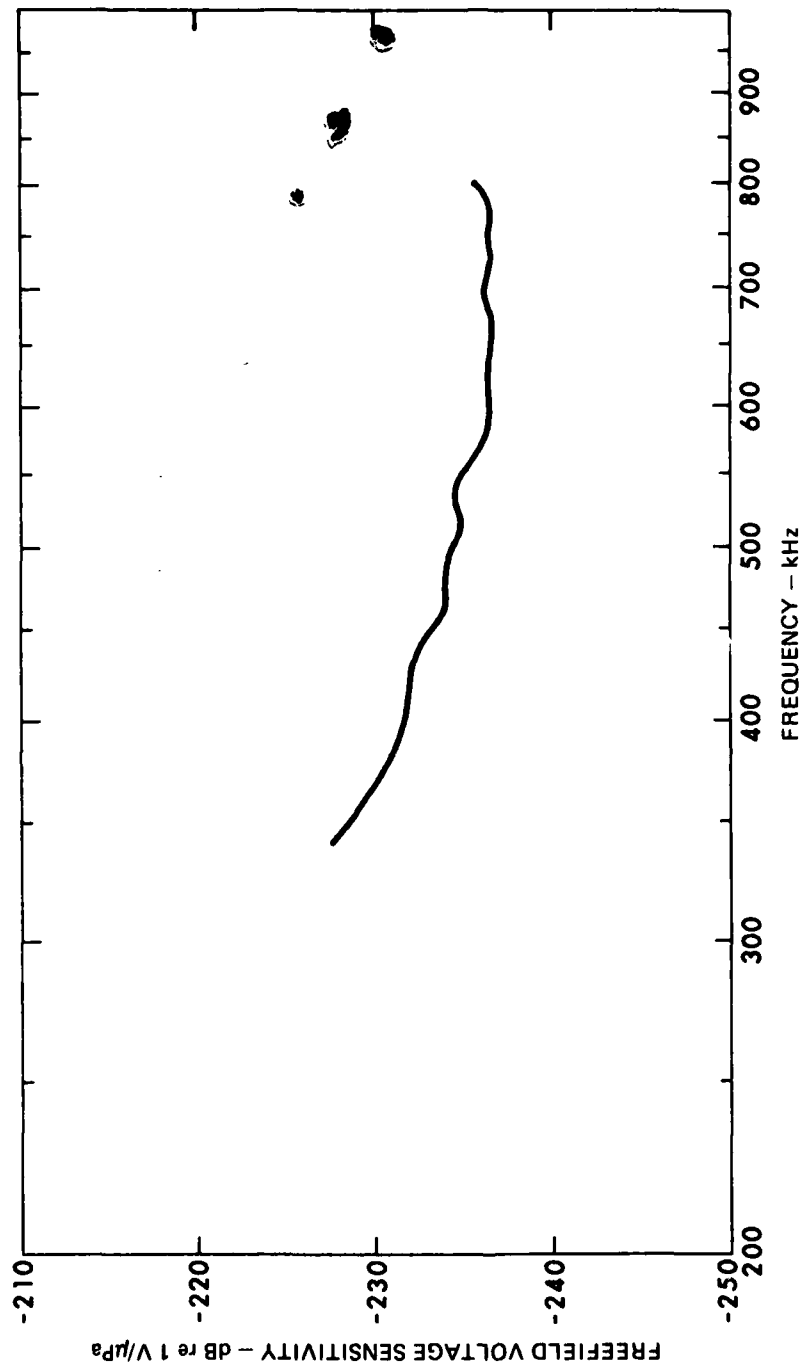


FIGURE B.11
FREEFIELD VOLTAGE SENSITIVITY FOR THE ARL 239-1 HYDROPHONE
(HIGH FREQUENCY)

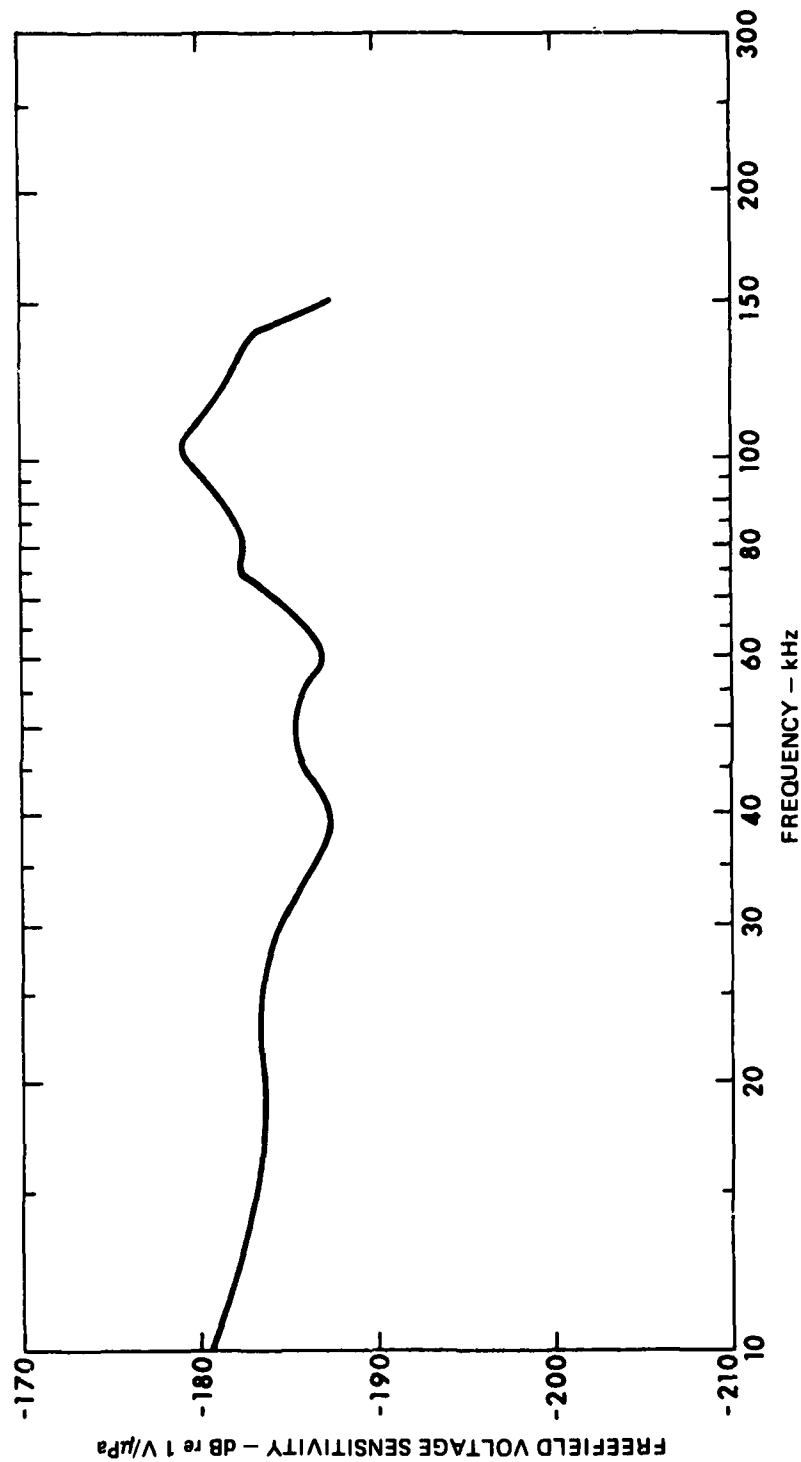


FIGURE B.12
FREEFIELD VOLTAGE SENSITIVITY FOR THE ARL 239-1
LOW FREQUENCY RECEIVER WITH 40 dB GAIN

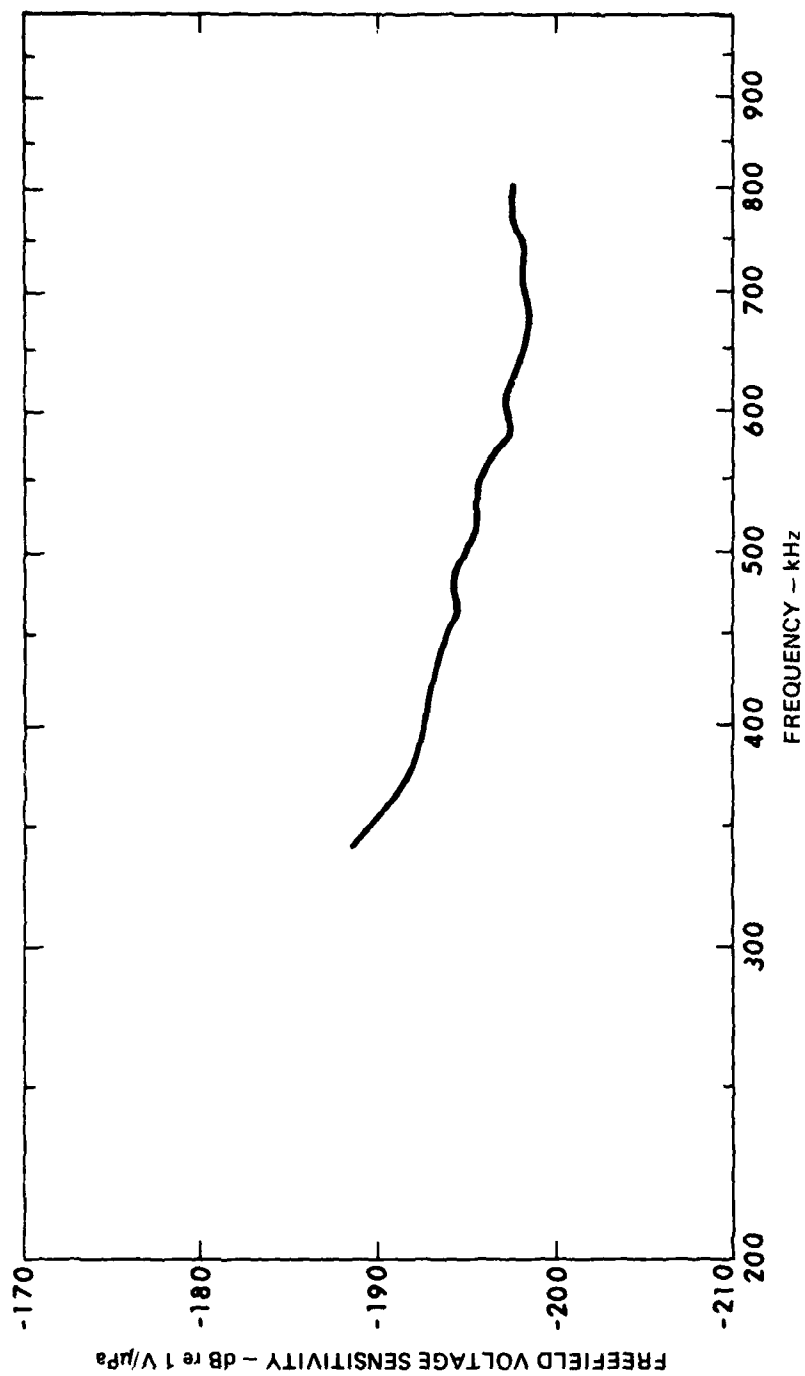


FIGURE B.13
FREEFIELD VOLTAGE SENSITIVITY FOR THE ARL 239-1
HIGH FREQUENCY RECEIVER WITH 40 dB GAIN

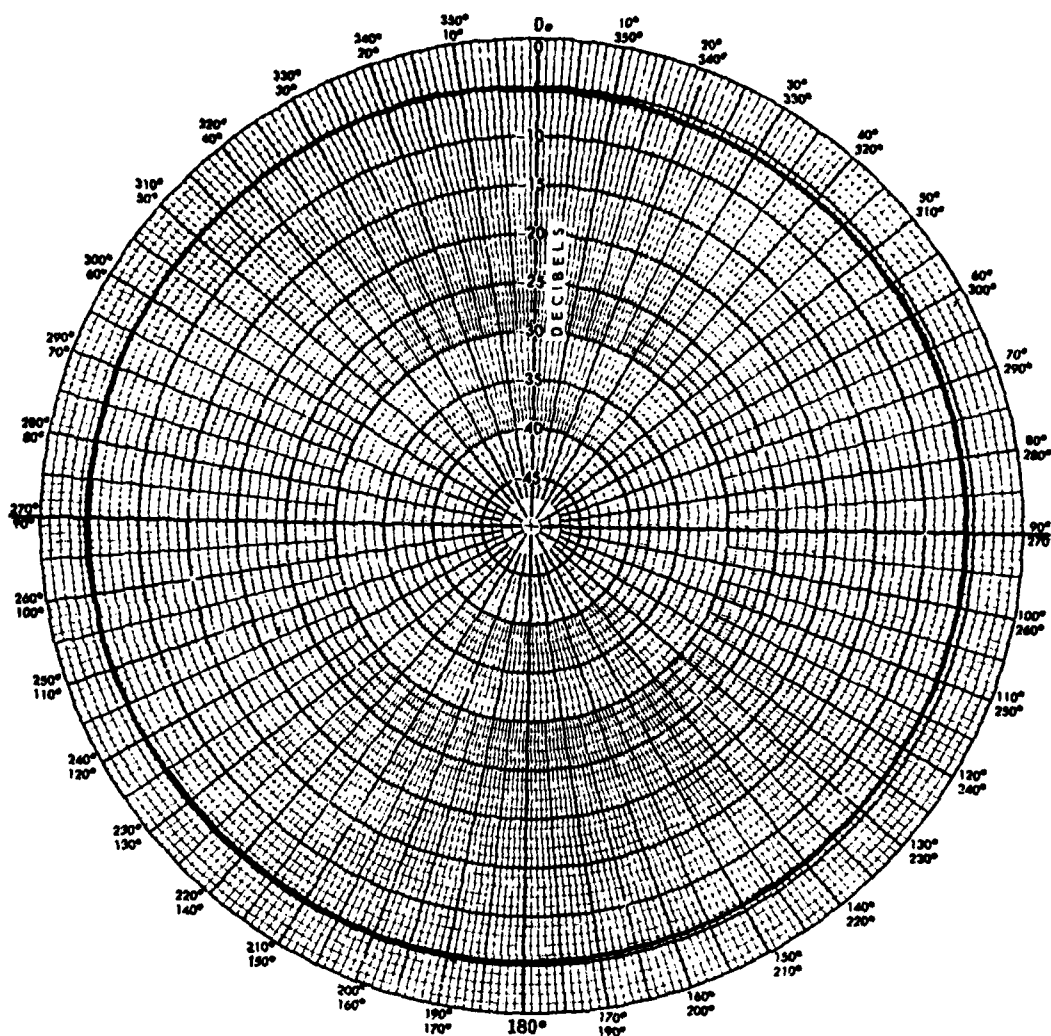


FIGURE B.14
FARFIELD BEAM PATTERN AT 150 kHz FOR THE
ARL 239-1 HYDROPHONE MEASURED AT 11.7 m

The freefield voltage sensitivity for the USRD-E-27-130P is shown in Fig. B.15. The frequency response varies a maximum of 3.5 dB from 70 to 400 kHz. Before use, the USRD-E-27-130P low frequency receive system was always calibrated with respect to the output of the ARL 239-1 receive system.

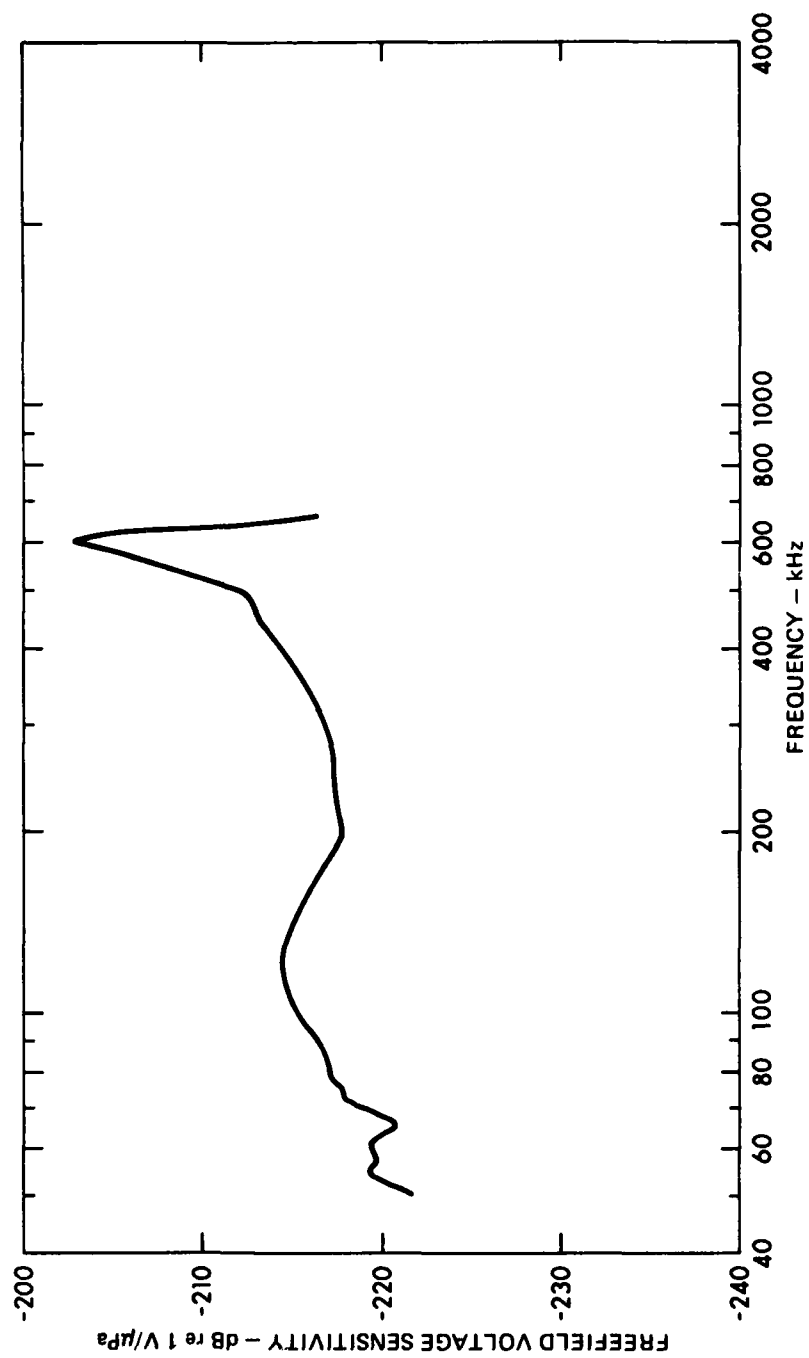


FIGURE B.15
FREEFIELD VOLTAGE SENSITIVITY, E27-130P

ARL:UT
AS-81-572
JMH - GA
6-16-81

APPENDIX C
ANALYSIS OF UNGATED SECONDARY OUTPUTS

The analysis presented in this appendix is directed toward the determination of secondary signal characteristics for the broadband parametric array based on a measurement at a hydrophone output. In particular, an evaluation of the artificial removal of energy which is characteristic of the impulse response of the hydrophone is addressed. This removal of energy is accomplished by the use of a receive signal gate and is termed artificial since it is simply ignored or replaced by zero for purposes of secondary signal analysis.

Given the experimental parameters of Table IV.1 and a circular piston of radius 8.89 cm, the secondary outputs as a function of angle off-axis measured at 23.6 m with a primary peak sound pressure level of 195.2 dB re 1 μ Pa are shown in Fig. C.1. Although the duration of the outputs is over about 60 μ sec, only the first 20 μ sec is representative of the secondary signal produced by the broadband parametric array with Gaussian pulse carrier transmission. The remaining 40 μ sec of the output result from the impulse response of the receiving hydrophone. It should be noted that a number of hydrophones were implemented and in each case the signal portions of the outputs were very similar and the remainder of the outputs (many of which were an additional 40-100 μ sec in duration) were very different. In going from on-axis to off-axis angles, the signal portion of the output changes from a dependence on the second derivative with respect to time of the square of the Gaussian envelope function to the first derivative. During this transition, the portion of the output that results from the impulse response of the hydrophone retains its longer duration features. Since the gain at each angle was adjusted to normalize the waveform presentations, subtle features in the output are obscured by noise as the angle off-axis is increased.

A more detailed analysis of the transient hydrophone outputs may be considered in the frequency domain. In Figs. C.2 and C.3 the normalized power density spectra for the measured hydrophone outputs

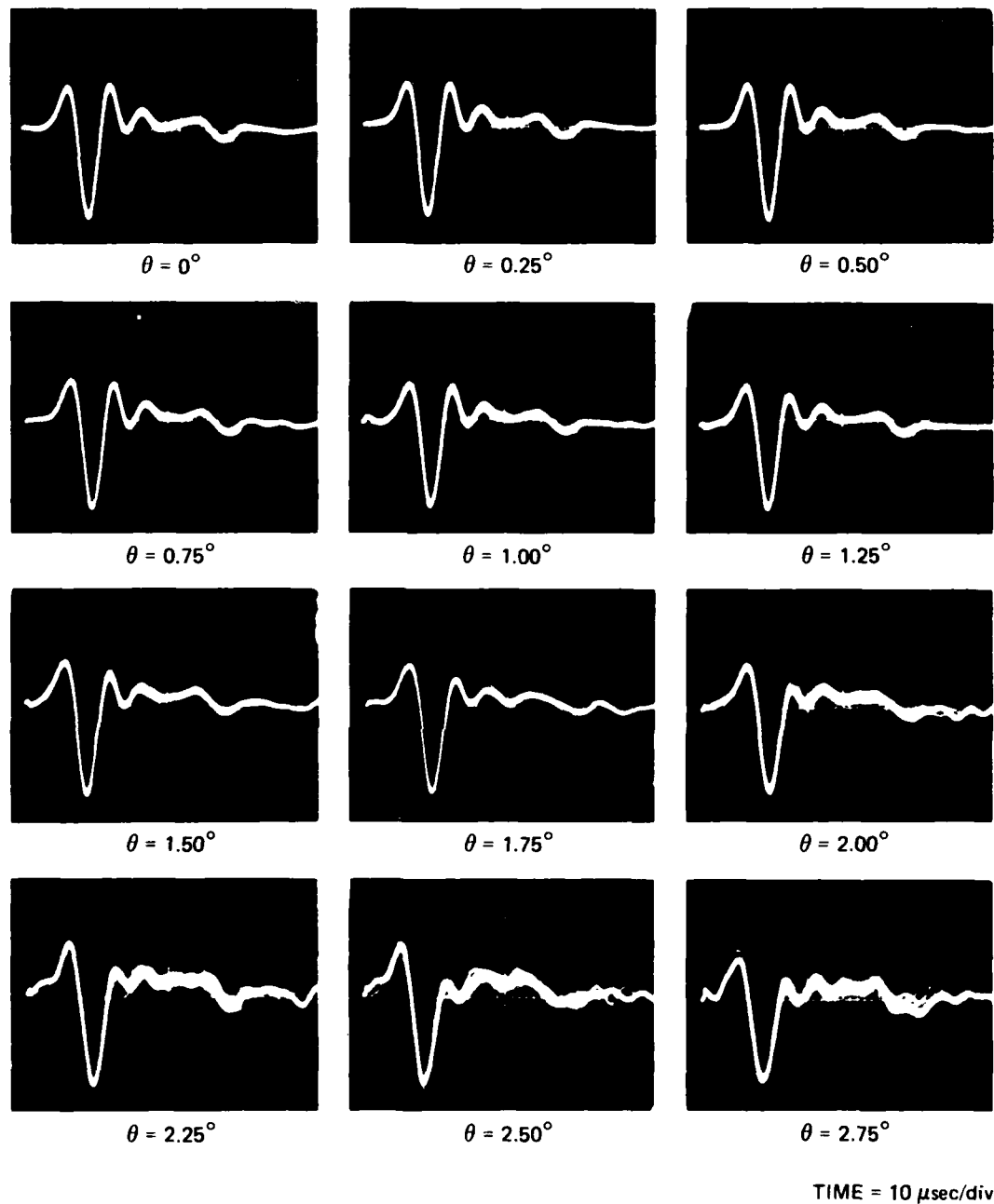


FIGURE C.1
OFF-AXIS ACOUSTIC WAVEFORMS FOR THE BROADBAND PARAMETRIC ARRAY
 UNGATED, $f(t)$ - GAUSSIAN, $f_{1c} = 600$ kHz, $SPL_1 = 195.2$ dB re 1μ Pa
 $a = 8.89$ cm, $R_0 = 10.07$ m, $r = 23.6$ m

ARL:UT
 AS-81-577
 JMH - GA
 6-16-81

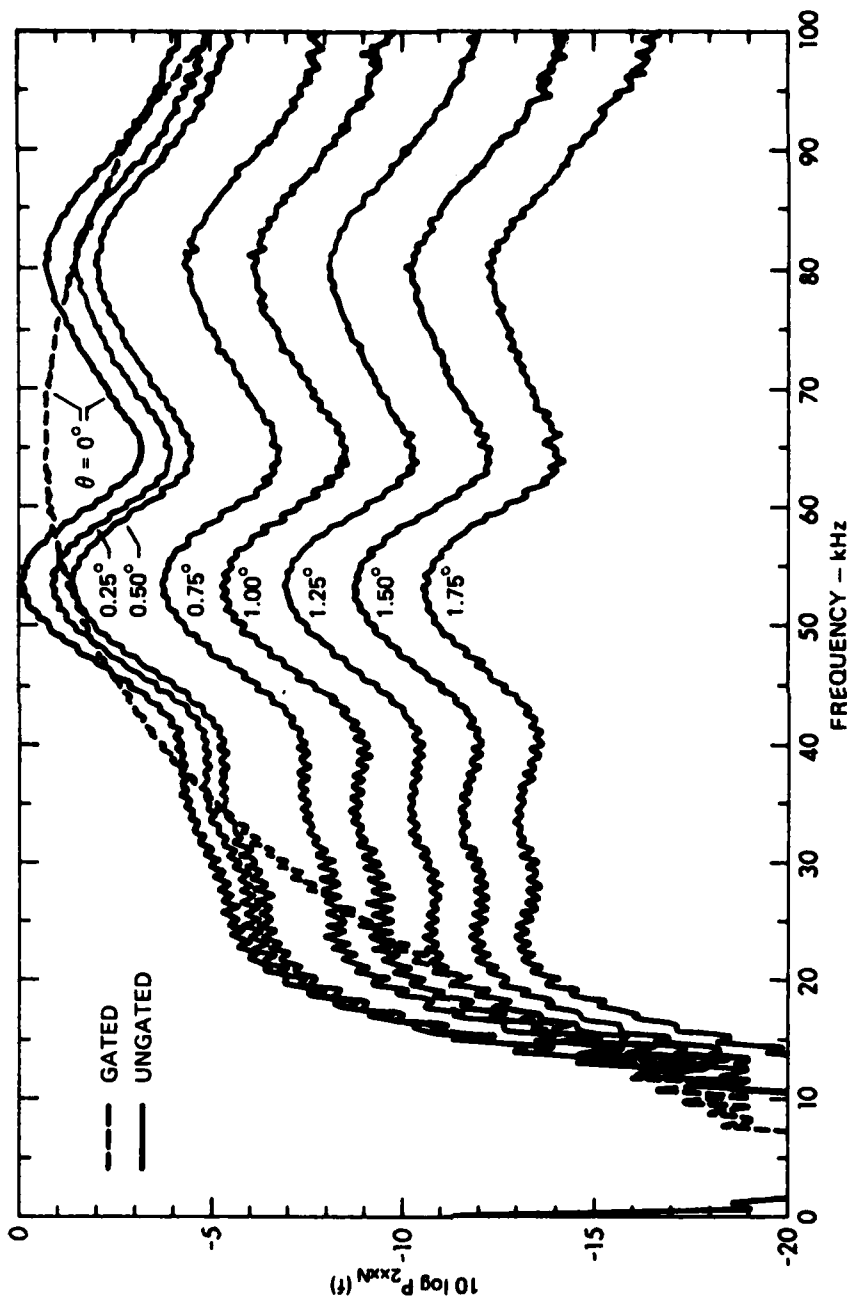


FIGURE C.2
 NORMALIZED POWER DENSITY SPECTRA FOR THE BROADBAND PARAMETRIC ARRAY
 AT OFF-AXIS ANGLES FROM 0.00° TO 1.75°
 $f(t)$ - GAUSSIAN, $f_{1c} = 600$ kHz, $SPL_1 = 195.2$ dB re $1 \mu\text{Pa}$
 $a = 8.89$ cm, $R_0 = 10.07$ m, $r = 23.6$ m

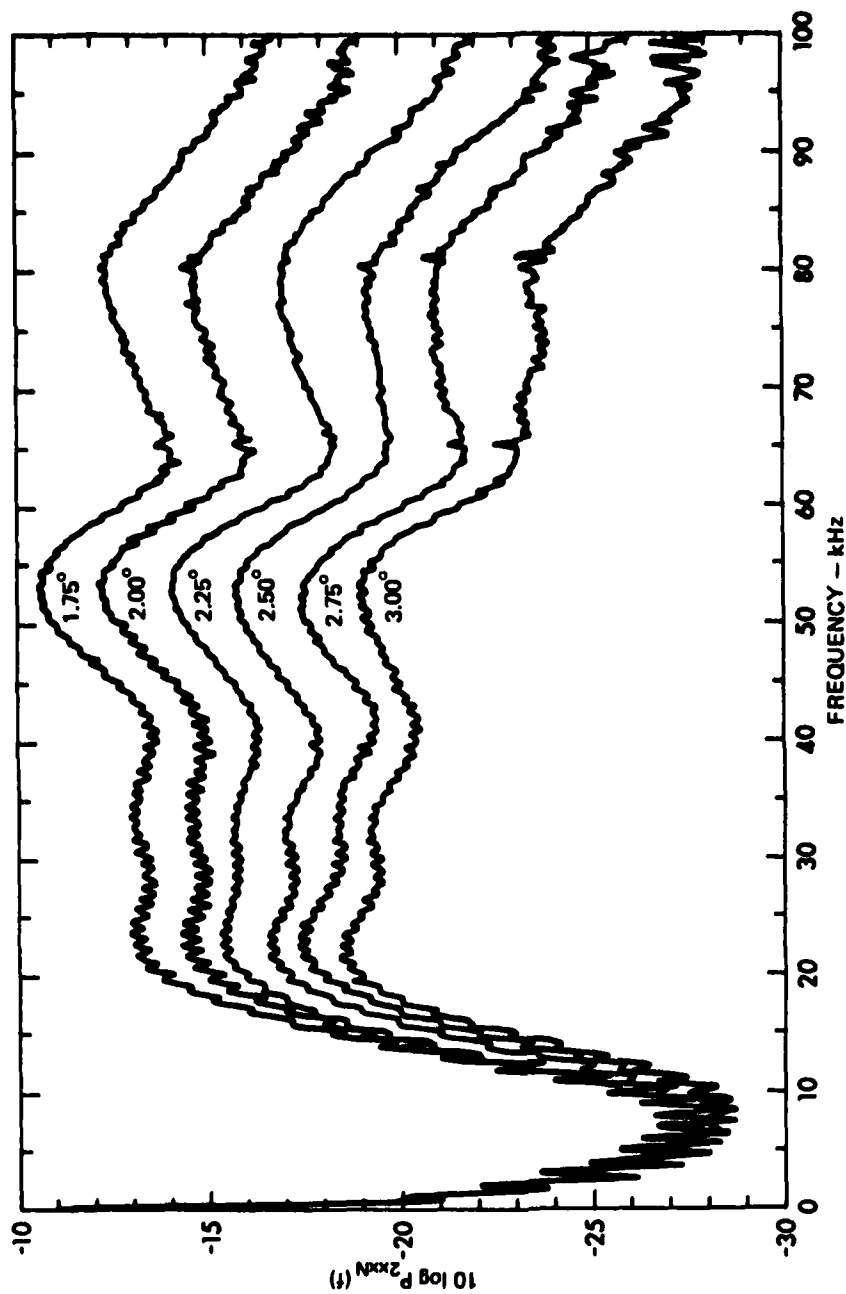


FIGURE C.3
NORMALIZED POWER DENSITY SPECTRA FOR THE BROADBAND PARAMETRIC ARRAY
AT OFF-AXIS ANGLES FROM 1.75° TO 3.00°

UNGATED, $f(t)$ - GAUSSIAN, $f_{ic} = 600$ kHz, $SPL_1 = 195.2$ dB re 1 μ Pa
 $a = 8.89$ cm, $R_0 = 10.07$ m, $r = 23.6$ m

are indicated. Each spectrum has 250 Hz resolution and was computed from the incoherent average of 100 spectra. The energy at 60 Hz and the low level oscillations on the spectrum, especially at low frequencies, are artifacts of the analysis and not a part of the data.

On-axis, the power spectrum of the ungated hydrophone output roughly extends from about 20 kHz to above 100 kHz with prominent peaks at about 55 and 81 kHz. As the angle off-axis is increased, the overall level decreases and the decrease in level of the higher frequency components is progressively greater than for the lower frequency components. This behavior is the effect of the off-axis transfer function for the broadband parametric array.

The hydrophone output may be represented by

$$O(t) = i(t) * h(t) \quad , \quad (C.1)$$

where

$O(t)$ is the hydrophone output,

$i(t)$ is the hydrophone input, and

$h(t)$ is the hydrophone impulse response (0 for $t < 0$).

When a receive signal gate is applied to the hydrophone output, the relationship becomes

$$O_g(t) = O(t) U(t) = (U(t) * h(t)) \quad (C.2)$$

where

$O_g(t)$ is the gated time function, and

$U(t)$ is a gate function

$$= \begin{cases} 0 & 0 \leq t \leq T \\ 1 & \text{otherwise} \end{cases} .$$

If the output is a transient that is shorter in duration than the impulse response, then the application of the gate function may be

interpreted as restrictions on the duration of the impulse response and Eq. (C.2) may be written as

$$O_g(t) = i(t) * h'(t) \quad , \quad (C.2)$$

where

$$h'(t) = \begin{cases} h(t) & 0 \leq t \leq T \\ 0 & \text{otherwise} \end{cases} .$$

From Eq. (C.2), the gate function, is shown to reject energy that results from the signal input, but is part of a bandlimited or signal dependent impulse response. The effect of the gate is to reduce the energy at the higher peaks in the bandlimited frequency response of the hydrophone.

Transforming to the frequency domain, the relationships are written

$$\mathcal{F}\{O_g(t)\} = \mathcal{F}\{U(t)\} * \left[\mathcal{F}\{i(t)\} \mathcal{F}\{h(t)\} \right] \quad (C.3)$$

$$= \mathcal{F}\{i(t)\} \mathcal{F}\{h'(t)\} \quad (C.4)$$

From Eqs. (C.3) and (C.4) it is shown that an additional effect of the gate function is to diminish resolution by averaging or smoothing in the frequency domain.

The effects of the receive signal gate are shown in Fig. (C.2) where the normalized power density spectrum for the on-axis gated signal is indicated. This spectrum may be compared directly with the on-axis ungated spectrum. It is observed that the levels at the frequency peaks near 20 kHz, 53 kHz, and 81 kHz have been reduced and that averaging or smoothing in the frequency domain has produced a smooth quasi-Gaussian shaped curve.

REFERENCES

1. P. J. Westervelt, "Parametric Acoustic Array," J. Acoust. Soc. Am. 35, 535 (1963).
2. M. J. Lighthill, "On Sound Generated Aerodynamically," Proc. R. Soc. London, Ser. A 211, 565 (1952).
3. M. J. Lighthill, "On Sound Generated Aerodynamically, II," Proc. R. Soc. London, Ser. A 222, 1 (1954).
4. P. J. Westervelt, "Scattering of Sound by Sound," J. Acoust. Soc. Am. 29, 199 (1957).
5. P. J. Westervelt, "Scattering of Sound by Sound," J. Acoust. Soc. Am. 29, 934 (1957).
6. R. T. Beyer, "Parameter of Nonlinearity in Fluids," J. Acoust. Soc. Am. 32, 719 (1960).
7. T. G. Muir, "An Analysis of the Parametric Acoustic Array for Spherical Wave Fields," Applied Research Laboratories Technical Report No. 71-1 (ARL-TR-71-1), Applied Research Laboratories, The University of Texas at Austin, May 1971 (Dissertation) (AD 723241).
8. J. J. Truchard, "A Theoretical and Experimental Investigation of the Parametric Acoustic Receiving Array," Applied Research Laboratories Technical Report No. 74-17 (ARL-TR-74-17), Applied Research Laboratories, The University of Texas at Austin, May 1974 (Dissertation).
9. P. J. Westervelt, "Virtual Sources in the Presence of Real Sources," in Nonlinear Acoustics, Proceedings of the 1969 Applied Research Laboratories Symposium, Applied Research Laboratories, The University of Texas at Austin, 1970.
10. P. M. Morse and K. U. Ingard, Theoretical Acoustics (McGraw-Hill Book Company, Inc., New York, 1968), p. 322.
11. J. L. S. Bellin and R. T. Beyer, "Experimental Investigation of an End-Fire Array," J. Acoust. Soc. Am. 34, 1051 (1962).

12. H. O. Berktaay and B. V. Smith, "End-Fire Array of Virtual Sound Sources Arising from the Interaction of Sound Waves," Electronics Letters 1, 6 (1965).
13. H. Hobaek, "Experimental Investigation of an Acoustical End-Fired Array," J. Sound Vib. 6, 460 (1967).
14. V. A. Zverev and A. I. Kalachev, "Measurements of the Scattering of Sound by Sound in the Superposition of Parallel Beams," Sov. Phys.-Acoust. 14, 173 (1968). (English translation)
15. T. G. Muir and J. E. Blue, "Experiments on the Acoustic Modulation of Large Amplitude Waves," J. Acoust. Soc. Am. 46, 227 (1969).
16. J. N. Tjøtta and S. Tjøtta, "Nonlinear Interaction of Two Sound Beams," J. Acoust. Soc. Am. 37, 174 (1965).
17. H. O. Berktaay, "Possible Exploitation of Nonlinear Acoustics in Underwater Transmitting Applications," J. Sound Vib. 2, 435 (1965).
18. V. R. Lauvstad, J. Naze, and S. Tjøtta, "Nonlinear Interaction of Two Sound Waves," Mat.-Nat. Wer. No. 12, Arbok University, Bergen, Norway, 1964.
19. V. R. Lauvstad, "Nonlinear Interaction of Two Monochromatic Sound Waves," Acustica 16, 191 (1965).
20. H. O. Berktaay, "Nonlinear Interaction of Two Sound Beams," J. Acoust. Soc. Am. 38, 480-481(L) (1965).
21. H. O. Berktaay, "Some Proposals for Underwater Transmitting Applications of Nonlinear Acoustics," J. Sound Vib. 6, 244 (1967).
22. R. H. Mellen and M. B. Moffett, "A Model for Parametric Sonar Radiation Design," JUA(USN) 22, 105 (1972).
23. M. B. Moffett and R. H. Mellen, "Model for Parametric Sources," J. Acoust. Soc. Am. 61, 325-337 (1977).
24. M. B. Moffett, R. H. Mellen, and W. L. Konrad, "Parametric Acoustic Sources of Rectangular Aperture," J. Acoust. Soc. Am. 63, 1326 (1978).
25. H. O. Berktaay and D. J. Leahy, "Farfield Performance of Parametric Transmitters," J. Acoust. Soc. Am. 55, 539-546 (1974).

26. R. L. Rolleigh, "Difference Frequency Pressure within the Interaction Region of a Parametric Array," J. Acoust. Soc. Am. 58, 964 (1975).
27. B. K. Novikov, O. V. Rudenko, and S. I. Soluyan, "Parametric Ultrasonic Radiators," Sov. Phys.-Acoust. 23, 354-357 (1977).
28. B. K. Novikov, M. S. Rybachek, and V. I. Timoshenko, "Interaction of Diffracting Sound Beams and the Theory of Highly Directional Ultrasonic Radiators," Sov. Phys.-Acoust. 23, 354-357 (1977).
29. M. B. Bennett and D. T. Blackstock, "Parametric Array in Air," J. Acoust. Soc. Am. 57, 562-568 (1975).
30. F. H. Fenlon, "On the Performance of a Dual Frequency Parametric Source via Matched Asymptotic Solutions of Burgers' Equation," J. Acoust. Soc. Am. 55, 35 (1974).
31. F. H. Fenlon and F. S. McKendrie, "Axisymmetric Parametric Radiation - A Weak Interaction Model," J. Acoust. Soc. Am. 66, 534-547 (1979).
32. J. N. Tjøtta and S. Tjøtta, "Nonlinear Interaction of Two Collinear Spherically Spreading Sound Beams," J. Acoust. Soc. Am. 67, 484 (1980).
33. T. G. Muir and J. G. Willette, "Parametric Acoustic Transmitting Arrays," J. Acoust. Soc. Am. 52, 1481 (1972).
34. J. E. Blue, "Nonlinear Acoustics in Undersea Communications," JUA(USN) 22, 177 (1972).
35. B. V. Smith, "An Experimental Study of a Parametric End-Fire Array," J. Sound Vib. 14, 7-21 (1971).
36. M. B. Bennett and C. M. Slack, "Design of a Curved-Face Parametric Projector," J. Acoust. Soc. Am. 63, 339 (1978).
37. J. M. Huckabay, "An Experimental Study of Parametric Acoustic Arrays with Intermediate Directivity in Water," J. Acoust. Soc. Am. 67 (1980).
38. M. B. Moffett and R. H. Mellen, "On Parametric Source Aperture Factors," J. Acoust. Soc. Am. 60, 581 (1976).
39. H. Hobaek and M. Vestrheim, "Parametric Acoustic Arrays Formed by Diverging Sound Beams," Acustica 37, 74 (1977).

40. M. B. Moffett, "Two Acoustic Transient Effects in Liquids," Ph.D. Dissertation, Brown University, Providence, R.I., 1970.
41. M. B. Moffett, "Large Amplitude Pulse Propagation, A Transient Effect," in "Nonlinear Acoustics," Proceedings of the 1969 Applied Research Laboratories Symposium, Applied Research Laboratories, The University of Texas at Austin, 1970.
42. M. B. Moffett, P. J. Westervelt, and R. T. Beyer, "Large Amplitude Pulse Propagation--A Transient Effect, I," J. Acoust. Soc. Am. 47, 1473 (1970).
43. M. B. Moffett, P. J. Westervelt, and R. T. Beyer, "Large Amplitude Pulse Propagation--A Transient Effect, II," J. Acoust. Soc. Am. 49, 339 (1971).
44. H. M. Merklinger, "High Intensity Effects in the Nonlinear Acoustic Parametric Array," Ph.D. Thesis, Electrical Engineering Department, University of Birmingham, Birmingham, England, 1971.
45. H. M. Merklinger, "Improved Efficiency in the Parametric Transmitting Array," J. Acoust. Soc. Am. 58, 784 (1975).
46. R. H. Mellen and D. G. Browning, "Self-Demodulation of Acoustic Waves," in "Nonlinear Acoustics," Proceedings of the 1969 Applied Research Laboratories Symposium, Applied Research Laboratories, The University of Texas at Austin, 1970.
47. B. A. Davy and E. L. Hixson, "Acoustic Self-Demodulation of Predistorted Pulsed Carriers," Technical Report No. 121, Electronics Research Center, The University of Texas at Austin, 21 February 1972.
48. T. G. Muir, "A Parametric Model for Porpoise Sonar," unpublished paper, Applied Research Laboratories, The University of Texas at Austin (1974).
49. T. G. Muir and J. E. Blue, "Transient Response of the Parametric Acoustic Array," in "Nonlinear Acoustics," Proceedings of the 1969 Applied Research Laboratories Symposium, Applied Research Laboratories, The University of Texas at Austin, 1970.
50. M. B. Moffett and P. Mello, "Parametric Acoustic Sources of Transient Signals," J. Acoust. Soc. Am. 66, 1182 (1979).

51. R. L. Rolleigh, "An Analysis of the Broadband Parametric Array with Gaussian Primary Directivity Patterns," submitted to J. Acoust. Soc. Am. (1979).
52. K. Mize, R. L. Rolleigh, W. F. Bateman, and H. Boehme, "Signal Processing Theory for the Nonlinear Acoustic Transmissions," Applied Research Laboratories Technical Report No. 77-15 (ARL-TR-77-15), Applied Research Laboratories, The University of Texas at Austin, 21 February 1977.
53. D. T. Blackstock, "History of Nonlinear Acoustics and a Survey of Burgers' and Related Equations," in "Nonlinear Acoustics," Proceedings of the 1969 Applied Research Laboratories Symposium, Applied Research Laboratories, The University of Texas at Austin, 1970.
54. D. T. Blackstock, "Propagation of Plane Sound Waves of Finite Amplitude in Nondissipative Fluids," J. Acoust. Soc. Am. 34, 9 (1962).
55. D. T. Blackstock, "Connection Between the Fay and Fubini Solutions for Plane Waves of Finite Amplitude," J. Acoust. Soc. Am. 39, 1019 (1966).
56. K. Brinkmann, "Die Wechselwirkung Zweier Ebener Schallwellen Endlicher Amplitude Und Gleicher Ausbreitungsrichtung," Acustica 20, 92 (1968).
57. J. F. Bartram and P. J. Westervelt, "Nonlinear Attenuation and the Parametric Array," paper presented at the 83rd meeting of the Acoustical Society of America, Buffalo, New York, April 1972.
58. J. F. Bartram, M. A. Chramiec, and G. M. Walsh, "Applications of Finite Amplitude Acoustics to High Resolution Depth Sounding-- Vol. 2, Theory, Stabilized Beam Feasibility, and System Concepts," Raytheon Company, Portsmouth, Rhode Island, 1971.
59. V. A. Zverev, A. I. Kalachev, and N. S. Stepanov, "Utilization of Nonlinear Effects in Underwater Acoustics," Sov. Phys.-Acoust. 13, 324-326 (1968).

60. R. H. Mellen, D. G. Browning, and W. L. Konrad, "Parametric Sonar Transmitting Array Measurements," J. Acoust. Soc. Am. 49, 932(L) (1971).
61. J. G. Willette and M. B. Moffett, "Harmonics of the Difference Frequency in Saturation Limited Parametric Sources," J. Acoust. Soc. Am. 62, 1377 (1977).
62. F. H. Fenlon, "An Extension of the Bessel-Fubini Series for a Multiple-Frequency CW Acoustic Source of Finite Amplitude," J. Acoust. Soc. Am. 51, 284-289 (1972).
63. F. H. Fenlon, "A Recursive Procedure for Computing the Nonlinear Spectral Interactions of Progressive Finite Amplitude Waves in Nondispersive Fluids," J. Acoust. Soc. Am. 50, 1299-1312 (1971).
64. A. G. Findeisen and S. A. Means, "A Self-Demodulation Detection Resistant Echo Ranging Sonar" (U), Final Report under Contract N00024-74-C-1069, Item 0005, Applied Research Laboratories Technical Report No. 75-16 (ARL-TR-75-16), Applied Research Laboratories, The University of Texas at Austin, 6 March 1975. (CONFIDENTIAL)
65. J. S. Bendat and A. G. Piersol, Engineering Applications of Correlation and Spectral Analysis (John Wiley and Sons, Inc., New York, 1980) p. 81.
66. M. Schulkin and H. W. Marsh, "Sound Absorption in Sea Water," J. Acoust. Soc. Am. 34, 864 (1962).
67. R. V. Ceen and N. G. Pace, "Acoustic Signals in Marine Sediments Due to Waterborne Parametric Arrays," Proceedings of the Institute of Acoustics, The University of Bath, Bath, England, 1979.
68. C. deBoor, "CADRE: An Algorithm for Numerical Quadrature," Mathematical Software, edited by John R. Rice (Academic Press, New York, 1971), Chap. 7.
69. J. A. Shooter, T. G. Muir, and D. T. Blackstock, "Acoustic Saturation of Spherical Waves in Water," J. Acoust. Soc. Am. 55, No. 1, 54 (1974).

70. D. T. Blackstock, "Nonlinear Acoustics (Theoretical)," Sec. 3n, American Institute of Physics Handbook, 3rd Edition (McGraw-Hill Book Company, Inc., New York), pp. 3-190, 3-193.

4 January 1982

DISTRIBUTION LIST FOR
ARL-TR-82-6
UNDER CONTRACT N00024-79-C-6358
UNCLASSIFIED

Copy No.

1 - 4
5
6
7
8
9
10
11
12
13
14
15 - 16

Commander
Naval Sea Systems Command
Department of the Navy
Washington, DC 20362
Attn: D. Porter (Code 63R1)
C. Smith (Code 63R)
E. Liszka (Code 63R1)
D. Baird (PMS 409B)
J. Neely (PMS 409C)
F. Romano (Code 63R)
D. Rilling (Code 63X11)
P. Hornick (Code 63X)
C. Fox (Code 632B)
B. Roderick (PMS-409)
L. Epperly (Code 63D)
Library (Code 9961)

17

Commanding Officer
Office of Naval Research
Arlington, VA 22217
Attn: A. Ellenthorp (Code 220)
R. Obrochta (Code 230)
CAPT A. Gilmore (Code 220)
P. Rodgers (Code 425AC)
L. Hargrove (Code 412)

18
19

Commanding Officer
Naval Research Laboratory
Underwater Sound Reference Detachment
P.O. Box 8337
Orlando, FL 32856
Attn: J. Blue
L. Van Buren

20

Commanding Officer
Naval Ocean Research and Development Activity
NSTL Station, MS 39529
Attn: S. Marshall

21

Office of Naval Research Detachment
ONRDET Code 420D
NSTL Station, MS 39529
Attn: A. Anderson (Code 420D)

Distribution List for ARL-TR-82-6 under Contract N00024-79-C-6358 (Cont'd)

Copy No.

22	Chief of Naval Operations Department of the Navy Washington, DC 20350 Attn: B. Gilchrist
23	Defense Advanced Research Projects Agency 1400 Wilson Boulevard Arlington, VA 22209 Attn: T. Kooij
24	V. Simmons
25	Naval Electronic Systems Command Department of the Navy Washington, DC 20360 Attn: R. Mitnik
26	Commander Naval Material Command Department of the Navy Washington, DC 20360
27	Officer in Charge New London Laboratory Naval Underwater Systems Center Department of the Navy New London, CT 06320 Attn: M. Moffett
28	W. Konrad
29	R. Mellen
30	Commander Naval Ocean Systems Center Department of the Navy San Diego, CA 92152 Attn: E. Hamilton
31	J. Reeves
32	R. Anderson
33	R. McLennan
34	H. Bucher
35	Commanding Officer Newport Laboratory Naval Underwater Systems Center Department of the Navy Newport RI 02840 Attn: T. Fitzgerald

Distribution List for ARL-TR-82-6 under Contract N00024-79-C-6358 (Cont'd)

Copy No.

	Commanding Officer Naval Oceanographic Office NSTL Station, MS 39522
36	Attn: W. Jobst
37	G. Lewis
	Commanding Officer Naval Coastal Systems Center Panama City, FL 32407
38	Attn: D. Skinner
39	L. Flax
	Commander Naval Surface Weapons Center White Oak Laboratory Silver Spring, MD 20910
40	Attn: Library
	Superintendent Naval Postgraduate School Monterey, CA 93940
41	Attn: H. Medwin
42	Library
43 - 55	Commanding Officer and Director Defense Technical Information Center Cameron Station, Building 5 5010 Duke Street Alexandria, VA 22314
	Applied Physics Laboratory University of Washington 1013 N.E. 40th Street Seattle, WA 98105
56	Attn: Library
	Applied Research Laboratory The Pennsylvania State University P.O. Box 30 State College, PA 16801
57	Attn: F. Fenlon
	Scripps Institution of Oceanography University of California, San Diego La Jolla, CA 92037
58	Attn: J. Curry
59	G. Shor

Distribution List for ARL-TR-82-6 under Contract N00024-79-C-6358 (Cont'd)

Copy No.

Electronic and Electric Engineering Division
University of Technology
Loughborough, Leicestershire
UNITED KINGDOM
60 Attn: R. Griffiths

Matematisk Institutt
Allegaten
53-55
5014 Bergen-U
NORWAY
61 Attn: S. Tjøtta
62 J. Tjøtta

Norwegian Institute of Technology
Electronics Research Laboratory
N-7034 Trondheim-NTH
NORWAY
63 Attn: J. Hovem

Department of Physics
The University of Texas at Austin
Austin, TX 78712
64 Attn: W. Nolle
65 T. Griffy

Department of Electrical Engineering
The University of Texas at Austin
Austin, TX 78712
66 Attn: E. Powers
67 A. Dougal
68 F. Bostick
69 T. Itoh
70 E. Hixson

Department of Mechanical Engineering
The University of Texas at Austin
Austin, TX 78712
71 Attn: W. Hadden

Westinghouse Electric Corporation
Oceanic Division
Ocean Research Laboratory
Box 1488
Annapolis, MD 21404
72 Attn: A. Nelkin
73 P. Welton

Distribution List for ARL-TR-82-6 under Contract N00024-79-C-6358 (Cont'd)

Copy No.

	Admiralty Underwater Weapons Establishment
	Portland, DORSET DT5 2JJ
	UNITED KINGDOM
74	Attn: I. Roebnck
75	T. Curtis
76	R. Bugler
77	D. Weston
	Director
	SACLANT ASW Research Centre
	La Spezia, ITALY
78	Attn: R. Goodman
	Scientific Director of GERDSM
	(Group d'Etude et de Recherche de Detection Sous-Marines)
	Le Brusc
	B.C.A.N. Toulon
	FRANCE
79	Attn: H. Mermoz
80	B. Lucas
	Norwegian Defense Research Establishment
	P.O. Box 115
	N-2191 Horton, NORWAY
81	Attn: M. Vestrheim
	Acoustics Laboratory
	Technical University of Denmark
	Building 352 Lundtoftevej 100
	DK-2800 Lyngby
	DENMARK
82	Attn: L. Bjorno
	Marine Physical Laboratory
	The Scripps Institution of Oceanography
	The University of California/San Diego
	San Diego, CA 92152
83	Attn: V. Anderson
84	W. Hodgkiss
	Defence Research Establishment Atlantic
	P.O. Box 101.
	Dartmouth, Nova Scotia B2Y 3Z7
	CANADA
85	Attn: H. M. Merklinger

Distribution List for ARL-TR-82-6 under Contract N00024-79-C-6358 (Cont'd)

Copy No.

86	School of Physics University of Bath Claverton Down BATH BA2 7AY UNITED KINGDOM Attn: H. O. Berkday
87	Department of Physics Hendrix College Conway, AR 72032 Attn: R. Rolleigh
88	Department of Physics Texas Tech University Lubbock, TX 79409 Attn: B. Sandlin
89	Engineering & Applied Sciences Yale University New Haven, CT 06520 Attn: P. Schultheiss
90	Department of Physics Brown University Providence, RI 02912 Attn: P. Westervelt
91	R. Beyer
92	Department of Electrical and Electronic Engineering University of Birmingham P.O. Box 363 Birmingham, B15 2TT ENGLAND Attn: N. Chotiros
93	B. Smith
94	Department of Physics The University of Auckland Private Bag Auckland, NEW ZEALAND Attn: A. Kibblewhite
95	Department of Physics The Catholic University 620 Michigan Ave., N.E. Washington, DC 20017 Attn: Library

Distribution List for ARL-TR-82-6 under Contract N00024-79-C-6358 (Cont'd)

Copy No.

96	Raytheon Company Submarine Signal Division West Main Road Portsmouth, RI 02871 Attn: R. Pridham J. Bartram G. Walsh
97	
98	
99	Tracor, Inc. 6500 Tracor Lane Austin, TX 78701 Attn: D. Webster D. Rohde
100	
101	Tracor, Inc. 1601 Research Blvd. Rockville, MD 20850 Attn: R. Urick
102	Tracor, Inc. 3420 Kenyon Street, Suite 209 San Diego, CA 92110 Attn: V. Holiday
103	Bolt Beranek and Newman, Inc. 50 Moulton Street Cambridge, MA 02138 Attn: J. Barger
104	Bolt Beranek and Newman, Inc. 1300 N. 17th Street Arlington, VA 22209 Attn: H. Cox
105	Radian Corporation P.O. Box 9948 Austin, TX 78766 Attn: R. Reeves
106	National Instruments 8900 Shoal Creek Austin, TX Attn: J. Truchard
107	Department of Electrical Engineering Texas A&M University College Station, TX 77843 Attn: Library

Distribution List for ARL-TR-82-6 under Contract N00024-79-C-6358 (Cont'd)

Copy No.

108	Western Offshore Group, Inc. 4204 Farhills Austin, TX 78731 Attn: W. Huckabay
109	Getty Oil Company Exploration and Production Research Center P.O. Box 42214 Houston, TX 77042 Attn: S. Rutherford
110	Acoustic Systems, Inc. 600 Norman Firestone Road Goleta, CA 93017 Attn: J. Fish
111	Radian Corporation 7927 Jones Branch Drive Suite 600, Lancaster Bldg. McLean, VA 22102 Attn: J. Caruthers
112	U.S. Geological Survey Denver West Bldg. No. 2 1527 Cole Blvd. Golden, CO 80401 Attn: R. Seely (MS 964)
113	Office of Naval Research Resident Representative Room No. 582 Federal Building Austin, TX 78701
114	Electroacoustics Group, ARL:UT
115	Signal Physics Group, ARL:UT
116	Environmental Sciences Group, ARL:UT
117	Sonar Engineering Group, ARL:UT
118	Physical Sciences Group, ARL:UT
119	Sonar Development Division, ARL:UT
120	Lewie M. Barber, ARL:UT
121	John A. Behrens, ARL:UT

Distribution List for ARL-TR-82-6 under Contract N00024-79-C-6358 (Cont'd)

Copy No.

122	David T. Blackstock, ARL:UT
123	H. Boehme, ARL:UT
124	Rod P. Chervenka, ARL:UT
125	James R. Clynch, ARL:UT
126	George P. Coble, ARL:UT
127	Bernie R. Criswell, ARL:UT
128	Charles R. Culbertson, ARL:UT
129	Allen G. Findeisen, ARL:UT
130	Karl C. Focke, ARL:UT
131	Terry L. Foreman, ARL:UT
132	Marshall E. Frazer, ARL:UT
133	Robert A. Gammill, ARL:UT
134	Greer S. Garrett, ARL:UT
135	Tommy G. Goldsberry, ARL:UT
136	Loyd Hampton, ARL:UT
137	Arthur C. Holly, ARL:UT
138	Claude W. Horton, Sr., ARL:UT
139	John M. Huckabay, ARL:UT
140	Stephen P. Hufnagel, ARL:UT
141	Herbert L. Kuntz, ARL:UT
142	Robert A. Lamb, ARL:UT
143	Chester M. McKinney, ARL:UT
144	E. Eugene Mikeska, ARL:UT

Distribution List for ARL-TR-82-6 under Contract N00024-79-C-6358 (Cont'd)

Copy No.

145	T. G. Muir, ARL:UT
146	S. Patrick Pitt, ARL:UT
147	Lee A. Puckett, ARL:UT
148	Thomas L. Riley, ARL:UT
149	Louis D. Rolleigh, ARL:UT
150	Jack A. Shooter, ARL:UT
151	Robert H. Stokes, ARL:UT
152	James A. Tencate, ARL:UT
153	Lewis A. Thompson, ARL:UT
154	Bernard F. Tupa, ARL:UT
155	Reuben H. Wallace, ARL:UT
156	Gary R. Wilson, ARL:UT
157	Suk Wang Yoon, ARL:UT
158	Library, ARL:UT
159 - 184	Reserve, ARL:UT